Experimental analysis of the unsteady flow and instabilities in a high-speed multistage compressor

Nicolas Courtiade

ECOLE CENTRALE DE LYON

Ecole Doctorale MEGA

Mécanique, Energétique, Génie Civil et Acoustique

THESE

Experimental analysis of the unsteady flow and instabilities in a high-speed multistage compressor

Soutenue le 22 Novembre 2012 par

Nicolas COURTIADE

En vue d'obtenir le titre de

DOCTEUR DE L'ECOLE CENTRALE DE LYON

Spécialité

MECANIQUE

Devant le jury composé de :

M. ROGER	Professeur, Ecole Centrale de Lyon	*Président du Jury*
I. DAY	Professeur, University of Cambridge	*Rapporteur*
J. SEUME	Professeur, Leibniz Universität Hannover	*Rapporteur*
E. LIPPINOIS	Responsable BE compresseurs HP Snecma	*Examinateur*
X. OTTAVY	Chargé de recherche, Ecole Centrale de Lyon	*Co-dir. de thèse*
I. TREBINJAC	Professeur, Ecole Centrale de Lyon	*Directrice de thèse*

Aeroplane
by The Red Hot Chili Peppers – Slap bass score

Remerciements

Comme ne le dit pas le proverbe, le meilleur pour le début (du mémoire tout du moins). Au moment où j'écris ces remerciements, ca y est, tout est bouclé. Mémoire rédigé, soutenance soutenue, thèse thésée. Bref, la fin d'une belle aventure, commencée un peu par hasard il y a trois ans. Ecrire une thèse, ça ne se fait pas seul, et les pages qui suivent n'auraient certainement pas vu le jour sans les nombreuses personnes qui m'ont entourées ces dernières années. C'est le moment de les remercier. Chaleureusement.

Sans surprise, mes premiers remerciements vont à Xavier Ottavy, qui a su brillamment m'encadrer durant ces trois ans. Travailler ensemble aura été un plaisir. Les heures passées à noircir un tableau blanc ou blanchir un tableau noir pour résoudre l'énigme des instabilités de CREATE (la solution se trouve dans ces pages !), se battre pour une virgule dans un papier jusqu'à 3h du mat'… Tout un programme! Mais surtout, plus qu'un directeur de thèse, c'est un ami, un pote, un « doode » que j'ai rencontré. En même temps, avec un zicos amateur de jeux-vidéo, ça ne pouvait que marcher! Merci pour tous ces bons moments passés aux quatre coins du monde, souvent dans des troquets (sans oublier le baptême de moto!). Go Canucks go!

Je souhaite également remercier Isabelle Trebinjac, ma directrice de thèse, et André « Dédé » Vouillarmet pour m'avoir incité et encouragé à faire ma thèse et initié aux turbomachines… et aux jeux de mots douteux. Merci pour votre encadrement, votre bonne humeur (particulièrement visible lors des montées d'octave d'Isabelle), et le soutien dans les moments durs!

Aucun des résultats présentés dans ce mémoire n'auraient vu le jour sans la « XP-team » du sous-sol, rencontrée tous les jours pour les traditionnels cafés du matin et du midi, les chevaliers blancs du banc, j'ai nommé Gilbert Halter « El Cigarillo » notre maitre torréfacteur, Benoit Paoletti le gourou de la pression instationnaire et ardent défenseur des bélugas, Sebastien Goguey qui me survivra, grand slappeur devant l'éternel et fan inconditionnel de Jean-Pierre François et pour finir Pierre Laucher, le missionnaire de la chapelle Fistine, véritable gladiateur du calembour à deux balles, malheureusement tombé maintes fois dans l'arène… Je me souviendrai longtemps de certains essais vraiment mémorables, aussi intenses qu'excitants (je pense notamment aux tests du système anti-pompage - mais non ça n'a pas pompé !). Bref, merci les gars, pour la qualité des mesures, mais surtout pour votre bonne humeur et pour votre accueil au sein de l'équipe.

Je souhaite vivement remercier les professeurs Ivor Day et Jorg Seume de m'avoir fait l'honneur de corriger mon travail. C'est quelque chose d'avoir dans son jury les têtes de série de sa biblio' ! Merci pour vos critiques et remarques pertinentes qui m'ont permis de finaliser mon mémoire, ainsi que pour la séance de questions très intéressante lors de la soutenance, où j'ai vraiment eu l'impression d'être traité comme un véritable chercheur plutôt que comme un étudiant. Merci également aux autres membres du jury Eric Lippinois et Michel Roger. Je remercie particulièrement Michel pour ses éclaircissements acoustiques qui m'auront été bien utiles cette dernière année…

Liste des publications

[1] N. Courtiade, X. Ottavy and N. Gourdain, « Experimental Investigation of Rotating Stall in a High-Speed Multi-Stage Axial Compressor », presented at the 9th **European Turbomachinery Conference**, Istanbul, Turkey, 2011.

[2] M. Mersinligil, J.-F. Brouckaert, N. Courtiade and X. Ottavy, « A High Temperature High Bandwidth Fast Response Total Pressure Probe for Measurements in a Multistage Axial Compressor », published in **Journal of engineering for gas turbines and power**, 2012, Vol. 134, No. 6

[3] N. Courtiade and X. Ottavy, « Modal decomposition for the analysis of the rotor-stator interactions in a high-speed multistage compressor », presented at the 10th International Symposium on Experimental Computational Aerothermodynamics of Internal Flows, Brussels, Belgium, 2011. Published in **Journal of Thermal Science** Vol. 21, No. 3

[4] X. Ottavy, N. Courtiade and N. Gourdain, « Experimental and CFD Methods for Flow Investigation in a High-speed Multi-stage Compressor», 2011-07-B34412. In press for **Journal of Propulsion and Power**.

[5] M. Mersinligil, J.-F. Brouckaert, N. Courtiade and X. Ottavy, « On using fast response pressure sensors in aerodynamic probes to measure total temperature and entropy generation in turbomachinery blade rows », in press for **Journal of engineering for gas turbines and power,** GTP-12-1437, 2012.

[6] N. Courtiade and X. Ottavy, « Experimental study of surge precursors in a high-speed multistage compressor », presented at the **ASME Turbo Expo 2012**, Copenhagen, Denmark, 2012. In press for **Journal of Turbomachinery** ref TURBO12-1152.

[7] N. Courtiade and X. Ottavy, « Acoustic resonance triggering rotating stall and surge in a multistage high-speed axial compressor», proposed for the 10th **European Turbomachinery Conference**, Lappeenranta, Finland, 2013.

Résumé

Ce travail est le produit d'une collaboration entre le LMFA (Laboratoire de Mécanique des Fluides et d'Acoustique, Ecole Centrale de Lyon – France), Snecma et le Cerfacs. Il vise à étudier l'écoulement se développant dans le compresseur haute-vitesse axial de 3.5 étages CREATE (Compresseur de Recherche pour l'Etude des effets Aérodynamique et TEchnologique – vitesse de rotation : 11543 tr/min, vitesse en tête de rotor 1 : 313 m/s), conçu et construit par Snecma et étudié au LMFA sur un banc d'essai de 2 MW. Pour étudier l'écoulement, des mesures stationnaires de pression et température, de la vélocimétrie laser et des mesures rapides de pression statique et totale ont été utilisées. L'analyse se concentre sur deux aspects principaux : l'étude de l'écoulement aux points de fonctionnement stables, avec un intérêt tout particulier pour les interactions rotor-stator, et l'étude des instabilités apparaissant dans la machine à faibles débits.

La description de l'écoulement instationnaire aux points stables est faite par le biais de mesures de pression statique en parois, de pression totale et de vitesse, mais également de température totale, entropie et angle d'incidence du fluide. Il est montré que la complexité et l'instationnarité de l'écoulement dans un compresseur multiétagé augmente fortement à l'arrière de la machine à cause des interactions entre les roues fixes et mobiles. Ainsi, une méthode d'analyse modale basée sur la décomposition de Tyler et Sofrin a été développée pour analyser ces interactions. Elle est d'abord appliquée aux mesures de pression afin d'extraire les contributions de chaque roue. Il est ainsi montré que les interactions complexes de pression dans CREATE peuvent être réduites à trois principaux types d'interactions. La méthode de décomposition est enfin appliquée au champ d'entropie dans toute la machine extrait de calculs CFD URANS réalisés par le Cerfacs, afin d'évaluer l'impact des interactions sur les performances de CREATE en terme de génération de pertes.

La dernière partie de ce travail est dédié à l'analyse des instabilités apparaissant dans CREATE à faible débit. Il est montré que des ondes de pression tournantes apparaissent aux points stables et augmentent en amplitude à mesure qu'on se rapproche de la ligne de pompage, jusqu'à atteindre une taille critique induisant l'apparition d'une cellule de décollement tournant sur toute la hauteur de veine. Cette cellule entraîne la machine en pompage en seulement quelques tours. L'étude de ces ondes de pression, et la compréhension de leur véritable nature sont réalisées grâce à l'application d'un modèle analytique aux mesures expérimentales. Une description précise du déclenchement et du cycle du pompage est également faite grâce aux mesures de pression statique au dessus des rotors. Un système de contrôle anti-pompage développé au laboratoire et basé sur la détection de l'amplitude des ondes de pression est finalement décrit.

Mots clés: compresseur axial haute-vitesse multi-étages, mesures expérimentales haute-fréquence, écoulements instationnaires, interactions rotor-stator, instabilités, résonance acoustique, pompage

Abstract

The present work is a result of collaboration between the LMFA (Laboratoire de Mécanique des Fluides et d'Acoustique, Ecole Centrale de Lyon – France), Snecma and the Cerfacs. It aims at studying the flow in the 3.5-stages high-speed axial compressor CREATE (Compresseur de Recherche pour l'Etude des effets Aérodynamique et TEchnologique - rotation speed: 11543 RPM, Rotor 1 tip speed: 313 m/s), designed and built by Snecma and investigated at LMFA on a 2-MW test rig. Steady measurements, as well as laser velocimetry, fast-response wall static and total pressure measurements have been used to experimentally investigate the flow. The analysis focuses on two main aspects: the study of the flow at stable operating points, with a special interest on the rotor-stator interactions, and the study of the instabilities arising in the machine at low mass flow rates.

The description of the unsteady flow field at stable operating points is done through measurements of wall-static pressure, total pressure and velocity, but also total temperature, entropy and angle of the fluid. It is shown that the complexity and unsteadiness of the flow in a multistage compressor strongly increases in the rear part of the machine, because of the interactions between steady and rotating rows. Therefore, a modal analysis method developed at LMFA and based on the decomposition of Tyler and Sofrin is presented to analyze these interactions. It is first applied to the pressure measurements, in order to extract the contributions of each row. It shows that all the complex pressure interactions in CREATE can be reduced to three main types of interactions. The decomposition method is then applied to the entropy field extracted from URANS CFD calculations performed by the Cerfacs, in order to evaluate the impact of the interactions on the performance of the machine in term of production of losses.

The last part of this work is devoted to the analysis of the instabilities arising in CREATE at low mass flows. It shows that rotating pressure waves appear at stable operating points, and increase in amplitude when going towards the surge line, until reaching a critical size provoking the onset a full span stall cell bringing the machine to surge within a few rotor revolutions. The study of these pressure waves, and the understanding of their true nature is achieved through the experimental results and the use of some analytical models. A precise description of the surge transient through wall-static pressure measurements above the rotors is also provided, as well as a description of a complete surge cycle. An anti-surge control system based on the detection of the amplitude of the pressure waves is finally proposed.

Keywords: high-speed multistage axial compressor, high-frequency experimental measurements, unsteady flows, rotor-stator interactions, instabilities, acoustic resonance, surge

Contents

Nomenclature

Latin characters:

A	Amplitude
c	Sound speed
C_P	Heat capacity – Pressure recovery ratio of a total pressure probe
CFD	Computational Fluid Dynamics
DAC	Data Acquisition Chain
DFT	Discrete Fourier Transform
k	Wave number
k_x	Axial wave number
F	Frequency
$f_{m,n}^{cut}$	Cut-off frequency of a wave with m azimuthal and n radial mode orders
F_i	Frequency associated to a mode order i
H	Enthalpy
HBT	Harmonic Balance Technique
L	Loaded operating point
LDA	Laser Doppler Anemometry
LE	Leading Edge
$\dot{m}$	Mass flow
M	Mach number
M_x	Axial Mach number
M_θ	Circumferential Mach number
Nn	Nominal shaft speed
NS	Near Surge operating point
O	Offset
P_s	Static pressure
P_t	Total pressure
PE	Peak Efficiency operating point
PS	Pressure side
RANS	Reynolds Averaged Navier-Stokes
RSI	Rotor-Stator Interactions
s	Entropy
S	Sensitivity
SM	Surge Margin
SS	Suction side
t	Time
T_{16}	Reduced temporal period of CREATE
T_s	Static temperature
T_t	Total temperature
TCF	Tip Clearance Flow
TCV	Tip Clearance Vortex
TCVB	Tip Clearance Vortex Breakdown
TSV	Tip Separation Vortex
TE	Trailing Edge

U	Rotation speed of the blades
URANS	Unsteady Reynolds Averaged Navier-Stokes
V	Velocity
W	Relative velocity
(x,r,θ)	Cylindrical coordinates
(x,y,z)	Cartesian coordinates

Greek characters :

α	Angle of the flow
α_s	Stagger angle
β	Yaw angle of a probe – Angle of incidence of a wave with the machine axis
γ	Laplace coefficient – Pitch angle of a probe
δ,Δ	Variations
ε	Small quantity
Θ_{16}	Reduced azimuthal period of CREATE
λ	Wave-length
μ	Efficiency
Π	Pressure ratio
ρ	Volumic mass
σ	Standard deviation
Φ	Phase
ω, Ω	Angular frequency
Ω_{shaft}	Rotation speed of the shaft

Exponents:

$\overline{}$	Average
$\widehat{}$	Fourier transform
*	Fluctuations
^{abs}	In the absolute frame
^{flow}	In the frame of flow
^{rel}or ^{rotor}	In the relative frame

Subscripts:

$_{\pm,\pm}$	Upstream resp. downstream travelling wave spinning with resp. against swirl
$_{i,j}$	Matrix coordinates
$_{inlet}$	At the inlet of the machine
$_{outlet}$	At the outlet of the machine
$_{raw}$	Raw data before non-dimensionalization
$_{ref}$	Reference quantity
$_{sensor}$	Data returned by a sensor before calibration
$_{std}$	Standardized data
$_{T}$ or $_{O}$	Total quantity

Introduction

In order to reduce their operating cost, the performance of the plane engines has been continuously increased over the last six decades. This research of improvement has accelerated in the last few years so as to face two major issues. First, the IATA (International Air Transport Association) forecasts a growth of the passenger transportation of around +5% per year, and a growth of cargo transportation of +12% per year. Then, the rarefaction of the fossil fuel induces an important increase in the price of kerosene. To propose an answer to these challenges, and in a matter of environmental protection, the ACARE (*Advisory Council for Aeronautics Research in Europe*) proposed strong objectives in order to reduce by 2020, among others, the specific fuel consumption by 20% and the CO_2 emission by 50%. Hence, the design of efficient "green" gas turbines points towards **compact, highly efficient,** with **wide operability** machines. The LEAP ® (see Figure 1) developed by CFM, is the perfect example of such engines: equipping the new aircrafts Airbus A320 Neo and Boeing 737 MAX, it offers a reduction of 15 % of the fuel consumption regarding to the current CFM-56 and up to 50 % of reduction of the NOx emissions.

Figure 1 Picture of a LEAP ® engine by CFM

Among all engine components, the compressor remains a critical part, especially regarding its efficiency and stability. For example, a deficit of 1% in the compressor efficiency induces an increase in the specific fuel consumption of the engine between 0.5% and 0.8%. The improvement of a compressor can be done through two main approaches. First, compact designs can be highly benefic for the engines. Indeed, the compressors represent roughly 40 % of the total weight of the machines [29]. A compact design implies a reduction of the compressors stages numbers and shorter axial

distances between the blade rows: the consequences are a higher loading applied to the blades and stronger interactions between the rows. However, the real impact of these interactions on the performances of the machines is still not clear. The second approach is to enhance the safety margin of the compressors, in order to increase their efficiency and reduce their sensitivity to environment disturbances and abrupt changes of operation. Indeed, under specific conditions of over-loading which can typically occur during the take-off phase, the compressors suffer from instabilities like rotating stall or surge inducing a complete flow breakdown. These phenomena, which can be very damaging for the engines, are still not well understood. Their prediction through the detection of precursors is a very important issue for the manufacturers, which tend to oversize the engines to avoid these instabilities.

Therefore, some experimental test-rigs have been developed all around the world to study the complex flows developing in these machines. Most rigs are low-speed, and allow to study relatively "easily" the unsteady flow phenomena and instabilities occurring in compressors. For example, the low-speed 4-stages compressor of Dresden already provides very useful data for the study of rotor-stator interactions ([55], [54]) and rotating stall [56]. However, only a few configurations consider flow conditions close to real engine operating conditions (high-speed flows, multistage machine), mainly due to their cost of development and exploitation. Some of these (rare) high-speed rigs dedicated to multistage compressors are presented in Table 1.

Localization	Number of stages	Tip inlet Mach number	Reference
Purdue University (**USA**)	1.5	0.92	Sanders *et* al [76]
University of Notre Dame (**USA**)	1.5	1.10	Bennington *et al.* [3]
Ishikawajima Harima Heavy Industries, Tokyo (**Japan**)	3	1.35	Nakakita *et al.* [64]
Aachen University (**Germany**)	2	0.89	Ernst *et al.* [25]
Technische Universitat Darmstadt (**Germany**)	1.5	1.35	Biela *et al.* [4]
Gottfried Wilhelm Leibniz Universität Hannover (**Germany**)	4.5	0.94	Fischer and Seume [27]
Ecole Centrale de Lyon (**France**)	3.5	0.92	Present test case – CREATE

Table 1 Overview of some research high-speed multistage compressor test rigs

This thesis thus proposes to study the flow in the 3.5-stage high-speed compressor CREATE, designed and built by SNECMA and investigated at LMFA (Laboratoire de Mécanique des Fluides et d'Acoustique - Ecole Centrale de Lyon – France). This machine is representative of a high-pressure compressor of modern turbojet engines: since the test rig is fully instrumented for unsteady pressure and laser measurements, it is an excellent opportunity to learn more about complex unsteady flows and instabilities found in multistage compressors. The following work will hence be split into three main parts.

After a bibliographic review and a description of the machine, all the measurements achieved in CREATE will be presented. The setup of the measuring techniques will be described in detail, as

they can be very sensitive in a high-speed compressor, because of the severe measuring conditions. A special attention will be paid to the uncertainties of measurements: this point is indeed particularly important, as CREATE has also been designed to become a reference test case for code validation, see for example the work of Riera *et al.* on *ZDES* [74] and Castillon*et al.* [12], [13] on multi-chorochronic calculation.

Then, an analysis of the flow relying on the experimental results at stable operating points will be done. This analysis, based on a modal approach, will focus on the study of the interactions between the rows, particularly strong in a multistage compressor. A modal decomposition method will therefore be presented. It will be applied to the measurements in order to understand the origin of the very complex aerodynamic structures induced by the interactions, and try to evaluate their impact on the performances of the machine.

Finally, a study of the instabilities arising in the machine at low mass flow will be performed. The determination of the nature of surge precursors found well before the flow breakdown and the understanding of the mechanisms responsible for their onset will be a matter of concern. Then, detailed measurements of the surge transient will be provided in order to precisely describe the mechanism of the flow breakdown in a high-speed multistage compressor. An anti-surge control system based on the detection of the precursors will finally be presented.

Chapter I
Aerodynamics in turbomachinery

I.1 Basics of turbomachinery

I.1.1 Functioning of a turbojet engine

The functioning principle of a turbojet engine is relatively simple and is based on the capacity of the air to exchange energy with the machine. The basic simple-flux configuration is composed of four main components: the compressor, the combustion chamber, the turbine and the nozzle, see the left illustration of Figure 2. The air is led into the machine through the compressor, in charge of giving energy to the fluid by increasing its pressure and temperature. It enters then into the combustion chamber where it will be brought to high temperature. In order to increase the efficiency of the combustion, it is important to have the highest possible pressure at the entrance of the chamber. The fluid is expanded and accelerated in the turbine. This generates the energy necessary to run the compressor, this energy being brought through a shaft. Finally, the ejection of air by the nozzle produces the thrust of the engine.

In the case of a double-flux engine, a fan is added at the inlet of the previous configuration, see the right illustration of Figure 2. The secondary flux it generates produces most of the thrust of the engine. Low-pressure compressor and turbine are added to the primary flux to run the fan through a low-pressure shaft. The simple-flux components then become the high-pressure compressor, turbine and shaft respectively: the study of the high-pressure compressor will be the focus of this thesis.
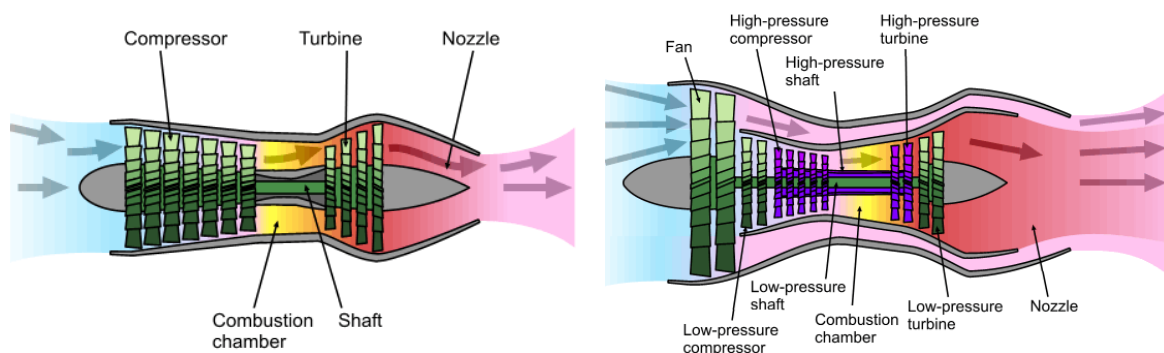
Figure 2 Scheme of a simple-flux (left) and double-flux (right) turbojet engines [23]

I.1.2 The compressors

A compressor stage is constituted of two blade rows: the first is rotating and called rotor, an the second is fixed and called stator, see Figure 3. The duty of the first row is to put the fluid in motion in order to provide it energy by means of kinetic and pressure energy. A part of this energy is

then transformed into pressure energy by the stator. Several stages of compressor are generally put in series to obtain a higher pressure ratio (ratio of the pressure at the outlet of the compressor over the pressure at the inlet).
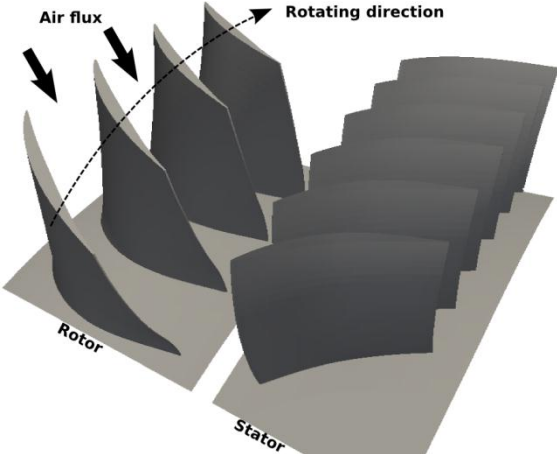
Figure 3 Illustration of a compressor stage

Figure 4 shows typical velocity triangles in a compressor operating in an adapted manner, i.e. the fluid enters and exits the rows nearly parallel to the blades. The fluid enters the rotor with a velocity V_1. In the relative frame, its velocity W_1 is almost parallel to the rotor blades at their leading edge. When traversing the rotor, the tangential velocity of the fluid is increased, which brings its velocity to V_2. Finally, the stator straightens the fluid up, which is then able to enter in another rotor.
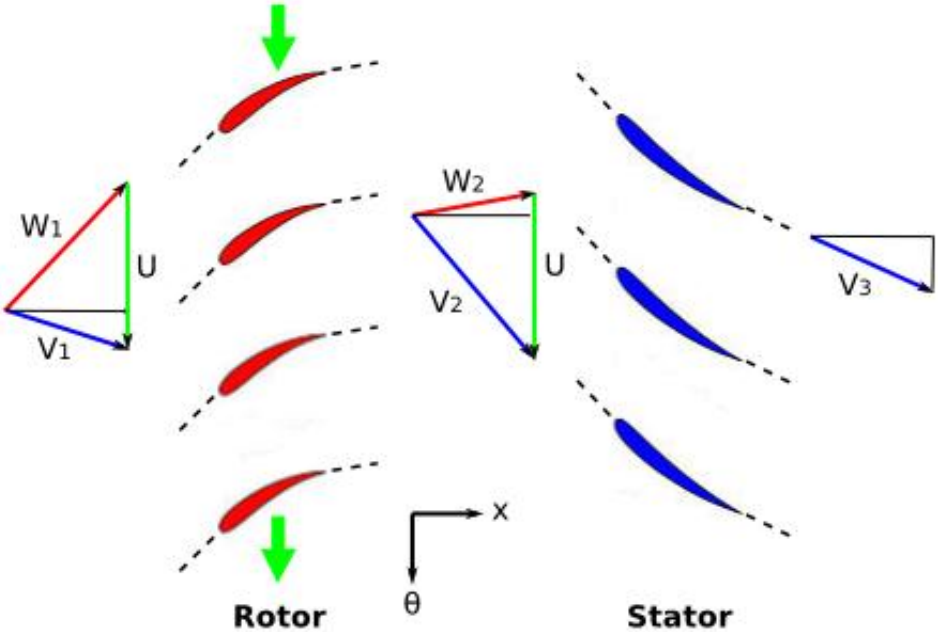
Figure 4 Velocity triangles in a compressor

The energy provided to the fluid by the rotor can be calculated by the Euler relation (I-1) applied to a streamline traversing a bladed zone [65].

$$\Delta h_0 = U \cdot (V_{\theta 2} - V_{\theta 1}) \tag{I-1}$$

I.1.3 Operating range of a compressor

A compressor is characterized by the evolution at a given shaft speed of its pressure ratio and efficiency versus the mass flow rate, see Figure 5. Each couple mass flow – pressure ratio - efficiency defines an operating point. Lines of iso-loading can then be defined as the evolution of any operating point versus the shaft speed. Point A is called choke point, and corresponds to the maximum mass flow able to go through the machine: this limitation is due to a sonic blockage appearing in the machine. The point of peak efficiency B is the design operating point of the machine. In Figure 5, when the mass flow is reduced from point B to C, two antagonist phenomena compete in the compressor: the work increases because of the Euler theorem (the angle of attack of the fluid on the blades increases as the axial velocity decreases), but the losses increase too. At the left of point C, the losses increase faster than the work, which leads to the unstable operating point in D. If the losses increase too much, the rotor is no more able to counter the adverse pressure gradients, and destructive instabilities like rotating stall and surge are likely to arise in the machine (see chapter I.3). Hence, the operating points A and D bound the operating range of a compressor. Today, it is unfortunately very difficult to sharply predict when the instabilities will occur. Therefore, the motorists define a surge margin (see Figure 6) to avoid bringing the machine too close to the surge line, this implying a reduction of the pressure ratio between 10% and 30% [31].
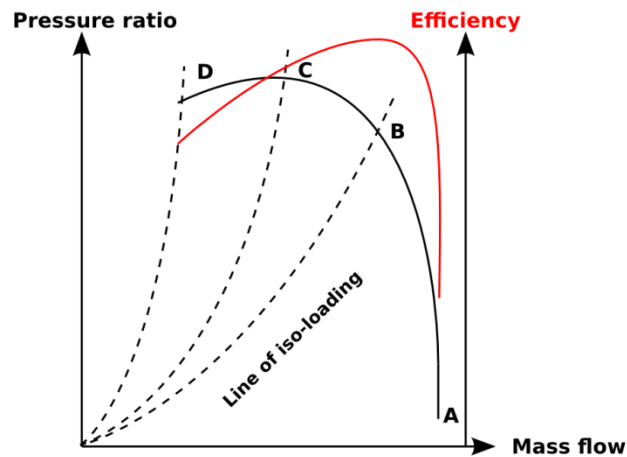
Figure 5 Performance lines of a compressor
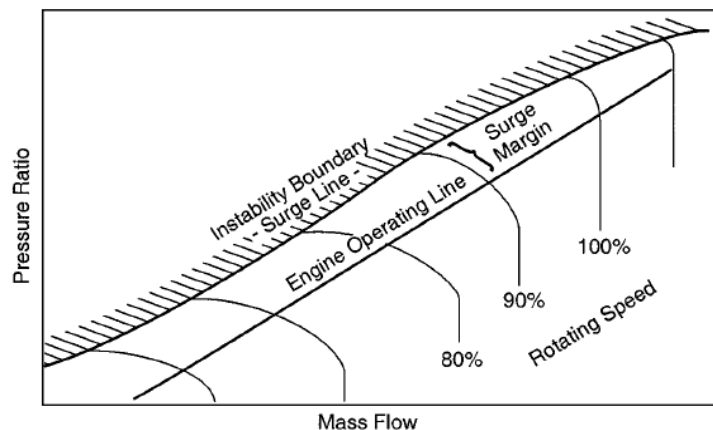
Figure 6 Compressor pumping characteristic, Paduano *et al.* (2001) [70]

I.1.4 Unsteadiness of the flow in a compressor

Due to the relative motion of the rotors blades to the stators blades, the flow in a compressor is highly unsteady: the free stream is indeed perturbed by all the rows which interact together via their wakes, potential effects, tip leakage flow etc… A classification of the different unsteady phenomena inspired by Callot (2002, [9]) is visible on Figure 7. The study of the aperiodic phenomena is not the subject of this thesis. It will rather focus on the rotor-stator interactions (*RSI*) appearing at stable operating points, and on the aerodynamic instabilities arising in the compressor CREATE at near surge operating point.
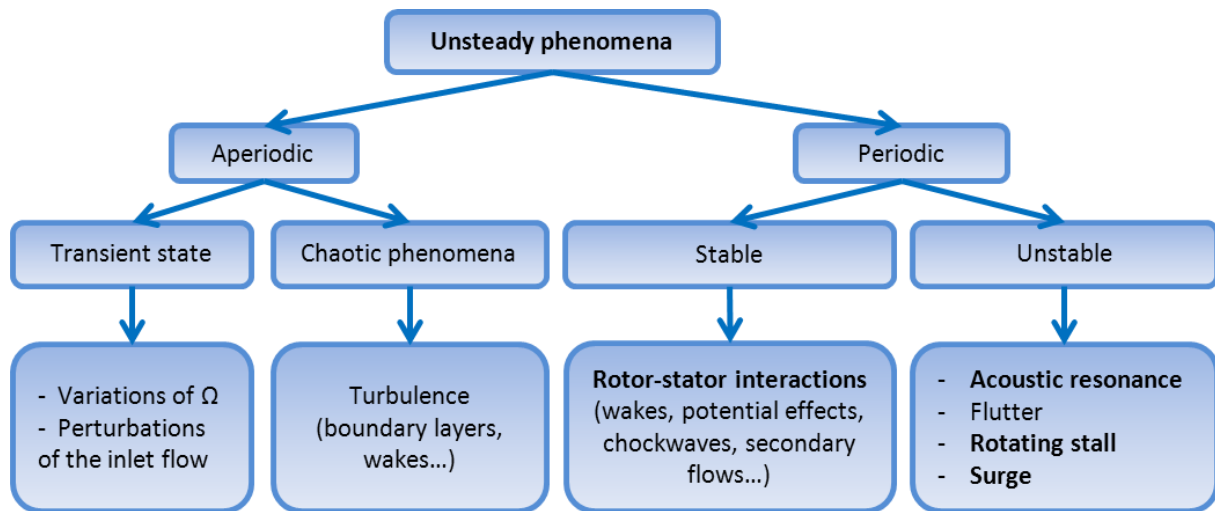
Figure 7 Classification of the unsteady phenomena in a compressor

I.2 Main aerodynamic structures encountered in a compressor

In the compressor CREATE, four main aerodynamic structures are responsible for the unsteadiness of the flow: the wakes, the potential effects, the tip-clearance flows and the wall boundary layers developing at hub and shroud. Other aerodynamic phenomena also affect the flow, but their influence is of less importance. Let us cite among others: the corner stalls, the recirculations of fluid under the stator vanes or the injection of hot fluid in the vein.

I.2.1 The wakes

The wakes are emitted at the trailing edges of the blades and only affect the downstream rows. They are produced by the viscosity effects around the blades (boundary layers) and are characterized by strong losses and low velocity in the frame of the row. Inside the wakes, the flow is very turbulent. Figure 8 shows the entropy field in the first stage of CREATE (the figure has been stretched in a matter of confidentiality): the wakes of the first rotor, visible through the zones of high entropy they induce, are chopped by the blades of stator 1 before they impact rotor 2. The blades of

this rotor spin at the same speed than these of rotor 1. Therefore, they do not chop once more the wakes of rotor 1, but because the number of blades of rotor 2 is different than in rotor 1, each inter-row passage receives a different flow: the resulting flow field is hence highly unsteady.
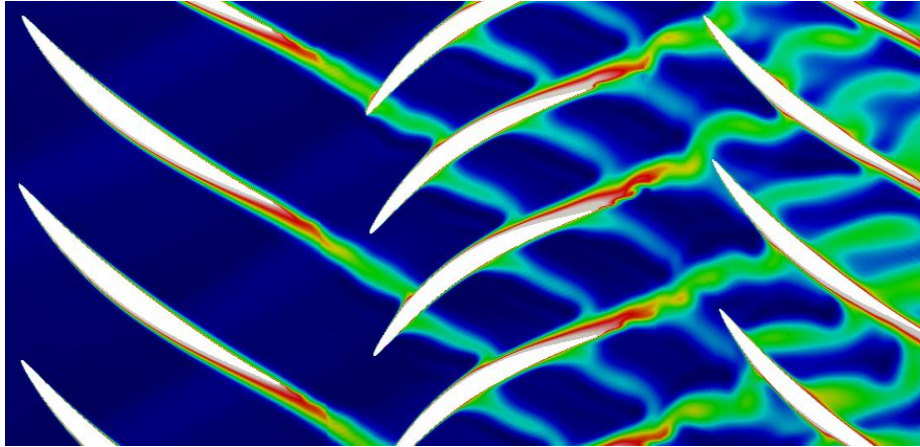
Figure 8 Visualization of the wakes in the first stage of CREATE

The mechanism of decay of the wakes, directly responsible for their influence on the downstream rows, has been highly studied. Three main phenomena are responsible for this decay. The first one is the viscous mixing, which reduces the velocity deficit of the wakes regarding to the free stream.

The second one is linked to the wake stretching when traversing the downstream row and is the principal cause of dissipation. Indeed, the wakes emitted for example by a rotor are sliced by the blades of the downstream stator in segments of length equal to the blade pitch, see Figure 8, and are therefore stretched when traversing the stator. Sanders *et al.* (2002, [76]) explain that in a first approximation, the Kelvin theorem imposes to the circulation of a segment of wake to be constant. Therefore, to maintain a constant vorticity, the wake gets thinner when stretching: the velocity deficit being proportional to its width, the stretching of the wake accelerates its decay. Van Zante *et al.*[89] have demonstrated in 2002 that this phenomenon also called "wake recovery" is the main mechanism of wake decay. Poensgen and Gallus [71] had also noticed in 1990 that the presence of a downstream stator induced a decay of the wakes of a rotor twice faster than an isolated rotor configuration.

Finally, the last mechanism called "negative jet" is due to the velocity deficit of the wake in comparison with the free stream. This produces a fluid accumulation on the pressure sides of the blades, as visible on Figure 9 extracted from Mailach *et al.* (2008, [52]). The velocity triangle at rotor inlet shows indeed that a slip velocity is responsible for the accumulation on the pressure sides. Therefore, the wakes get locally thinner in the blade passages near suction side and thicker near pressure side which thickens the boundary layers. This phenomenon is clearly visible on the second row of Figure 8. This mechanism of fluid transport induces also contra-rotating vortices, the fluid coming from the wakes being ejected near the pressure sides and then replaced by clean flow at the suction sides.
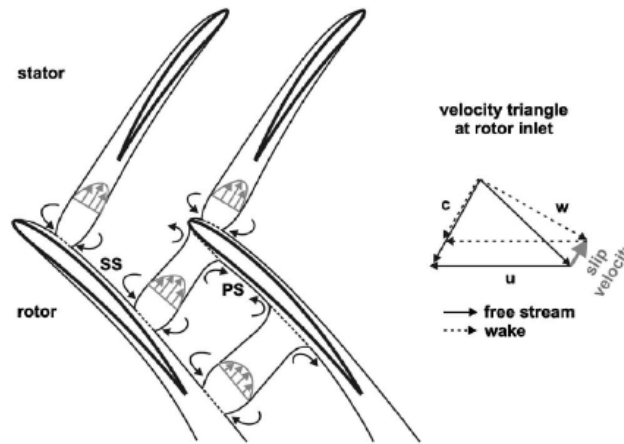
Figure 9 Illustration of the slicing of the wakes at the rows interface (Mailach *et al.*, 2007,[52])

I.2.2 The potential effects

The potential effects emitted by a row correspond to the adaptation of the downstream and upstream pressure field to the presence of the blades. These effects propagate upstream (only for a subsonic flow) and downstream as pressure waves. The axial damping D of these effects can be estimated by relation (I-2) (Leboeuf [49])

$$D(x) = exp(-2\pi\sqrt{1 - M^2}\frac{x}{\Delta\theta})$$ (I-2)

Where x is the axial distance from the emission point, $\Delta\theta$ the blade pitch and M the Mach number.

Hence, the potential effects are few damped in the case of a transonic flow (M≈1) and can propagate far from the source in the machine. The influence of the potential effects is all the more strong when the inter-row distance is reduced.

I.2.3 The tip clearance flow

In most of compression systems, a gap exists between the tip of the rotor blades and the casing. This tip gap induces a leakage flow which reduces the work of the machine (decrease in the pressure forces) and generates strong losses. The structure of the tip clearance flow (*TCF*) is highly unsteady. Lakshminarayana *et al.* (1995,[48]) showed that it depends on numerous parameters, as the pressure difference between the pressure side and the suction side, the size of the gap, the shape of the blades… At the exit of the tip clearance region, a main vortex is generated along the blade, see Figure 10. It interacts with the free stream. Other small induced vortices are also formed between the blade and the main tip clearance vortex (*TCV*). Note that tip separation vortices (*TSV*) can also be found at the rear part of the blade. Numerical studies of the complex interactions between the different vortical structures of the tip clearance flow using Large-Eddy Simulation have notably been performed lately by You *et al.* [86],[87].

The trajectory of the *TCV* has great influence on the stability of the machine, whether the vortex flows downstream in the blade passages or aligns on the leading edges of the blades (Tan *et al.*,2010,[79], for more details, see chapter I.3). Hence, many studies, like März *et al.* in 2002 [58], focused on the *TCF* and show that an increase in the tip clearance induces a decrease in the stability of the compressor.
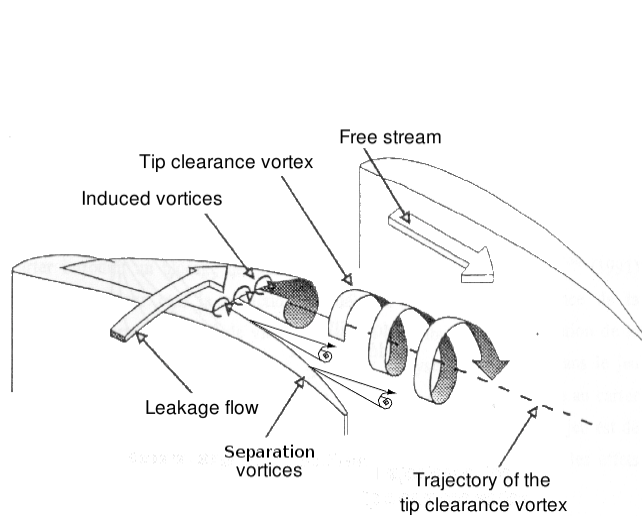
Figure 10 Illustration of the tip clearance flow (*TCF*) above a rotor blade	Figure 11 Interaction wake – *TCF* (Mailach *et al.,* 2007,[53])
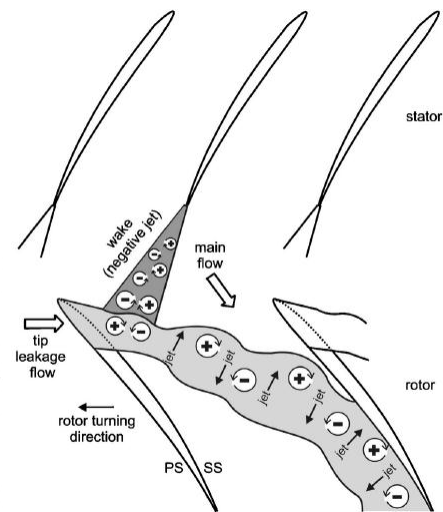
Mailach *et al.* realized in 2007 [53] a detailed study based on laser measurements of the interaction between the leakage flows and the wakes of the upstream stator in a subsonic compressor. The authors showed that the regular impingement of the wakes on the rotor led to a periodic redistribution of the pressure field around the blades. The separation point from the blade of the leakage vortex corresponds to the location where the pressure difference between pressure side and suction side is the highest. Therefore, the periodic redistribution of the pressure field induces an oscillation of the trajectory of the vortex and thus strongly increases the unsteadiness of the flow. The authors also showed that a strong interaction exists between the wakes and the vortex itself. Figure 11 is an illustration of this interaction. The *negative-jet* coming from the wakes is constituted of pairs of contra-rotating vortices. When impinging the leakage vortex, these pairs of vortices will induce other pairs of vortices convected by the leakage vortex. The *TCF* will thus be constituted of an alternation of zones of under- and over-deviation of the flow, able to create regions of reversed flow, which strongly decreases the stability of the machine if the mass flow is decreased too much. This phenomenon has also been observed by Ernst et al. [25] through fast-response total pressure measurements.

I.2.4 The rotor-stator interactions

They result from the interaction of all the flow structures emitted by the rows: potential effects, wakes, *TCF* etc… In 1962, Tyler and Sofrin [81] showed that the *RSI* of an isolated compressor stage can be seen as spinning spatial modes with modal orders being linear combinations between the number of blades of the rotor and the stator involved in the interaction. Depending on the

location in the machine, the *RSI* can be very strong. In the case of multistage compressors, the interactions can indeed induce very complex structures of the flow as all the rows interact together. Figure 12 is extracted from Courtiade and Ottavy (2011,[14]) and shows the wall static pressure field behind the first rotor of the high speed multistage compressor CREATE: they showed that at this location in this machine, the *RSI* are predominant.
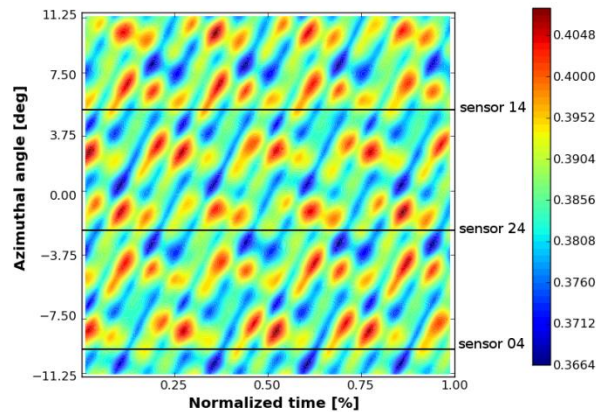
Figure 12 Wall static pressure field behind the first rotor (Courtiade and Ottavy, 2011, [14])

The rotor-stator interactions are known to have significant effects on the global performance of multistage compressors, and have been subject of many researches. In 2004 ([55], [54]), Mailach *et al.* published a study of the *RSI* in a low-speed four-stages axial compressor based on pressure measurements. Their compressor exhibited a very complex pressure field in whole machine, due to the superimposition of the influences of all the rows interacting through the wakes and potential effects. The authors explained that the unsteady pressure profiles on the blades depended on the interactions, and thus were highly time-dependent. They showed furthermore that the interactions were responsible for fluctuations of the blades loadings with amplitudes up to 15 % to 35 % of their mean values. Finally, they showed that the wake and potential influences of the rows could travel through several blade rows in their multistage machine, this being a cause of increase of the complexity of the pressure field. Similar observations have been done by Ottavy *et al.* [68] and Ernst *et al.* [26], with laser and total pressure measurements. In their paper, Ernst *et al.* presented an experimental study of the *RSI* in a two stages high-speed compressor. As well as Mailach *et al.*, they showed complex interactions between rows taking place in their machine, which was especially visible in pressure spectra exhibiting a lot of frequencies proceeding from the interactions.

In addition to the previous observations, Ernst *et al.* found the *RSI* very sensitive to the effect of clocking. The notion of clocking comes when two rows (rotors or stators) have the same number of blades: the question is if there is an optimal angular position for one row over the other, despite the presence of a third row between them. Mailach *et al.* [55] studied experimentally this question applied to the *RSI* in 2004 on a low-speed multistage compressor. The authors showed that they were able to increase by a factor 2.5 the pressure fluctuations due to the *RSI* by shifting the position of a stator. This result is of particular interest for the compressor CREATE: indeed, the second and third rotors have the same number of blades and strong interactions have been found between these two rows, see chapter IV.5.3.
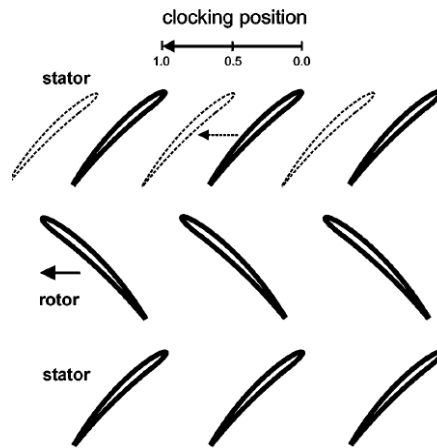
Figure 13 Illustration of the clocking for two stator rows (Mailach *et al.,* 2004, [55])

Overall, the consequences of the *RSI* on the performance and on the onset of the instabilities are still not well understood. The first objective of this thesis will be therefore to evaluate the influence of the *RSI* on the flow field of the compressor CREATE and evaluate their impact on the performance of the machine in term of losses. This will be done in Chapter IV.

I.3 The aerodynamic instabilities

The two most common aerodynamic instabilities occurring in a compressor when decreasing the mass flow are rotating stall and surge. They can be very damaging for the machine: they provoke indeed very strong flow fluctuations inducing strong stresses to the blades. Although many researches have been done over the last five decades, these phenomena are still not well understood, especially their mechanism of onset. The study of the instabilities arising in the high-speed compressor CREATE is the second objective of this thesis. Note that the flutter, a fluid-structure instability which can also be very damaging for a compressor, is not the subject of our study.

I.3.1 The rotating stall

I.3.1.1 Description of the phenomenon

The rotating stall is a three dimensional instability characterized by the presence of one or more cells of stalled fluid spinning slower than the rotor. It has been first described by Emmons *et al.* in 1955 [24]. This instability appears when the machine is over-loaded and often defines the maximum pressure ratio that the compressor can deliver. Indeed, the cells induce a partial blockage of the machine and important losses, leading to a decrease in the pressure ratio and mass flow. The blades are also extremely agitated by the vibrations produced by the stall cells, which can be very damaging for the machine.

The rotating stall cells:

The rotating stall cells are regions of separated fluid with low axial velocity, covering one or more blade passages. A model of propagation of the cells has first been presented by Emmons *et al.* in 1955 [24] : the presence of a cell generates a local blockage, forcing the incoming fluid to skirt the blocked passages, as indicated on Figure 14. This induces on the sides of the cell an under-deviation (blade 1) and an over-deviation (blade3) of the flow. The regions with higher angle of attack are more likely to stall, contrary to the regions with lower angle of attack, which reattach: the cells propagate therefore in the opposite direction of the rotor rotation. Thus, in the absolute frame, the cells seem to spin at a lower rotation speed than the rotor.
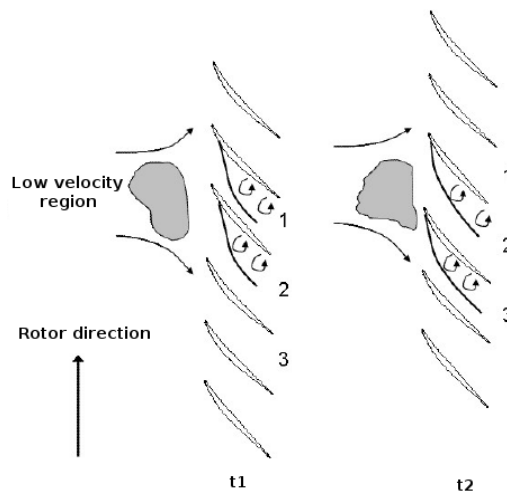
Figure 14 Illustration of the propagation of a stall cell in the relative frame

The stall cells can be divided in two families: the part-span cells located at the tip of the vein (on the left of Figure 15), and the full-span cells, extending on the whole span-height (right of Figure 15). The part-span cells are usually numerous, equally spaced around the circumference of the vein and cover one or several blade passages. They spin at 50% to 80% of the shaft rotation speed and are usually encountered in machines with thin and long blades, as in the first stages of multistage compressors (Day, 1992, [17]). Because they induce a small blockage at the tip of the vein, they provoke an acceleration of the fluid at hub, and only cause a small reduction of the pressure ratio. It is possible to stop part-span rotating stall by increasing the mass flow in the machine. This type of stall is usually associated to low-speed compressors, but some cases have also been observed on the rear stages of high-speed machines, see Day *et al.* (1999, [20]): indeed, the stall of one rear stage in a high-speed multistage axial compressor is possible as the first stages maintain the machine stable (see the discussion of Mailach *et al.* (2001, [51]) by N. A. Cumpsty).

The second type of rotating stall involves a full-span cell occupying the whole span height (full span rotating stall with more than one cell is very seldom seen). It usually starts as a single spike. The cell provokes a very strong blockage which induces a strong decrease in the pressure ratio of the compressor: the only way to stop rotating stall is indeed to unload the blades by strongly increasing the mass flow through the machine. Full-span rotating stall occurs generally in multi-stages compressors with short blades. The rotation speed of a cell depends on its circumferential extent, and is between 30% and 50% of the rotor speed (the larger the cell is, the slower it spins), see

Day (1992) [17]. A full-span rotating stall can trigger surge if the cell extends over the whole annulus and blocks the entire annulus. Marsh and Lakhwani (1973) [57] have shown that such a cell develops in a dozen of rotor revolutions, but faster evolutions have also been observed (three revolutions) by Courtiade *et al.* (2011) [15].

Part-span cells   Full-span cell
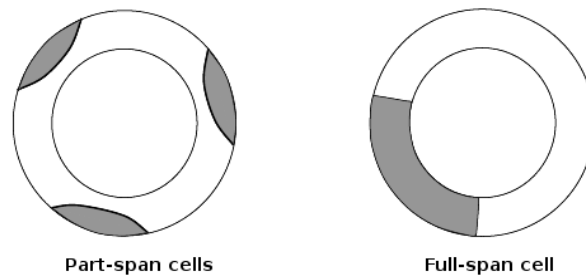
Figure 15 The different types of stall cell, Gourdain (2005) [31]

Structure of the stalled flow:

The flow in a stall cell is extremely complex and has been studied for the first time by Day and Cumpsty in 1978 [21]. The authors showed that generally, a full-span cell extends backwards and forwards extremely quickly. It slips moreover towards the inlet of the machine, as the fluid within the cell does not have sufficient momentum to counter the adverse pressure gradient.
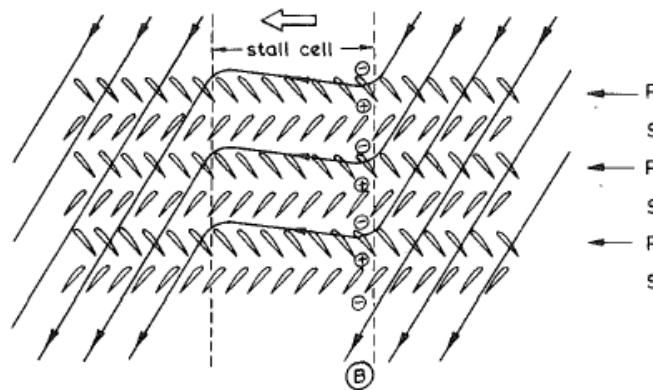
Figure 16 Propagation of a full-span stall cell in a multistage compressor, (Cumpsty and Greitzer, 1982, [16])

A simplified model describing the full-span rotating stall has been developed by Cumpsty and Greitzer in 1982 [16]. Figure 16 represents the flow in a multistage compressor facing full-span stall. In the frame of the cell, the blades of the rotors come from behind the cell at the speed of *(U-V_s)*, V_s being the rotation speed of the cell. The stator blades come from the front of the cell at the speed of V_s. Thus, at the trailing boundary of the cell, the fluid will enter in the cell passing through a rotor and will considerably slow down, contrary to the fluid passing through a stator, which will get out of the cell, and accelerate. The boundary of the cell being abrupt, Cumpsty and Greitzer supposed that the unsteady effects are predominant and thus that the pressure rise *ΔP* will be proportional to the speed variation $\frac{\partial V}{\partial t}$. Thus, at the trailing boundary of the cell (*TB*), a pressure peak will appear when

crossing a rotor, and a valley when crossing a stator. The peak is always stronger than the valley as the speed of a full-span cell is between 30% and 50% of the machine rotation speed (and thus the deceleration is stronger than the acceleration). The opposite phenomenon occurs at the leading boundary (*LB*) of the cell, but the peaks are more difficult to detect as the variation of speed is smaller. Mailach and Vogeler (2007) [56] have experimentally verified this phenomenon on a low-speed axial compressor (see Figure 17).
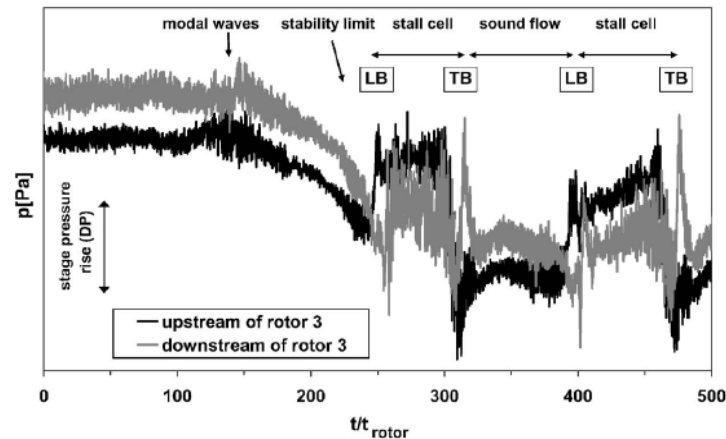
Figure 17 Unsteady pressure signals of a stalled compressor stage, (Mailach and Vogeler, 2007, [56])

I.3.1.2 The onset of rotating stall

The mechanism of inception of rotating stall is very complex and is still not well understood. When a compressor is brought very close to the surge line, the smallest perturbation of the flow, as the insertion of a probe for example, can trigger rotating stall: this makes this phenomenon particularly difficult to study. As written previously, the detection of precursors is a major issue for the manufacturers, as rotating stall usually arises in a very brutal manner.

In most cases, it arises following two inception processes. The first is called modal inception: 2-dimensional modal sinusoidal and axisymmetric waves appear in the flow. Their amplitude increases very slowly without any brutal temporal variation. The typical period of the modal oscillations is three to five rotor revolutions, see Camp and Day (1998, [10]), and they spin around the annulus at constant speed, usually lower than 50% of the shaft rotation speed. They are system instabilities as they affect the flow in the whole machine. They can appear hundreds of rotor revolutions before the stall onset. Moore and Greitzer have been the first in 1986 [63],[34], to identify this inception process and to formulate a model describing it, confirmed by Garnier *et al.* in 1991 [28].

The second process is called spike inception and involves a very quick and brutal perturbation. Contrary to the modal inception, only a few rotor revolutions lead to rotating stall. The perturbation is completely 3-dimensional and very localized: a stall cell covering one or two blade passages appears at the tip of a rotor and starts spinning at roughly 70% to 80% of the rotor rotation speed. The phenomena involved in this inception process are highly non-linear and have been studied for the first time by Day in 1993 [18]. The two inception processes are not exclusive to each other: Figure 18 shows hot wire velocity measurements in a low speed compressor. The modal waves spinning at 20% of the rotor speed are clearly present during the first twenty revolutions. Then, a spike cell appears and brings the machine to rotating stall two revolutions later. A neat difference in term of

scale is visible here for the two perturbations, the wavelength of the modal waves being much larger than for the spike perturbation.
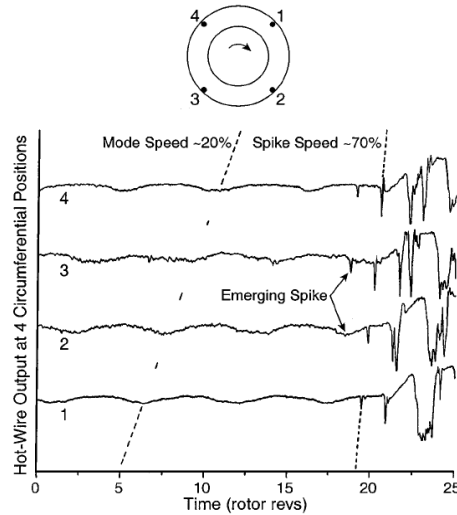
Figure 18 Velocity measurements in a compressor facing modal and spike rotating stall inception, (Day, 1993, [18])

Numerous studies have been done to know which stall inception process will occur in a machine, as control strategies of rotating stall are completely different depending on the type of inception. A first criterion has been stated by Camp and Day in 1997 [10]. It is based on two observations. First, a modal-stall inception generally occurs when the evolution of the total-to-static pressure ratio versus mass flow reaches a maximum: at this point, the slope tends to zero and any weak variation of the pressure coefficient induces a strong variation of the mass flow. Thus, a weak perturbation can grow and turn to modal waves. Second, the authors noticed that a spike-stall inception occurred when one of the rotors of the machine reached a critical incidence. The choice of the inception process follows therefore the criterion schematized by Tan *et al.* (2010, [18]) in Figure 19 : if one rotor reaches the critical incidence before the maximum of the characteristic, the machine will face spike type inception, otherwise modal type inception will occur.
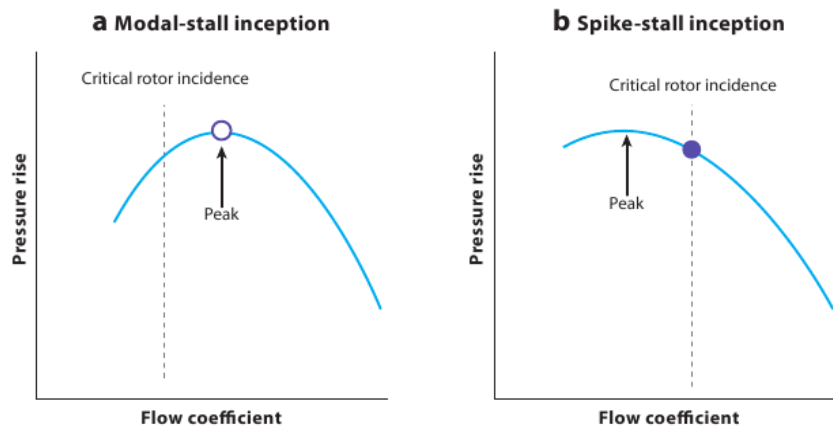
Figure 19 Camp and Day's criterion of rotating stall onset, Tan *et al.* (2010) [80]

It is thus essential for a given machine to determine which are the stages that are the most likely to stall. Day gives us another criterion [17]. For a multistage compressor without blade

adaptation system (variable stator), the blades are designed for a given rotation speed. If the compressor runs at a lower speed than the nominal speed, the first stages will not be able to perform a sufficient compression of the air to pass through the rear part of the machine, and the rear stages will be choked: the first stages will then be starved of air and will run close to their stalling point. The reverse phenomenon occurs when the compressor runs at higher speed: in this case, the front stages are choked, and the rear stages, starved of air, will be more likely to stall.
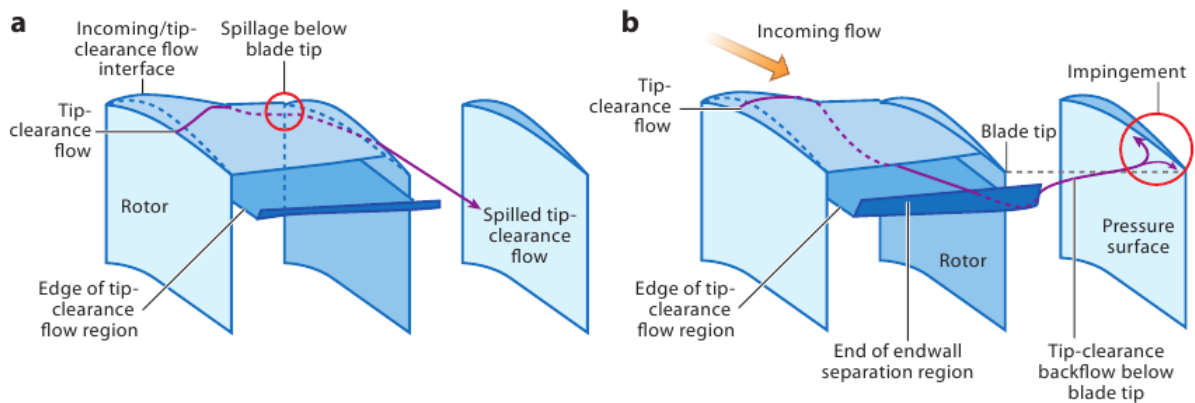
Figure 20 Spillage and backflow responsible for the spike onset of rotating stall, Tan *et al.* (2010) [80]
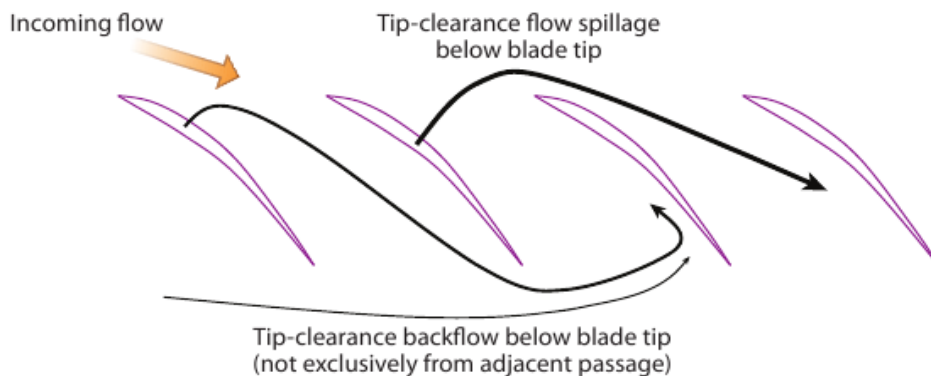
Figure 21 Illustration of the synergy between spillage and backflow during spike onset of rotating stall, Tan *et al.* (2010) [80]

A finer criterion has been stated by Hoying *et al.* in 1999 [39] who performed numerical simulations of spike type inception: rotating stall occurs when the tip clearance vortex aligns with the leading edges of the rotor blades. Two phenomena, first studied by März *et al.* [59] and Mailach *et al.* [51] in 2001 and then by Vo *et al.* in 2005 [82], provoke the onset of a stall cell when such an alignment occurs. The first phenomenon is a spillage of the tip clearance vortex below the tip region, see Figure 20a: the vortex spills into the next passage by passing around the blade leading edge. The second phenomenon is a backflow produced by the flow passing around the trailing edge of the blade, see Figure 20b. The tip flow impinges then the pressure side of the next blade, and some fluid go backwards in the passage, generating a strong blockage. Vo *et al.* showed in 2005 [82] that spike rotating stall occurs when spillage and backflow are present simultaneously in the flow, as the spillage enhances the backflow. Indeed, the spilling tip clearance vortex can be replaced by the

reverse flow coming from the impingement of the backflow, which go further upstream in the passage, see Figure 21. The enhanced blockage effect finally leads to the onset of a stall cell. Broukaert showed experimentally in 2009 [6] that in the case of modal inception, the tip clearance vortex follows the same trajectory in the blade passage, and thus a stall control system affecting only the tip clearance vortex is only efficient when the machine faces spike type inception.

I.3.2 The mild instabilities

Contrary to the rotating stall, some mild instabilities allowing the machine to keep running in a stabilized state can arise in the flow under specific conditions. They are the subject of the following bibliographic review.

The mild stall:

Sometimes, some small disturbances can appear in the flow well before the stall or surge transient. They have been described since the late 90's by numerous researches mostly carried out on low speed compressors. Inoue *et al.* presented a lot of studies on those disturbances since 2000 ([40],[41],[42],[43]) introducing the concept of mild stall, which is a particular type of rotating stall which allows the machine to keep running in a pseudo- stabilized state.

Figure 22 shows a typical total-to-static characteristic of a 1.5 stages low-speed compressor affected by mild stall. In the following section, all the results presented come from this machine. The machine is first throttled to point A. From this point, the mass flow and the pressure rise decrease by themselves to reach point B in a hundred of rotor revolutions. From point B to C, the machine can run at stabilized operating point and is throttled very carefully. The pressure rise decreases with the mass flow, and the compressor faces mild stall. Reaching point C on the characteristic, the compressor falls by itself to point D and enters in "true" rotating stall.
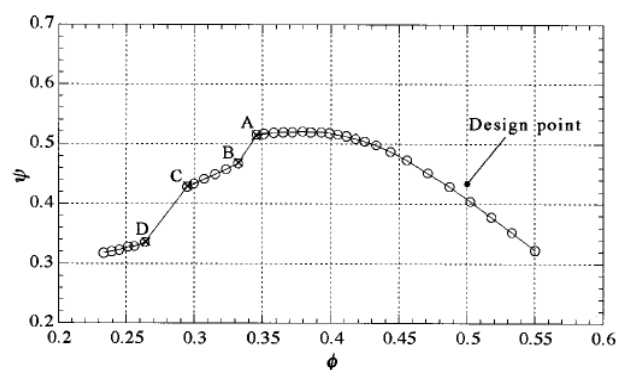
Figure 22 Characteristic of a low-speed compressor facing mild stall, (Inoue *et al.,* 2001, [41])

The mild stall, which occurs from point B to C is characterized by the presence of short length scale disturbances (*SLSD*) and long length scale disturbances (*LLSD*) which coexist in the flow at the leading edge of the blades. Figure 23 shows the wavelet transform of eight pressure sensors located at the tip of the rotor of the previous compressor, for two scales centered on each disturbance. The presence of oscillations in those signals is the signature of the SLSD and the LLSD, spinning roughly at respectively 70% and 30% of the rotor rotation speed.
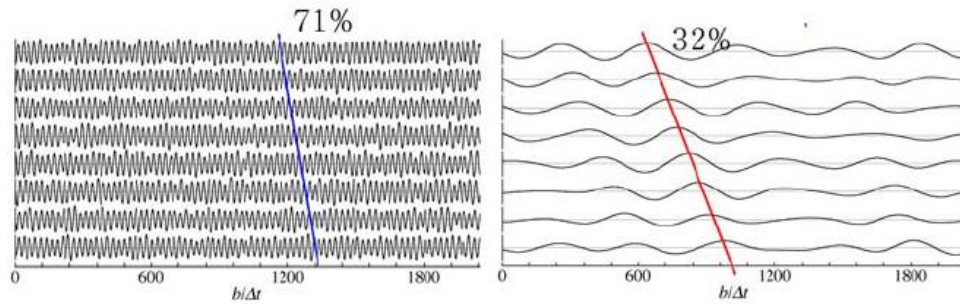
Figure 23 Evolution of short and large length-scale waves, (Inoue *et al.,*(2004, [43])

Structure of the SLSD and LLSD:

The structure of the short length scale disturbances are characterized by a low pressure bubble travelling ahead of the rotor, as it can be seen on Figure 24 (pressure distribution above the previous rotor). Inoue *et al*. ([40], 2000) stated that this low pressure region was produced by a separation vortex moving upstream of the rotor. According to the vortex theory, bound vortices are distributed along an unstalled blade surface, producing a circulation around the blade and thus a lift force. When a separation occurs at the leading edge of the blade, a vortex is released at the blade suction surface to reduce the blade circulation, as illustrated in Figure 25. This tornado-like vortex spans to the casing wall and moves upstream of the rotor to form the low pressure bubble. As the vortex travels, its leg is stretched and finally broken, and flows downstream of the rotor. Meanwhile, the head of the vortex increases the angle of attack of the flow on the next blade, and provokes a local separation, which leads to the appearance of a new vortex.

Figure 24 Pressure distribution over the rotor – visualization of the SLSD, (Inoue *et al,* 2001, [41])
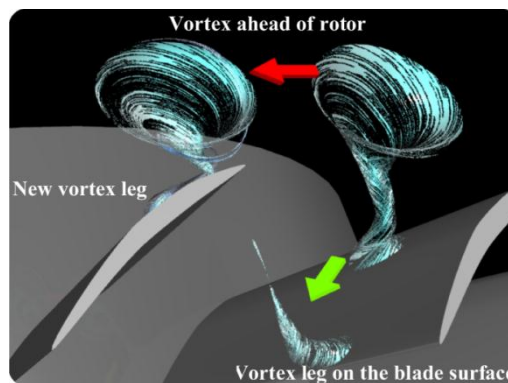
Figure 25 Illustration of a flow model for SLSD, (Inoue *et al.*, 2001, [41])

Unlike the *SLSD*, no low-pressure bubble characterizes the structure of the *LLSD*. Those disturbances, which grow when the compressor enters in rotating stall, can be assimilated to full span rotating stall cells.

When mild stall occurs in a machine with enhanced tip gaps, the number of the *SLSD* highly fluctuates although their rotation speed remains constant, see Inoue *et al.* (2004) [43]. Some small rotating disturbances appear indeed intermittently in the flow. Those disturbances, already studied and called rotating instabilities by Mailach *et al.* [51] and März *et al.* [59] in 2001, can be detected with static pressure measurement as they produce a low frequency hump in the pressure spectra: Figure 26 shows an example of pressure spectra taken in the previous rotor with and without the rotating disturbances. This hump has been observed too in another low speed compressor by Young *et al.* in 2011 [88]. Mailach *et al.* and März *et al.* explain that an interaction between the incoming flow, the reverse tip flow and the tip leakage flow is responsible for the creation of some vortices travelling from the suction side to the pressure side of the blade, in the passage.
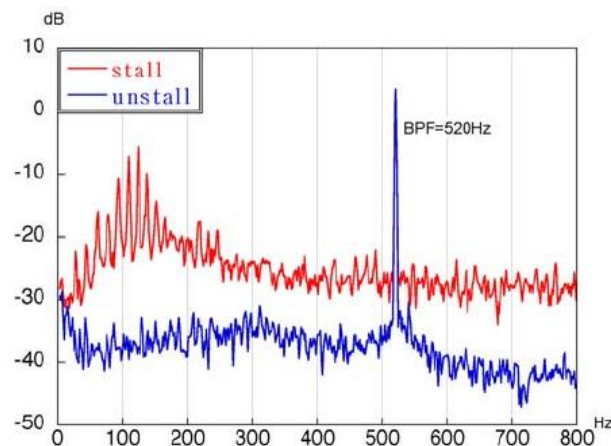
Figure 26 Pressure spectra of a rotor with rotating disturbances, (Inoue *et al.,*(2004, [43])

For Inoue *et al.* [43], the disturbances are produced by an interaction between the *SLSD* and the tip leakage vortex breakdown (*TLVBD*). Figure 27 is a perspective view of the vortical structures when the rotor faces rotating disturbances: it shows that some *TLVBD* and separation vortices (the *SLSD*) coexist in the flow.

The propagation of the disturbances is done in two steps. First, in the left passage, the breakdown of the tip leakage occurs. It generates a blockage in the blade passage which increases the angle of attack of the flow in the middle blade passage. This induces a separation vortex at mid-chord on the pressure side of the next blade which spans to the casing wall. This vortex being too weak to move upstream of the rotor because of the large tip gap, it stays in the blade passage and moves from the suction side to the pressure side of the next blade because of the relative movement of the casing, as previously described by März *et al.* [59]. Then, the *TLVBD* of the left passage flows downstream and the flow becomes clean again. In the middle passage, a new tip leakage flow is generated at the leading edge and the separation vortex begins to flow downstream. The remaining separation vortex interacts with the tip leakage flow and makes it break down. The disturbance propagates in the opposite direction of the rotor.
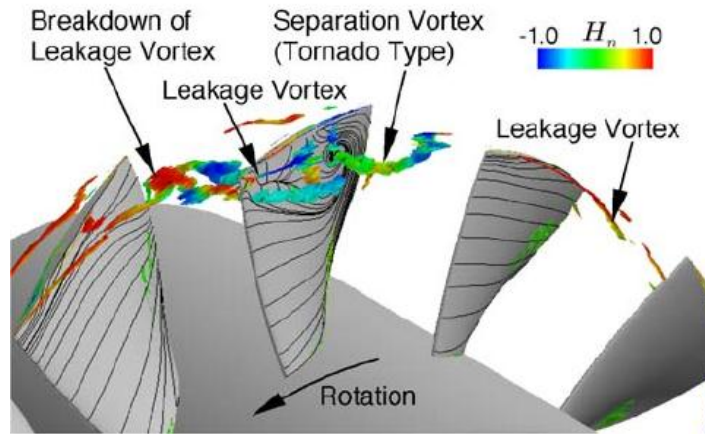
Figure 27 Numerical simulation of the rotating disturbances occurring in a rotor, (Inoue *et al.,* 2004, [43])

Link between spike inception and mild stall:

Although the inception processes of rotating stall, and especially spike inception, are studied for around fifty years, real advances concerning the understanding of these phenomena have only been achieved since the last ten years. Inoue *et al.* [41] have been the first in 2001 to describe the spikes as tornado like separation vortices. The authors explained indeed that a spike cell is a particular type of non-fully developed transient *SLSD*, produced by a separation vortex at the tip of the blade, contrary to the classical *SLSD* whose vortex is released at mid-span.

Many studies of spike inception have lately been achieved, like Weichert and Day (2012, [83]) through an experimental study of a low speed compressor, or Yamada *et al.* (2012,[85]) and Pullan *et al.* (2012, [72]) through numerical simulations. All these authors confirm that the spike is caused by a leading edge separation inducing a separation vortex. For Yamada, the mild stall is even a particular state of the flow where many spikes at embryonic state develop and form the multiple *SLSD*. Hence, these new studies tend to call into question the inception mechanisms involving the tip clearance vortex as presented in chapter I.3.1.2: for Pullan, the leading edge separation vortex is independent of the clearance flow which does not trigger the leading edge separation. In their experimental study, Weichert and Day show that no alignment of the tip leakage vortices with the leading edges of the blades is observed before spike inception, which tend to confirm the observations of Pullan. Finally, Weichert and Day suggest that the spillage (see chapter I.3.1.2) could be a consequence and not a cause of spike inception: this is confirmed by Yamada who explains that the flow skirts the separation vortex which induces a blockage in the passage, and then spills upstream of the leading edges.

Note that other inception routes also exist. Consider for example the work of Hellmich and Seume [36] who reported in 2008 a phenomenon of acoustic resonance triggering rotating stall in a high-speed compressor. This will be the subject of an in-depth study in chapter V.5

I.3.3 The surge

The surge is a mono-dimensional axial instability affecting the whole machine. It produces a low frequency oscillation of the mass flow (from a few Hertz to a few dozen of Hertz) which can lead sometimes to a reversal of the flow direction. Surge occurs when the machine is no more able to

supply sufficient energy to the fluid to resist the adverse pressure gradient, and is usually preceded by full-span rotating stall, as stated by Day in 1993 [18]. The extreme fatigue induced by the surge can lead to the rupture of the blades (see Figure 28), and only a strong increase in the mass flow through the machine to discharge the rows can stop the surge.

Figure 28 Blade damage due to surge (source: NASA)

In 1978 Greitzer ([32], [33]) showed that the intensity of the surge depended not only on the design of the compressor but also on the whole geometry of the system. He modeled any compression system as a Helmholtz resonator composed of a collection of lumped components: compressor, ducting, storage volume and exit throttle valve (see Figure 29). For a real engine, the plenum would correspond to the combustion chamber. In the literature ([32], [17]), it is commonly found that the quantity of injected fuel can play the role of the throttle valve.

Thus, if the volume of the plenum at the outlet of the compressor is sufficient, when the compressor will stall, the fluid will no more be able to counter the energy stored in the plenum and will flow back in the machine until the compressor recovers. And an infinitely repeating surge cycle can occur while the discharge valve is not opened. Thereby, two types of surge exist, classical surge and deep surge.
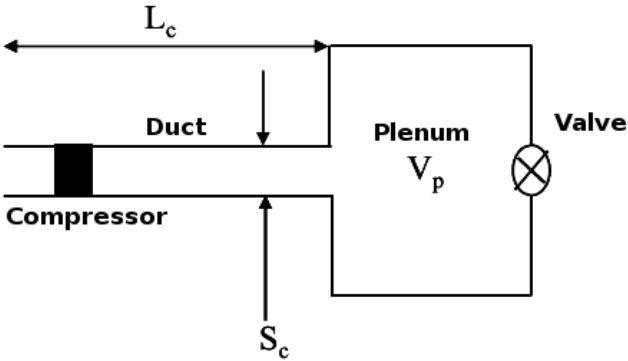
Figure 29 Greitzer's modeling of a compression system (1978, [32])

Classical surge is characterized by alternating phases of clean flow and rotating stall, and induces small oscillation of the mass flow around a mean operating point, see Figure 30 (left). It occurs usually when the plenum has a small storage volume, and on compressors with small pressure ratio. Deep surge is much more violent, as it induces very strong oscillations of the pressure ratio and of the mass flow, which becomes periodically negative, see Figure 30 (right). It occurs on systems with big storage volume, and on compressors with high pressure ratio. Figure 31 shows hot wire velocity measurements during deep surge. The surge cycle is clearly visible, with a reverse flow occurring during the half of the cycle. A deep surge cycle is usually longer than a classical surge cycle, see Day (1992) [17].
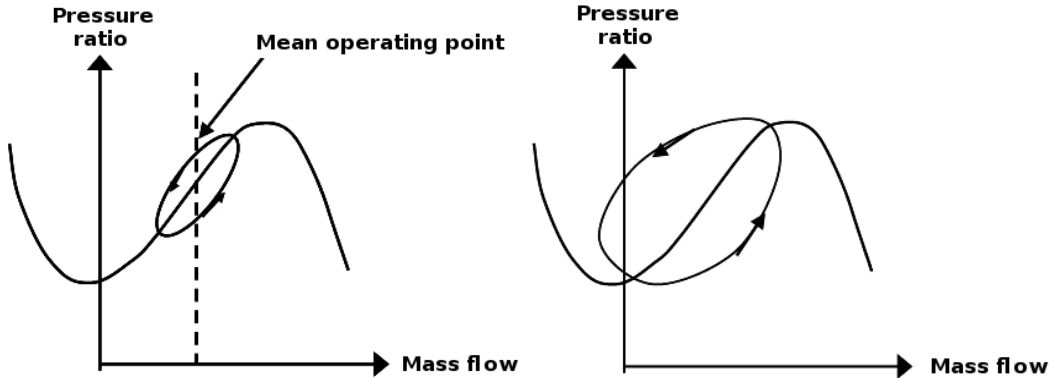
Figure 30 Classical (left) and deep (right) surge cycles, inspired by Greitzer [33]
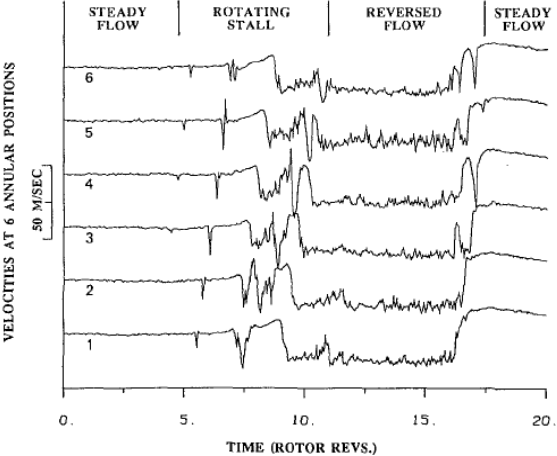
Figure 31 Hot wire measurements in a compressor facing deep surge, Day (1993) [19]

According to its model, Greitzer considers a compression system as a Helmholtz resonator. The equation of the dynamics in such a system is:

$$\frac{d^2x}{dt^2} = -(2\pi f_h)^2 \cdot x \qquad \text{(I-3)}$$

With the Helmholtz frequency $\qquad f_h = \dfrac{c}{2\pi} \cdot \sqrt{\dfrac{S_c}{V_c L_c}}$ (I-4)

L_c, S_c: length and section of the duct (see Figure 29)
V_p: volume of the plenum
c: sound speed

This simple model explains the origin of the surge cycles and allows to evaluate their frequency. Because of its simplicity and especially because it does not take into account the characteristics of the compressor, the model cannot estimate the starting point of the surge (Gourdain 2005, [31]). The higher the difference of pressure is, the stronger will be the surge. And the bigger the plenum volume is, the more the surge – and especially the deep surge – is privileged, and the lower is its frequency. Note that an improvement of this model taking into account the viscosity of the fluid has been made by Zhang *et al.* in 2012 [90].

I.3.4 Control strategies of the instabilities

As the instabilities arising in compressors are very damaging, numerous studies have been done to try to control their onset and thus to reduce the surge margin: indeed, an increase in the stable operating zone would increase the efficiency too, and thus decrease the cost of operation. The two principle approaches of control are the use of components with variable geometry, as stator blades with variable stagger angles, and the use of blowing valves in the machine able to re-inject some mass flow if any instability arises, as proposed by Day *et al.* in 1993 [19], Weigl *et al.* in 1997 [84] and Paduano *et al.* in 2011 [70]. However, the main difficulty remains to be able to detect precursors sufficiently early to allow the control system to operate.

Hoenen and Gallus (1995) [38] and Hoenen and Arnold (2003) [37] have shown that it is possible to detect the onset of an instability a few dozen of revolutions before it arises, by measuring the blade passage frequency which tends to decrease as the stability limit is approached, although other parasite frequencies appear in the measurements spectra. Another approach chosen by Dhingra *et al* [22], Nakakita *et al.* [64] in 2007 and lately by Young *et al.* [88] in 2011 is to evaluate the loss of periodicity from one revolution to another of some pressure signals. Indeed, as the machine is throttled closer to surge, small perturbations in the pressure signals can be detected.

I.4 Conclusion

The following work will focus on the study of the flow in a multistage compressor at stable and unstable operating points. At stable operating points, it has been shown that strong interactions between the rows affect the flow and generate strong unsteadiness. As the designs of the compressors tend to become more compact, with especially a reduction of the inter-row spacing, the interactions between the rows are stronger and stronger. However, their impact on the performance of the machines is still unclear. A first objective of the present work will therefore be to answer this

question through the analysis of the flow of the high-speed multistage compressor CREATE which will be presented in Chapter IV.

Then, the mechanisms of onset of the compressors instabilities are not fully understood and require further experimental and numerical investigations to improve the efficiency of the control systems. Chapter V of this thesis forms part of these researches, as it will provide description and analysis of experimental measurements of the instabilities in a high-speed multistage compressor, which are still not commonly found in the literature. The second objective of this thesis will therefore be to understand the mechanisms responsible for the rise of the instabilities in the compressor CREATE in order to try to control the surge onset.

Chapter II
Description of the machine

II.1 The compressor

Figure 32 Picture of the compressor CREATE

The test rig considered for this study is a research multistage compressor dedicated to aerothermal and aerodynamic studies. This 3½-stages axial compressor, named CREATE (Compresseur de Recherche pour l'Etude des effets Aérodynamiques et TEchnologiques) has been designed and built by Snecma and is investigated at LMFA. Its geometry and rotation speed are representative of high-pressure compressor median-rear blocks of modern turbojet engines. The number of stages was chosen in order to have a magnitude of the secondary flows effects similar to a real compressor, and to be within the rig torque and power limitations. Some of the characteristics of the machine at nominal rotation speed are available in Table 2.

Cylindrical outer casing diameter	0.52m
Core speed	11 543 rpm
Rotor 1 tip speed	313 m/s
Rotor 1 tip inlet Mach number	0.92

Table 2 Characteristics of the compressor at design rotating speed

Snecma and the research team of the LMFA have taken into account technological constraints coming from the experimental part of the project, very early in the compressor design:

- In order to traverse probes between blade and vane rows, the axial gap has been slightly increased compared to current compressors and an outer-case moving-rings technology has been implemented to perform probe measurements in the circumferential direction at

constant radius location. The meridian view of the compressor and the inter-row measurement sections are presented in Figure 33.

- The circumferential periodicity of the whole machine (obviously 2π in general case with primary blade numbers) has been reduced to $2\pi/16$ on the compressor CREATE, choosing the number of blades of each rotor and stator (Inlet Guide Vane -IGV- included) as a multiple of 16 (see Table 3). Consequently, measurements carried out over a sector of only $2\pi/16$ (namely 22.5 °) should contain all the spatial information (in the case of stabilized operating points) and are very useful when devoted to detailed studies, such as rotor-stator interaction analysis. Unless otherwise specified, the reduced numbers of blades are used in the following work.

- The first rotor has conventional tip gap, whereas the tip-gaps of the second and third rotors have been enlarged in order to study their influence on the performance and stability of the machine.

- The stagger angle of the blades of the IGV can be shifted of ±5°. In the following study, it has been kept at its nominal value

Row	IGV	R1	S1	R2	S2	R3	S3
Number of blades (2π)	32	64	96	80	112	80	128
Number of blades (2π/16)	2	4	6	5	7	5	8

Table 3 Blades numbers of the compressor rows
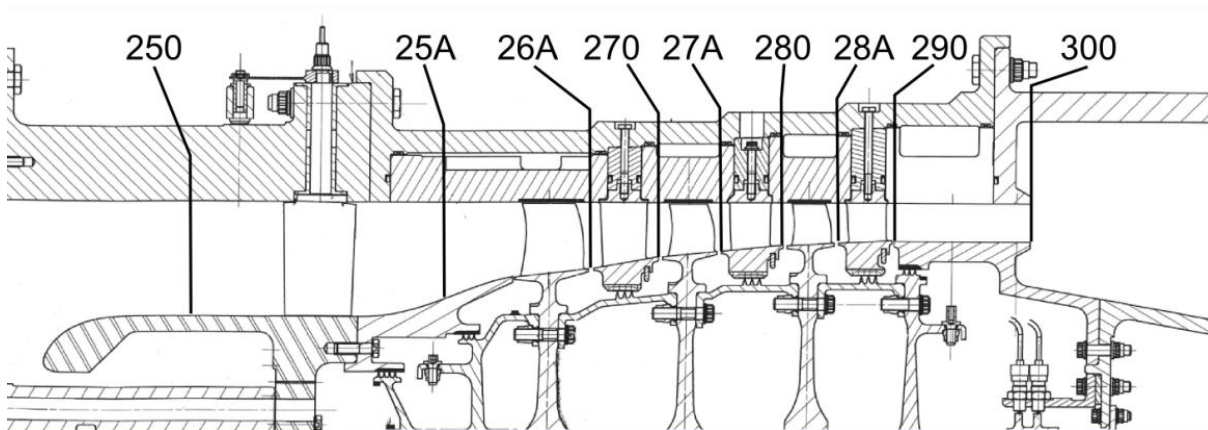
Figure 33 Meridian view of the 3.5-stage axial compressor CREATE

The performance lines at design shaft-speed are presented in Figure 34. Note that the mass flow rate and the total pressure ratio are reduced by their value at the design operating point. In the following study, four operating points will be of particular interest:

- **PE**: Peak Efficiency operating point

- **L**: Loaded operating point

- **SM**: Surge Margin operating point

- **NS**: Near Surge operating point

PE operating point corresponds to the design point where the isentropic efficiency is maximum. The *L* point has been chosen by Snecma to perform experimental measurements at a lower mass flow than PE, without any risk of surge. It is encountered at roughly half-way between PE and the surge line. The *SM* operating point defines the surge margin at design shaft speed, and therefore the lowest mass flow allowing the reconstruction of the measurements over the spatial periodicity of the machine at stable operating points, see Chapter III. It has been experimentally determined by the *LMFA*. Finally, the *NS* point corresponds to the last stable point before the machine falls into surge. The study of the onset of the instabilities in the machine has thus been done at this operating point.
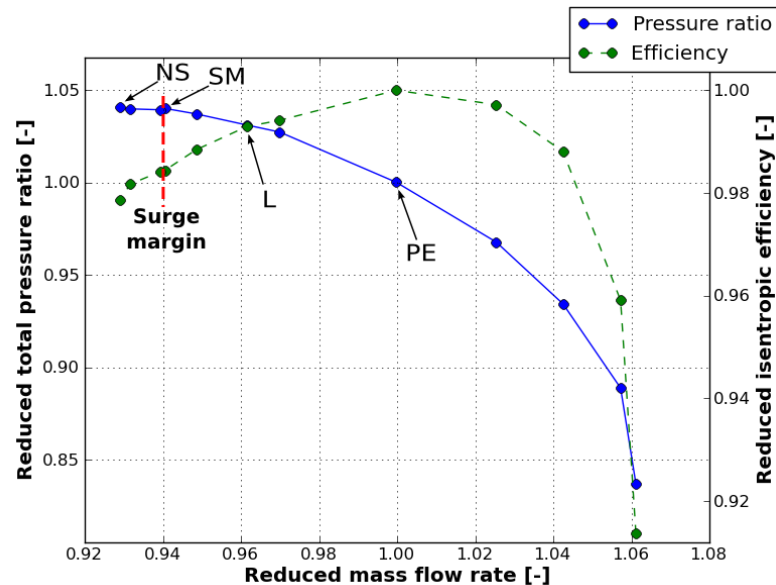
Figure 34 Pressure ratio and isentropic efficiency versus mass flow rate for the design shaft-speed of the compressor CREATE

II.2 The test rig

The compressor CREATE is tested at Ecole Centrale de Lyon in LMFA. The test stand, designed as an open loop is visible on Figure 35. The ambient air is led into the compressor through a settling chamber with air filters and a throttle that drops the inlet total pressure to 74 % of the atmospheric pressure and enables to decrease the needed electric power. The rotors shaft is driven at the design speed of 11,543 rpm by a 2 MW three-phases AC drive coupled with a gearbox. At this rotational speed, the Mach number at the tip of the first stage is 0.92. Indeed the flow is slightly transonic in the first stage and fully subsonic in the two last ones. A throttling butterfly-type valve is used downstream of the collector to control the mass flow rate, which is measured using a Venturi nozzle (not presented in Figure 35) located just before the exhaust of the test-rig. The anti-surge valve is located just upstream of the throttling butterfly-type valve. In case of surge, this valve is very quickly operated to discharge the system in about 0.5 seconds. More details about the compressor and the test rig are available in Ottavy *et al.* (2012) [66] .
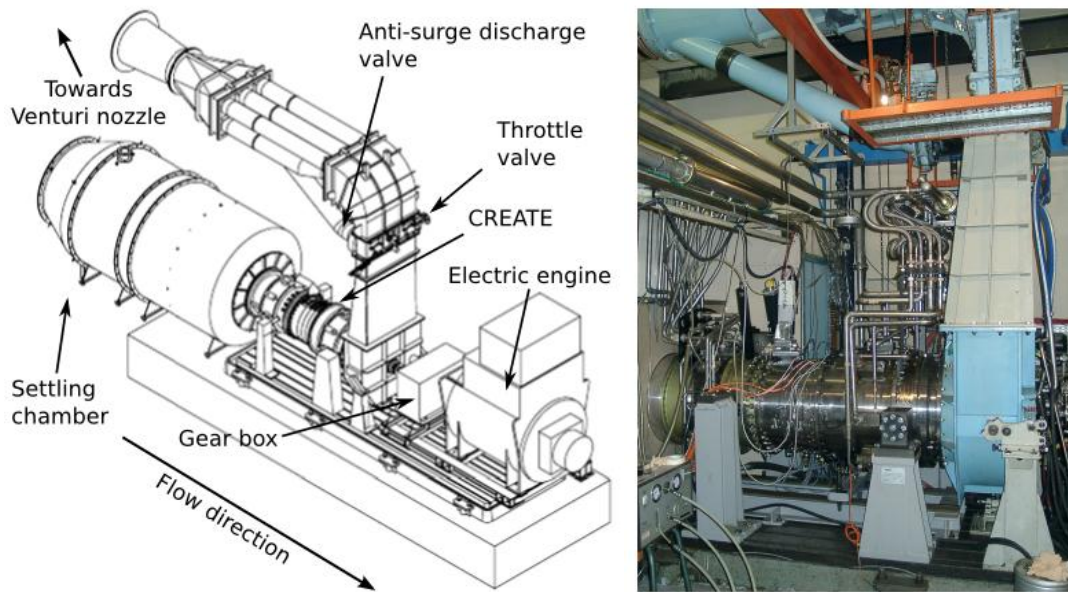
Figure 35 The compressor CREATE test rig in LMFA at Ecole Centrale Lyon

II.3 Measurements of the global performance

In order to have a global picture of the aerodynamic and mechanical state of the rig, a set of 210 measurements is performed every two seconds. It contains temperature and pressure measurements for the flow and the oil, as well as accelerometers and strain gauges. Hence, an *'operating point'* containing the mass flow, the pressure ratio and the isentropic efficiency, but also all the inlet and outlet information of the rig is acquired before each specific local measurement. Each operating point is stored in a MySQL data-base.

Ten sensors measure the inlet temperature in the settling chamber. The inlet total pressure is obtained with a Kiel probe in section 250 in front of the compressor (see Figure 33). Total pressure and total temperature probe rakes, located at six circumferential and five radial positions in the outlet section 300 upstream of the discharge collector, give the exit flow conditions. As mentioned before, the operating point of the compressor is adjusted by throttling a butterfly-type valve downstream of the compressor. The performance lines of the compressor are obtained from the pressure ratio, the isentropic efficiency and the mass flow rate, for a given rotation speed. Their uncertainties are quite constant over the operating speed range and are given in Table 4. More details about the calculations of these quantities and their uncertainties are available in Ottavy *et al.* (2012) [66].

Pressure ratio ψ	±0.07%
Isentropic efficiency η	±0.20%
Mass flow ϕ	±0.35%
Rotation speed Ω_{shaft}	±0.01%

Table 4 Relative experimental uncertainty levels at the nominal operating point

To get rid of the influence of the variations of atmospheric pressure and temperature during the experimental campaign, all the measurements are standardized according to the following relations:

$$P_{ref} = 101325 Pa \qquad\qquad T_{ref} = 288.15\ ^{\circ}K$$

$$\dot{m}_{std} = \dot{m}_{mes} \sqrt{\frac{T_{inlet}}{T_{ref}}} \frac{P_{ref}}{Pt_{inlet}} \tag{II-1}$$

$$\Omega_{shaft\ std} = \Omega_{shaft\ mes} \sqrt{\frac{T_{ref}}{T_{inlet}}} \tag{II-2}$$

$$P_{std} = P_{mes} \frac{P_{ref}}{Pt_{inlet}} \tag{II-3}$$

$$T_{std} = T_{mes} \frac{T_{ref}}{T_{inlet}} \tag{II-4}$$

$$V_{std} = V_{mes} \sqrt{\frac{T_{ref}}{T_{inlet}}} \tag{II-5}$$

With the subscripts **P** for pressure, **T** for temperature, **m** for mass flow, **N** for rotation speed, **V** for velocity, $_{std}$ for standardized and $_{mes}$ for measured.

Note that the influence of the humidity has been checked and found negligible. Moreover, the Laplace coefficient γ is calculated at the inlet and at the outlet of the machine for each operating point. Typical values at the inlet and outlet are 1.401 and 1.393 respectively, mostly depending on the inlet temperature. An average value of 1.40 has been chosen for all the post-treatments presented in the following study.

Chapter III
Description of the measurements

III.1 Introduction

Many measuring techniques are available to study the flow in a compressor. They are generally associated to a specific aerodynamic quantity as pressure, temperature or velocity. However, the choice of using one or another is most of the time dictated by the strong constraints imposed by the machine, especially in the case of a high-speed compressor. Indeed, measurements are usually performed in confined spaces, with a difficult access to the measuring points. Then, the conditions imposed by the environment can be very severe (high-pressure, high-speed, high-temperature, strong electro-magnetic interferences…) and thus induce strong stresses to the instrumentation and/or prevent its use. As the scale of the aerodynamic phenomena involved in aeronautic compressors are usually small (a few millimeters in the rear stages of a high-speed compressor), the miniaturization of the instrumentation is one of the first preoccupation in order to be able to catch the physics of these phenomena. Nevertheless, as it tends to weaken the instrumentation, a fine balance has to be found between size and strength. Finally, the temporal resolution is also very important for unsteady measurements in high-speed machines, and developing fast measuring techniques with sufficient frequency response (which can be in our case up to 200 kHz, see chapter III.4) can be very complicated.

Two principal parameters are taken into account to choose a measuring technique: the intrusiveness and the temporal resolution:

- A measuring technique can be intrusive or non-intrusive. The intrusive techniques, like total pressure measurement with probes, require to introduce some instrumentation in the flow. This induces some perturbations, which have to remain as small as possible. This implies that such techniques can only be used at stable operating points, as very small perturbations of the flow can trigger the instabilities when going towards the surge line, see chapter I.3.

- The response time of a technique is particularly important. Instantaneous techniques, like fast pressure measurements are complementary to statistical measurements, as laser velocimetry. Whereas the former are able to catch transient phenomena, and provide a direct measurement of the flow, the later require a longer acquisition time, and the data has to be reconstructed by ensemble-averaging (see chapter III.7.2). Statistical measurements have to be distinguished from steady measurements, which provide a direct measurement but with a long response time.

In the compressor CREATE, during the experimental campaign, the flow has been investigated through steady measurements of pressure and temperature, unsteady wall static pressure measurements, unsteady total pressure measurements and laser velocimetry. The different characteristics of each technique are available in Table 5 and detailed descriptions will be provided in the next sections of Chapter III.

Measuring technique	Intrusiveness - characteristic size	Temporal resolution	Localization	Operating points
Steady measurements (Ps, Pt, Tt)	Yes (probe) 1.8 mm	Steady	Inter-row planes Whole span	Stable OP
Unsteady wall static pressure measurements	No 1 mm	Unsteady ≈ 150 kHz	Inter-row planes and above the rotors at casing	Stable and unstable OP
Unsteady total pressure measurements	Yes (probe) 2.5 mm	Unsteady ≈ 200 kHz	Inter-row planes Whole span	Stable OP
Laser Doppler Anemometry (axial and circumferential velocity)	No 0.92 x 0.07 mm²	Unsteady (Statistic) <20 kHz	Inter-row planes and in the rotors Whole span	Stable OP
Unsteady CFD calculations (whole flow)	-	Unsteady ≈ 120 kHz (*)	Whole machine	5 OP

Table 5 Pros and cons of the different measuring techniques

(*): the maximum frequency has been calculated from the size of the largest cell of the CFD mesh at tip of rotor 1 (see Appendix: The numerical simulations)

III.2 The steady measurements

Steady measurements of the static pressure, total pressure, total temperature and angle of the flow have been performed in the compressor, in all the inter-row sections for three operating points: at nominal speed, for peak efficiency point **PE** and loaded point **L** (see Chapter II for the definition of these operating points), and at 95% of nominal speed for loaded point **L**. The flow has been investigated over the azimuthal period Θ_{16} of 22.5° and along the span. An azimuthal resolution of 0.4° (57 points over Θ_{16}) has been chosen. This corresponds to 7 to 14 points per blade pitch, depending on the considered row. The measurements have been done for 13 span heights for the nominal speed points and 11 for the 95% of nominal speed point.

Seven 5-holes probes have been used, each hole being equipped with an independent pressure sensor of ZOC *Scannivalve* type. The total temperature has been obtained with a thermocouple and the module "Fieldpoint" of *National Instruments*. A radial spacing of 1 mm is found between the pressure and temperature sensors, which is a significant fraction of the span-height in the rear stages. The alignment of the probes has been done automatically with a *CIVA* module developed by Snecma, visible on Figure 36. As steady measurements are very common, no details about the calibration and the experimental campaign will be presented in this manuscript. More details are available in Goguey *et al.* [30].
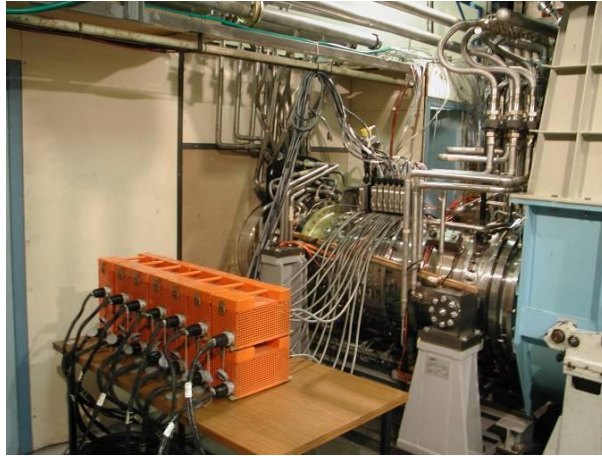
Figure 36 View of the machine equipped with the CIVA during the steady measurements

III.3 The high-frequency wall static pressure measurements

III.3.1 Principle of the measurements

It is nowadays very common to use pressure measurements to study the unsteadiness of the flow field in compressors. As such measurements provide "instantaneous" information and are non-intrusive, they are particularly useful to study the onset of the instabilities that occurs at the boundary of the operating range of a compressor.

To be able to catch correctly all the energetic part of the pressure signals, it is important to have a high temporal resolution, typically superior than ten times the *BPF* (around 150kHz in the case of CREATE). Such a high resolution with acceptable sensitivity remains very seldom in the literature: let us mention for example the works carried out at Technische Universität Darmstadt by Biela *et al.* (2008) [4] in a high speed single stage compressor with a sampling rate of 125 kHz, and of Ernst *et al.* in 2011 on the 2-stages transonic axial compressor of Aachen with a sampling rate of 640 kHz [25]. Hence, the LMFA developed skills in acquiring unsteady pressure data in high speed compressors, see Bulot *et al.* (2009) [8]. A description of the data acquisition chain (*DAC*) used during the experimental campaign is presented hereafter. During the whole thesis, the acquisition chain has been continuously improved, and only the last version will be presented.

III.3.2 The data acquisition chain

A schematic diagram and a picture of the *DAC* can be seen on Figure 37 and Figure 38. It can be divided into three parts: the pressure signals are first acquired by pressure transducers (48 in the case of CREATE), then they are analogically amplified and low-pass filtered by in-house conditioners, and finally digitized and numerically stored. The signals are acquired at a sampling rate of 500 kHz.

Because of the presence of the 2MW electric engine of the test rig in the measurements room, the experimental environment is strongly affected by electromagnetic perturbations: indeed, high frequency parasites (700 kHz) produced by the regulation of the engine could be seen in the signals

acquired by the first version of the acquisition chain. The *DAC* has therefore been placed in a faraday cage and completely insulated from the electric grid to avoid any electromagnetic perturbation. Wi-Fi has also been used for the communication between the *DAC* and the work station in the control room to avoid the perturbations which would have been encountered with a wired analogic connection. Figure 39 shows two raw signals acquired by a free sensor placed near the engine and treated by the first and the last version of the conditioners respectively: it can be seen that the amplitude of the parasites produced by the engine has been divided by 20.
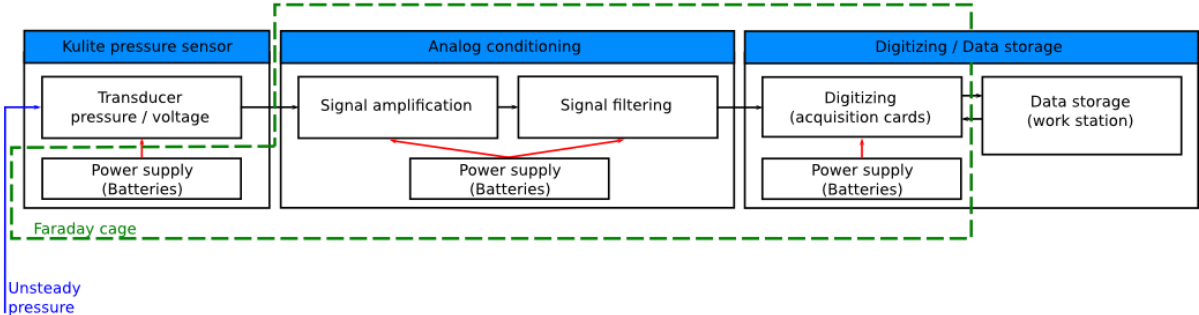
Figure 37 Block diagram of the pressure acquisition chain

Figure 38 Picture of the *DAC* in its Faraday cage
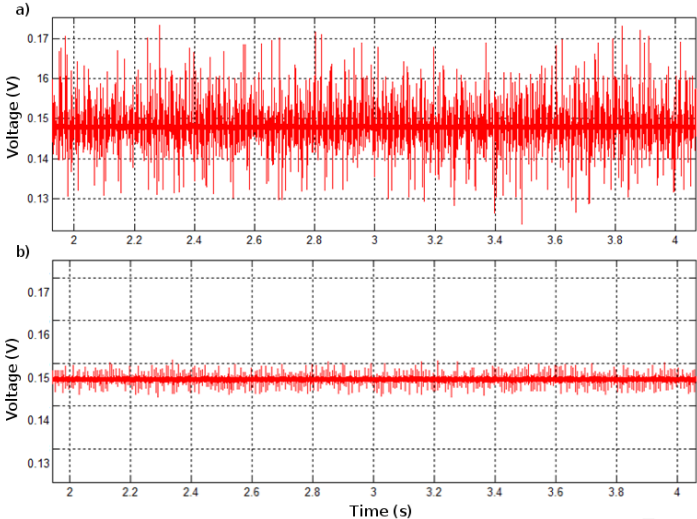
Figure 39 Raw signals of a free sensor using the first (a) and the last (b) versions of the *DAC* respectively

The pressure transducers:

The pressure signals have been acquired by pressure transducers manufactured by *Kulite* (reference family *XTE-190*). The temperature compensation modules equipping the sensors have been used: they have been found reliable over the whole temperature range encountered in CREATE. Three different pressure ranges have been used: 15, 25 and 50 PSI, depending on the sensor location along the compressor (remember that the inlet pressure is set to 74 % of the atmospheric pressure). The sensors with a larger pressure range have been used at the outlet of the machine where the pressure is higher. The characteristics of the sensors are available in Table 6. In order to increase the bandwidth of the transducers, their protective grid has been removed although it induces a reduction of their service life: Nicolas Bulot [7] estimated with shock tube test the resonance frequency of the sensors to be between 290 kHz and 440 kHz. As the manufacturer *Kulite* recommends to use the sensors up to the third of their resonance frequency, the measurements were considered to be valid up to 145 kHz. A picture of the sensitive part of the transducers is available on Figure 40. It is important to notice that the pressure signal produced by the sensors is integrated over their surface of 1mm², that is to say 1mm axially (which represents around 2.8% of the mean axial chord of rotor 1) and 0.22° azimuthally at casing (0.98% of the circumferential period). Finally, the sensors have been fed over 12 V with batteries in order to improve their sensitivity of 20%, instead of 10 V as recommended by *Kulite*.
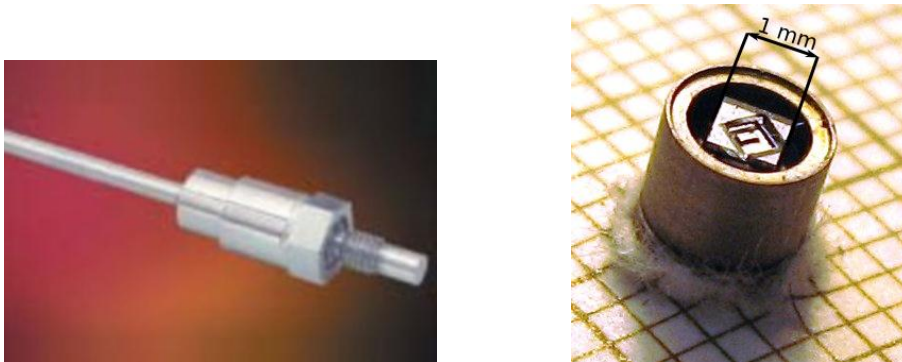
Figure 40 Close-up and general view of a pressure transducer

	XTE-190-15PSIA	XTE-190-25PSIA	XTE-190-50PSIA
Power supply	10 / 15 V	10 / 15 V	10 / 15 V
Output sensitivity	6.56 mV/PSI	3.95 mV/PSI	2.01 mV/PSI
Natural frequency (shock tube)	290 kHz	330 kHz	440 kHz
Compensated temperature range	25-232 °C	25-232 °C	25-232 °C

Table 6 Characteristics of the pressure transducers

The conditioners:

Six conditioners of eight channels each have been built (see Figure 41). To avoid any problem of interaction between the different channels, each circuit is insulated from the others, and the grounds of each channel are disconnected from each other. The circuits are constructed with surface-mount technology (instead of the classic through-hole technology), in a matter of miniaturization and in order to diminish the perturbations induced by the electromagnetic parasites.

The role of the conditioners, whose schematic diagram is visible on Figure 42, is to amplify and then analogically low-pass filter the signals of the sensors. The amplification is only needed to adapt the signal to the electronic components of the filtering stage. A gain of 10 is applied. The purpose of the filtering process is to cut the frequencies of the signal above 250 kHz (i.e. half of the acquisition frequency according to the Shannon theorem, to avoid any aliasing problem). The high-frequency part of the signal is mainly induced by the resonance of the transducers and the electromagnetic radiations emitted by the electric engine. The low-pass filter is a 4th-order *Bessel filter with constant group delay*, performing an attenuation of 3 dB at 150 kHz and 10 dB at 250 kHz.

Figure 41 Pictures of the conditioners used for the unsteady pressure measurements (surface mount technology)
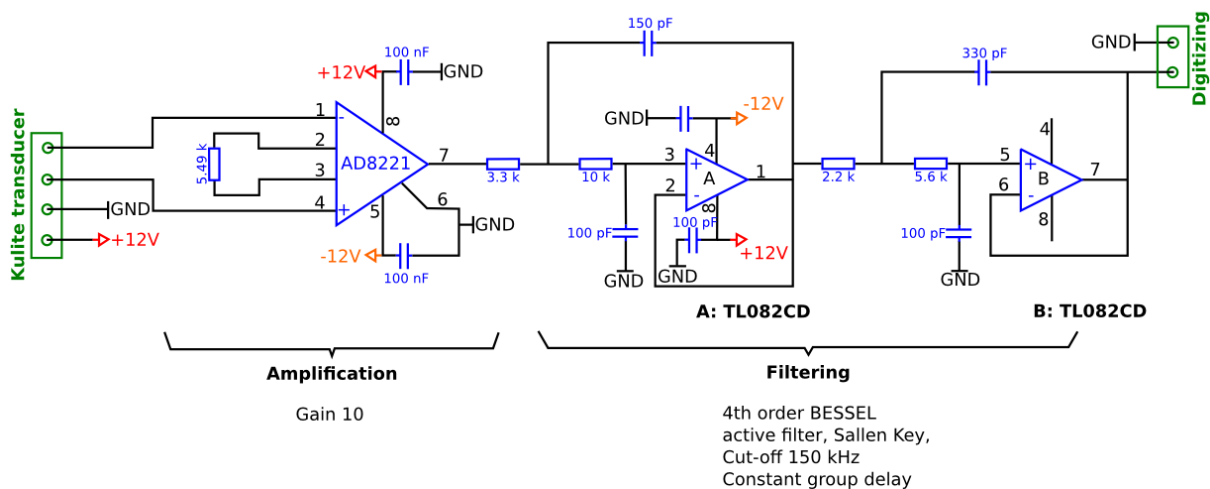
Figure 42 Schematic diagram of the conditioners

Two conditioners have first been developed (called type 1), and then four others (called type 2). The transfer functions of the two types of conditioners are visible on Figure 43. They have

been obtained by averaging the frequency responses of the eight channels of each conditioner, which only differed by less than 0.5 %. These two transfer functions have been used to post-treat all the pressure measurements.

Note: In order to completely cut the frequencies above 150 khz, a perfect digital filter is systematically applied to the measurements, during the data processing. Unless otherwise specified, all the following results have been filtered at 150 kHz.
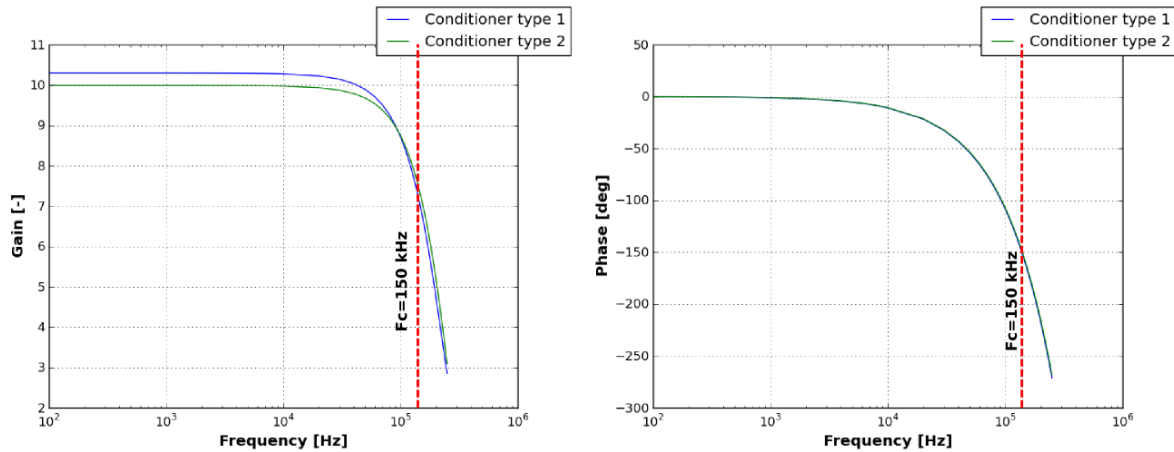
Figure 43 Transfer functions (gain and phase) of the two types of conditioners

Digitizing of the data:

The digitizing is done with the *National Instruments PXI Modular Instrumentation System* (visible on top-left of Figure 38). The *PXI-1062Q* system was selected because it offers rugged, shielded construction that provides a low-noise environment for data acquisition and signal conditioning. The core of the system is a set of up to eight *PXI-6123* data acquisition boards with a sampling frequency of 500 kHz. Each board accepts eight differential analog inputs. The boards have a 16-bit resolution and communicate with the data acquisition computer (*Dell T7400*) via two communication boards (*NI PXIe-8370* in the PXI and *NI PCIe-8371* in the station). The data are finally stored in binary format in blocks of 1024 samples.

Two types of acquisition have been performed during the experimental campaign. At stable operating points, the data was acquired during four seconds, in order to have a file of 2048 blocks. For 48 sensors, this represents a file of around 188 Mo. At near surge operating points, the procedure was to start the acquisition, then slowly throttle the compressor until it surges, and finally manually stop the acquisition. This procedure could last up to five minutes, and produce a file of around 15 Go. To be able to read and post-treat such files, specific post-treatment programs have been developed, and particular attention has been paid to their efficiency.

III.3.3 Localization of the measurements

The casing of the compressor has been equipped with 48 pressure transducers. From section 260 to 28A, each inter-row plane contains six sensors regularly spaced around the circumference (at 04, 14, 24, 34, 44, 54 minutes, the zero-minute position corresponding to the vertical) to be able to catch any rotating pressure wave during the investigation of the flow at near surge operating point.

Furthermore, twelve additional mobile sensors are available to study the flow developing at the tip of the rotors. Indeed, these sensors can be mounted on removable blocks, which can be placed at the tip of each rotor, see Figure 44. It is hence possible to completely fill a block or to distribute the twelve sensors on several blocks. All the transducers from the inter-row planes plus the blocks are attached to outer-case moving rings able to rotate over 22.5°, allowing to perform measurements over the whole spatial period.
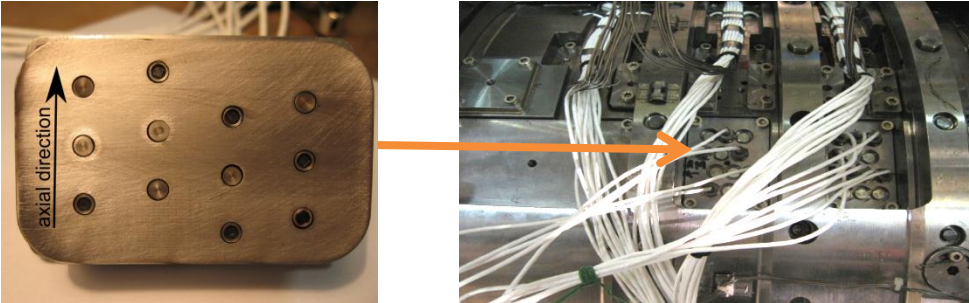
Figure 44 View of a removable block equipped with six sensors and mounted on the compressor

Each removable block can contain up to twelve sensors, spaced over twelve axial positions and four azimuthal angles over 9°, as visible on Figure 45. For the rotors 2 and 3, two blocks have been designed: although the first one has symmetrical axial positions, the second one has shifted axial positions. It is therefore possible to use this second block in a reversed position to double the number of axial positions. Hence, at stable operating points (from choke until surge margin operating point *SM*), 36 axial positions are available for the two last rotors, which allows to perform reconstructed measurements with an axial resolution of one millimeter. It is important to notice that the machine has to be stopped for each block replacement, that's why only twelve axial positions are available for the operating points beyond the surge margin line, as the instabilities like rotating stall or surge are transient phenomena, and therefore only raw measurements can be used. For rotor 1, only one block with shifted positions exists, that is to say a total of 24 axial positions.
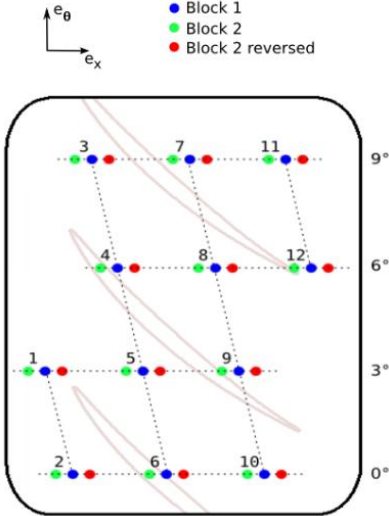
Figure 45 Scheme of a removable block

III.3.4 Data treatment

The treatment of the raw data proceeding from the measurements is done in three steps for each sensor. First, a compensation of the gain **G** and phase shift produced by the conditioners is performed. Then, the data is converted from Volts to Pascals. Before each acquisition, the atmospheric pressure is measured by an outer sensor located at the inlet of the rig. Then, the voltage of the *Kulite* sensor is measured in order to determine an offset voltage, its sensitivity **s** being considered constant. The pressure is finally given by equation (III-1).

$$P_{s\,raw}(\text{t}) = \frac{1}{G \cdot s} \cdot \left(U_{sensor}(\text{t}) - U_{offset} \right) + P_{atmo} \qquad \text{(III-1)}$$

The last step consists in non-dimensionalizing the raw pressure Ps_{raw} by the inlet total pressure and the total pressure ratio at nominal operating point, see equation (III-2). In the following work, every pressure result will be presented non-dimensionalized.

$$P_s(\text{t}) = \frac{\dfrac{P_{s\,raw}(\text{t})}{P_{t_{inlet}}}}{\Pi_{Nominal}} \qquad \text{(III-2)}$$

III.3.5 Global review of the wall static pressure measurements

During the whole experimental campaign, two types of pressure measurements have been done. First, some measurements using the 48 sensors have been performed at different rotor speeds. Every time, the whole characteristic of the compressor was investigated from choke to surge: the machine has finally been brought to surge 24 times. Second, the flow has been investigated at nominal speed, for 11 stable operating points from choke to *SM* operating point over the whole azimuthal period. To perform those measurements, only 24 sensors have been necessary, as only two inter-row planes and the twelve removable sensors were investigated at a time. Therefore, the removable blocks of rotors 1, 2 and 3 have been successively fully equipped and the casing rings been moved by steps of 0.2°, which represents 3.56 % of the blade pitch of rotor 1. The rotor 1 has only been investigated over 11.3°: it is indeed possible to reduce the periodicity of the first stage of CREATE to $\frac{2\pi}{32}$ because the numbers of blades of the *IGV*, rotor 1 and stator 1 (being respectively 16, 64 and 96) are proportional to 32.

All the pressure measurements are summarized in Table 7 and Table 8. This represents a total amount of data of 960 Go.

Investigated rotor	Ω_{shaft}	Nb of operating points	Nb of axial positions	Angular range	Number of azimutal angles
Rotor 1	Nn	11	24	11.3°	57
Rotor 2	Nn	11	36	22.5°	112
Rotor 3	Nn	11	36	22.5°	112
Amount of data					670 Go

Table 7 Pressure measurements at stable operating points

Objective	Ω_{shaft}	Number of operating points	Position of the removable sensors
Performance characterization	0.8 Nn	7	Rotor2 and rotor3
	0.85 Nn	8	
	0.9 Nn	8	
	0.95 Nn	7	
	Nn	8	
Performance characterization	0.95 Nn	8	Rotor2 and rotor3
	Nn	8	
Surge measurements	0.95 Nn	8	Rotor2 and rotor3
	Nn	12	
Surge measurements	Nn	3	Rotor 3
Surge measurements	Nn	4	Rotor 1
		1	Rotor 2
		9	Rotor 2
Total amount of data			290 Go

Table 8 Pressure measurements from choke to surge

III.4 The high-frequency total pressure measurements

III.4.1 General points

Purpose of the measurement:

The total pressure is an energetic quantity. Therefore, it provides very useful information for the analysis of the performance of the machine, like the zones of losses in the compressor for example. The Gibbs equation (III-3) links the total pressure to the total enthalpy, representing the work exchanged between the fluid and the machine, and the entropy, representing the losses. By applying the ideal gas law (III-4) and the definition law of the enthalpy (III-5) to relation (III-3), relation (III-6) can be written. It links the total temperature, total pressure and entropy.

$$dh_0 - \frac{1}{\rho_0}dP_0 = T_0 ds \qquad (III-3)$$

$$P_0 = \rho_0 r T_0 \qquad (III-4)$$

$$h_0 = C_p dT_0 \qquad (III-5)$$

$$C_p \cdot \frac{dT_0}{T_0} - r \cdot \frac{dP_0}{P_0} = ds \qquad (III-6)$$

Therefore, by combining measurements of total pressure and total temperature, it is possible to evaluate the losses in the machine. Unfortunately, unsteady total temperature measurements are difficult to achieve with a sufficient temporal resolution. Thus, only the total pressure is generally used to evaluate the losses, which induce a total pressure drop. Note that the total pressure field additionally highlights the exchanged work between the machine and the fluid. Hence, in addition to the wall static pressure measurements, spanwise total pressure measurements have been performed in all the inter-row planes. However, contrary to the wall static pressure, the measurement of the total pressure is an intrusive technique, as probes have to be inserted in the flow. Hence, the total pressure has only been investigated at stable operating points, as the presence of a probe in the flow at an operating point close to the surge line could have triggered the surge.

State of the art:

Total pressure measurements for high speed compressors are rarely seen in the literature. Indeed, as for the wall static pressure, a very high temporal resolution is required. Moreover, the probes have to resist to high temperatures (above 120 °C) while remaining as thin as possible, in order to induce the smallest possible perturbations to the flow. To overcome the temperature problem, cooling systems are generally used, but they tend to enlarge the probes too much, see Mersinligil *et al.* (2012) [60] for a complete bibliographic review. Therefore, the VKI developed two pioneering total pressure probes, able to perform measurements up to 150 °C with a very high bandwidth of 250 kHz. Their diameter is of 2.5 mm, which represents 2.65% of the azimuthal

periodicity at casing. These probes, named 510 and 511 (because of their serial numbers!) have been used during the whole campaign. A detailed description is available in Mersinligil *et al.* (2012) [60] and [61]. The same *DAC* as static pressure measurements has been used.

III.4.2 Probes characterization

Figure 46 Close-up and general view of a probe

The two probes, visible on Figure 46 have been developed from a 25 psi fast pressure sensor (*Kulite XCE-062*). They have been coated with isolating paint to avoid any electromagnetic coupling with the casing of the machine. The probes were equipped with a temperature compensation module, supposed to ensure a maximum zero and sensitivity shift of ±1%/55 °C between 25 °C and 235 °C. Nevertheless, it has been found that while the temperature compensation module performed its duty well, the offset values changed quite dramatically. For the quoted temperature range, the slope changed from 349.46 mbar/V to 344.69 mbar/V, whereas the offset changed from 469.54 mbar to 1032.58 mbar, see the static calibration presented in the next section. This rendered the compensation module unusable for DC component measurements at varying temperature conditions. It was therefore decided to operate the sensor without temperature compensation module but with an electronic circuitry visible on Figure 47, delivering an additional voltage output proportional to the sensor temperature, monitoring the change in overall bridge resistance. Finally, the circuitry delivers two voltage outputs: a high-frequency signal V_p proportional to the total pressure and a low-frequency signal V_s proportional to the total temperature.
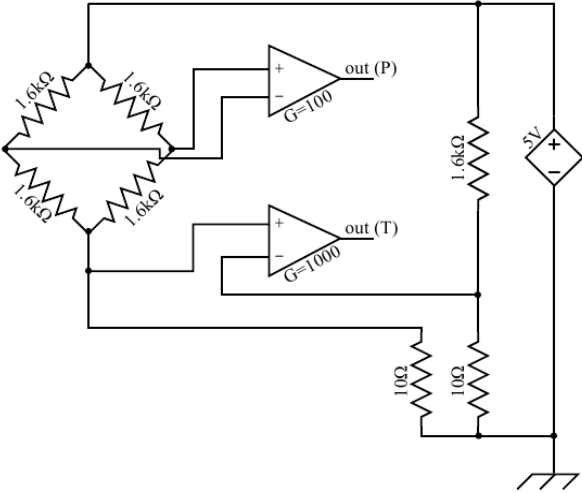
Figure 47 Amplifier circuit diagram showing pressure and temperature outputs

Figure 48 is an example of a discrete Fourier transform calculated from the measured signal V_p obtained with the probe 510 downstream of the second rotor of CREATE. Plotted in blue, is the spectrum obtained with an acquisition system having a sampling frequency of 1 MHz. The resonance frequency of the probe around 335 kHz appears clearly. In red, the same spectrum acquired with the *DAC* presented in chapter III.3.2 is plotted (acquisition frequency of 500 kHz). Aliasing effects appear around 165 kHz (=250-(335-250) kHz). This was due to a failure in the electronics, hence no analog low-pass filter could be used during the acquisition of the pressure signal. However, to avoid any bias in the results, especially for the determination of the standard deviation, a numerical low-pass filter with a cut-off frequency of 150 kHz has been used to post-treat the data. The aliasing effects induced on the second probe measurements are of lower importance and are not presented. They have been filtered using the same method.

Finally, the response time of the temperature signal V_s is around 100 Hz. Note that the measurements of pressure and temperature by a same sensor, i.e. at the rigorous same location, is of particular interest as it allows to accurately calculate the entropy field. In comparison, a significant radial shift exists between the pressure and temperature measurements with a steady probe, see chapter III.2. Finally, note that because of the response time of the temperature measurements, it has only been possible to plot time-averaged total temperature and entropy maps. They are presented in chapter IV.2.
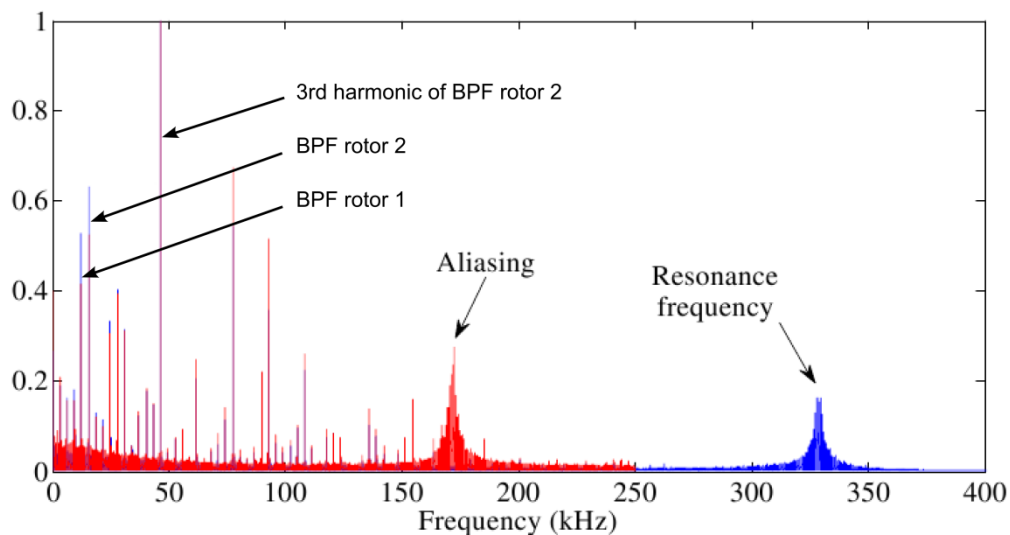
Figure 48 Spectrum downstream of the second rotor using probe 510 and a 500 kHz acquisition system (red) or a 1 MHz acquisition system (blue)

III.4.3 Calibration of the probes

The calibration of the probes has been made in two steps. The first step was a static calibration to characterize the evolution of the sensitivity and offset of the probes versus temperature and pressure. The second step was an aerodynamic calibration, used to correct the measured pressure and temperature when the probe was immerged in the flow. Those two calibrations are detailed hereafter.
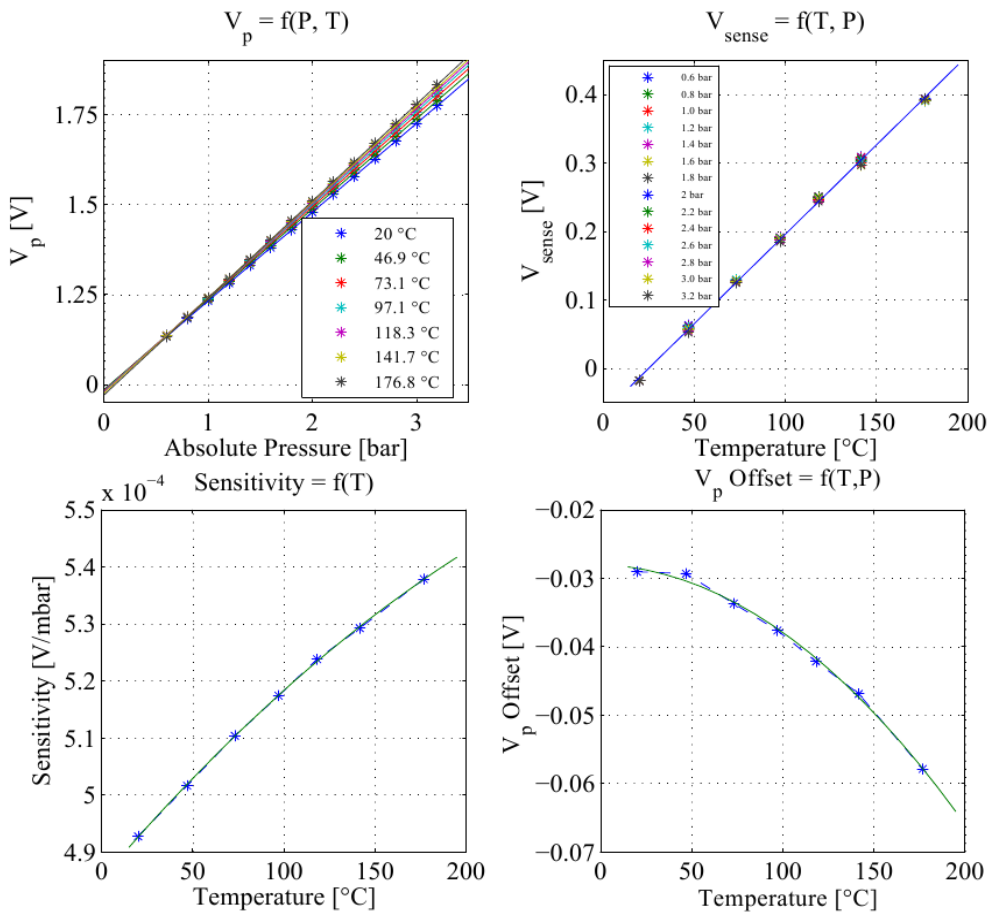
Figure 49 Static calibration data for probe 510

The calibration data of probe 510 are given in Figure 49. For both probes, the effect of pressure on temperature calibration has been found to be negligible, allowing the determination of sensor temperature using only V_s. Hence, the pressure is determined using the sensor's temperature and then determining the correct sensitivity and offset for V_p. From the static calibration, equations (III-7), (III-8) and (III-9) can be written. In equation (III-7), a_0 and b_0 are known (determined from the top-right graphic of Figure 49). The sensitivity (*S*) of the sensor, which depends only on the temperature, is then calculated (a_1, b_1 and c_1 are constants given by the static calibration, see bottom-left of Figure 49). The offset of the voltage V_p, noted O in equation (III-9), is also a function of the temperature (a_2 and b_2 are known from the static calibration, see bottom-right of Figure 49). The value of c_2 is determined using the ambient absolute pressure measured with a reference manometer and compared to the measurement of the probe sensor using the calculated sensitivity inserted in equation (III-8). Once c_2 is determined, the pressure is calculated using equation (III-10).

$$T_{sensor}(V_s) = a_0 V_s + b_0 \tag{III-7}$$

$$S(T_{sensor}) = a_1 T_{sensor}^2 + b_1 T_{sensor} + c_1 \tag{III-8}$$

$$O(T_{sensor}) = a_2 T_{sensor}^2 + b_2 T_{sensor} + c_2 \qquad \text{(III-9)}$$

$$P_t = \frac{V_p - O}{S} \qquad \text{(III-10)}$$

Aerodynamic Calibration:

This second step is performed after the static calibration. The probes have been angularly calibrated using the VKI *C-4 free jet calibration facility* at five different Mach numbers of 0.2, 0.3, 0.4, 0.6 and 0.8 for yaw angles ranging from -30 ° to 30 ° and pitch angles ranging from -20 ° to 20 °. The yaw and pitch angles are positive when the incident flow comes from the right of the probe and looking down the length of the probe from the connector end respectively. The pressure recovery ratio C_{Pt} is defined by relation (III-11). This allows to correct the total pressure values measured when the flow angle is known. The calibration curve of the unsteady port is shown below for Mach 0.8 in Figure 50.

$$C_{P_t} = \frac{P_t - P_{t_{probe}}}{P_t - P_s} \qquad \text{(III-11)}$$
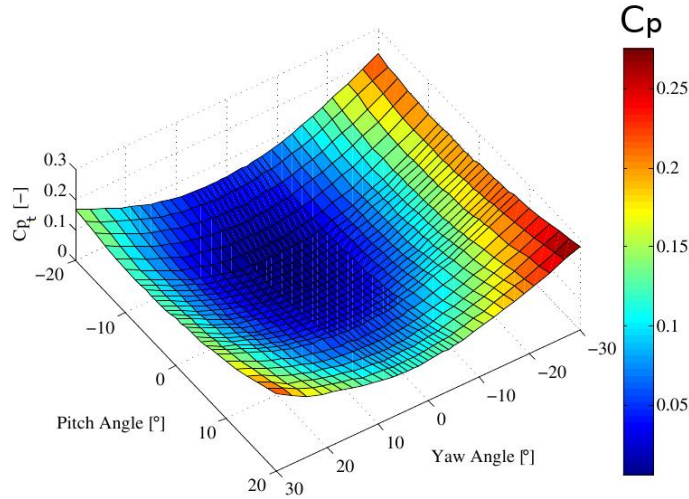
Figure 50 Aerodynamic surface plot of unsteady pressure port for probe 510 M=0.8

The calibration coefficients resulting from the aerodynamic calibration of the probes were obtained for steady conditions in a wind tunnel. To be able to use these steady calibration coefficients, which give the response of the pressure probe as a function of the flow angles (pitch and yaw) at different Mach numbers, the measurements of pneumatic probes acquired during the steady measurements campaign were used. Steady coefficients were interpolated from the calibration curves with the flow angles (pitch and yaw) and the Mach number given by the pneumatic probes. The static pressure of the pneumatic probes and the calibration coefficient were then used in equation (III-11) to correct the mean total pressure. Note that for the measurements presented in this thesis the yaw angle is always close to zero because the probe was aligned with the mean flow in the blade-to-blade direction (obtained from the pneumatic measurements) before each

measurement. This corresponds to a time averaged angle: obviously, the flow angle is not constant with time, but only its steady value has been used for the pressure measurements.

All the total pressure results presented hereafter have been non-dimensionalized by the inlet total pressure and the total pressure ratio at nominal operating point, see equation (III-12), as for the static pressure results. The total temperature measurements have been non-dimensionalized by the dynamic temperature downstream of rotor 1 as written in relation (III-13), C_p being the heat capacity of air and U_{ref} the value of the nominal speed of rotor 1 at mid-span in section 26A.

$$P_t = \frac{\dfrac{P_{t\,raw}}{P_{t_{inlet}}}}{\Pi_{Nominal}} \tag{III-12}$$

$$T_t = \frac{C_p}{U_{ref}^2} \cdot T_{t\,raw} \tag{III-13}$$

III.4.4 Global review of the high-frequency total pressure measurements

The total pressure measurements have been performed for all the inter-row planes from section 26A to section 290, along the span-height and the azimuthal period. Three operating points have been studied: nominal speed at peak efficiency *PE* and loaded *L* points, and 95% of nominal speed at *L* point. The sections downstream of the rotors have been investigated azimuthally with a step of 0.4 °. The angular step downstream of the stators has been reduced to 0.2 ° in order to capture well the sharp structures of the wakes produced by the stators. A picture of the experimental setup with the two total pressure probes mounted on the machine is visible in Figure 51. All the total pressure measurements are summarized in Table 7.

Figure 51 Experimental setup of the total pressure measurements

Location	Number of azimutal angles	Ω_{shaft}	Operating point	Number of spans
Downstream of rotors	57	Nn	*PE*	11
			L	11
		0.95Nn	L	7
Downstream of stators	113	Nn	*PE*	11
			L	11
		0.95Nn	L	7
Total amount of data				50 Gb

Table 9 The total pressure measurements done during the experimental campaign

Note: In the middle of the campaign, the steady part of the total pressure signals has been lost due to a problem with the probes. Hence, for the points obtained during the last part of the campaign, the steady total pressure measurements have been added to the unsteady part of the signals. This will be discussed in the chapter III.4.5 hereafter.

III.4.5 Comparison between steady and high-frequency measurements

Several comparisons have been performed between the pressure measurements obtained with the pneumatic probes during the steady measurements campaign and those obtained with the high frequency response probes. Figure 52 presents these comparisons over a circumferential period of the compressor for three span-heights, downstream of stator 1 (section 270) and downstream of rotor 2 (section 27A). The agreement is very satisfactory, with a difference between the two ways of measuring the mean pressure never exceeding 0.4% downstream the stators, which is coherent with the uncertainties study (see chapter III.6.4); and 1% downstream the rotors. This justifies the treatment done on the measurements after the loss of the steady part of the signal.

Comparisons for the temperature measurements have also been done: as example, Figure 53 shows a comparison between the spanwise evolution of time-averaged measurements and thermocouple steady measurements upstream and downstream of the third rotor. The agreement is excellent with less than half a Kelvin as the largest difference upstream of the rotor and about one to two Kelvins downstream of rotor 3 (the uncertainty of the temperature measurement with the thermocouple is found to be ±0.8 K for a 95% confidence interval). Note also that the geometry of the two probe types is very different: a "cobra" shape for the pneumatic probes and a cylinder for the fast-response probes. The points very close to the shroud have then to be taken with caution due to the different interactions between the probes and the casing at this location.
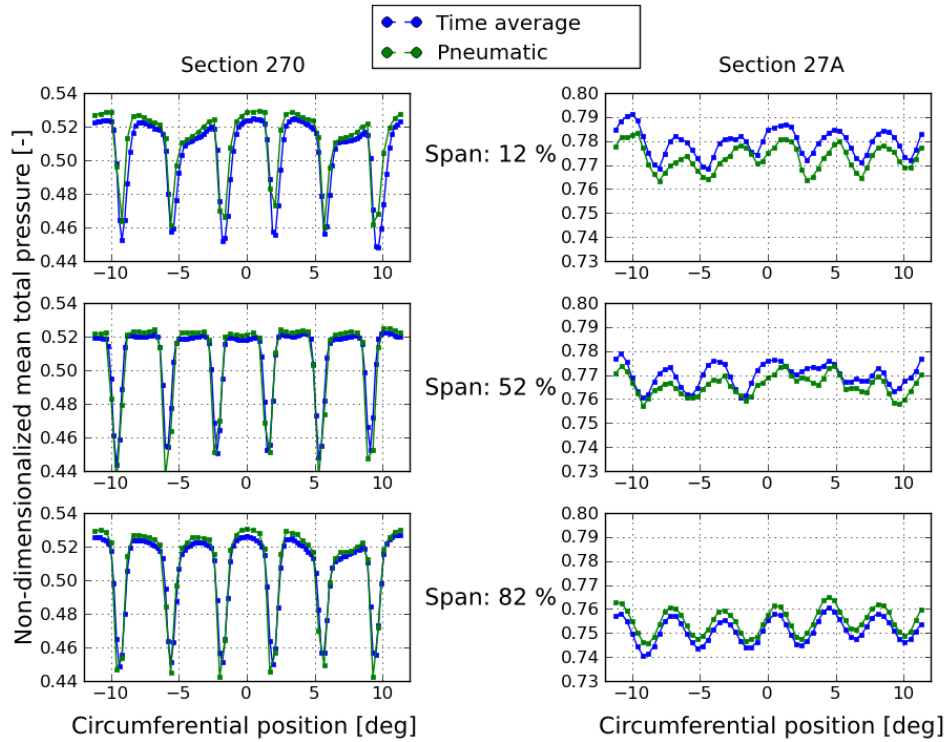
Figure 52 Steady pneumatic versus time averaged measurements for three spanwise positions – sections 270 downstream of stator 1 and 27A downstream of rotor 2
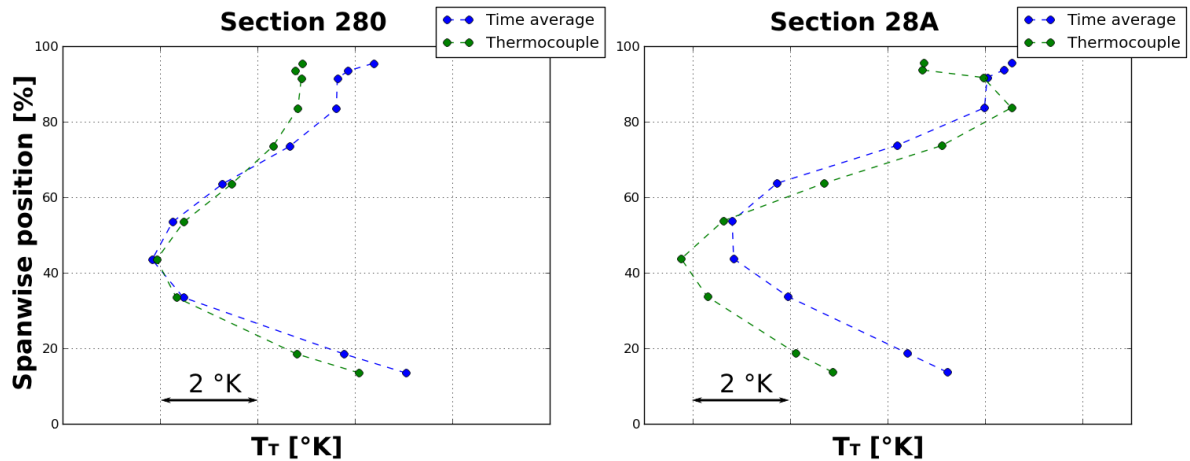
Figure 53 Steady temperature versus time averaged measurements – spanwise evolutions in sections 280 and 28A

Total temperature comparisons are also achieved in the same sections, over the circumferential period for three span-heights see Figure 54. The fluctuations around the mean value at each spanwise location are plotted. Note that the spatial discretization is twice better with the fast-response probes in section 280 than with the thermocouple. This leads to a better characterization of the effects induced by the wakes and explains the differences in the temperature deficit, larger with the fast probes. In the two sections the comparison is obviously excellent. It demonstrates the capability of the probes to measure correctly the total temperature in the vicinity of the last rotor. This justifies the calculation of the entropy field in each inter-row section of CREATE, presented in chapter IV.2.2.
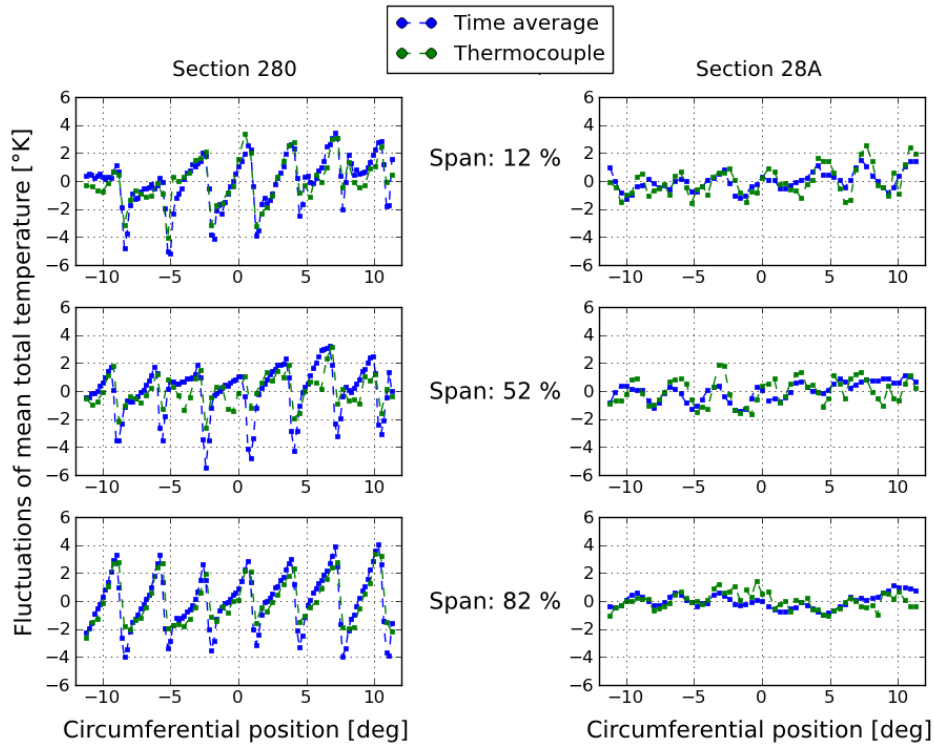
Figure 54 Steady temperature versus time averaged measurements for three spanwise positions –sections 270 and 27A

III.5 The Laser Doppler Anemometry (*LDA*)

The *LDA* is a non-intrusive optical technique allowing to evaluate one, two or three velocity components of the flow. The flow is seeded at the inlet of the machine with small particles (in our case polydisperse aerosol of paraffin oil with particles smaller than 1 µm) supposed to perfectly follow its main direction. A network of interference fringes is produced by two identical laser beams: the light signal re-emitted by the particles when passing through this network allows to calculate their velocity. As many laser frequencies are required as the number of components to measure. *LDA* is a statistical measuring technique, as the velocity of the flow is obtained by averaging (or ensemble-averaging, see chapter III.7.2) the velocity of all the particles recorded for the measuring point. Thus, this technique is only suited to perform measurements for stable operating points, as a long acquisition time is required. Only a brief description of *LDA* will be done, as it is a very common technique very well studied in the literature, see for example the work of Bulot [7] and Godard [29].

III.5.1 Descriptions of the technique and the acquisition system

Description of the technique:

The intersection of two coherent laser beams produces an ellipsoidal measurement volume of interference fringes, containing an alternation of dark and light fringes. The fringe spacing *d* is given by relation (III-14) and depends on the wavelength λ_L of the laser beams and the angle θ between them, see Figure 55.
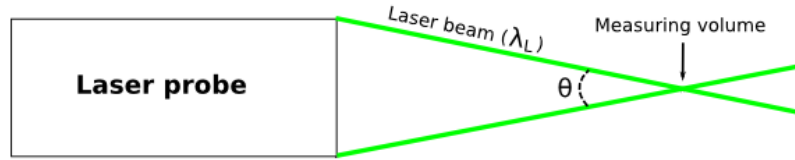
Figure 55 Scheme of a laser probe

$$d = \frac{\lambda_L}{2 \sin \frac{\theta}{2}}$$ (III-14)

When passing through the measurement volume, a particle following the flow scatters the incoming laser light (introducing a frequency shift f_D depending on its velocity - Doppler effect). The scattered light wave is then captured by an optical receptor and converted to an electric signal via a photomultiplier, called "Doppler burst". This signal is characterized by a sinusoidal wave modulated by a Gaussian envelop. The frequency of the wave corresponds to the frequency of passage of the particle through the successive fringes of the measurement volume and is function of the fringe spacing d, the speed of the particule $\vec{V}$ and the normal to the fringes $\vec{n}_f$ see relation (III-15).

$$f_s = \frac{\vec{V}.\vec{n}_f}{d}$$ (III-15)

At this point, there is no information about the direction of the particle. Therefore a Bragg cell is used to impose a frequency shift f_b on one beam to be able to discriminate if the particle moves downstream or upstream. The velocity projected on the normal direction to the fringes is hence expressed by equation (III-16), the sign of the result depending on the direction of the particle.

$$\vec{V}.\vec{n}_f = \frac{\lambda_L}{2 sin \frac{\theta}{2}} (f_s - f_b)$$ (III-16)

Description of the acquisition chain:

In the experimental campaign, the axial and tangential velocity components have been measured by superimposing two emission/reception systems with different frequencies focalized on the same volume. Figure 56 is a scheme of the whole _LDA_ acquisition system which can be divided into three parts. Two pictures of the system are visible on Figure 57.

- The optical conditioner is composed of a 1.8 W power _Laser_ separated into two beams: a green one for the axial component (λ_L = 514.5 nm) and a blue one for the circumferential component (λ_L = 480.0 nm). Each beam is then divided into two other beam by the Bragg cell, which adds a phase shift on one of them (f_b = 40 MHz). The four beams are then brought to the measurement volume by an optical fiber. Note that a Pockell cell is inserted between the fiber and the Bragg cell. Its role is to cut the beams when a blade passes in front of the volume when measurements are done in the rows, in order to avoid a saturation of the photomultiplier.

- The optical probe allows to position the four beams and to make them converge on the measurement volume, passing through a lens of 250 mm focal length. The volume is an ellipsoid with a long dimension of 925 µm and a short dimension of 72 µm, which represents

2 % of the span height and 0.07 % of the azimuthal period in the first stage. 23 and 22 fringes are respectively created for the green and blue beams. The spatial positioning is performed by a six-axis articulated arm robot manufactured by *Kuka*, visible on Figure 57. This system prevents the optical probe from being sensitive to machine vibrations. Due to the axial thrust and thermal dilatation of the machine, a procedure was defined for the positioning of the *LDA* control volume during the compressor operation. The uncertainty of the location of any measurement point is estimated to be of ±0.10 mm.

- The transducer/conditioner developed by *Dantec* converts the light signal into an analog signal with a photomultiplier. The signal is then treated in a spectral analyzer to calculate the velocity components. The output of the system are files containing the arrival times of the particles, their two velocity components and a "top-blade" signal, used to perform ensemble averages, see chapter III.7.2.
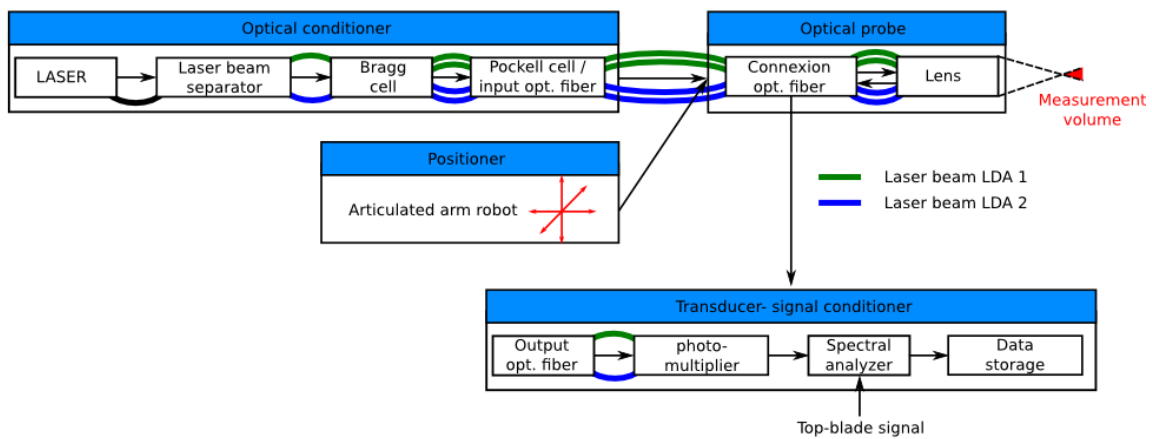
Figure 56 Block scheme of the *LDA* acquisition chain
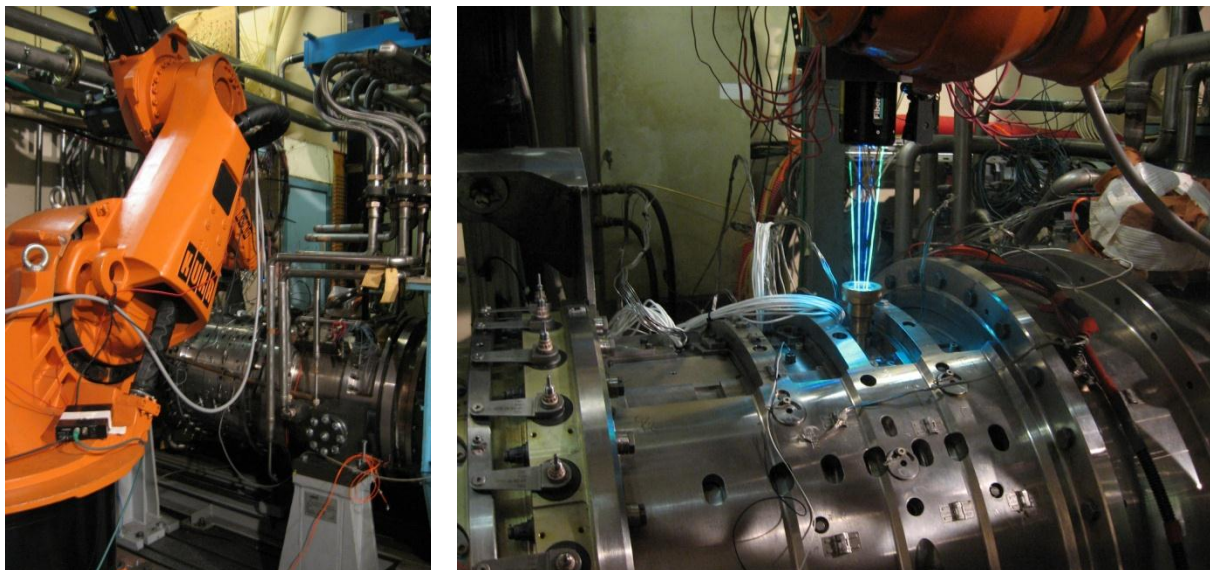
Figure 57 Pictures of the positioning system and focus on the optical probe during measurements

III.5.2 Localization of the measurements

The *LDA* measurements have been performed in all inter-row planes and above the rotors 1 and 3. The optical accesses are portholes mounted on the moving rings to be able to measure velocity over the whole circumferential period. As for the static pressure measurements, removable blocks equipped with eleven slots of portholes have been used to investigate the flow above the rows, see Figure 58. To avoid fouling the portholes, hopper extensions have been used to place the glass out of range of the oil projections due to centrifugation by the rows. Moreover, the diameters of the portholes have been adapted to the span-height of the measurements in order to have smallest diameters as possible: larger diameters were used for the measurements near hub.

Figure 58 Removable block with a hopper extension mounted on the porthole

III.5.3 Review of the *LDA* measurements done during the campaign

During the whole *LDA* campaign, measurements have been performed all along the machine at nominal speed for *PE* and *L* operating points. The flow has been investigated over the complete span-height and azimuthal period of 22.5 ° (11.3 ° for the first stage, as for the pressure measurements).

Depending on the location, different radial and azimuthal resolutions have been chosen. In order to have a sufficient precision in the data, it has been chosen to perform acquisitions of 300 000 particles for each measuring point (details about the calculation of the precision are given in chapter III.6.2). However, depending on the location, the acquisition frequency of the particles may vary a lot: it can be up to 40 kHz at mid-span at the inlet of the machine and dramatically fall to less than 2 kHz in the last stage at casing or hub, where the boundary layers, less seeded in particles, tend to thicken a lot. Therefore, a different radial and azimuthal discretization has been chosen depending on the location of the measuring point, to shorten the campaign. Thus, more spans have been investigated at the inlet of the machine. Similarly, as the flow tends to become complex at casing due to the tip clearance flows, two azimuthal refinements have been used, the number of azimuthal angles being only increased at the upper part of the span.

Special measurements have also been done for the rotor 3, focusing on the tip clearance flow behaviour at the surge margin. The flow has indeed been investigated at tip over a little more than a stator 1 azimuthal pitch at *PE* and *SM* operating points. More information about those measurements is available in chapter IV.3.2.2.

Note: All the velocity measurements results presented hereafter have been non-dimensionalized by the nominal speed U_{ref} of rotor 1 at mid-span of section 26A, see equation (III-17).

$$V = \frac{V_{raw}}{U_{ref}}$$

(III-17)

Location	Operating point	Number of spans	Angular range	Number of azimutal angles
25A	PE	14	11.3°	29 and 57
	L	14	11.3°	29 and 57
26A	PE	14	11.3°	29 and 57
	L	14	11.3°	29 and 57
270	PE	14	22.5°	57
	L	13	22.5°	57
280	PE	12	22.5°	57 and 113
28A	PE	11	22.5°	57 and 113
290	PE	11	22.5°	57 and 113
RM1 slot 3	PE	3	11.5°	57
RM1 slot 5	PE	4	11.5°	57
RM1 slot 7	PE	4	11.5°	57
RM1 slot 9	PE	4	11.5 °	57
RM3 slot 2	PE	4	4.8°	25
	SM	4	4.8°	25
RM3 slot 3	PE	6	4.8°	25
	SM	6	4.8°	25
RM3 slot 4	PE	6	4.8°	25
	SM	6	4.8°	25
RM3 slot 5	PE	6	4.8°	25
	SM	6	4.8°	25
RM3 slot 6	PE	6	4.8°	25
	SM	6	4.8°	25
Amount of data				110 Gb

Table 10 Review of the velocity measurements done on CREATE

III.6 Uncertainties of measurements

III.6.1 General points

The calculation of the uncertainties of all the measurements has been done by applying the propagation law of the uncertainties [44]. This law, expressed in relation (III-18), allows to take into account all the different sources of error $\sigma(g_i)$ to obtain a global error σ for the measurement of a quantity G. It is therefore necessary to identify all the elemental sources of error for each measurement technique. This will be detailed in the chapters hereafter for velocity measurements, wall static pressure measurements and total pressure measurements.

$$\sigma^2\big(G(g_1, g_2, \dots, g_n)\big) = \sum_{i=1}^{n} \left(\frac{\partial G}{\partial g_i} \cdot \sigma(g_i) \right)^2 \qquad \text{(III-18)}$$

Where **G** is the quantity to measure, and **g$_i$** all the factors having influence on **G**.

Note: the uncertainties of steady measurements have been evaluated to be below 0.15 %. Their calculation will not be developed. More details are available in [30].

III.6.2 Uncertainties of velocity measurements

The calculation of the uncertainties of the *LDA* measurements is the most complex to achieve, and will thus be detailed first. To apply the relation (III-18), it is necessary to decompose the global uncertainty σ made on the measurement of each component of velocity V_i into elemental errors. Indeed, σ is produced by a combination of a systematic error σ_S and a random error σ_R. Each error can then be decomposed, as shown in Figure 59. Hence, the error made on the laser measurements are produced by: the laser probe error $\sigma_L(V_i)$ coming from the *Dantec* acquisition system, the error of positioning of the measuring volume $\sigma_P(V_i)$, and the statistical error $\sigma_{St}(V_i)$ which appears because the velocity of a given measurement is estimated from a finite number of particles.

The application of relation (III-18) leads to the following relations:

$$\sigma(V_i) = \sqrt{\sigma_S^2(V_i) + \sigma_R^2(V_i)} \qquad \text{(III-19)}$$

$$\sigma(V_i) = \sqrt{\sigma_L^2(V_i) + \sigma_P^2(V_i) + \sigma_{St}^2(V_i) + \sigma_{Sd}^2(V_i)} \qquad \text{(III-20)}$$

The details of the calculations of the four elemental errors are explained hereafter. As the velocity of the flow tends toward zero at wall, the *LDA* uncertainties will be presented in m.s^{-1} and not in percent, to avoid infinite values.
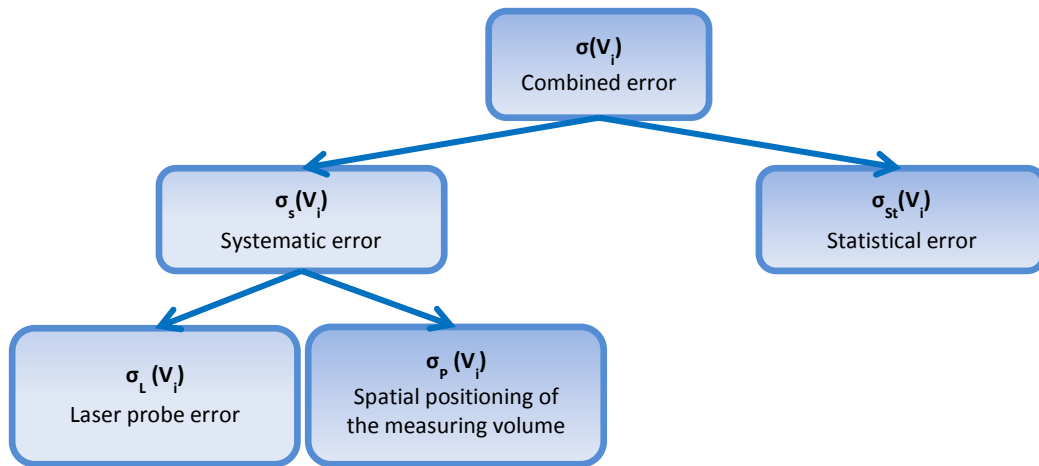
Figure 59 Decomposition of the _LDA_ uncertainties

III.6.2.1 Evaluation of the laser probe error

It is produced by the errors of calibration and treatment of data made by the _Dantec_ acquisition system. The expression of $\sigma_L(V_i)$ can be deduced by applying relation (III-18) to relation (III-15):

$$\sigma_L(V_i) = \sqrt{f_s^2 \cdot \sigma^2{}_d + d^2 \cdot \sigma^2{}_{f_s}}$$

(III-21)

d being the fringe spacing and f_s the frequency of the Doppler burst.

The first term of relation (III-21) corresponds to the error of calibration of the laser probe, i.e. the error done on the evaluation of the fringe spacing: indeed, the laser beams are positioned according to the tolerances given by _Dantec_. It is easy to calculate $\sigma_d(V_i)$ with relation (III-14), by supposing the laser perfectly monochromatic. The second term is produced by the sampling of the signal by the Doppler analyzer. This term is much more complicated to evaluate, as the data acquisition system acts like a black box during the signal treatment. Some relations allow to approximate this error, as stated by Antoine Godard [29] but no confirmation came from the manufacturer _Dantec_.

Therefore, it has been decided to experimentally evaluate the global error $\sigma_L(V_i)$ at LMFA using a rotating disk : the principle is to measure the rotation speed of a regulated disk with the _LDA_ probe, the rotation speed of the disk being known with a precision of 0.033 %. The deviation between the measured speed and the speed imposed by the regulation gives the error of the laser probe. The error done by the laser probe has finally been estimated to be lower than 0.3 % for the axial velocity and lower than 0.1 % for the circumferential velocity, that is to say:

$$\frac{\sigma_L(V_i)}{V_i} < 0.3\%$$

(III-22)

Note: It is important to notice that this estimation has been done on a calibration rig. Therefore, the uncertainties may have been a little underestimated in comparison with those of the measurements done in the machine, where other perturbations like vibrations or temperature

fluctuations can affect the laser measurements. Anyway, this error term is negligible in comparison with the three others.

III.6.2.2 Evaluation of the positioning error

This error is produced by the uncertainties in positioning the laser probe by the *Kuka* robot. The error produced by the temporal positioning of the particles relatively to a rotor revolution has been found negligible. By considering the fringe spacing constant (the angle of intersection of the beams being fixed), the positioning error is only done on the burst frequency: relation (III-15) can be written as follows:

$$V_i = V_i(x, y, z) = d \cdot f_s(x, y, z) \tag{III-23}$$

By applying the law of propagation, this leads to:

$$\sigma_P^2(V_i) = d^2 \cdot \left(\left(\frac{\partial f_s}{\partial x} \cdot \sigma_x \right)^2 + \left(\frac{\partial f_s}{\partial y} \cdot \sigma_y \right)^2 + \left(\frac{\partial f_s}{\partial z} \cdot \sigma_z \right)^2 \right) \tag{III-24}$$

$$\sigma_P^2(V_i) = \left(\frac{\partial V_i}{\partial x} \cdot \sigma_x \right)^2 + \left(\frac{\partial V_i}{\partial y} \cdot \sigma_y \right)^2 + \left(\frac{\partial V_i}{\partial z} \cdot \sigma_z \right)^2 \tag{III-25}$$

The spatial positioning of the probe is ensured by the robot with an uncertainty of ±0.1 mm, that is to say:

$$\sigma_x = \sigma_y = \sigma_z = 0.1 \ mm \tag{III-26}$$

It is therefore possible to calculate the uncertainties for each measuring point: according to relation (III-25), it is obvious that the uncertainties of positioning highly depend on the gradient of velocity. Thus, these errors will be stronger in the zones of strong gradient, like in the wakes produced by the rows or at the tip of the rotors, where the tip gap flows are found. The average positioning uncertainties are presented in Table 11 for each velocity component.

Average positioning error	In weak gradient zones	In strong gradient zones
Axial velocity	0.2 m.s^{-1}	3.0 m.s^{-1}
Circumferential velocity	0.2 m.s^{-1}	1.0 m.s^{-1}

Table 11 Positioning uncertainties for each measuring plane at nominal operating point

III.6.2.3 Statistical error

The statistical error corresponds to the bias of a measurement calculated from an average with a finite number of samples. In our case, it corresponds to the evaluation of the velocity of the fluid at a given position from the measured velocities of *N* particles. According to Moffat [62], the statistical

error can be deducted from the *RMS* value of velocity, i.e. from the turbulence level of the flow, and the number *N* of particles with the relation (III-27). With this definition, the real value of the velocity has 95% chance to be contained in the interval [$V_i - \sigma_{St}(V_i)$, $V_i + \sigma_{St}(V_i)$].

$$\sigma_{St}(V_i) = 2 \cdot \frac{V_{i\,RMS}}{\sqrt{N}} \qquad \text{(III-27)}$$

To perform the *LDA* measurements, the compressor was seeded with a polydisperse aerosol of paraffin oil, upstream of the settling chamber. The size of the particles at the outlet of the seeding generator has been measured and its mean value has been found smaller than 1 μm. In such a flow configuration (low centrifugal forces and moderated decelerations), Ottavy et al. (2001, [67]) proved the reliability of this technique. However, the seeding is identified to be the most important source of bias in this configuration. First, the oil, needed to operate the compressor, is also present in the flow field, with some particles whose size is not controlled and may be larger than 1 μm. The concentration of these particles is higher in the wakes of the rotors, because centrifuged and spread by the blades at the trailing edge.

Then, the concentration of the seeding is not homogenous in the flow field, particularly in the wakes and tip flows, where in some specific cases downstream of a rotor, the number of particles during the acquisition decreases by a factor of five in comparison with the freestream. This increases a lot the statistical error. Note that high *RMS* values are generally found at the same locations, which further increases the error. Fewer particles are also found in the rear part of the machine and at hub, because of difficulties of seeding and development of the wall boundary layers. Figure 60 shows the space-time evolution of the number of particles during a *LDA* measurement at peak efficiency, at tip and hub downstream of the third rotor. For both span-heights, a strong decrease in the number of particles is visible in the wakes. In addition to the wakes, the influence of the tip flow, which enlarges the zones of low particles is visible at tip. Finally, it is worth to notice the global number of particle at hub, nearly three times lower than in the upper part of the vein.
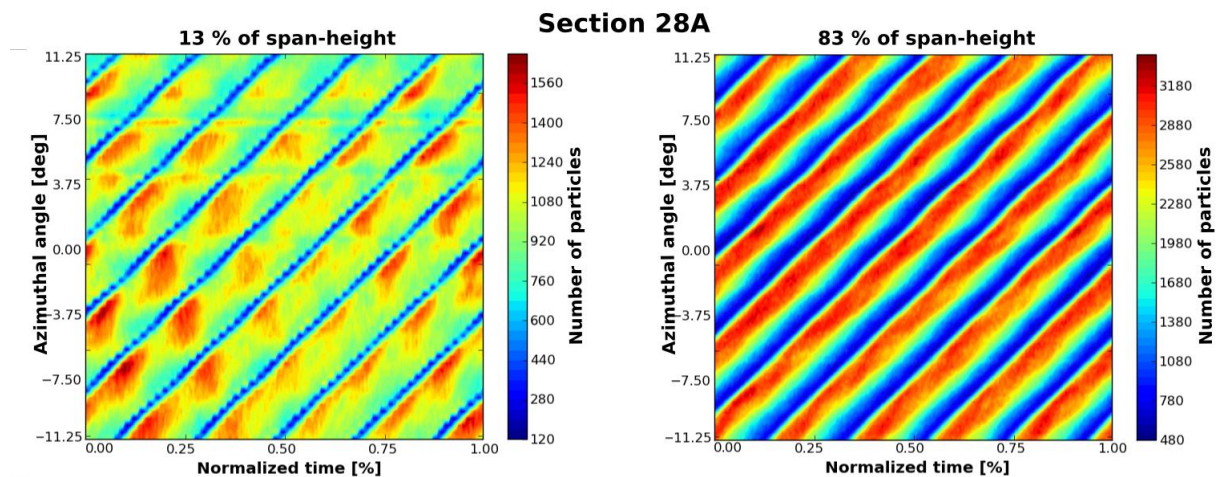
Figure 60 Number of particles in a measuring point downstream of the third rotor at two span-heights – *PE* operating point

In order to maintain a high level of confidence when calculating the ensemble averages, between 3.10^5 and 5.10^5 particles are acquired for each measuring point. The compressor temporal period is discretized over 200 time intervals which leads to an average of 2000 particles per time

interval, with a minimum of about 120 particles observed for the worse intervals. The average statistical error is presented in Table 12 for each velocity component.

Average statistical error	In normal seeded zones	In less seeded zones
Axial velocity	0.2 m.s^{-1}	2.0 m.s^{-1}
Circumferential velocity	0.3 m.s^{-1}	1.5m.s^{-1}

Table 12 Statistical error for velocity measurements at nominal operating point

III.6.2.4 Combined *LDA* error

As previously seen, the *LDA* uncertainties depend on the location of the measurements, as all the different sources of error superimpose, see Figure 61 for an example of the axial velocity uncertainties downstream of rotor 3 for an arbitrary time step. To be perfectly rigorous, it would be therefore necessary to plot the uncertainties for each measuring point for each time step. However, for conciseness considerations, the average and the max values in each section of the *LDA* uncertainties will only be considered. They are presented for each velocity component in Table 13.
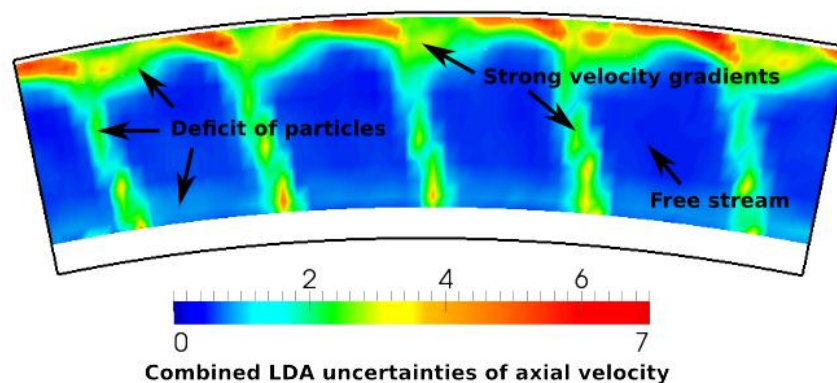
Figure 61 Combined axial velocity uncertainties in section 28A for an arbitrary time step – *PE* operating point

Combined *LDA* uncertainties	Mean value	Max value
Section 25A	0.61 m.s^{-1}	2.09 m.s^{-1}
Section 26A	1.06 m.s^{-1}	9.33 m.s^{-1}
Section 270	0.88 m.s^{-1}	5.51 m.s^{-1}
Section 280	1.12 m.s^{-1}	7.04 m.s^{-1}
Section 28A	1.72 m.s^{-1}	6.80 m.s^{-1}
Section 290	1.74 m.s^{-1}	10.26 m.s^{-1}

Table 13 Combined uncertainties of axial velocity at nominal operating poin

Combined *LDA* uncertainties	Mean value	Max value
Section 25A	0.85 m.s^{-1}	4.13 m.s^{-1}
Section 26A	0.32 m.s^{-1}	1.85 m.s^{-1}
Section 270	1.44 m.s^{-1}	11.81 m.s^{-1}
Section 280	2.49 m.s^{-1}	12.75
Section 28A	0.70 m.s^{-1}	3.59 m.s^{-1}
Section 290	2.59 m.s^{-1}	12.75 m.s^{-1}

Table 14 Combined uncertainties of circumferential velocity at nominal operating point

III.6.3 Uncertainties of high-frequency wall static pressure measurements
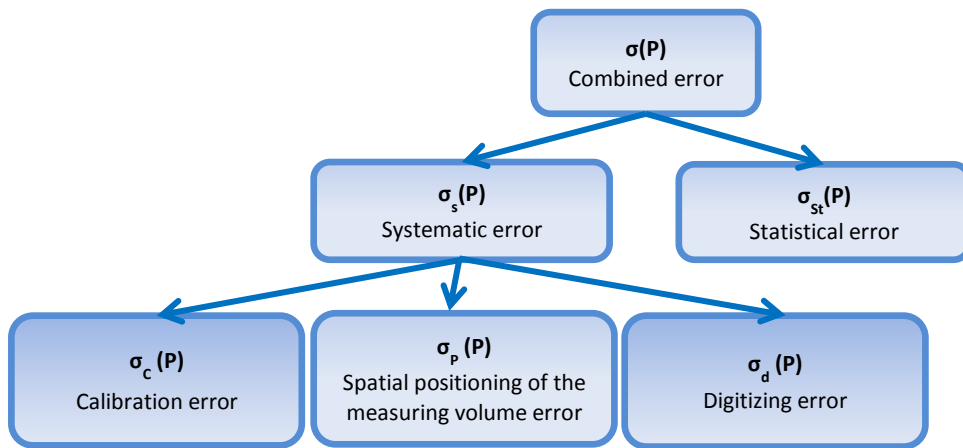
Figure 62 Decomposition of the static pressure uncertainties

The principle of the calculation of the uncertainties of pressure measurements is the same as for the *LDA* measurements. The decomposition of the uncertainties is visible on Figure 62. It is important to distinguish the uncertainties on the steady and fluctuating parts of the pressure signals. Indeed, the analysis of the pressure field is done most of the time with the pressure fluctuations, as well as the comparisons between experimental and numerical results. The measurements have been done in each inter-row plane plus at the tip of each rotor. Therefore, the uncertainties will be presented for each rotor, including the inter-row planes upstream and downstream of the rows.

Statistical error:

The statistical error has to be calculated only for the ensemble averaged pressure signals. All the ensemble-averages have been done for signals of 2048 blocks length, i.e. roughly 13000 temporal periods with 200 temporal windows, the signals being sampled at 500 kHz. This represents more than 10 000 points for each temporal window: therefore, the random uncertainty is negligible for the pressure measurements.

Spatial positioning error:

As the pressure sensors are located at fixed locations (holes in the casing), the positioning error comes only from the uncertainty on the azimuthal position of the moving rings, which is around 0.02 ° (0.09 % of the azimuthal period). This induces at casing an error of roughly 0.09 mm. The spatial positioning error of static pressure, visible in Table 15, has been calculated as for the *LDA* measurements. As well as before, the uncertainties are higher in the zones of strong pressure gradient. Note that in the absolute frame, the gradients of the steady pressure field produced by the rotors are not detectable. Therefore the uncertainties on steady pressure are negligible.

Average positioning error of pressure fluctuations	In weak gradient zones	In strong gradient zones
Rotor 1	0.47 %	3.3 %
Rotor 2	0.51 %	3 %
Rotor 3	0.60 %	3 %

Table 15 Positioning uncertainties of static pressure for each rotor at nominal operating point

Digitizing error:

The digitizing error is done during the encoding of the pressure signals delivered by the sensors. The signals are encoded over 16 bits, that is to say 65536 values are used to describe the full scale of each sensor. Therefore, as the maximum scale is of 3.45 bar (50 PSI), the sampling error is below 5.3 Pa, which is negligible.

Calibration error:

The remaining uncertainty term comes from the systematic error made by the sensor and the acquisition chain during the measurement. From relation (III-1), the expressions of the mean static pressure $\overline{P_s}$ and of the fluctuating pressure $P_s^*(t)$ can be deduced:

$$\overline{P_s} = \frac{1}{G \cdot s} \cdot \left(\overline{U_{sensor}} - U_{offset}\right) + P_{atmo} \tag{III-28}$$

$$P_s^*(t) = P_s(t) - \overline{P_s} = \frac{1}{G \cdot s} \cdot \left(U_{sensor}(t) - \overline{U_{sensor}}\right) \tag{III-29}$$

The uncertainties of calibration of these two terms can be calculated by applying the propagation law of the uncertainties to relations (III-28) and (III-29):

$$\sigma_C^2(\overline{P}) = \frac{1}{G^2 \cdot s^2}\left(\left(\overline{U_{sensor}} - U_{offset}\right)^2 \cdot \left(\frac{\sigma_s^2}{s^2} + \frac{\sigma_G^2}{G^2}\right) + \sigma_{U_{sensor}}^2 + \sigma_{U_{offset}}^2\right) + \sigma_{P_{atmo}}^2 \tag{III-30}$$

$$\sigma_C^2(P^*) = \frac{1}{G^2 \cdot s^2}\left(\left(U_{sensor}(t) - \overline{U_{sensor}}\right)^2 \cdot \left(\frac{\sigma_s^2}{s^2} + \frac{\sigma_G^2}{G^2}\right) + 2\sigma_{U_{sensor}}^2\right) \tag{III-31}$$

By considering the zero shift error $\sigma^2_{Offset\ Kulite}$ of the pressure sensors, relation (III-30) can be also written as:

$$\sigma^2_C(\bar{P}) = \frac{1}{G^2 \cdot s^2}\left(\left(\overline{U_{sensor}} - U_{offset}\right)^2 \cdot \left(\frac{\sigma^2_s}{s^2} + \frac{\sigma^2_G}{G^2}\right) + \sigma^2_{U_{sensor}}\right) + \sigma^2_{Offset\ Kulite} + \sigma^2_{P_{atmo}} \qquad \text{(III-32)}$$

The term $\sigma^2_{Offset\ Kulite}$ is largely predominant in relation (III-32): the manufacturer *Kulite* announces indeed a shift on the zero of the pressure measurement done at operating temperatures other than a normal ambient temperature of 24 °C. Knowing the outlet temperature of the machine, the error has been estimated to be below 2.4% of the full scale of the sensor. Note that the scales of the sensors are adapted to their location in the machine (the 50 PSI sensors are located at the rear part of the machine). Therefore the relative uncertainties of steady static pressure are almost constant in the machine.

The error on the pressure fluctuations is a combination of the error done on the estimation of the gain of the conditioners, evaluated to be around 0.5 %, the error done on the voltage measurement which is negligible and the error on the sensitivity of the sensor. Once again, *Kulite* announces a shift in temperature for the sensitivity inducing an error estimated below 2.4 %. This term is largely predominant for the error on the fluctuations, which has been found to be always below 130 Pa in the whole machine.

Combined error:

The combined error is calculated from the terms of positioning error and calibration error. As written before, the uncertainties on the steady and fluctuating parts of the pressure signals have been distinguished in Table 16.

Combined uncertainties of static pressure	Fluctuations (mean value)	Fluctuations (max value)	Steady value
Rotor 1	0.64 %	3.33 %	2.51 %
Rotor 2	0.61 %	3.02 %	2.71 %
Rotor 3	0.65 %	3.01 %	3.58 %

Table 16 Combined uncertainties of wall static pressure measurements

III.6.4 Uncertainties of unsteady total pressure measurements

The total pressure uncertainties come from the calibration error and the spatial positioning error, as visible on Figure 63. The evaluation of the positioning error is the same as for the laser measurements. The calibration error is a bit more difficult to calculate, as this has to be done in two steps: first the static calibration error has to be evaluated and then the aerodynamic calibration error. This will be detailed hereafter.
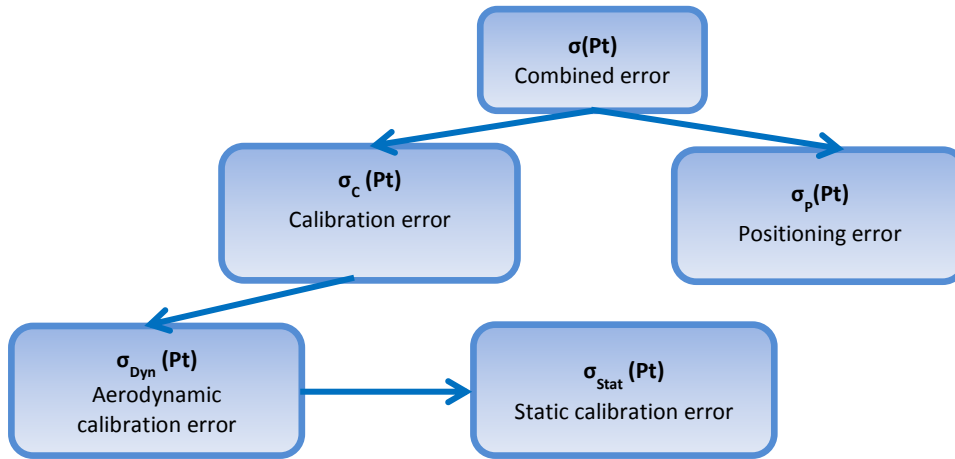
Figure 63 Decomposition of the total pressure uncertainties

III.6.4.1 Positioning error

The total pressure measurements are done with probes along the span over the whole azimuthal period. Therefore, the positioning error comes from the uncertainty of the azimuthal position of the moving rings (around 0.02°) and from the uncertainty of the radial position of the probe (around 0.1 mm). The spatial positioning error of total pressure, visible in Table 15, has been calculated as for the *LDA* measurements.

Average positioning error of total pressure	Fluctuations (weak gradient zones)	Fluctuations (strong gradient zones)	Steady value (weak gradient zones)	Steady value (strong gradient zones)
Section 26A	1.3 %	5.6 %	< 0.01 %	0.19 %
Section 270	4.8 %	14 %	0.16 %	0.46 %
Section 27A	1.4 %	3.1 %	< 0.01 %	0.22 %
Section 280	3.2 %	8.3 %	0.17 %	0.45 %
Section 28A	1.5 %	3.5 %	< 0.01 %	0.06 %
Section 290	2.6 %	7.6 %	0.13 %	0.39 %

Table 17 Positioning uncertainties for each measuring plane at nominal operating point

III.6.4.2 Static calibration error

The static calibration is done in two steps: the temperature is first determined from the voltage V_s, and then the pressure is deduced from the voltage V_p with the calculated sensitivity and offset at the given temperature. From relation (III-10), it can be seen that to estimate the errors due to the static calibration, the error of temperature measurement has to be first determined, then the

error of sensitivity and finally the error of offset. The errors presented hereafter correspond to the maxima of the errors obtained for each temperature over the whole temperature range.

Error of temperature:

To obtain the expression of the temperature versus V_s (see relation (III-7)), several measurements of V_s at different temperature and pressure conditions have been done. Then, a linear regression of these results led to the coefficients a_0 and b_0. The precision in temperature during the calibration was 0.14 °C. From the parameters of the linear regression (number of points etc…), the error done by this regression has been estimated to be 0.023 °C (according to [5]), which is completely negligible. Using the propagation law, this leads to a total error of temperature measurement of:

$$\sigma_T = 0.14 \text{ °C}$$

Error of sensitivity:

As for the temperature calibration, the expression of the sensitivity versus temperature (see relation (III-8)) has been obtained by a quadratic regression of calibration measurements at several temperature and pressure conditions. The error of sensitivity comes from three terms:

- The error due to the precision of the pressure and temperature measurements during the calibration: they have been made with a precision of respectively 10 Pa and 0.14 °C. Using the propagation law, this leads to an uncertainty of **0.63 %**.

- The error due to the quadratic regression: the regression has been done by a *Matlab* instruction. The error induced by this data processing has been evaluated to be **0.13 %**.

- The error due to the uncertainty of temperature: the application of the propagation law to the relation (III-8) leads to:

$$\sigma_{S_T} = (2a_1 \cdot T + b_1) \cdot \sigma_T = \mathbf{0.01} \text{ \%} \tag{III-33}$$

The term due to the precision of measurements during the calibration is thus largely predominant. This leads to:

$$\boldsymbol{\sigma_S} = \mathbf{0.64}\% \tag{III-34}$$

Error of offset:

As for the sensitivity, the error of offset can be decomposed in three terms. The error of offset will be expressed in mV (the average voltage of the measurement of atmospheric pressure being around 500 mV):

- The error due to the precision of calibration has been evaluated to be **4.9 mV**

- The error due to the regression has been found negligible

- The error due to the uncertainty of temperature: by combining the relations (III-9) and (III-10), the expression of the offset versus the temperature can be deduced:

$$O(T) = V_p(T_{amb}) - S(T_{amb}) \cdot P(T_{amb}) + a_2 \cdot \left(T^2 - T_{amb}^2\right) + b_2 \cdot (T - T_{amb}) \tag{III-35}$$

The application of the propagation law to the relation (III-35) leads to an uncertainty of offset of **26.7 mV**. This term is thus largely predominant. This leads to:

$$\sigma_0 = 27.1 \text{ mV} \tag{III-36}$$

Combined error of static calibration:

The application of the propagation law to relation (III-8) leads to:

Maximum Static calibration error	
Total pressure fluctuations	30 Pa
Steady total pressure	60 Pa

Table 18 Maximum static calibration error of total pressure

III.6.4.3 Aerodynamic calibration

The second step for the calculation of the uncertainties is the evaluation of the error done during the aerodynamic calibration. From relation (III-11), the expression of this error can be deduced with the propagation law for the pressure fluctuations and the steady total pressure:

$$\sigma_{aero}^2(P_t^*) = \frac{1}{(1-C_P)^2} \cdot \sigma_{static}^2(P_t^*) + \frac{P_t^{*2}}{(1-C_P)^4} \cdot \sigma_{C_P}^2 \tag{III-37}$$

$$\sigma_{aero}^2(\bar{P}_t) = \frac{1}{(1-C_P)^2} \cdot \sigma_{static}^2(\bar{P}_t) + \frac{(\bar{P}_t - P_s)^2}{(1-C_P)^4} \cdot \sigma_{C_P}^2 + \frac{C_p}{(1-C_P)^2} \cdot \sigma_{P_s}^2 \tag{III-38}$$

With σ_{Static} the error made during the static calibration and σ_{P_s} the error made during the pneumatic measurements of static pressure (0.15 %). To calculate the term σ_{Cp}, the same procedure as for the calculation of the error of spatial positioning has to be applied. Indeed, the correction coefficient C_P depends on three quantities: the Mach number *M*, the yaw angle β and the pitch angle γ. Therefore, the error of the estimation of *Cp* can be written as:

$$\sigma_{C_P}^2 = \left(\frac{\partial C_P}{\partial M}\right)^2 \cdot \sigma_M^2 + \left(\frac{\partial C_P}{\partial \beta}\right)^2 \cdot \sigma_\beta^2 + \left(\frac{\partial C_P}{\partial \gamma}\right)^2 \cdot \sigma_\gamma^2 \tag{III-39}$$

The errors of Mach, pitch and yaw angle have been evaluated from the steady measurements as follows:

- The steady temperature has been measured with a precision of 0.5 °C in the machine. This leads to an uncertainty on the Mach number of roughly 0.05.

- The uncertainty of pitch angle has been evaluated to 0.4 °

- The uncertainty of yaw angle has been evaluated to 0.4 ° downstream of the stators. Nevertheless, downstream of the rotors, the incoming wakes induce an unsteady shift of the flow angle of 15 ° which cannot be taken into account by the total pressure probes (the angles

have been determined during the steady measurements). Therefore, the uncertainty of yaw angle is of 15 ° behind the rotors, which increases a lot the uncertainties.

This finally allows to calculate the calibration error (see Table 19). As written before, this error is quite strong downstream of the rotors.

Calibration error of total pressure	Fluctuations	Steady value
Section 26A	3.69 %	0.10 %
Section 270	0.70 %	0.06 %
Section 27A	4.10 %	0.07 %
Section 280	0.84 %	0.08 %
Section 28A	4.35 %	0.06 %
Section 290	0.8 %	0.06 %

Table 19 Calibration error of total pressure

III.6.4.4 Combined uncertainties of total pressure

The combined uncertainties of total pressure can be deduced from the terms of positioning error and calibration error. They are summarized in Table 20.

Combined error of total pressure	Fluctuations (mean value)	Fluctuations (max value)	Steady value (mean value)	Steady value (max value)
Section 26A	3.91 %	6.71 %	0.10 %	0.21 %
Section 270	4.85 %	14.02 %	0.17 %	0.46 %
Section 27A	4.33 %	5.14 %	0.07 %	0.23 %
Section 280	3.31 %	8.34 %	0.19 %	0.45 %
Section 28A	4.60 %	5.58 %	0.06 %	0.08 %
Section 290	2.72 %	7.64 %	0.14 %	0.39 %

Table 20 Combined error of total pressure

III.6.5 Conclusion

Overall, high-frequency measurements of velocity, static pressure and total pressure have been achieved. The study of the uncertainties of each measurement showed that the experimental results are reliable.

- *Velocity measurements:* in the low gradient zones, the averaged error remains very low (around 1 m/s^{-1}). It tends to increase when going towards the rear part of the machine. A special attention must be paid when investigating the flow inside the wakes and the boundary layer near casing, when the uncertainties are enhanced.

- *Wall static pressure measurements:* because no compensation of temperature has been done, the uncertainties on the steady values of pressure are quite high (around 3%). However, the uncertainties on the fluctuations remain very low (around 0.6 %) which justifies the study of the unsteady flow in Chapter IV and of the instabilities in Chapter V.

- *Total pressure measurements:* for these measurements, a compensation of temperature has been used, allowing to reduce the uncertainties on the steady values of pressure to 0.2 %. The uncertainties on the fluctuations are however higher (around 4 %) because of the fluctuations of the flow angle that cannot be known in real-time, which decreases the efficiency of the correction done during the aerodynamic calibration.

III.7 Signal processing methods

III.7.1 Spatial and temporal averages

Many averages have been performed in this study. They are generally used to reduce the order of complexity of a given problem (for example treat a 2-dimensional problem in 1 dimension). Two types of averages have been used:

- The arithmetic average: defined in relation (III-40) for a given quantity x. It is used for temporal averages and spatial average of static pressure.

$$\bar{x} = \frac{1}{N} \sum_{i=0}^{N-1} x_i \qquad \text{(III-40)}$$

- The weighted arithmetic average, used for spatial averages of convected quantities: the average is weighted by the mass flow $\rho.Vx$ at the measuring point in order to highlight the zones of strong mass flow. Unfortunately, as no measurement of density is available in CREATE, the spatial averages have only been weighted by axial velocity, see relation (III-41):

$$\bar{x} = \frac{1}{N \cdot \overline{V_x}} \sum_{i=0}^{N-1} x_i \cdot V_{x_i} \qquad \text{(III-41)}$$

III.7.2 Ensemble averages

The ensemble averaging of a signal consists in performing an average phase-locked to a given periodicity. The principle is to split the main signal into sub-signals of equal length, and then average

those sub-signals together. The chosen period of the sub-signals has generally a physical meaning: for example, a pressure signal in CREATE could either be ensemble averaged phase-locked to the blade passing frequency or to some other periodic phenomenon as rotating stall, see chapter I.3.1.1. Figure 64 illustrates this technique applied to an arbitrary unsteady pressure signal phase-locked to the temporal period of CREATE with 200 temporal windows. All the samples of the signal are plotted in grey and their average in black.
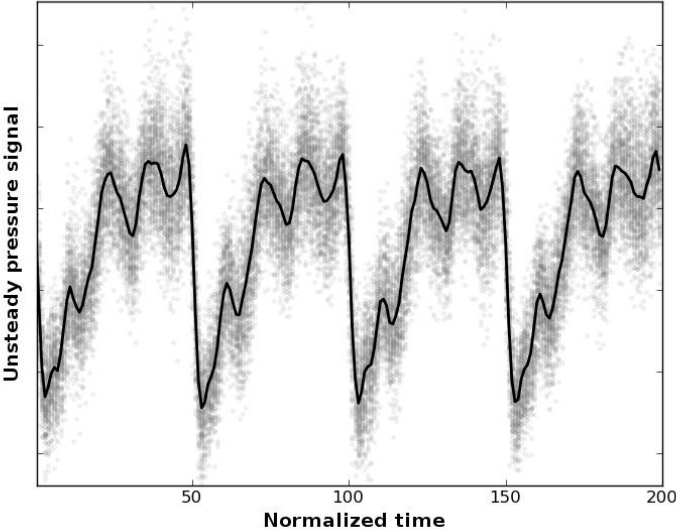
Figure 64 Illustration of the ensemble average of an arbitrary pressure signal over CREATE temporal period – 200 windows

Thus, this technique provides two important pieces of information:

- The deterministic part of the signal, given by the ensemble average: very useful to study the flow at stable operating points for example.

- The non-deterministic part, provided by the standard-deviation: it highlights the dispersion of the measurements around the average, produced by turbulence, unsteadiness (for example the fluctuation of a wake), and the uncertainties. The standard deviation is directly visible on Figure 64 as the envelope of the grey samples. It is calculated for a given quantity at a given position with relation (III-42).

$$\sigma_x = \sqrt{\frac{1}{N} \sum_{i=0}^{N-1} (x_i - \bar{x})^2} \qquad \text{(III-42)}$$

Therefore, this technique permits to reconstruct the flow field over its periodicities (temporal, azimuthal…). Figure 65 shows an example of a reconstruction at an arbitrary time of the wall static pressure and total pressure fields in rotor 3 at peak efficiency. The ensemble average of the static pressure field is plotted above the rotor, in order to highlight the aerodynamic structures, and the standard deviation of total pressure is plotted in the inter-row section, to highlight the zones of

strong mixing and losses, as the wakes or the leakage flows, visible as red stains at tip. Similar maps will be presented in Chapter IV.
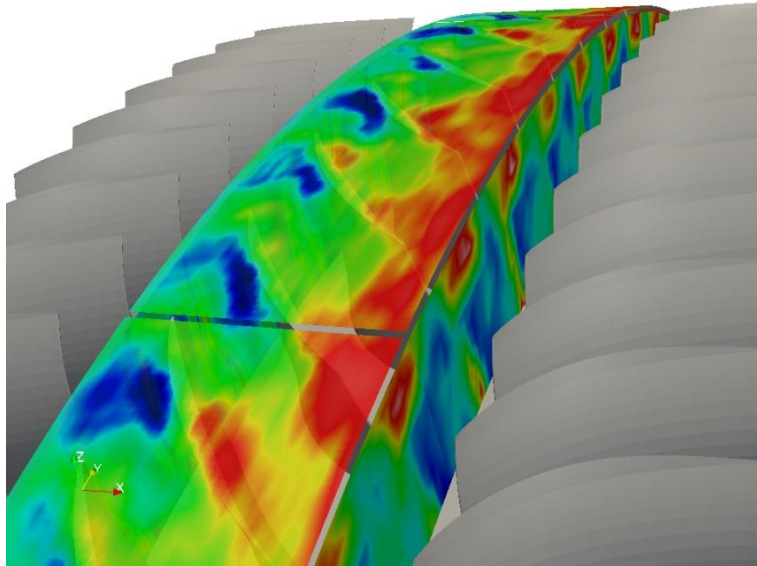
Figure 65 Example of a reconstruction at peak efficiency of the wall static and total pressures fields in rotor 3 at an arbitrary time step

Unless otherwise specified, in the following study ensemble averaging is done with 200 windows on signals of 13000 periods (corresponding to a data of 2048*1024 samples at 500 kHz).

III.7.3 The Fourier transform

The Fourier transform expresses a mathematical function of time as a function of frequency, known as its frequency spectrum. When working with digitized data, the function –called signal- is no more continuous but discrete. All the recordings of the signal constitute the sampling of the signal. Considering a periodic signal *s(t)* of period *T* with *N* samples regularly spaced of *Δt*, its frequency spectrum $\hat{s}(k)$ is calculated with the Discrete Fourier Transform (*DFT*) defined as:

$$\hat{s}(k) = \sum_{n=0}^{N-1} s(n) \cdot e^{-2i\pi k \frac{n}{N}} \qquad with\ 0 \leq k < N\ and\ T = N.\Delta t \qquad \text{(III-43)}$$

This frequency spectrum is complex and can be decomposed as:

- A spectrum in amplitude, which quantifies the influence of each harmonic in the signal:

$$|\hat{s}(k)| = \sqrt{Re\big(\hat{s}(k)\big)^2 + Im\big(\hat{s}(k)\big)^2} \qquad \text{(III-44)}$$

- A spectrum in phase, which indicates the phase shift of each harmonic :

$$\Phi\big(\hat{s}(k)\big) = \arctan\left(\frac{Im\big(\hat{s}(k)\big)}{Re\big(\hat{s}(k)\big)}\right) \tag{III-45}$$

From relation (III-45), it is seen that only a discrete number of harmonics can be calculated from the signal: the Shannon theorem says that the maximum of the observable frequencies in a signal spectrum equals half the sampling frequency of the signal. It is therefore important to have the highest possible acquisition frequency when performing the measurements, to be sure to capture all the physical phenomena. Finally, the Parseval theorem allows us to calculate the energy *E(s(k))* of a signal with relation (III-46). The energy allows us to compare the unsteadiness (in signal processing the quantity of information) of several signals [77]. For example, considering the two signals $s_1(t)=sin(\omega t)$ and $s_2(t)=2.sin(\omega t)$ which have the same mean value, the energy will tell us that signal s_2 is more energetic than signal s_1. In this thesis, when the term "*energy*" will be used for an aerodynamic quantity (for example energy of the pressure field), it will refer to the signal processing definition of the energy.

$$E\big(s(k)\big) = \sum_{k=0}^{N-1} |\hat{s}(k)|^2 \tag{III-46}$$

III.7.4 The windowed Fourier transform

The *DFT* can be used to calculate the spectrum of a stationary signal, for example a pressure signal ensemble averaged over the temporal period of the compressor. In the case of a non-stationary signal, it is possible to split the main signal into short sub-signals considered as stationary: by performing the *DFT* of each sub-signal, it is hence possible to calculate the temporal evolution of the spectrum of the main signal and to plot 2D-diagrams (time versus spectrum) called spectrograms. They are of particular interest for the study of transient phenomena, as the onset of the instabilities in the machine.
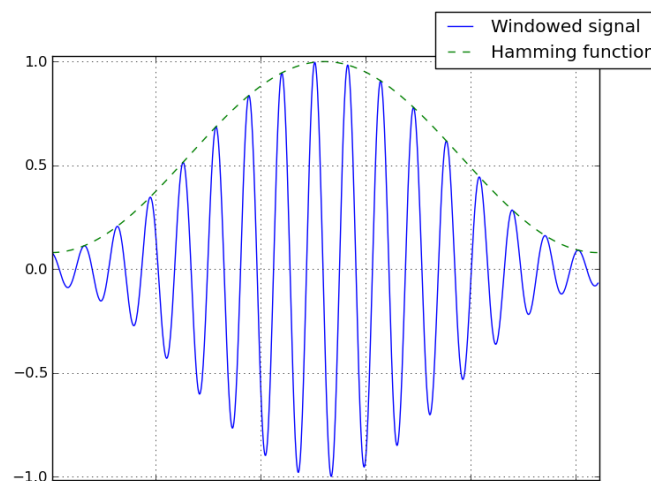
Figure 66 Example of a signal windowed with a Hamming function

To extract the sub-signals, the main signal *s(t)* is multiplied with a window function *w(t)*: in signal processing, a window function is a mathematical function that is zero-valued outside of some chosen interval. An example of windowed signal is visible in Figure 66. The windowing of a signal causes its Fourier transform to develop non-zero values commonly called spectral leakage at frequencies not belonging to its spectrum. Therefore some special window functions have been developed in order to minimize this spectral leakage, as the well-known Hamming function [77]: this window function has been chosen for the treatment of the data presented in this study.

The choice of the length of the window is imposed by the Heisenberg uncertainty principle, stating that the temporal precision is inversely proportional to the frequency resolution, see relation (III-47). Hence, depending on the phenomenon observed, the choice of the window's length is a compromise between the temporal localization of the phenomenon and the precision of its characterization in frequency. Unless otherwise specified, the windowed Fourier transform have been performed with windows of 2^{14} samples, in order to use fast Fourier algorithms. With an acquisition frequency of 500 kHz, this represents sub-signals extending over around 6 rotor revolutions ($\approx$33 ms), allowing a frequency resolution of 30 Hz.

$$\Delta t \cdot \Delta f = 1 \tag{III-47}$$

Chapter IV
Description and modal analysis of the flow at stable operating points

IV.1 Introduction

The flow in a multistage compressor is driven by a succession of rotating and fixed blade rows. These rows emit aerodynamic structures which interact together and are sources of strong unsteadiness: the rotor-stator interactions (*RSI*) can indeed severely perturb the flow, especially at the rear part of the machine, where the influences of all the rows superimpose. Their real impact on the performance of aeronautic compressors are however still unclear. The goal of this chapter is to present an experimental analysis of the flow focusing on the *RSI* developing in a multistage machine. In this chapter, an experimental study of the flow in CREATE will therefore be presented. It will be based on high-frequency measurements of wall static pressure, total pressure and velocity. A description of the flow will first be given, followed by a modal analysis of the measurements.

The unsteady description of the flow field in a compressor is a complex 5-dimensional problem. Indeed, the flow field extends over three spatial directions, plus time and depends on the operating point. Moreover it can be described through numerous aerodynamic quantities. In order to propose an intuitive study of the flow in the first part of this section, the analysis will be done from global to detailed points of view. Therefore, the following section will first present a global overview of the performance of the machine through spanwise evolutions of several aerodynamic quantities. The following chapters will then investigate the unsteady flow by focusing on more and more local phenomena.

The second part of this chapter will present a modal analysis of the flow based on high-frequency pressure measurements. A modal decomposition method will hence be presented and then applied to the experimental results in order to understand the mechanisms responsible for the appearance of the *RSI* and try to evaluate their impact on the performance of the machine.

Finally, note that in a matter of confidentiality, all the figures presenting a view of the flow in the physical frame have been stretched.

IV.2 Global overview of the performance of CREATE

IV.2.1 Spanwise evolution of the main aerodynamic quantities

This chapter proposes to study the spanwise evolutions of pressure, temperature, entropy and angle of the flow in order to draw an overview of the performance of CREATE. They are presented in

Figure 67 and Figure 68: Figure 67 shows the spanwise distributions of each quantity downstream of each row, and Figure 68 shows their evolution through each row. The meaning of these quantities in term of performance comes from the relations (III-5) and (III-6).

They allow to state that:

- The variations of total temperature represent the work exchanged between the fluid and the machine. Overall, the high temperatures highlight the zones of strong work. Note that the losses produced by viscous dissipation increase the static temperature and thus also affect the total temperatures. It is therefore interesting to couple the total temperature measurements with the incidence angle measurements, which also point out the exchanged work through the Euler relation (I-1).

- The entropy field represents the losses in the machine. The high entropy zones highlight the zones of strong losses.

- The total pressure field is a combination of the two previous fields. The losses produced in a row will induce a decrease in total pressure as well as a high exchanged work will increase the total pressure.

When looking at the performance of a compressor, the first quantity to analyze is the work exchanged between the machine and the fluid, visible through the increase in total temperature when crossing the rotors.

Note first that the increase in total temperature (and entropy) in the bottom part of the span visible in Figure 67 for all the inter-row sections is due to a hot flow injection (coming from the inside of the compressor) upstream of the *IGV*. It creates a thermal boundary layer, visible in section 25A, which propagates in the whole machine.

Crossing the rotors

In CREATE, the work appears to be roughly well distributed along the rotor span, with an increase of the total temperature in the upper part of the span-height, which becomes stronger downstream of the rotors 2 and 3, see Figure 68. For these two rows, a large hump of total temperature is indeed visible up to 50% of span-height (less visible for rotor 1). These humps are due to the balance of three effects. First, the tangential velocity of the blades and their stagger angle increase with the radius. This tends to increase the work exchanged (see Euler equation (I-1)). Second, the casing boundary layers and the tip clearance flows (*TCF*) particularly strong behind the two last rotors are responsible for the decrease of the axial velocity from 70 % of span-height to casing, which leads to an increase of the angle of incidence and an over-deflection of the flow (visible through the increase in the variations of α in this region). This over-deflection of the flow has also a positive effect on the work exchanged between the machine and the fluid. Third, the velocity of the fluid decreases dramatically close to the casing due to the boundary layer and the *TCF*. As a consequence, when this effect starts to be predominant, the Euler equation gives a decrease of the total temperature and of the work.

When looking at entropy, one can note that the losses generation in the compressor are found stronger at hub and casing. Downstream of the rotors, a huge zone of high entropy is visible at tip. Its maximum value is encountered at roughly 90 % of span-height: these zones of strong losses are

produced by the wall boundary layer and the *TCF* (see the high amplitude behind the rotors 2 and 3), which are zones of high mixing inducing losses production. Their influence is also visible in the total pressure distributions which show strong pressure decreases from roughly 80 % of span-height to casing: indeed, in this region, the work decreases behind the rotors and the entropy keeps increasing. As a general trend, the losses increase when going towards the outlet of the machine, as the contributions of each row superimpose.

Crossing the stators

Downstream of the stators, the zones of production of losses are encountered in the bottom part of the span, see the distributions of entropy. Note that these zones are already visible upstream of rotor 1 (section 25A): indeed, the *IGV* blades are equipped with a system of variable stagger angles, generating some leakage flows at tip and hub. An increase of entropy is visible close to the tip. This is less visible close to the hub, because the losses generates by the leakage flows are not significant compared to the increase of entropy induced by hot fluid injection upstream of the IGV (as already mentioned).

When traversing the stators, the temperature should remain constant, as no work is exchanged with the fluid. Thus, the decrease in total pressure only highlight the losses (a similarity between the total pressure and entropy distributions – appearing mirrored in Figure 67 - is visible). This is almost the case in the compressor, but one can note that slight negative variations of the temperature exist in the upper part of the vein. On one hand, the uncertainties of the temperature measurements could explain a part of these variations. One the other hand, the conservation of the total enthalpy should be true only along a streamline. In the figures, the variations have been calculated using the data acquired at the same span height, which lead to incorrect conclusions if the streamlines do not follow these span-heights. The study of the *TCF* will prove later in this chapter that the tip leakage vortices tend to go deeper in the vein at the outlet of the rotor, but also when passing through the stators. This radial convection would explain the negative variation of the temperature and entropy combined with a quasi-null variation of total pressure in the upper part of the passage downstream of the stators, and also the increase of the losses just below this zone.

Overall, all the rows (rotors and stators) produce roughly the same losses.

Operating points

Finally, the spanwise evolutions of each quantity at *Loaded* operating point are very similar to *PE* operating point. It appears indeed that these two operating points have been chosen too close one from each other to see the appearance of phenomena that highlight a change in the flow topology. Therefore, the total pressure increases with the load on the machine, as well as the total temperature and entropy. It is however worth to notice that these increases are significantly stronger in section 28A, downstream of the third rotor. More generally, the differences between *PE* and *L* operating points are stronger in the second and third stage than in the first. Having described these general tendencies, the next chapter will present time-averaged maps of the flow at *PE* operating point in order to have a first visualization of the structures of the flow.
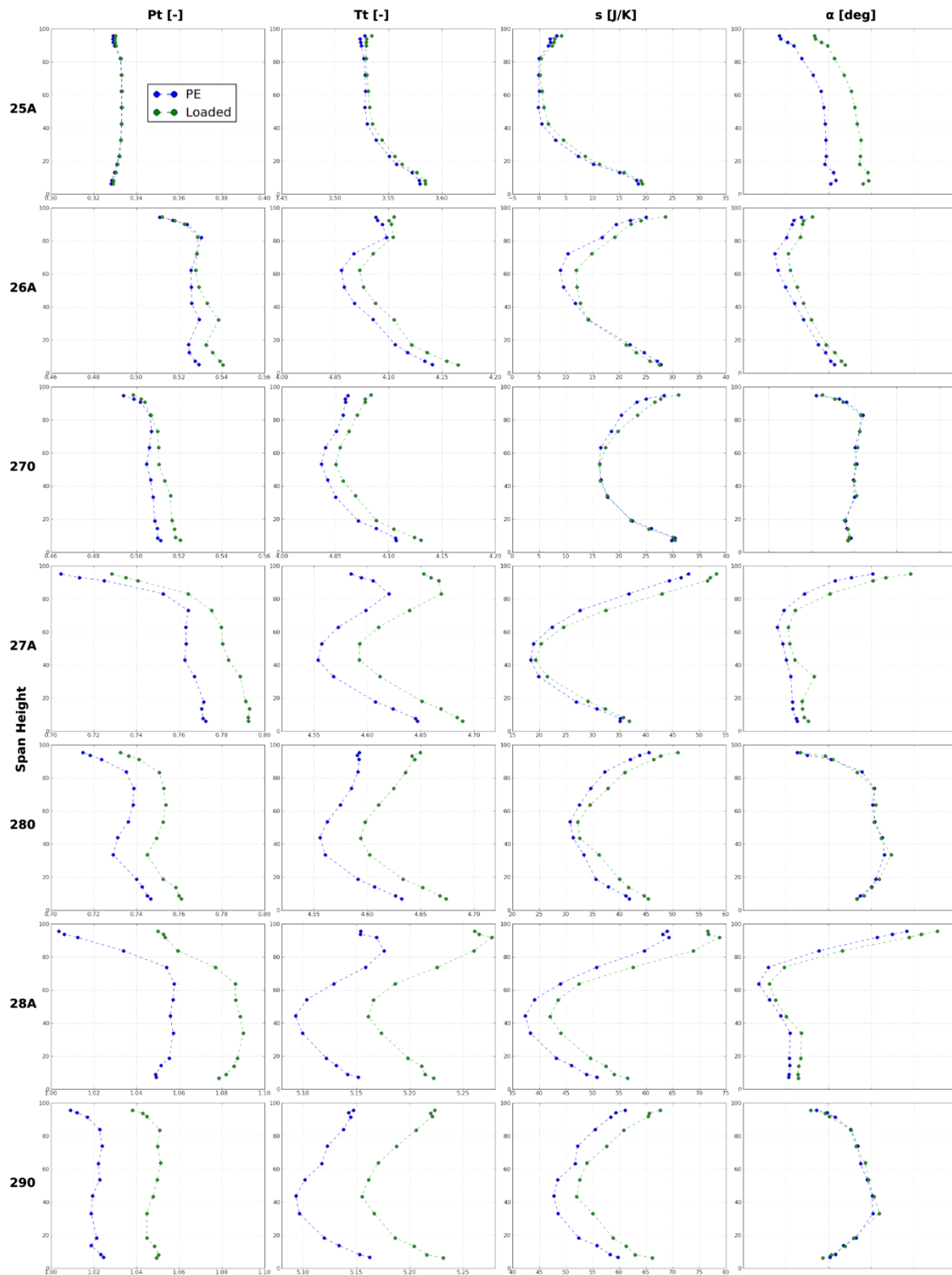
Figure 67 Spanwise distributions of total pressure, total temperature, entropy and flow angle for all inter-row sections at *PE* and Loaded operating points
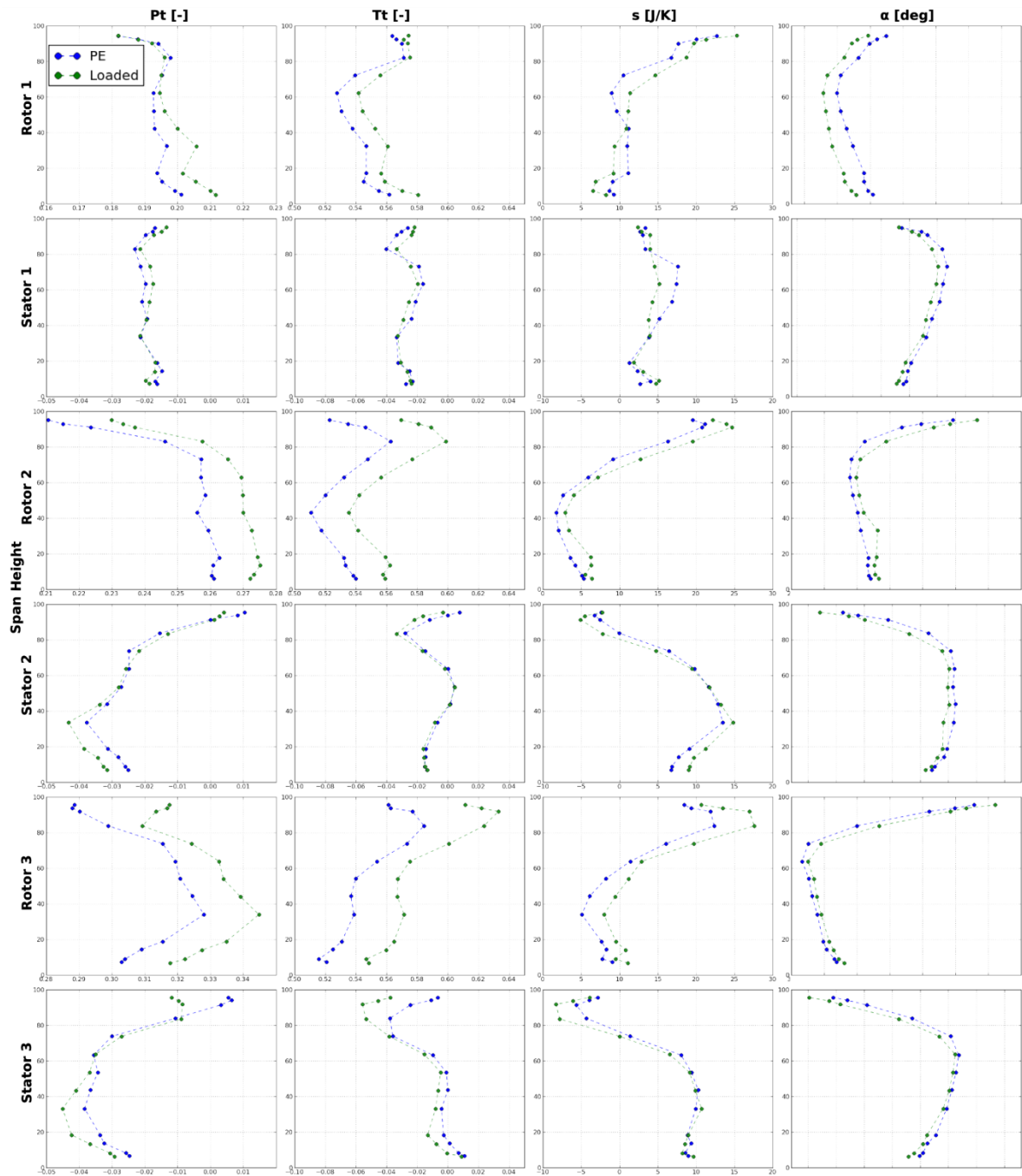
Figure 68 Spanwise distributions of the evolution of total pressure, total temperature, entropy and flow angle through each row at *PE* and Loaded operating points

IV.2.2 Description of the time-averaged flow at peak efficiency

This section is dedicated to the study of the time-averaged flow in all the inter-row sections at *PE* operating point. Figure 69, Figure 70 and Figure 71 show respectively the time-averaged total pressure, total temperature and entropy fields obtained with the unsteady total pressure measurements: as previously shown is chapter III.4.5, the comparison between steady and time-averaged high frequency total pressure measurements showed very satisfactory results. The pressure and temperature are measured with the same sensor in the high frequency probes (see chapter

III.4.2) contrary to the steady probes, where the pressure and temperature sensors are spaced of 1 mm (see chapter III.2). This is particularly important to calculate the entropy field. It has therefore been decided to use the high-frequency probes to study the time-averaged flow fields. The iso-contour maps are plotted over a spatial period of the compressor, Θ_{16} (sector of 22.5 °) over the whole span-height. CREATE has a constant radius at the casing. For reasons of confidentiality, the value of the radius at the hub has been arbitrarily chosen and kept constant for all the sections. This non-dimensionalization has been done for every (R-θ) maps presented in this chapter.

The influence of each stator is very well captured by the probes (only the contributions of the stators and the mean contributions of the *RSI* can be seen in maps time-averaged in the absolute frame). Downstream of these rows, the influence of the wakes is very strong, see for example in Figure 69 the six stripes of low total pressure in section 270 downstream of the first stator (six blades). These zones of high mixing are sources of high losses, as it is visible on the entropy map in Figure 71. On the contrary, the influence of the stators is less marked on the total temperature maps, see Figure 70. This could be explained as this quantity is proportional to the work exchanged with the fluid, which is null in the stators. Therefore, the azimuthal gradients are only due to the influence of the upstream rotors. Indeed, high total temperature is found inside the wakes of the rotors because the tangential velocity is increased (see chapter IV.3.1.1), as well as the work. The accumulation of the hot wakes generated by the rotor blades at the pressure sides of the stators (because of the "negative-jet" phenomenon, see chapter I.2.1) is responsible for the temperature gradients in the stators wakes. Therefore, the temperature maps are a superposition of the azimuthal effects of the upstream rotors and the radial distribution of temperature found upstream of the stator row, the high temperatures found at hub being due to the hot fluid injection upstream of the *IGV*.
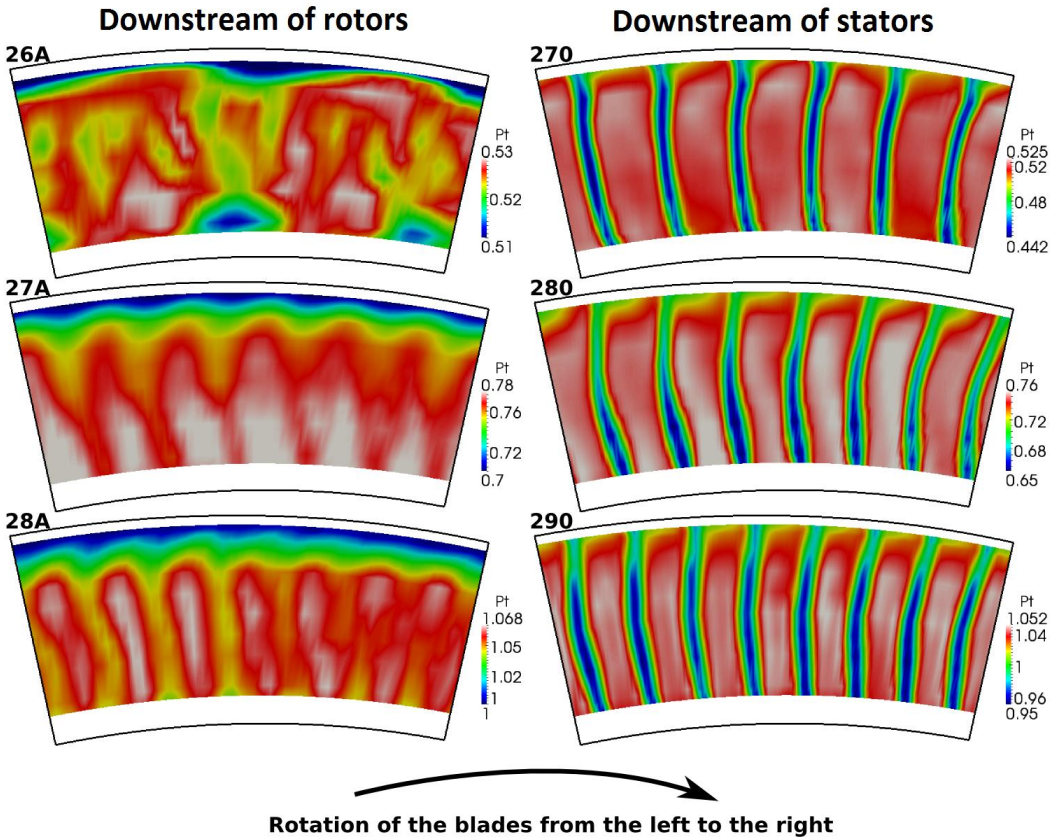
Figure 69 Time averaged field of total pressure in all inter-row sections at *PE*

Downstream of rotors   **Downstream of stators**

26A   270

27A   280

28A   290

Rotation of the blades from the left to the right
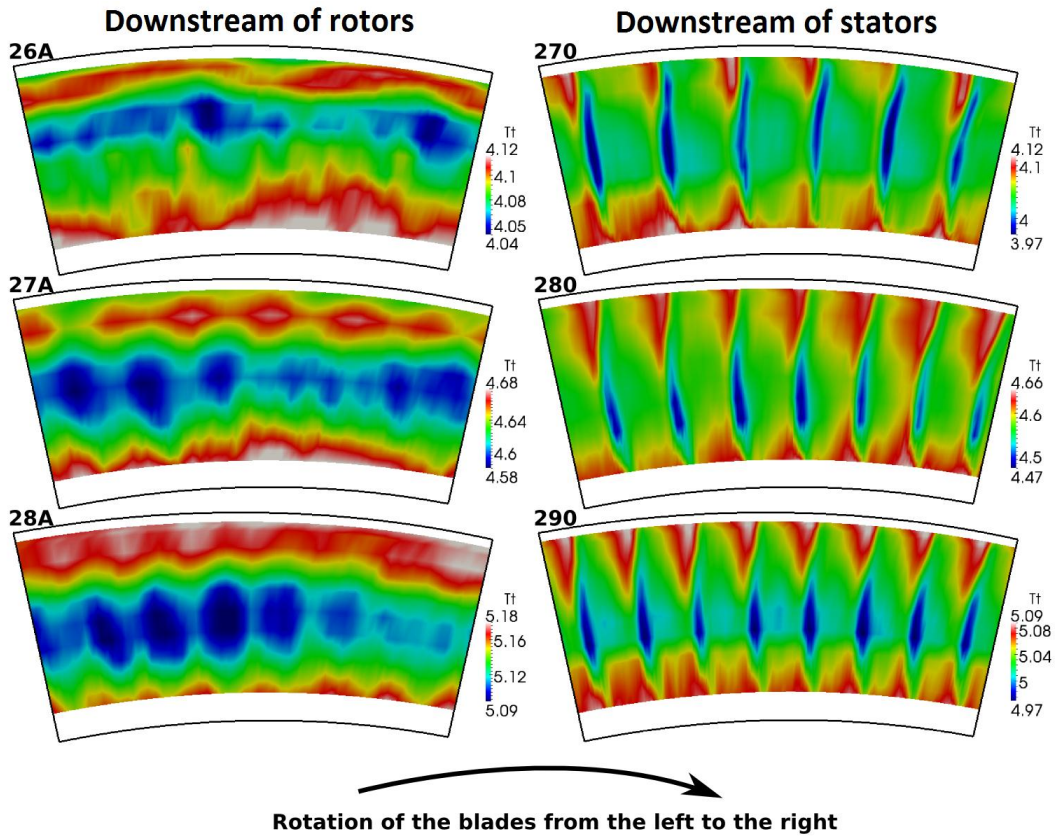
Figure 70 Time averaged field of total temperature in all inter-row sections at *PE*

Downstream of rotors   **Downstream of stators**

26A   270

27A   280

28A   290

Rotation of the blades from the left to the right
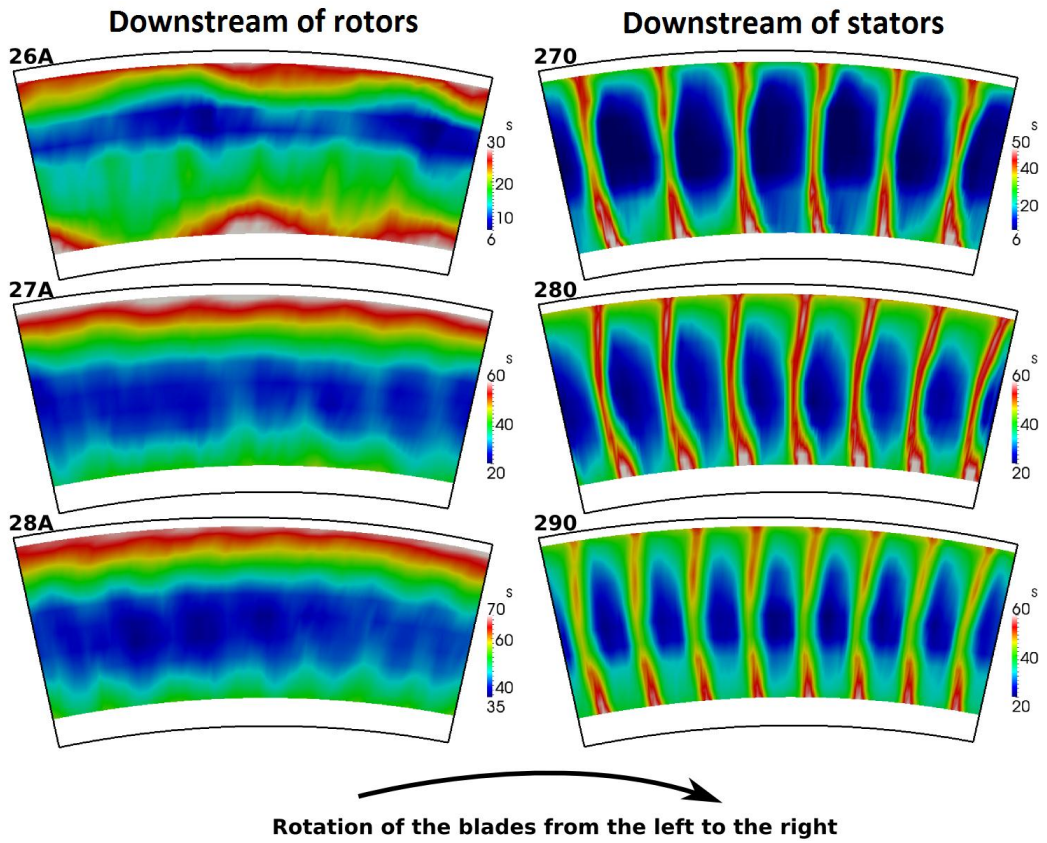
Figure 71 Time averaged field of entropy in all inter-row sections at *PE*

The influence of the stators is more diffused downstream of the rotors. A modulation of the total pressure field by the two blades of the *IGV* is visible in section 26A, as well as in section 27A and 28A by the six and seven blades of stator 1 and 2 respectively. Nevertheless, contrary to the downstream-stator sections, the low pressure zones are less marked: for the temperature and entropy maps, the influence of the stators blades is even less visible.

At casing, zones of low pressure are visible downstream of the rotors. These zones of high losses visible on the entropy maps are produced by the *TCF* and boundary layer at casing that tend to increase when going towards the outlet of the machine (see the spanwise evolution of entropy in Figure 67). In the temperature maps, the maxima of temperature are located just below the casing: they correspond to the humped distributions seen in the previous chapter. The influence of the *TCF* is also felt downstream of the stators: the flow upstream of the stators is indeed perturbed by the *TCF* and the incidence angle increased. This tends therefore to thicken the stator wakes and the boundary layers at casing, see the pressure maps. In the entropy maps, the zones of high losses extend from casing to roughly 80 % of span-height. As previously seen, the stators produce few losses at casing: the losses observed at tip behind the stators, which also induce the high temperatures, are therefore emitted by the upstream rotors which propagate through the stators. Note that the losses generated by the rotors tends to accumulate in the stator wakes, because of the negative jet effect and the passage vortex.

Zones of strong losses are also visible at hub through temperature or entropy increases. For example two spots of low pressure (and high temperature and entropy) are visible in section 26A. They could be produced by a corner stall occurring in the *IGV*. Those spots, also visible in section 270, correspond to two zones of high entropy. As written in the previous chapter, the highest zones of entropy are found at hub behind the stators.

Overall, wakes and boundary layers tend to thicken when going toward the outlet of the machine, and the losses increase. Indeed, the flow becomes more and more complex, with increasing mixing processes, as the influence of each row superimposes to each other.

IV.3 Description of the unsteadiness of the flow at peak efficiency

After the analysis of the time-averaged flow, this section is a study of the unsteadiness of the flow. It is based on the high frequency measurements of total pressure, velocity and wall static pressure. In a first part, snapshots of the flow in the inter-row sections at a given time will be presented. Then, the study will focus on the flow developing at the tip of the rotors.

IV.3.1 Flow field in the inter-row sections

IV.3.1.1 Unsteady pressure and velocity fields at a given time step

This section is dedicated to the study of the unsteady flow in all the inter-row sections using total pressure and velocity measurements (LDA). Figure 72, Figure 73 and Figure 74 give an overview

of the ensemble averaged axial velocity field, tangential velocity field and total pressure field respectively (left part of the figures) in all the inter-row sections at the same arbitrary time step chosen as reference. The inter-row sections from 26A to 290 are presented from the top to the bottom of the figures. The iso-contour maps are plotted over the spatial period of the compressor Θ_{16}. For the three figures presented hereafter, the blades are indicated with spanwise dotted lines. On the right side of each figure is plotted the standard deviation corresponding to each quantity: these maps highlight the zones where some phenomena not phased with the temporal period of the compressor, like turbulence, take place. They are generally sources of high losses. The standard deviation is therefore particularly high in the wakes or *TCF*, where the random unsteadiness is high. Finally, the following nomenclature is used: *W* for wake, *R* for rotor, *S* for stator, and the digit for the stage number (e.g. *WS1*: wake generated by a blade of the stator 1). Note that specific spans are highlighted with azimuthal-wide dotted lines: these spans will be subject of particular attention in the next chapter.

The wakes emitted by the rows are well caught in all the maps. In each section downstream of the rotors, the influence of the row just upstream is indeed clearly visible in the axial velocity maps through the velocity deficits induced by the wakes, see in section 26A for example the four wakes produced by the blades of the first rotor. In the tangential velocity maps, the wakes are visible as zones of increased velocity of the fluid: indeed, the reduction of relative velocity induces an over-deviation of the flow in the absolute frame which increases the tangential velocity. Note that in the sections 26A and 28A, the zones of high tangential velocity in the bottom part of the span are due to the radial equilibrium law chosen for the compressor. Finally, the influence of the wakes is less marked in the total pressure maps. The pressure deficits produced by the losses in the wakes are quite diffuse: in rotor 3, they are even no more discernible. To have a clear visualization of the wakes downstream of the rotors, one should have plotted the relative total pressure. In all the standard deviations fields, the strong turbulence of the wakes produces zones of high standard deviation, with a maxima encountered in the center of the wakes.

Downstream of the stators, the wakes are also very strong. As for the sections downstream of the rotors, the wakes produce axial velocity deficits. Their signature is very different in the tangential velocity maps, as they only produce weak azimuthal gradients of velocity. As for the temperature measurements behind the stators presented in chapter IV.2.2, this is due to the "negative-jet" effect. Indeed, the wakes coming from the rotors, characterized by high tangential velocities in the absolute frame, accumulate on the pressure sides of the stators. This produces the azimuthal gradients visible in the wakes downstream of the blades. A description of this phenomenon had already been done by Mailach *et al.* in 2007 [52]. The wakes are however very well caught by the pressure measurements with marked zones of low pressure. The standard deviation maps of pressure are interesting as they present two stripes of high standard deviation values at each side of the wakes center lines, where any fluctuations of the flow in these zones with high gradients produce high values in the standard deviation. This phenomenon can also be explained by the turbulence intensity which is not maximal at the center of wakes. A reason why only one stripe per wake is caught in the velocity maps could be the coarser refinement of the velocity experimental mesh.

The development of the losses at casing when traversing the whole compressor is clearly visible in the three sets of maps, through the pressure deficits and high values of standard-deviation encountered at tip, especially downstream of the rotors affected by the leakage flows. As presented

in chapter IV.2.1, the intensity of the *TCF* increases a lot in rotor 2 and 3 in comparison with rotor 1. In section 28A, in the axial velocity map, the *TCF* is particularly strong and induces a zone of high standard deviation at the left of each channel, i.e. at the pressure side of the adjacent blade (the blades going from left to right). At this location the axial velocity is strongly reduced and a huge blockage occurs. This is visible in the total pressure map as a strong decrease in pressure at casing due to the increase in losses. In the corresponding standard-deviation map, it can be seen that the casing boundary layer produces a huge zone with high level of losses extending over more than one third of the blade span. As a general trend, the random unsteadiness increases when going towards the outlet of the machine, as the boundary layers and the wakes thicken. It is visible in the velocity maps of section 290 for example that the free stream regions in the bottom part of the passage are significantly reduced. This is consistent with the observations of the time-averaged flow which showed a global increase in the losses at the rear part of the machine.

Figure 74, Figure 72 and Figure 73 also show that there are some significant differences between one inter-blade channel and its neighbors. These differences, not only in the thickness and the losses of the wakes but also in the mean level and the radial distributions of pressure and velocity in the channels, increase with the number of rows the flow passes through. This is obviously induced by the interactions between the rows, mostly generated by the wakes and the tip leakage flows. The potential effects here have less significant impact on the velocity and total pressure fields, except in terms of blockage effects. For example, downstream of the stage 1 (section 270) the flow field is dominated by the six wakes of stator 1 (*WS1*), the four wakes of rotor 1 (*WR1* in the standard deviation maps), the *TCF* of rotor 1 (green zones at the casing in the standard deviation maps), where there is no significant influence of the five blades of rotor 2 located just downstream. A modulation of the flow by the two wakes of the *IGV* is also visible in the total pressure map, as two zones of pressure deficit at casing in the passages 1 and 4. This modulation is very strong in the bottom part of the passage of section 26A for tangential velocity. In stages 2 and 3, the role of the interactions between the rows is much more complex as the contribution of each row superimposes. The velocity maps remain however very understandable, as the wakes are very marked in the whole machine, and the interactions only produce zones of low and high speed in the passages. The standard deviation maps are much more affected by the interactions, see for example the tangential velocity in section 28A where the influence of the wakes of all the rows are captured, or the differences in the *TCF* intensity when they interact with the wakes of stator 2. This is all the more true for the total pressure maps, which become too complex in the rear part of the machine to be simply explained with a snapshot at a given time.

Overall, the unsteadiness of the flow increases a lot in the rear part of the machine as all the rows interact together. An analysis of the spatial flow field is not sufficient to study these interactions which are highly time-dependent: the study of the temporal evolution of velocity and pressure is the subject of the next chapter.
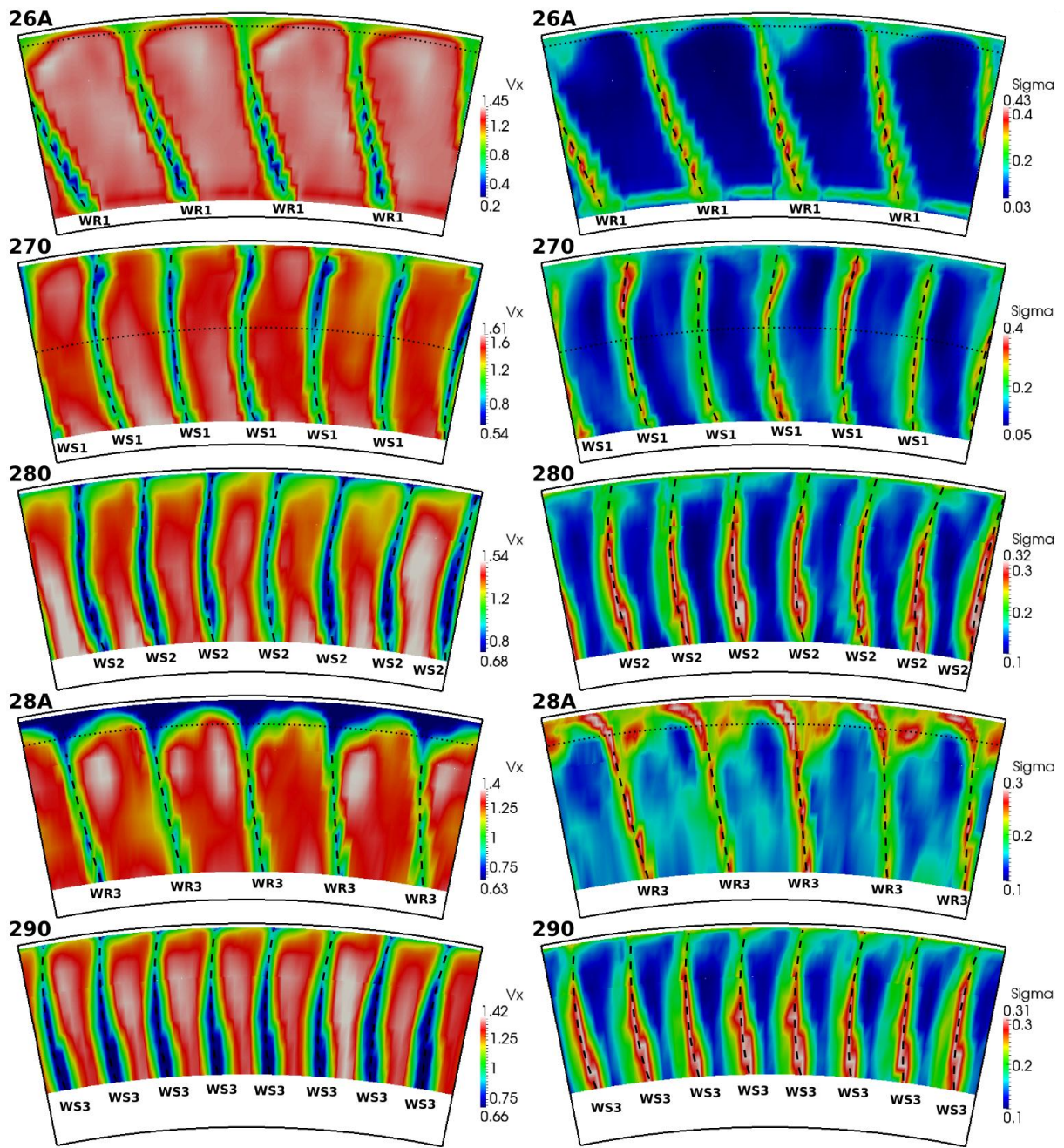
Rotation of the blades from the left to the right

Figure 72 Non-dimensionalized axial velocity and standard deviation fields in the six inter-row sections at the reference time – LDA measurements
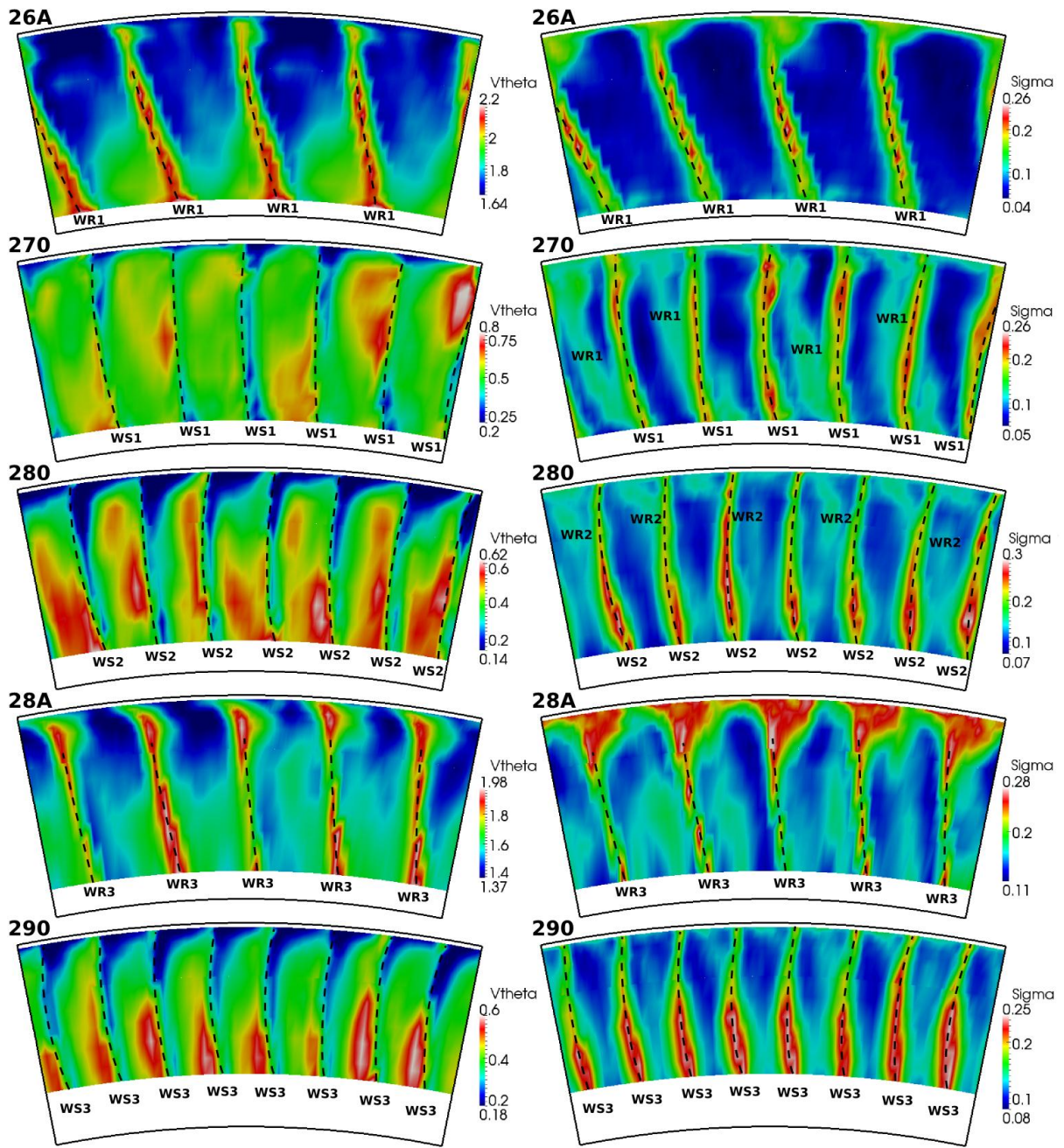
Rotation of the blades from the left to the right

Figure 73 Non-dimensionalized tangential velocity and standard deviation fields in the six inter-row sections at the reference time – LDA measurements
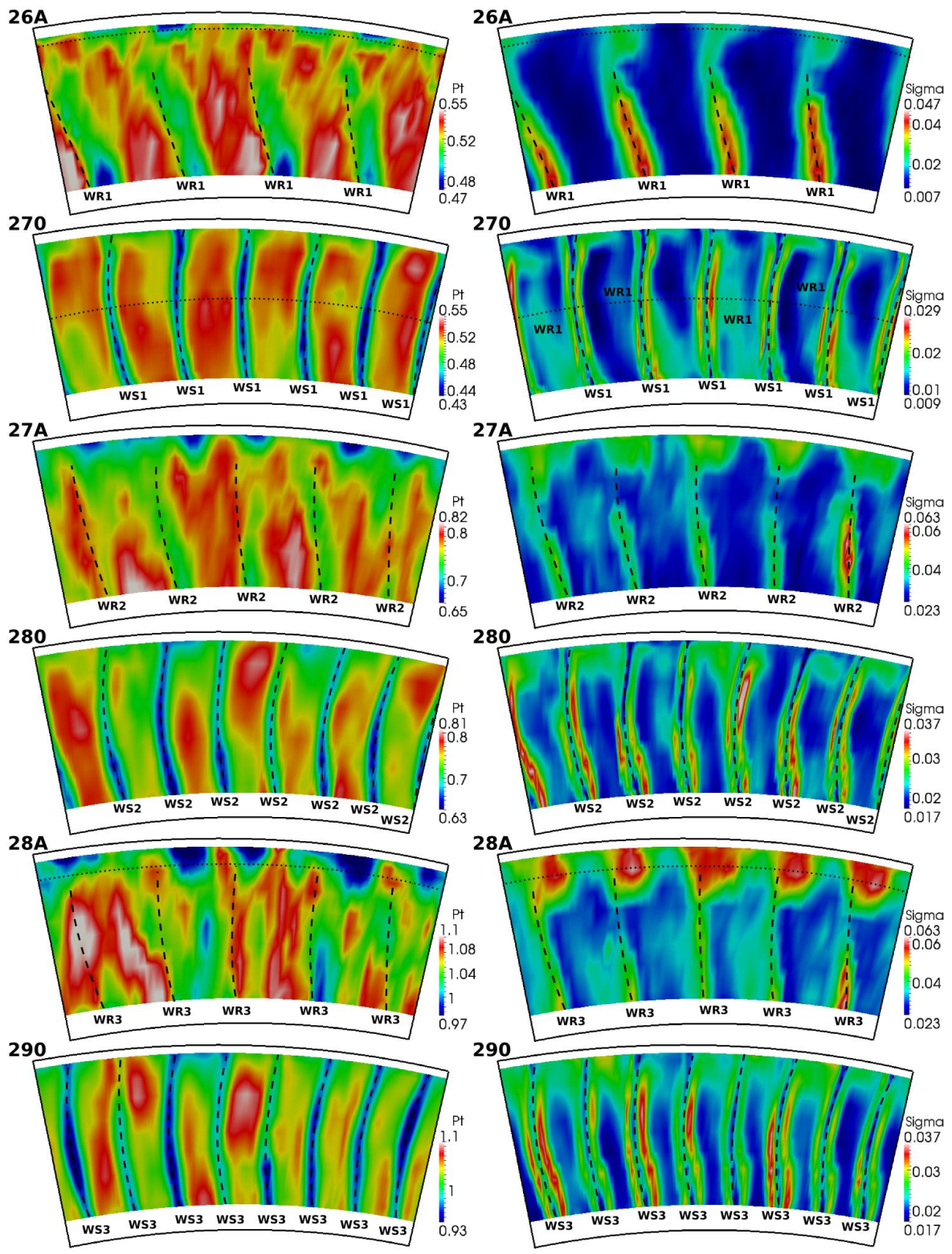
Figure 74 Non-dimensionalized total pressure and standard deviation fields in the six inter-row sections at the reference time

IV.3.1.2 Temporal evolution of the pressure and velocity fields

As shown before, the complex azimuthal structures of the flow come from the contributions of the rows and their interactions. This chapter proposes to study their impact on the temporal evolution of the unsteady flow. Figure 75, Figure 76 and Figure 77 show space-time diagrams of total pressure and axial velocity at different positions in the machine: 94% of span-height in section 26A, 52% of span-height in section 270 and 91% of span-height in section 28A respectively. The corresponding span-heights are highlighted in Figure 72, Figure 73 and Figure 74 by dotted lines. The maps are plotted over the azimuthal and temporal period Θ_{16} and T_{16} of CREATE. On the left of each map, the temporal average is visible in order to see the influence of the stators. On the right, the temporal signal ensemble averaged and its corresponding standard-deviation are plotted for two specific azimuthal angles: the same angles are selected for axial velocity and total pressure. The locations of the maps have been chosen in order to highlight the main phenomena responsible for the high unsteadiness of the flow: the superimposition of the influence of the wakes of each rows, the interaction between the rows and the tip clearance flows.

Velocity and pressure maps in section 26A downstream of rotor 1 – 94% of span-height:

Figure 75 shows the axial velocity and total pressure fields at tip of section 26A: this location has been chosen to highlight the impact of the *TCF* and the *RSI* on the flow in a simple configuration: indeed, the first stage of CREATE behaves almost like a single stage compressor. In the space-time diagram of axial velocity, the four wakes emitted by the first rotor, spinning at the rotation speed of the rotor Ω_{shaft} are very well captured by the measurements. On the left side of each wake (see the blue lines of low speed) the *TCF* are visible as they enlarge the zone of low velocity (see the green stripes). An azimuthal modulation of the velocity field can also be observed: two periods of low pressure are indeed produced by the two blades of the *IGV* whose influence is still strong downstream of the first rotor. However, the temporal average of axial velocity shows six oscillations superimposed to the modulation of *IGV*. They are produced by the potential effects of stator 1. It is worth noticing that at mid-span (not presented here), the time-averaged velocity signal would show only the two oscillations produced by the *IGV*.

The temporal evolutions of the ensemble average and standard deviation of velocity have been plotted for two azimuthal positions corresponding to the minimum and the maximum of the modulation. For both locations, the wakes and *TCF* are visible. The wakes produce sharp peaks of standard deviation, whereas the signatures of the *TCF* are humps with less intensity. Indeed, the shape of the *TCF* is more spread than the sharp wakes. This is visible at location 1 in the ensemble averaged signals: the wakes produce the sharp decrease in velocity, and the *TCF* the small step on the left of each wake. At location 2, the *TCF* are less visible: they have indeed shifted and merged with the wakes, because of their interactions with the *IGV* wakes. Note that for both locations, a small shift exists between the averaged and standard-deviation signals (see the wakes at location 1 for example): the peaks of standard deviation are found in the zones of strong gradient of averaged value. Indeed, as explained for the pressure wakes in the previous chapter, any fluctuation of the flow at these locations induces strong fluctuations in the averaged signals. This shift can be observed for each quantity exposed in Figure 75, Figure 76 and Figure 77.

The total pressure field is more complex. At tip behind the first rotor, twelve stripes corresponding to spinning structures rotating at twice Ω_{shaft} are indeed visible in the flow, and no

simple evidence of the wakes appear. The temporal average confirms that the influence of the *IGV* is very strong at this location. Note that contrary to the velocity field, the potential effects of stator 1 do not appear in the total pressure field. The temporal evolution of pressure has been plotted at the same two azimuthal positions as for axial velocity (right hand side of Figure 75). For both positions, the influence of rotor 1 is very strong and produces four oscillations in the standard-deviation signals. The ensemble-averaged signals are more complex. At location 1, twelve oscillations (three per blade passage) are visible. The hollows adjacent to the highest peaks are produced by the wakes and highlight the losses they produce. They are nevertheless far less visible than in the velocity field. At location 2, the twelve oscillations still exist but seem much difficult to detect: indeed, the pressure signal appears shifted, and the four groups of oscillations seem to have merged together. In fact, the pressure field is dominated by the *RSI* behind the first rotor at tip, and their influence differs according to the azimuthal position. That's why the shapes of the two signals are so different. The origin of these *RSI*, occurring behind each rotor, will be discussed in chapter IV.5.2.
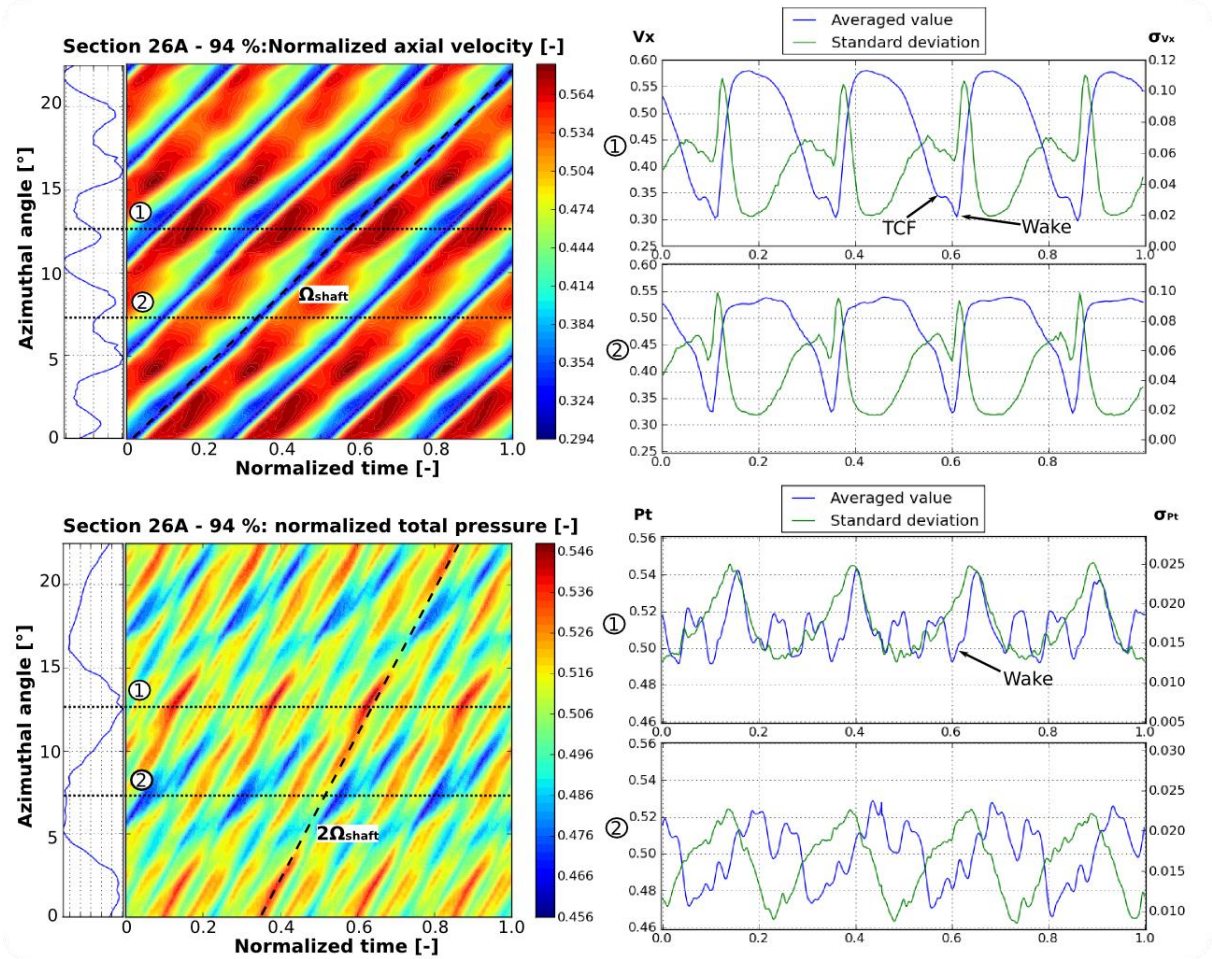
Figure 75 Space-time diagrams of axial velocity and total pressure in section 26A – *PE* point

Velocity and pressure maps in section 270 downstream of stator 1 – 52% of span-height:

This location has been chosen to illustrate the superimposition of the influence of the wakes when going towards the rear part of the machine. At mid-vein behind the first stator, the flow is mainly dominated by the six wakes of stator 1, producing six horizontal stripes of low-speed in the

space-time diagram. Moreover, bursts of low-speed are also visible in each passage. They are coming from the four wakes emitted by rotor 1 and are sliced by the stator blades (this phenomenon is illustrated in Figure 8). The effects of "wake-recovery" described in chapter I.2.1 are visible as the burst emitted by the rotors are stretched and distorted in stator 1, and accumulate on the pressure sides (in this figure this corresponds to the bottom-side of each wake): this is particularly visible in the passage extending from the azimuthal position 0° to 4°.
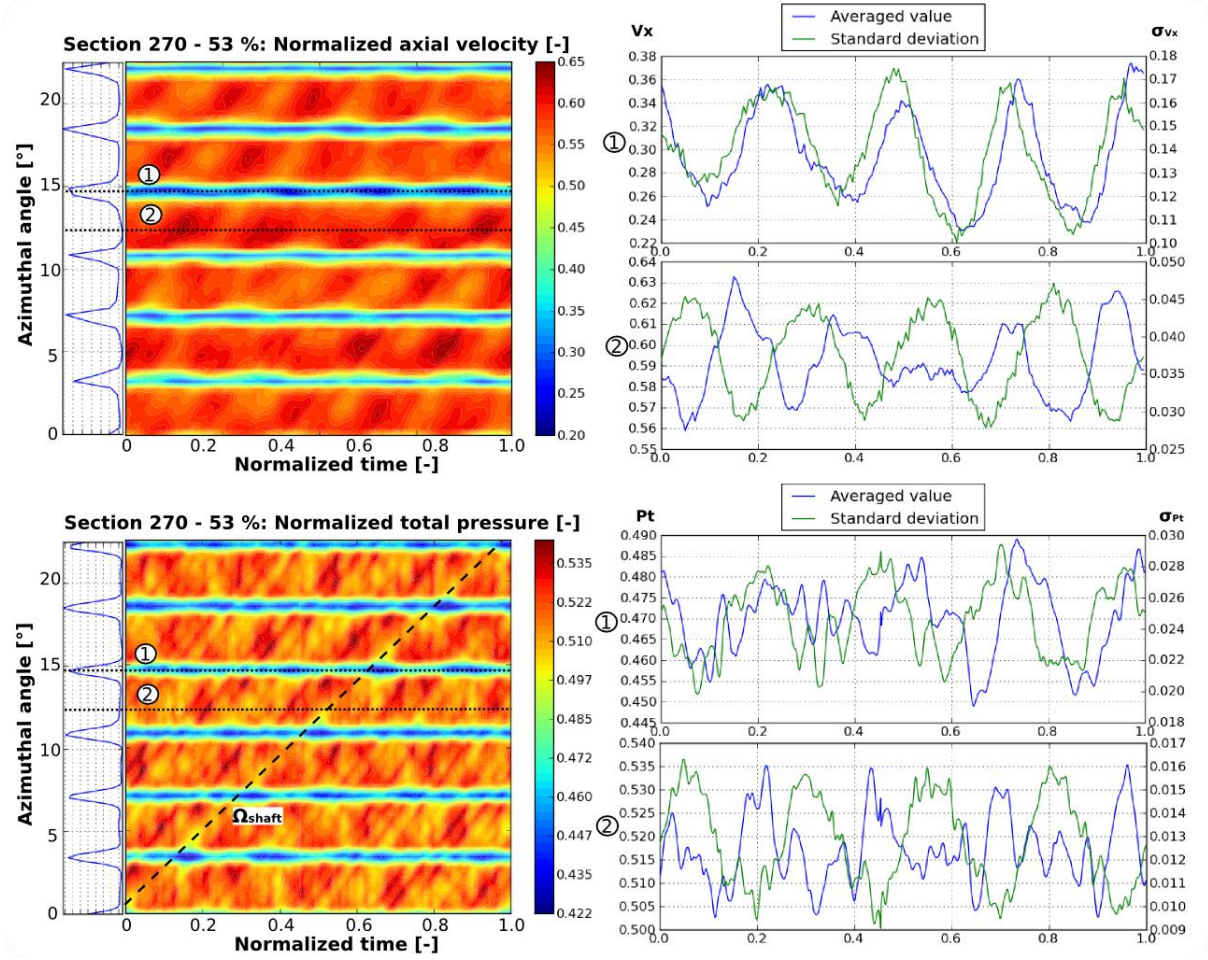
Figure 76 Space-time diagrams of axial velocity and total pressure in section 270 – *PE* point

At azimuthal position 1, located in a wake of stator 1, the four oscillations are produced by the sliced wakes of rotor 1. Here, the turbulence is very high, as shown by the very high values of standard-deviation and the flow is mainly influenced by the first rotor: the averaged and standard-deviation values are indeed almost in phase (the maximum of standard deviation is found in the zone of strong gradient). At location 2, in the clean flow, the standard deviation is much lower than in the wakes (beware of the scales that are different for the two signals). An interesting phenomenon occurs: although the bursts emitted by rotor 1 influence the standard deviation signal (see the four oscillations), the averaged signal appears sensitive to the potential effects emitted by the five blades of rotor 2. Indeed, as written previously, the effects of the wakes are much stronger in the machine than these produced by the potential effects: at location 2, in the clean flow, no direct wake perturbs the flow and the potential effects become detectable.

The total pressure diagram looks very similar to the velocity diagram. The six wakes emitted by stator 1 appear through the zones of low pressure produced by the losses they induce. The sliced wakes of rotor 1, producing bursts of low pressure, are even more visible than for velocity. The temporal repartition of these burst (see the dotted line) indicate the rotation of the rotor wakes, spinning at the rotor speed before their impact on the stator. Note that the bursts themselves do not spin downstream of stator 1. As for axial velocity, these bursts produce four oscillations in the temporal evolution of standard deviation at locations 1 and 2. The level of standard deviation appears much stronger as well at location 1 in a wake, than at location 2 in the free stream. However, the ensemble averaged signals are much more complex for pressure than for velocity, and the burst are more difficult to detect. This highlights the importance of the influences of the *RSI*.

Velocity and pressure maps in section 28A downstream of rotor 3 – 91% of span-height:

At tip behind the third rotor, the *RSI* and the tip leakage flows reach their highest value in the machine. In the map of velocity, the five wakes emitted by rotor 3 and spinning at the shaft speed fluctuate indeed a lot around their main trajectories, because of their interaction with the wakes of the previous rows and the *TCF*. In the space time diagram, seven spots are noticeable in the orange oblique stripe with the black dotted line. They indicate the direct influence of the seven passages of stator 2. It is interesting to notice that the time-averaged signal of velocity presents a less obvious signal: the mean influence of stator 2 with seven blades would have been expected. In fact, the six wakes of stator 1 and the potential effect generated by the eight blades of stator 3 modulate the seven periods of the velocity field in this section. The azimuths of locations 1 and 2 correspond to a minimum and a maximum of the time-averaged signal. At azimuthal position 1, the tip clearance flows and the wakes are visible on the blue and green signals. The wakes correspond to the sharp peaks of standard deviation and the *TCF* to the small humps: as for section 26A, the *TCF* reduce the axial velocity and thus enlarge the zones of low-speed. In the ensemble averaged signals, they appear however much stronger than downstream of the first rotor. At azimuthal position 2, the *TCF* are shifted and merge with the wakes.

Because of the *RSI*, the space-time diagram of pressure appears even more complex than in section 26A: the influence of rotor 3 is marked by the five blue spots visible for each azimuthal angle. The shape of the time-averaged signal of pressure differs from the signal of velocity. Indeed, the seven oscillations produced by stator 2 are here perfectly visible (no influence of stator 3 downstream is visible, but a modulation of the signal is created by the effects of the six wakes of stator 1.) The wakes of stator 2 appear to interact with those of rotor 3, and produce the stripes of blue spots in the map (seven spots are visible along one stripe) spinning at 3.3 times the shaft rotation speed. For the two azimuthal positions 1 and 2, the five oscillations produced by the rotor 2 are visible in the ensemble averaged and standard-deviation signals (note that the level of standard deviation is three-times higher than in section 26A). As for section 26A, the shapes of the averaged signals are very different for the two locations because of the *RSI*. Note that at location 2, three oscillations per row are visible, as for rotor 1 (see for example between 0.8 and 1). Finally, low pressure peaks are observable at the same time and angular position as these of the wakes and *TCF* visible in the velocity measurements: this highlights the important losses generated here by this interaction between wakes and *TCF*.

Overall, two mechanisms seem responsible for the increase in the losses at the outlet of the machine: first the influences of the wakes superimpose when going through the machine and produce strong *RSI*, especially at tip. Then, tip clearance flows strongly affect the flow at tip behind the rotors: the losses are produced by the interactions between the incoming wakes and the *TCF*.
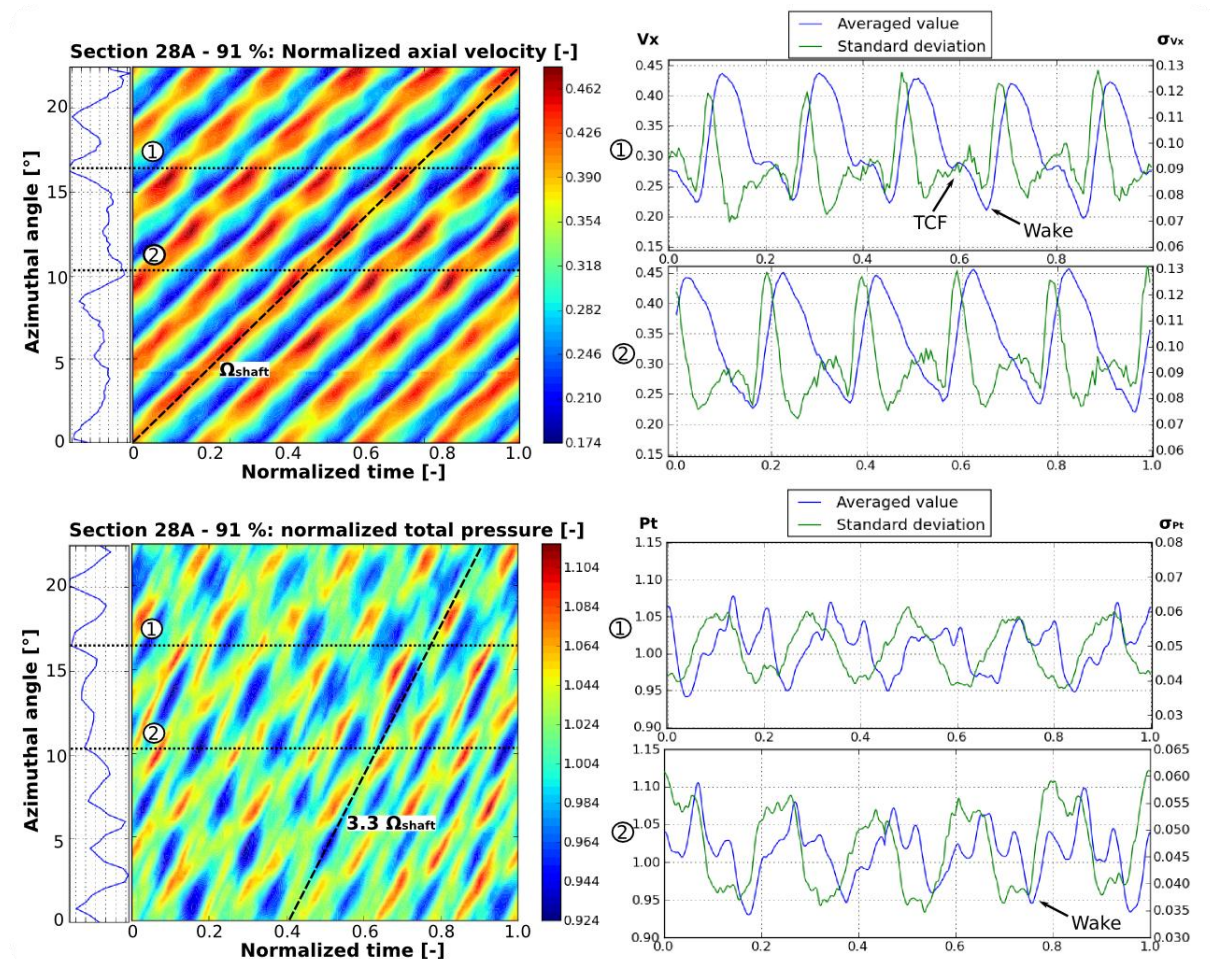
Figure 77 Space-time diagrams of axial velocity and total pressure in section 28A – *PE* point

IV.3.2 Flow field above the rotors at peak efficiency

In this chapter, a brief description of the flow at the tip of the rotors will be given. It will rely on high frequency measurements of wall static pressure and laser velocimetry performed at the tip of the rotors.

IV.3.2.1 Description of the wall static pressure field

Figure 78 shows the non-dimensionalized unsteady wall static pressure field above the three rotors at *PE*, at the same arbitrary time step. The iso-contour maps are plotted over the spatial period of the compressor Θ_{16} and along the machine axis (the flow goes from left to right, and the blades from bottom to top). Each map is delimited axially by the upstream and downstream inter-row sections, for example sections 270 and 27A for rotor 2.
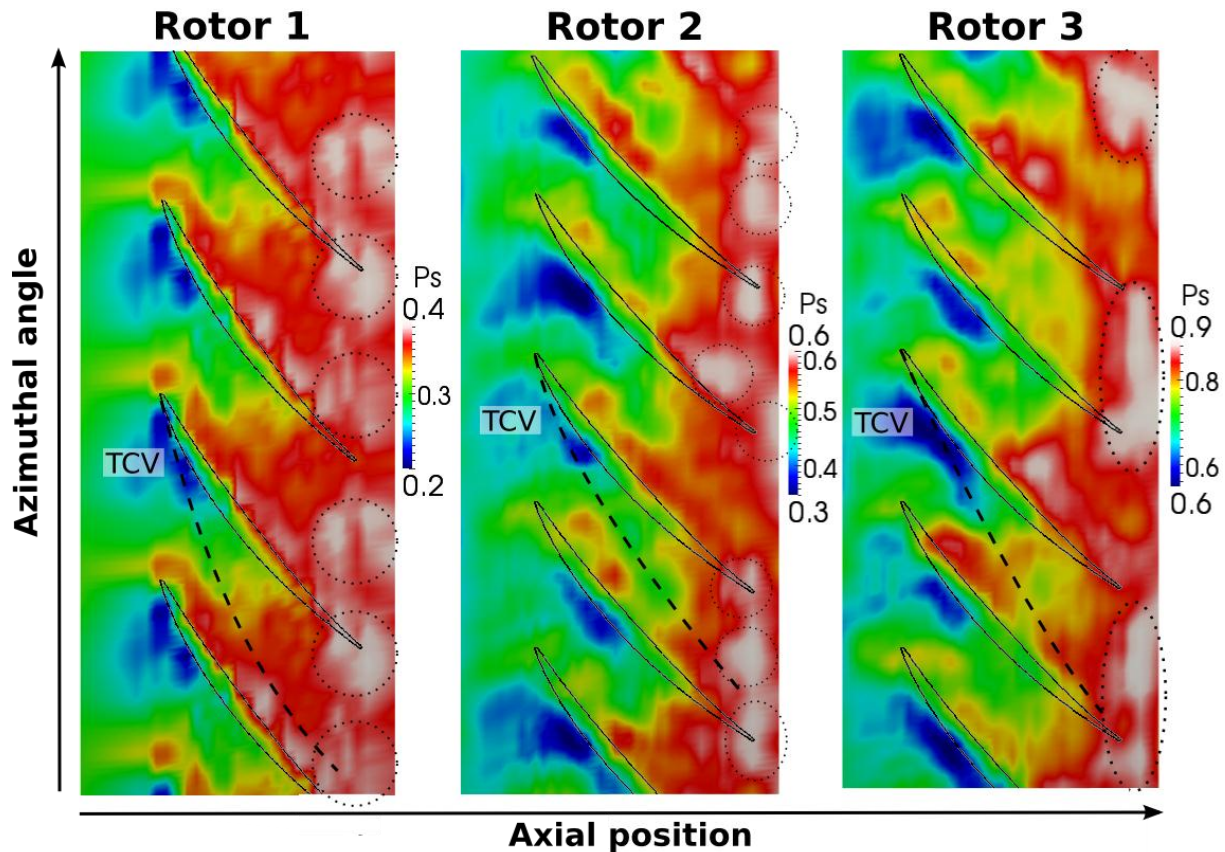
Figure 78 Wall static pressure field above the rotors at peak efficiency for an arbitrary time step

In the three maps, the pressure gradients generated by the blades appear very clearly at the leading edges. The *TCF* are visible through low pressure zones and are bounded by the trajectory of the main tip clearance vortices visible in each row, indicated with dotted lines in the figure. At peak efficiency, the *TCV* lies in the passages and goes out of the blade channel close to the pressure side at the trailing edge of the adjacent blade.

In each row, complex high-pressure structures develop at mid-chord on the pressure sides and merge together at the trailing edges of the blades. These structures are highly time dependent, and are produced by the rotor-stator interactions: their number are not directly proportional to the blade numbers of the rotors. Indeed, six structures can be seen at the trailing edges of rotor 1, eight (regrouped in two groups) in rotor 2 and three structures behind the last rotor (see the dotted circles in the figure). The different spatial locations of the structures explain the time dependence of the *RSI*: in rotor 2 for example, the eight structures migrate to the trailing edges of the blades but are never exactly at the same position at the same time, which generates strong fluctuations of intensity for the azimuthal harmonic 8. Space-time diagrams of pressure (not visible here) similar to those presented in Figure 77 would show similar results, that is to say that the pressure field is significantly affected by the rotor-stator interactions at tip of the rotors.

Therefore, as for the flow in the inter-row sections, the flow seems very sensitive to the *RSI* at the tip of the rotors. In chapter IV.3.1.2, it has been seen that the interaction between the wakes and *TCF* is important above the rotors: the next section will focus on the tip clearance flows.

IV.3.2.2 Study of the tip clearance flows

Flow at the tip of rotor 1 at peak efficiency

In order to describe the tip clearance flows, laser velocimetry has been performed from 75 % to 95 % of span height in rotor 1 at four axial positions at *PE* operating point. The azimuthal period reduced to two blade passages (see chapter III.3.5) has therefore been investigated. Hence, Figure 79 shows the superposition of the fields of static pressure and relative velocity (vector plot) at the tip of rotor 1 (95% of span height) at an arbitrary time. Black contours of static pressure have been superimposed in order to highlight the main pressure structures. The axial positions of the laser measurements are numbered from 1 to 4 and the two blades are labeled b_1 and b_2 respectively. The trajectories of the main tip clearance vortex (*TCV*) and of a tip separation vortex (*TSV*) are indicated with the dotted line.
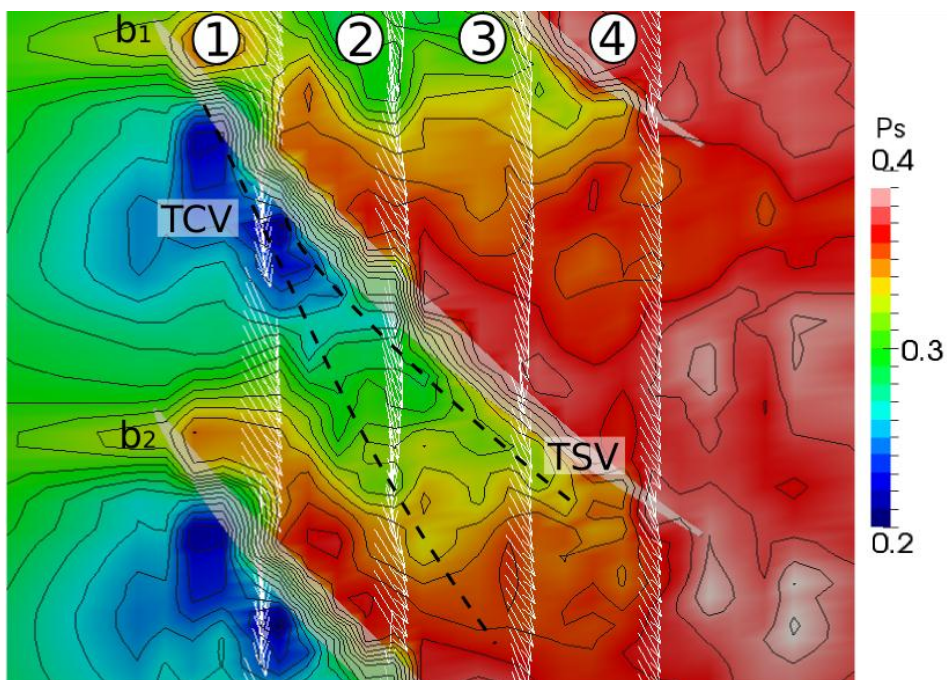
Figure 79 Wall static pressure field (iso-contour values) and relative velocity (vectors) at the tip of rotor 1 at an arbitrary time – *PE* operating point

The tip leakage flows are very visible at the tip of rotor 1 through the modulation of the pressure field they induce. At axial positions 1 and 2, the axial velocity is very weak near the suction side. As it remains always positive, no reversed flow is observed in rotor 1. The *TCF* only affects the half of the passage close to the pressure side of blade b_1 until roughly mid-chord. The trajectory of the main tip clearance vortex is also very well caught by the measurements. It is bounded by the boundaries between the free stream and the zones of low axial velocity: as previously written, the *TCV* lies in the middle of the passage. Along the pressure side of b_1, pressure oscillations are visible from mid-chord to the trailing edge. They are produced by a tip separation vortex, see chapter I.2.3. Note that another *TSV* could be the source of the pressure oscillations visible between the two trajectories (dotted lines). These three vortices could be the sources of the three humps visible per passage in the total pressure measurement at casing in section 26A, see Figure 77. This enforces the hypothesis of a strong interaction downstream of the rotor involving the *TCF*.

In order to describe the radial trajectory of the *TCF* in rotor 1, Figure 80 shows the axial velocity field (looking upstream) for the four axial positions in the upper part of the vein at an arbitrary time. Note that the flow has been investigated deeper in the vein at the trailing edge to capture the *TCF* which dives in the vein downstream of the rotor. The blades are indicated with grey squares labeled '*B*'. Three iso-contours of axial velocity have been superimposed to highlight the different structures of the flow. Note that the size of the blades is just indicative as it has been slightly modified in a matter of confidentiality.
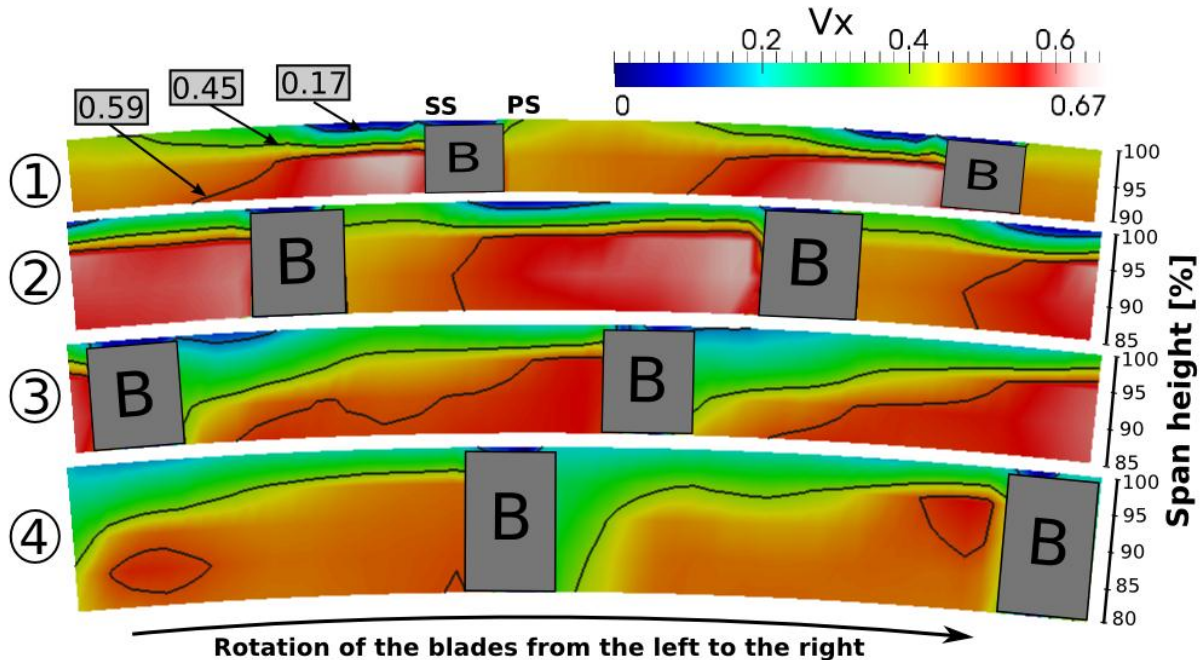
Figure 80 Axial velocity field (LDA) at the tip of rotor 1 at an arbitrary time – *PE* operating point

As previously seen, the *TCF* is characterized by low axial velocity. At axial position 1, just downstream of the leading edge, it is still very reduced: the iso-contour 0.17 shows the tip clearance vortex, at the suction side (*SS*) of the blades (left side of the squares). As the flow is scraped by the blades against the casing, the *TCV* spreads in the passage near the suction side. The frontier between the free stream and the *TCF* is shown by the iso-contour 0.45. Below the *TCF*, near the suction side, a zone of high velocity is classically found. It is produced by the bowing of the blades which induces an acceleration of the fluid at the leading edge. When going downstream, at axial position 2, the vortex is shifted in the middle of the passage, and still bounds the *TCF*. The vortex reaches the next blade at axial position 3. A weak spillage over the blade occurs at tip but the *TCV* remains mainly trapped in the passage, as already shown in Figure 79. Near the trailing edge, at position 4, the vortex accumulates on the *PS* of the adjacent blade and extends radially over 20 % of span-height. The *TCF* extends azimuthally over the whole passage and radially until roughly 92% of span-height. In section 26A, downstream of the rotor, the *TCF* is visible until 80% of span height.

Flow at tip of rotor 3 at PE and SM operating points

It will be shown in Chapter V that at low mass flow, instabilities arise in CREATE in the third rotor. Therefore, the tip flows have been investigated with laser velocimetry at *PE* and *SM* operating points to see if significant changes could be found in the structure of the *TCF* when approaching the

surge line. Because of time constraints to do the measurements, the flow has not been investigated over the complete azimuthal periodicity, but only over a stator 1 pitch (the largest stator pitch in the machine) in order to capture any non-spinning structure emitted by a stator. Five axial positions labeled 1 to 5 have been investigated along the blades: from one position to another, the azimuthal range has been shifted following the mean deviation imposed by the rotor to the fluid in order to follow roughly the trajectories of the particles, see Figure 82.
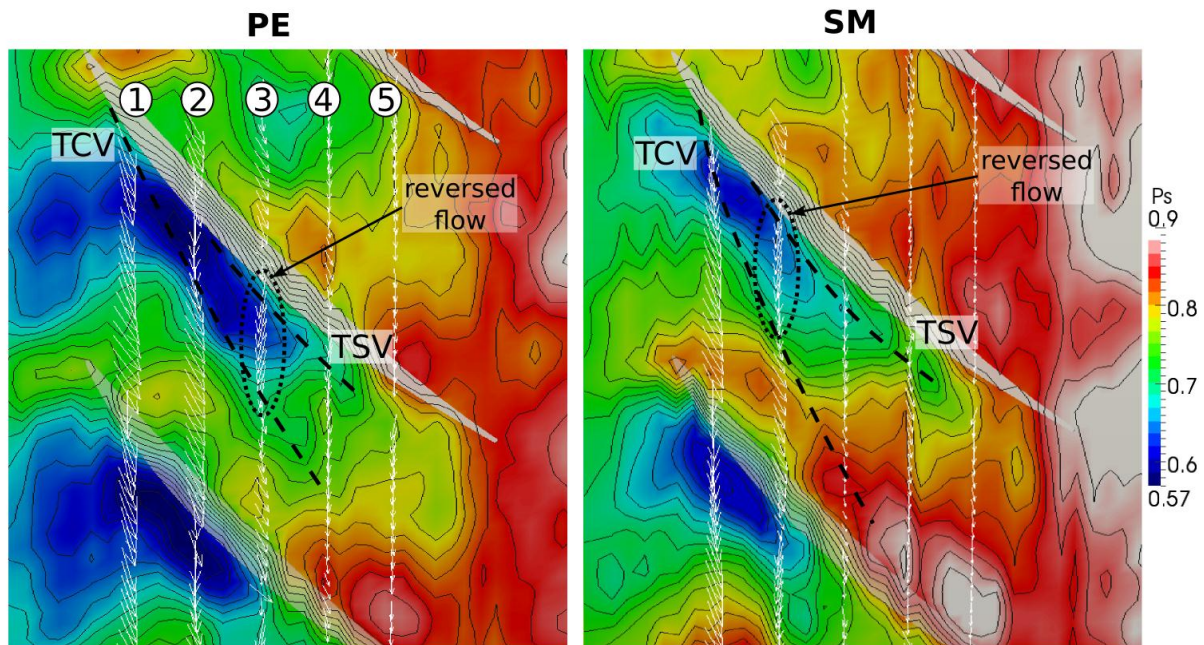
Figure 81 Comparison of the relative velocity field at *PE* and *SM* operating points at an arbitrary time - tip of rotor 3

As for rotor 1, the *TCF* is visible through the zones of low axial velocity and pressure it induces near the pressure sides of the blades. However it appears much stronger in rotor 3 and generates zones of reversed flow. Moreover, contrary to the first rotor, the passage is here completely blocked by the *TCF* at casing, see the very low values of axial velocity. Finally, note that adding to the main tip clearance vortex, a separation vortex producing a modulation of the pressure field is visible from roughly mid-chord of the blade for the two operating points.

When the mass flow is reduced from *PE* to *SM* operating points, the trajectory of the *TCV* changes and moves towards the pressure side of the adjacent blades. Indeed, the reduction of mass flow induces first a reduction of the axial velocity. Then, this reduction increases the incidence angle of the flow impinging the rotors, and thus the load applied to the blades. This reinforces the intensity of the tip clearance flow. Finally, at *SM*, the vortex keeps flowing in the passage and does not seem to align with the front line of the row: this result has to be kept in mind for the study of the instabilities which will be done in Chapter V. Note that the *SM* operating point is very close to the surge line but additional slight modifications of the *TCF* may occur just before surge. However, it seems reasonable to state that no major changes will appear for the trajectory of the *TCV*.

Figure 82 shows a comparison between *PE* and *SM* operating points of the R-θ map of the axial velocity fields at the five axial positions of rotor 3 defined in Figure 81. The scale of axial velocity is colored from blue to white for the positive values and black for the negative values.
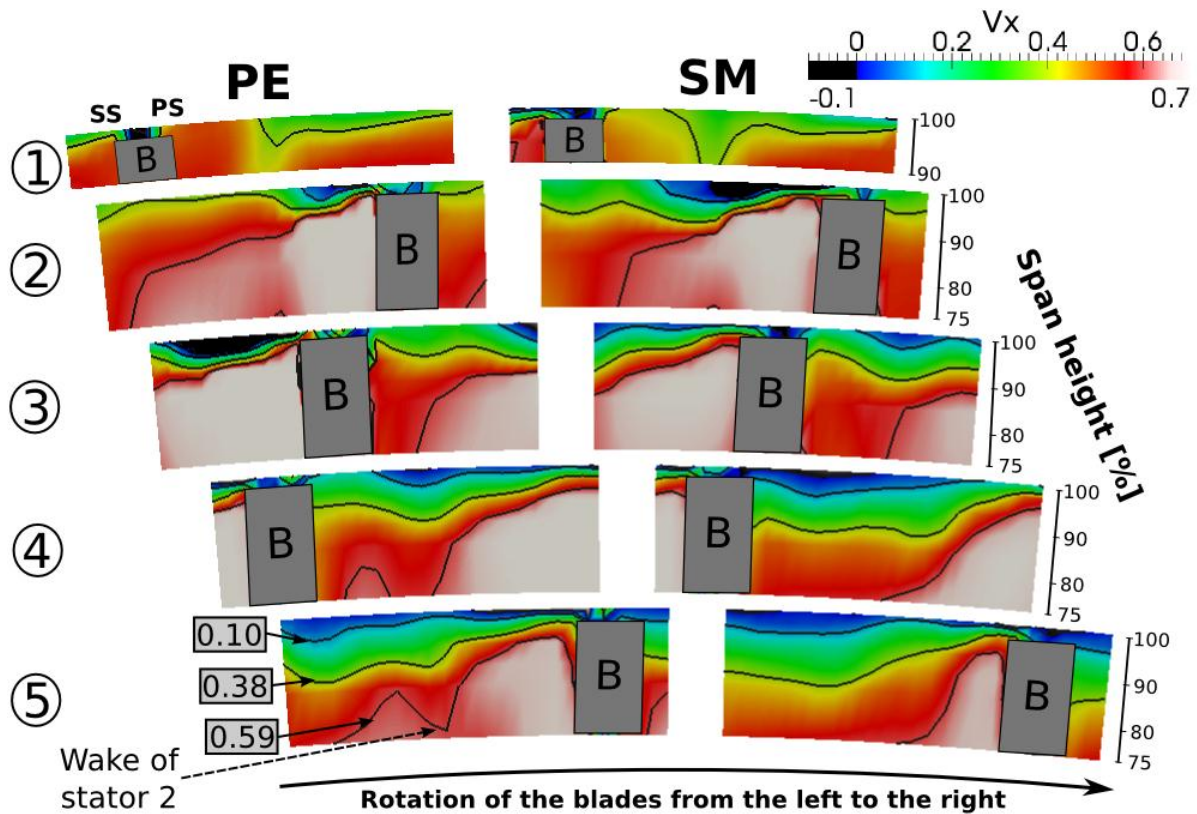
Figure 82 Comparison of the axial velocity fields at the tip of rotor 3 at an arbitrary time between *PE* and *SM* operating points

The description of the radial distribution of axial velocity in rotor 3 is quite similar to rotor 1, but the *TCF* is stronger. At axial position 1, a wake of stator 2 enters in a passage of rotor 3 and a thick boundary layer extending from 97 % of span-height to casing is visible: at *SM* operating point, the boundary layer and the wake are much stronger than at *PE*. At axial position 2, the *TCF* is confined near the *SS* at *PE* operating point. It is much more spread at *SM* and is visible through the zone of reversed flow it induces (in black). The boundary layer is also very thick at *SM* (nearly 10 % of span height) in comparison with *PE*. At position 3, the zone of reversed flow is visible at *PE*: as the *TCF* is shifted upstream from *PE* to *SM*, the reversed flow has already appeared at position 2 for *SM*. When going through the trailing edge of the blades, the *TCF* and the boundary layers keep extending spanwise even if no more reversed flow is observed: their radial extent is comparable between *PE* and *SM*, reaching nearly 20% of the vein. However, the zone of axial velocity below the *TCF* falls very low in the vein for *SM* (below than 75% of span height). This is consistent with the total pressure measurements in section 28A presented in chapter IV.3.1.1: even at *PE* operating point, a massive blockage is found behind rotor 3.

It is interesting to notice that the angular shift along the blade allowed to follow the velocity deficit produced by a wake of stator 2 (particularly visible at positions 3, 4 and 5 of *PE*) which is barely damped: this shows how the influences of the rows can propagate in the machine.

IV.3.3 Conclusion

From these descriptions of the flow in the inter-row sections and at the tip of the rotors, it appears that:

- The unsteadiness and complexity of the flow increases when going towards the rear part of the machine, as visible in the standard-deviation maps of total pressure and velocity. It is due to the different structures emitted by the rows which are convected downstream and interact together.

- The strongest interactions are those involving only wakes or wakes and tip clearance flows, especially in the second and third rotors, where the *TCF* are very strong. This is especially visible in the total pressure measurements at tip behind the third rotor, where the standard deviation reaches very high values over nearly a third of the span-height.

- The *RSI* strongly affect the flow in the rear part of the machine and at tip. They induce complex spatial and temporal structures. They are particularly strong at tip downstream of each rotor.

- The strength of the *TCF* in rotor 3 has been confirmed by the *LDA* measurements. They have been indeed found much stronger than in rotor 1, as they produce reverse flow and generate strong blockage even at *PE* operating point. When going towards the surge line, they increase in intensity but do not seem to align with the leading front of rotor 3.

In order to deeper analyze the flow in the machine and to understand the origin of the structures of the flow, a modal description of the pressure measurements in the inter-row sections and at tip will be performed in the next section.

IV.4 Modal description of the pressure field

In this chapter, a description of the pressure fields will be given using a modal approach: indeed, the total and static pressure appear to be very sensitive to the *RSI*. In the first part, the inter-row sections will be investigated through the total pressure measurements. Then, the flow above the rotors will be studied with the wall static pressure measurements, and compared to the results found in the inter-row sections.

IV.4.1 Modal description of the flow in the inter-row sections

IV.4.1.1 Time-averaged spectra of total pressure at *PE*

The space and time influence of the rows are summarized in Figure 83. This figure presents the time-average of the spatial spectra of total pressure, calculated with a discrete Fourier transform for each time steps in all the inter-row sections. This is thus the radial evolution of the mean spatial harmonics in each section. Only the sixteen first harmonics are presented in order to show the first two harmonics of each row. The spectra have been calculated over the circumferential period of the compressor Θ_{16}. The spectra plotted in the left and right parts of the figure are for the sections

downstream of the rotors and the stators respectively. Note that the harmonic 0, i.e. the mean value of the pressure has been removed.

The first spectrum in the top left of the figure is calculated downstream of rotor 1. The harmonics 4 is clearly the most significant, and represents the impact of the four wakes of rotor 1 on the flow-field. Close to the hub, the wakes are more visible and the circumferential gradients of the pressure increase (see Figure 74 - section 26A): this explains the increase in the amplitude of the harmonic 4 close to the hub. However, close to the casing, one can note a peak in the amplitude of the harmonics 4 (and in a weaker measure of harmonic 8 and 12) induced by the presence of the tip leakage flow (see the temporal evolution of pressure in section 26A presented in Figure 77). The harmonics 2 and 6 could either be the direct contributions of the *IGV* and stator 1, or be produced by an interaction (2=6-4 and 6=2+4, see chapter I.2.4). In the other sections, the five wakes proceeding from the rotors 2 and 3 obviously impact the spectra downstream of these rows, as well as the seven and eight blades of the stators 2 and 3 respectively reveal the harmonics (7, 14, . . .) in section 280 and (8, 16, . . .) in section 290.

The complexity of the flow in the last sections of the machine is captured by the *DFT*, as the amplitudes of harmonics not proportional to a blade number become very important in the spectra. This is the case for example for harmonics 2, 3 and 8 in section 27A or 2, 3 and 7 in section 28A. However, for each section, only two or three interaction harmonics are largely predominant: a special attention will be paid to these harmonics in the next chapter.
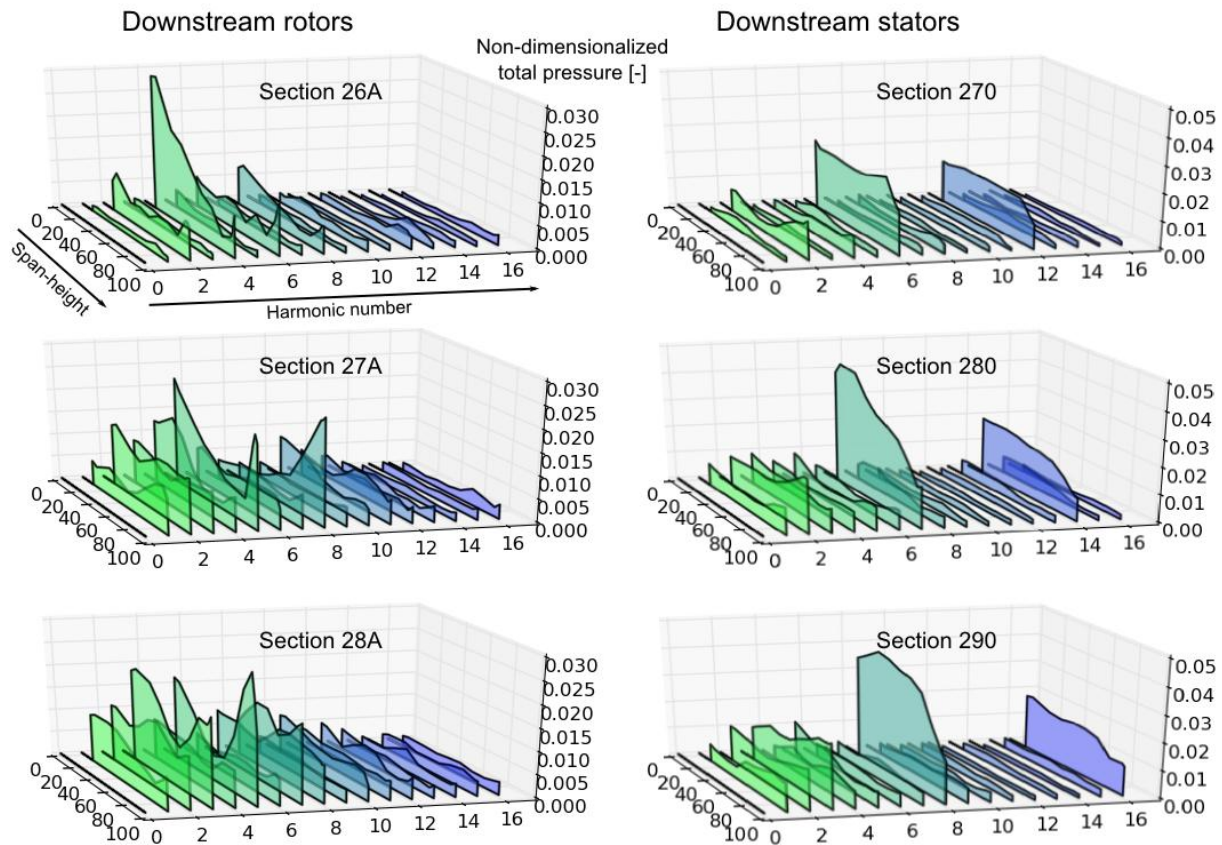
Figure 83 Spanwise evolution of the time-averaged spectra of total pressure in the inter-row sections at *PE*

IV.4.1.2 Spanwise evolution of the main harmonics of the flow at *PE* and *Loaded* operating points

Figure 84 shows the spanwise evolutions of the main harmonics of total pressure for each inter-row section, which have been calculated the same way as for Figure 83, for *PE* and *L* operating points. Specific colors have been chosen to plot the harmonics: the red and black curves are the direct contributions of the rotors and the stators respectively. The interaction harmonics are plotted in blue, green and cyan. It is worth to notice that the 'cyan' harmonics (i.e. 6, 8 and 7) are only present downstream of the rotors.

As previously mentioned, the harmonics of the rotors are very strong at hub, as for rotor 1 for example. For rotor 2 and 3, very high values are also observable at tip: indeed, the enhanced tip-gaps of these two rows produce five strong *TCF* (see chapter IV.3.1.2). When going through the rotor blades, the *TCF* dive in the passage, as shown in chapter IV.3.2.2: at section 27A and 28A, they reach their maximum amplitude at 90% of span-height. The harmonics of the stators have a hump-shape, with a maximum at the mid-bottom part of the vein (the shape for stator 1 is flatter than the others). Indeed, as previously seen in Figure 69, the stator wakes tend to thicken at hub. One can notice that the mean influences of the stators are stronger than the rotors, as the total pressure results are presented in the absolute frame.

At peak efficiency, downstream of the rotors, the interactions are very strong at tip. As it has been shown in chapter IV.3, the intensity of the interactions increases a lot at the rear part of the machine. They reach their climax in section 28A. Nevertheless, even if they appear relatively weak in section 26A in comparison with sections 27A and 28A, the *RSI* have a very strong influence on the flow behind the first rotor from tip to 80% of span-height (the amplitude of the harmonics 2 and 6 have comparable or higher amplitude than the harmonic 4). Behind the second rotor, the *RSI* dominate the flow until 50% of span height. In section 28A, beside the tip zone between 73 % and 95 %, the interactions are stronger than the direct contribution of the third rotor along the whole vein. Downstream of the stators, the amplitudes of the harmonics of the *RSI* are comparable to downstream of the rotors. The amplitudes of the stators harmonics being stronger than the rotors, the zone of predominance of the *RSI* is however smaller than behind the rotors: it extends at peak efficiency from casing to 85 % of span-height. It is noticeable that downstream of the stators, the amplitudes of the harmonics of the rotors are very low as they combine with those of the stators to form interaction harmonics. This is particularly obvious in section 29O, where the amplitude of spatial mode 5 decreases a lot as well as the amplitudes of the spatial modes 2 and 3 increase a lot.

The loading has not much influence on the amplitudes of the direct harmonics of the rows: overall, they tend to increase a little. Note that the data has been interpolated at tip of rotor 2 and 3 because the experimental mesh was a bit too coarse. On the contrary, the amplitudes of the interaction harmonic 2 and 3 increase a lot in the last two stages. At *L* operating point, the flow is dominated by the interaction harmonic 2 in section 27A over a large zone at mid-span, and by the harmonic 3 over nearly the whole span of section 28A. As a general trend, the amplitude of the interactions tends to increase with the load. An exception can be mentioned for the 'cyan' harmonic (6, 8 and 7): this will be explained later in section IV.5.3.
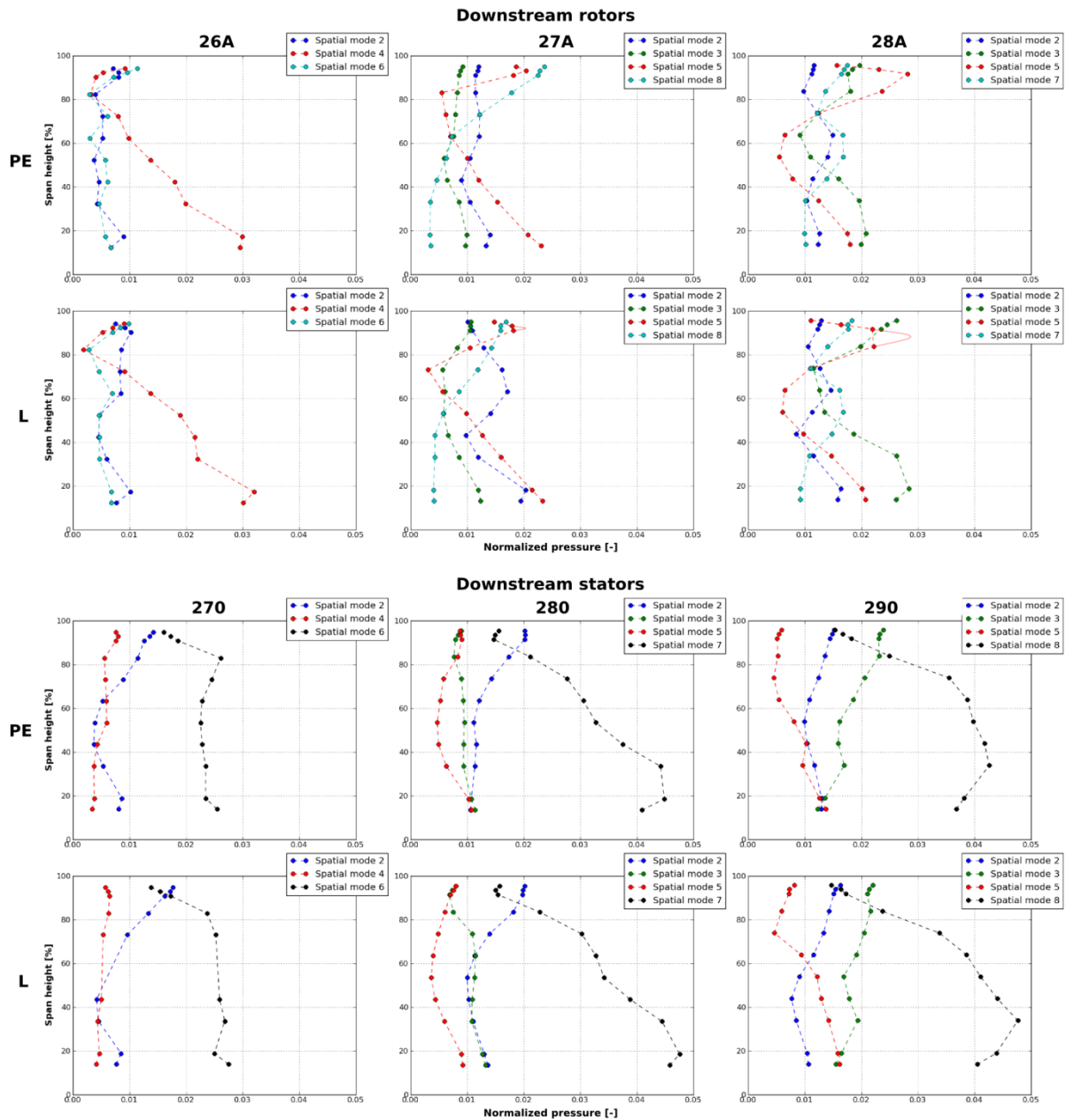
Figure 84 Spanwise evolution of the main harmonics of total pressure at *PE* and Loaded operating points

IV.4.2 Modal description of the flow above the rotors

The previous chapter showed that three main interaction harmonics were responsible for the complexity of the flow in the inter row sections. This chapter focuses on the modal description of the wall static pressure field, in order to see if the same tendencies appear above the rotors. Figure 85 shows time-averaged static pressure spectra calculated for each axial position in each rotor. The data processing is the same as for Figure 83. Therefore, this figure presents the axial evolution of the mean spatial harmonics for each rotor (only the first 10 harmonics are presented). The spectra have been calculated over the circumferential period of the compressor Θ_{16}. The axial positions have been non-dimensionalized, 0 and 1 corresponding to the axial limits of each map of Figure 78 (i.e. the

positions of the inter-row sections). As for total pressure, the harmonic 0 of the spectra has been removed.

On the three maps of Figure 85, the direct influences of the rotors are clearly visible for each rotor, see the harmonics 4 and 8 for rotor 1, and 5 and 10 for the two last rotors. Moreover, the shape of the amplitude of the main harmonic of each row can be seen as the distribution of the mean load applied to the blades. Therefore, the load appears to be very localized, the maximum being encountered at 25 % of axial chord for each row at peak efficiency.

The main interaction harmonics (i.e. not proportional to the blades numbers of the rotors) are the same as for the inter-row sections: harmonics 2 and 6 dominate in the first rotor, 2 and 8 in rotor 2 (the amplitude of harmonic 3 is a bit weaker) and harmonics 2, 3 and 7 in the last rotor. The amplitude of the harmonics 2 and 3 are almost equally distributed along the machine axis. The origin of the three structures visible at the rear part of rotor 3 in Figure 78 is associated with the increase in the harmonic 3 at the trailing edge. It is worth to notice that the axial distribution of the amplitudes of the harmonics 6, 8 and 7 (denominated *'cyan'* harmonics in chapter IV.4.1.2) have the same shape for each rotor: very low along the axis, their amplitudes increase a lot at the rear part of the rotors. They are hence responsible for the structures of the rotors 1 and 2 highlighted in Figure 78. Overall, the interaction harmonics dominate the flow at the rear part of the blades, and the main harmonics at the leading part of the blades.

Non dimensionalized static pressure [-]
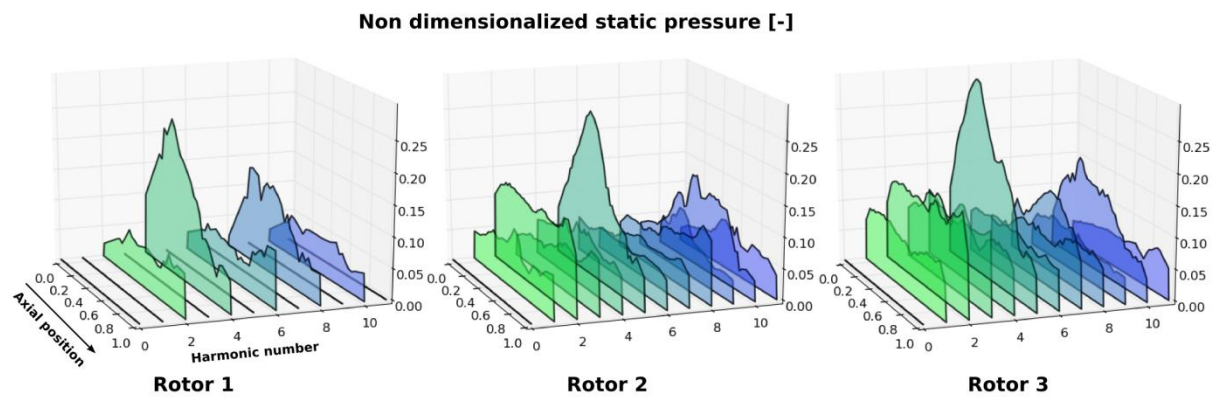
Figure 85 Time averaged spectra of static pressure along the machine axis at peak efficiency

Overall, the main interaction harmonics detected at the tip of the rotors are the same as these found in the inter-row sections, i.e.:

- Rotor 1: harmonics 2 and 6
- Rotor 2: harmonics 2, (3) and 8
- Rotor 3: harmonics 2, 3 and 7

IV.4.3 Conclusion

The combination of two previous modal overviews of the pressure fields showed us that:

- The amplitude of the interactions increases a lot at the outlet of the machine: they completely dominate the flow in section 28A, downstream of the third rotor. Moreover, at tip, as the direct influences of the rotors are very localized at the leading edge of the blades, the interactions dominate the flow at the trailing edges.

- Three main interactions named *'blue'*, *'green'* and 'cyan' mainly affect the flow in the inter-row sections and above the rotors.

- They tend to strengthen with the load, except for the 'cyan' harmonics (6, 8 and 7), which are only present above and downstream of the rotors. Note that the *'cyan'* harmonics have also the same axial distribution of amplitude. They must be produced by a similar mechanism.

In order to identify and understand the mechanism responsible for these three interactions, a modal analysis method will be presented in the next section. It will then be applied to the pressure results.

IV.5 Modal analysis of the pressure field

In this chapter, a modal analysis method of the flow will be presented and then applied to the experimental results in order to understand the origins of the interactions. The previous chapter showed that the same interaction harmonics were present above the rows and in the inter-row sections: the following modal analysis will focus on the wall static pressure measurements done above the rotors. The analysis of the *RSI* will then be extended to the radial distributions of the interactions in the inter-row sections calculated from the total pressure results.

IV.5.1 Modal analysis method

IV.5.1.1 The rotor-stator interactions

As written in chapter I.2.4, the rotor-stator interactions are produced by the interactions between all the flow structures proceeding from the rows, as wakes and potential effects, but also tip leakage flows, corner stalls etc… In order to understand what the *RSI* field is and how to quantify its energy, Figure 86 presents a decomposition of the wall static pressure field in the inter-row region between rotor 1 and stator 1 of the compressor CREATE at *PE* operating point. The abscissas show the axial position between the two rows labeled R_1 and S_1 and the ordinates the azimuthal angle over the circumferential periodicity θ_{16}. The pressure has been normalized by its maximum value. It has been extracted from a URANS CFD calculation at a fixed arbitrary time. The first signal, labeled *Ps(x,θ,t)* in the left of the figure, corresponds to the static pressure field. Adamczyk [1] proposed in 1984 a decomposition of any aerodynamic quantity which can be applied to the pressure field Ps(x, θ, t) as follows:

- *$Ps_{axi}(x)$*, a constant axisymmetric value.

- *$Ps'_{rel}(x,\theta)$*, which is a steady field in the rotor frame, but which becomes unsteady in the stator frame. The influence of the four blades of the first rotor is clearly visible through the four pressure gradients produced by the wakes.

- *$Ps'_{abs}(x,\theta)$*, which is a steady field in the stator frame. The six zones of low pressure visible on the right side of the pressure field are induced here by the potential effects of the six blades of stator 1. It is worth to notice the short range of influence of the potential effects in CREATE.

- *$Ps^*(x,\theta,t)$*, which is the remaining field, once the three others have been subtracted. This is the *RSI* field, which is purely unsteady and does not depend on the frame in which it is expressed.

The goal of the modal analysis method presented hereafter is first to be able to separate each term of the Adamczyk decomposition, in order to study the *RSI* occurring in the machine, and then to decompose the global *RSI* term into a sum of simple understandable interactions.
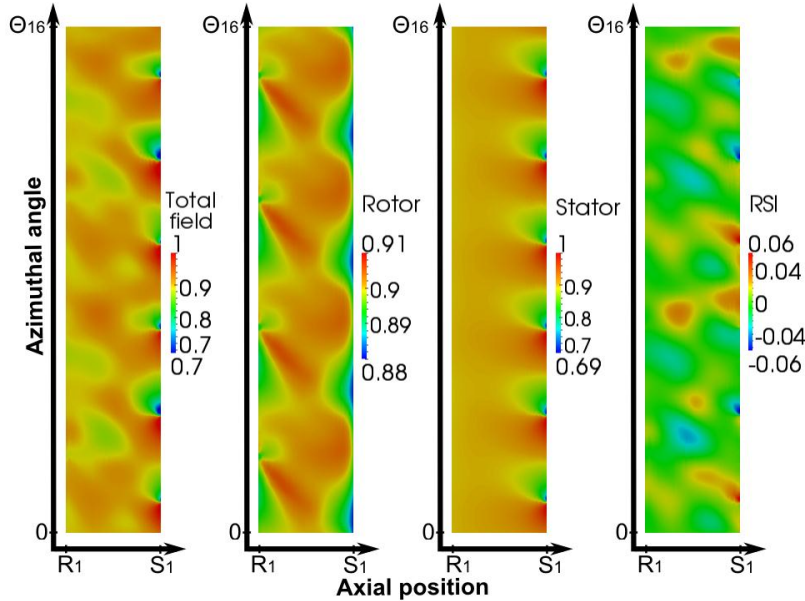
Figure 86 Wall static pressure field decomposition downstream of the first rotor of the compressor CREATE – URANS simulation

When measurements or numerical simulations are achieved for a stable operating point over the machine periodicity, the flow field can be easily reconstructed over 2π. Any aerodynamic quantity $f(x,r,\theta,t)$ can therefore be expanded into Fourier series, double in space over 2π and in time over a machine period $2\pi/\Omega$, as originally proposed by Tyler and Sofrin [81] for an acoustic study, and illustrated by relation (IV-1).

$$f(x,r,\theta,t) = \sum_{n=-\infty}^{\infty} \sum_{m_\theta=0}^{\infty} A_{m_\theta}(x,r) \cdot \cos\left(m_\theta \cdot \theta - nN_R\Omega \cdot t + \phi_{m_\theta,n}(x,r)\right)$$

(IV-1)

Tyler and Sofrin describe indeed the flow field as a superposition of an infinite number of circumferential spinning lobed structures, whose number of lobes m_θ is a linear combination of the number of blades of the rotor and stator, respectively N_R and N_S (see relation (IV-2)). Note that in the case of a multistage compressor, N_R and N_S can correspond to any rotor and stator number of blades.

The circumferential position of the modes being related to time with a propagation equation, a rotation speed $\omega_{m_\theta,n}$ can be defined for each spatial spinning mode m_θ, as in relation (IV-3):

$$m_\theta = n \cdot N_R + k \cdot N_S \qquad (n,k) \in (\mathbb{Z}, \mathbb{Z}) \qquad \text{(IV-2)}$$

$$\omega_{m_\theta,n} = \frac{n \cdot N_R}{m_\theta} \cdot \Omega \qquad \text{(IV-3)}$$

The decomposition of Figure 86 can again be achieved by identifying each term regarding to the rotation speed of the spatial modes:

- Ps_{axi} corresponds to the spatial mode m_θ =0.

- $Ps'_{rel}(x,\theta)$ corresponds to the sum of the spatial modes rotating at the compressor rotation speed ($\omega_{m_\theta,n} = \Omega$).

- $Ps'_{abs}(x,\theta)$ corresponds to the sum of the spatial modes which do not rotate in the absolute frame ($\omega_{m_\theta,n} = 0$).

- $Ps^*(x,\theta,t)$ corresponds to the sum of all the other modes.

Hence, the spatial modes can be identified through the determination of the two integers n and k. However, several sets of (n,k) are possible to explain one spatial mode: the double sum in the relation (IV-1) indicates this multiplicity of possible combinations and implies that a given spatial mode m_θ may result from the superposition of several n-modes with the same number of lobes, spinning at different rotation speeds $\omega_{m_\theta,n}$. Figure 87 is an illustration of the axial evolution of the amplitude of an arbitrary aerodynamic quantity between stator 1 and rotor 2. Here, a spatial mode m_θ=10 located downstream of stator 1 could either be produced by an interaction between rotor 1 and stator 1 (10=6+4) or by a direct contribution of rotor 2 (10=2x5), see Table 3. Thus, the understanding of a given spatial mode, i.e. the determination of the right (n,k) combination, is not obvious, and can become very complex in the case of a multistage compressor, where several N_R and N_S are involved. This had already been observed in 2004 by Arnaud et al. [2]
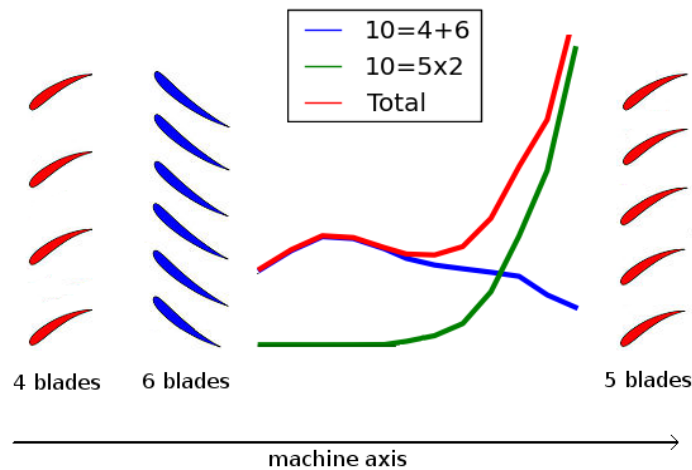
Figure 87 Illustration of the axial evolution of the amplitude of an arbitrary aerodynamic quantity downstream of the first stage of CREATE

IV.5.1.2 The double modal decomposition

A decomposition method is therefore required to discriminate the sets (*n,k*) responsible for the appearance of a given spatial mode, in order to identify the *RSI* arising in the flow. This method, sketched in Figure 88, consists in extracting the interaction modes of a discrete signal *f(θ,t)* defined on spatial (circumferential direction) and temporal periodicities, at a given axial position and span height in the machine.

Spatial DFT   **Temporal DFT**

Space-time diagram f(θ,t)	→	Azimuthal modes $\hat{f}(m_\theta,t)$	→	Temporal modes $\hat{F}(m_\theta,m_t)$
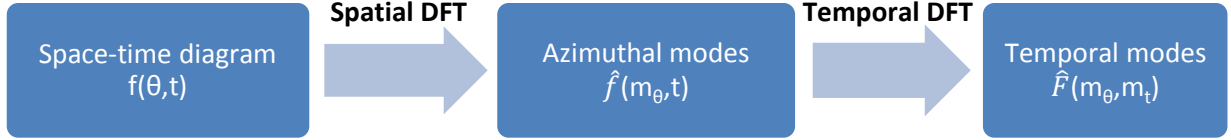
Figure 88 Scheme of principle of the double modal decomposition

First, a spatial Fourier transform of the signal is performed for each time step, to build the complex function $\hat{f}(m_\theta, t)$ which describes the temporal evolution of the spatial modes m_θ. Then a temporal Fourier transform of the spatial modes is performed and leads to the function $\hat{F}(m_\theta, m_t)$ that defines all the temporal modes which constitute the spatial modes. The azimuthal and temporal sampling of the signal will define the maximum number of detectable spatial and temporal modes, M_θ and M_t respectively. The spectrum of $\hat{f}(m_\theta, t)$, i.e. the absolute value of its Fourier Transform $\hat{F}(m_\theta, m_t)$, corresponds to all the temporal modes m_t of each spatial mode m_θ. By analogy with relations (IV-4) and (IV-5), one can define a rotation speed for each temporal mode as written below:

$$m_\theta = m_t + k \cdot N_S \tag{IV-4}$$

$$\omega_{m_\theta,m_t} = \frac{m_t}{m_\theta} \cdot \Omega \tag{IV-5}$$

The relation (IV-6) expresses the amplitude and the phase coefficients involved in the relation (IV-1), using modal matrices. The signal *f(θ,t)* is then characterized by a set of coefficients, which are no longer dependent of space and time. In the matrix *A* of the amplitudes, each column corresponds to the temporal spectrum of a spatial mode, i.e. all the *(n,k)* combinations associated to a spatial mode. The mode $A_{0,0}$ corresponds to the axisymmetric value of the signal.

$$A = \begin{bmatrix} 0 & A_{1,M_t} & \cdots & A_{M_\theta,M_t} \\ \vdots & \vdots & A_{i,j} & \vdots \\ 0 & A_{1,1} & \ddots & \vdots \\ A_{0,0} & A_{1,0} & \cdots & A_{M_\theta,0} \\ 0 & A_{1,-1} & \ddots & \vdots \\ \vdots & \vdots & & \vdots \\ 0 & A_{1,-M_t} & \cdots & A_{M_\theta,-M_t} \end{bmatrix} \quad \phi = \begin{bmatrix} 0 & \phi_{1,M_t} & \cdots & \phi_{M_\theta,M_t} \\ \vdots & \vdots & \phi_{i,j} & \vdots \\ 0 & \phi_{1,1} & \ddots & \vdots \\ \phi_{0,0} & \phi_{1,0} & \cdots & \phi_{M_\theta,0} \\ 0 & A_{1,-1} & \ddots & \vdots \\ \vdots & \vdots & & \vdots \\ 0 & \phi_{1,-M_t} & \cdots & \phi_{M_\theta,-M_t} \end{bmatrix} \tag{IV-6}$$

Note that the function $\hat{f}(m_\theta, t)$ being complex, the spectrum of its temporal *DFT* will not be pair, i.e. it will contain some negative and positive temporal modes m_t. This indicates the presence in the flow of two sets of modes: the first ones rotate in the same positive direction of the rotor shaft and the second ones rotate in the opposite direction. As a direct wave is characterized by a

propagation equation (IV-7), a mode spinning in the positive direction will induce a negative harmonic in the temporal spectrum. Therefore, the **negative part** of the temporal spectrum of the spatial modes represents the modes m_t that propagate **in the positive direction**.

$$A(\theta, t) = A_0 \cdot \cos(\theta - \omega t) \tag{IV-7}$$

Finally, this decomposition permits to perform the reconstruction of the pure interaction modes by a filtering process, see relations (IV-8) and (IV-9). Indeed, one can calculate the *RSI* modes by subtracting to the flow the modes with a zero rotation speed (corresponding to a direct contribution of the stators) and the modes rotating at the rotor speed (steady in the relative frame, corresponding to a direct contribution of the rotors). This is achieved in practice by setting to 0 the coefficients *(i=0)* and *(i=j)* in the modal matrix A.

$$\omega_{m_\theta, m_t} = 0 \rightarrow m_t = 0 \rightarrow j = 0 \tag{IV-8}$$

$$\omega_{m_\theta, m_t} = \Omega \rightarrow m_t = m_\theta \rightarrow i = j \tag{IV-9}$$

Hence, it is possible to calculate the energy of the *RSI* modes (in the signal processing meaning) at each location in the machine (i.e. at each fixed axial and radial positions). The application of relation (III-46) to the filtered modal matrix A leads to relation (IV-10) written hereafter. This will be used later in sections IV.5.3 and IV.6 to isolate particular *RSI* to study, and plot energetic meridian maps of the *RSI* in the whole machine.

$$E_{RSI} = \sum_{i \in m_\theta} \sum_{j \in m_t} \left| A_{i,j} \right|^2 \tag{IV-10}$$

IV.5.2 Modal description of the flow above the rotors

Chapter IV.4.2 showed that only a few harmonics were present in the spectra of each rotor. The axial evolution of the amplitude of these harmonics being continuous (see Figure 85), the modal analysis of the interactions will first be done at a fixed axial position, corresponding to the inter-row section downstream of each rotor (section 26A for the first rotor, for example). Then, the analysis will be extended to the whole rotors. In the following study, which focuses on the unsteadiness of the flow, the spatial harmonic 0 which corresponds to the axisymmetric part of the flow field will be removed from every spectrogram.

IV.5.2.1 Detailed analysis of the first rotor

Modal analysis in section 26A:

On the left of Figure 89, the space-time diagram of wall static pressure at section 26A is plotted. The measurements have been done at *PE* operating point. The diagram is plotted over the spatial and temporal periods θ_{16} and T_{16}. The flow appears to be complex even if the first stage of CREATE almost behaves like in a single compressor stage at this position. The influence of rotor 1 is visible with the four spots of high pressure over a temporal period for each azimuthal angle. As for

the total pressure results presented in chapter IV.3.1.2, twelve strong stripes appear in the diagram (see the dotted line).
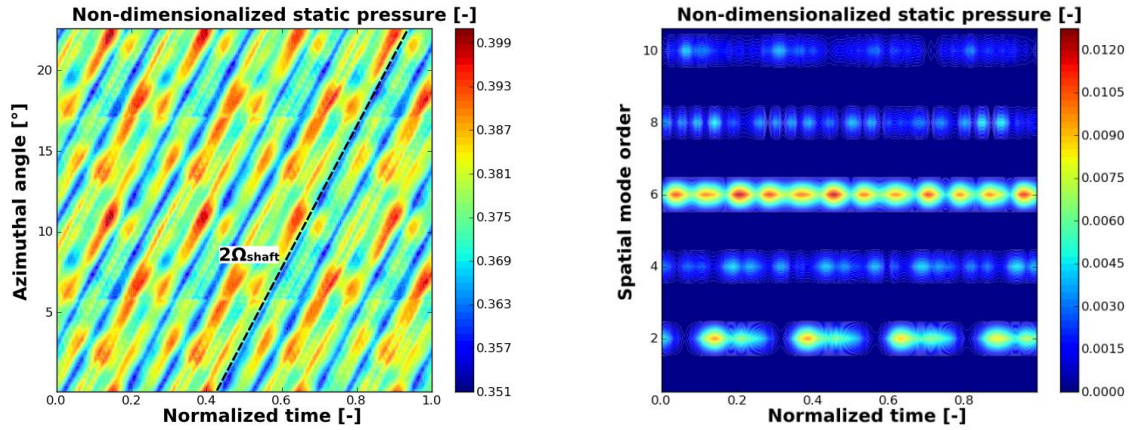
Figure 89 Space-time diagram and temporal evolution of the spatial modes of wall static pressure at peak efficiency – section 26A

In order to explain the temporal evolution of the flow, the azimuthal *DFT* of the space-time diagram is presented on the right side of Figure 89. It shows the temporal evolutions of the spatial modes of the wall static pressure. In those spectrograms, four spatial modes are predominant: $m_\theta = 2$, $m_\theta = 4$, $m_\theta = 6$ and $m_\theta = 8$. The spatial mode $m_\theta = 10$ is also present but weaker. It is worth to notice that only the harmonics multiple of two are visible in the spectrogram: indeed, at this location, the periodicity of the machine is $\frac{2\pi}{32}$, as previously written in chapter III.3.5.

The spatial modes $m_\theta = 4$ and $m_\theta = 8$ corresponds to the first and second harmonics induced by the four blades of rotor 1. At this location, the amplitude of the first harmonic $m_\theta = 4$ is hardly comparable to the second harmonic: as previously seen in chapter IV.4.2, the amplitudes of the main harmonics of the rotors have a very sharp shape, with a maximum at around 25 % of axial chord. Behind the blades, the amplitude of this mode is thus very reduced.

Because of their important pulsations with time, the spatial modes $m_\theta = 2$ and $m_\theta = 6$ are meanly induced by *RSI*. Their temporal spectra are plotted in Figure 90. The temporal spectrum of the spatial mode 6 shows two strong harmonics: $m_t = 12$ and $m_t = 0$ (remember that a negative harmonic corresponds to a positive temporal mode). It shows that this spatial mode is mainly induced by the temporal mode $m_t = 12$, and proceeds from the interaction between the third harmonic of rotor 1 and the first harmonic of stator 1: $(n,k) = (3,-1)$. This temporal mode induces the twelve strong spots in the spectrograms of Figure 89. It corresponds to a spinning structure rotating at twice the rotation speed Ω_{shaft} of the rotor, as calculated with relation (IV-11) and illustrated in Figure 89 with the black dashed line. At this location, this *RSI* obviously dominate the flow. The steady direct contribution of the stator characterized by the non-spinning temporal mode $m_t = 0$ ($\Omega_{6,0} = 0$) is here very weak compared to the *RSI* mode $m_t = 12$. Therefore, the spatial mode $m_\theta = 6$ will be designated as *"$3R_i$-S_i"*, as it is formed by the third harmonic of the rotor and the first harmonic of the stator of the current stage.

$$\Omega_{6,12} = \frac{m_t}{m_\theta} \cdot \Omega_{shaft} = \frac{12}{6} \cdot \Omega_{shaft} = 2\Omega_{shaft} \qquad \text{(IV-11)}$$

The temporal spectrum of the mode $m_\theta = 2$ shows that it appears to be a combination of three major *RSI* modes:

- $m_t = -4$, (2=-1×4 + 1×6), i.e. $(n,k) = (-1,1)$, which corresponds to an interaction between the first harmonics of rotor 1 and stator 1, traveling backwards with a rotation speed of $-2\Omega_{Shaft}$

- $m_t = 4$, (2=1×4 - 1×2), i.e. $(n,k) = (1,-1)$, which corresponds to an interaction between the first harmonics of rotor 1 and the *IGV*, traveling with a rotation speed of $2\Omega_{Shaft}$,

- $m_t = 8$, (2=2×4 - 1×6), i.e. $(n,k) = (2,-1)$, which corresponds to an interaction between the second harmonic of the rotor 1 and the first harmonic of the stator 1, traveling at the rotation speed of $4\Omega_{Shaft}$.
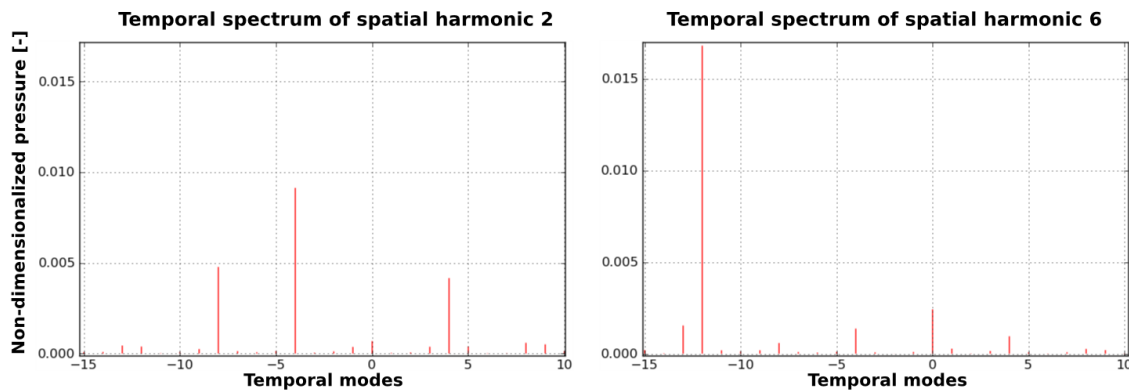
Figure 90 Temporal spectra of spatial harmonics 2 and 6 of wall static pressure – section 26A - *PE*

Axial evolution of the temporal spectra in the first rotor:

Figure 91 shows the axial evolution of the temporal spectra of the spatial modes 2 and 6, located respectively on the left and right hands of the figure. As defined before, the axial positions 0 and 1 correspond respectively to the sections 260 and 26A. Along rotor 1, the spatial harmonic m_θ = 2 is mostly produced by the interaction between rotor 1 and the *IGV* (m_t = 4). The amplitude of this temporal mode is hence almost constant along the axis, as the wakes of the *IGV* propagate through rotor 1. However, a local maximum can be found at the axial position 0.3, with coincides with the maximum of spatial harmonic m_θ = 4. The explanation of the slight increase in the amplitude at the rear part of the rotor is not obvious.

The evolution of the spectra of the spatial harmonic m_θ = 6 shows that at the rear part of rotor 1, the temporal mode m_t = 12 is largely predominant. Its amplitude strongly decreases when going towards the inlet: indeed, the *"3R_i-S_i"* interaction is produced by the potential effects of stator 1, which explains why its zone of influence is located at the rear part of rotor 1. This is consistent with the observations done in chapter IV.4.2. It is worth to notice that at the axial position [0.3-0.5], the spatial harmonic m_θ = 6 is no more produced by the *"3R_i-S_i"* interaction but by another interaction between the second mode of the rotor 1 and the *IGV* (6=2x4-2). Let us mention that in the first rotor, the temporal spectra are very simple, and few temporal harmonics interact to form spatial modes: the first stage behaves almost like a single stage compressor.

Non dimensionalized static pressure [-]
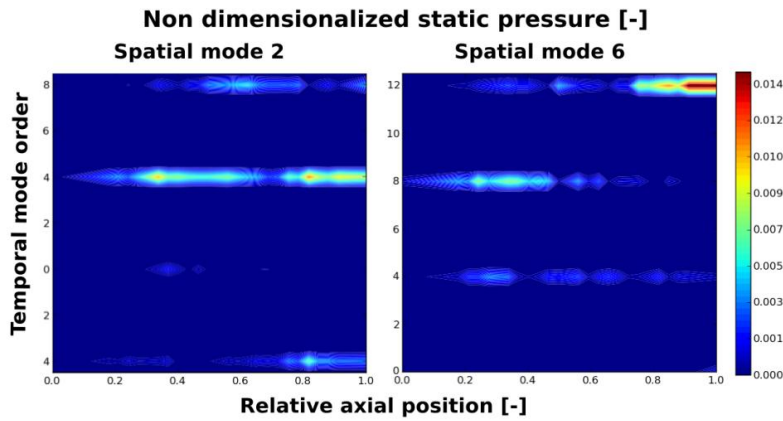
Figure 91 Axial evolutions of the temporal spectra of spatial harmonics 2 and 6 of wall static pressure – sections 260 to 26A – *PE*

IV.5.2.2 Analysis of the flow in the 2nd and 3rd rotor

In this chapter, the same analysis as for rotor 1 will be performed for rotors 2 and 3.

Modal analysis of rotor 2:
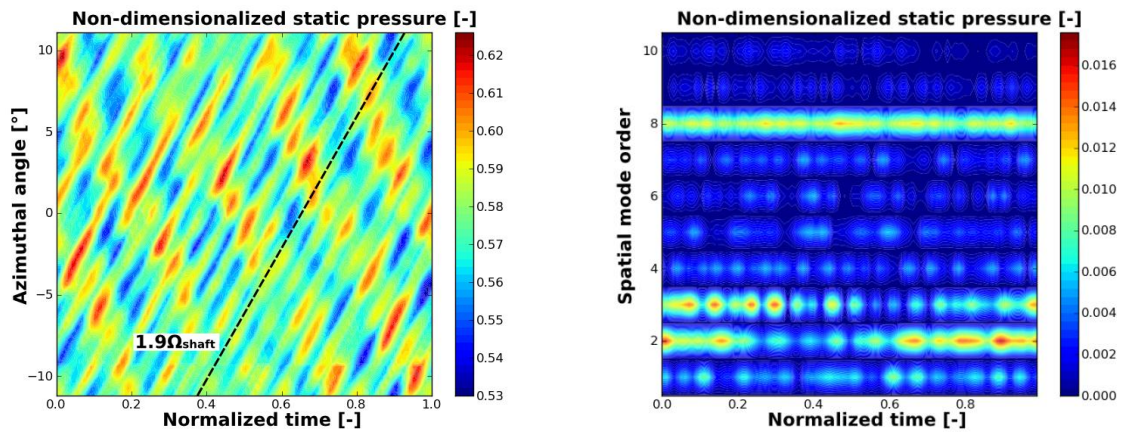
Figure 92 Space-time diagram and temporal evolution of the spatial modes of wall static pressure at peak efficiency – section 27A

Figure 92 shows the space time diagram and the temporal evolution of the spatial modes of wall static pressure at section 27A. The data has been post-treated the same way as for Figure 89. As for section 26A, strong stripes are visible in the pressure field. Nevertheless, the flow appears to be more perturbed than in the first rotor. The temporal evolution of the spatial modes shows that the flow is dominated by three spatial harmonics: $m_\theta = 2$, $m_\theta = 3$ and $m_\theta = 8$. They are the three main harmonics pointed out in chapter IV.4.1.2 and IV.4.2. It is worth to mention that no harmonic linked to rotor 2 is visible in this spectrogram.

As for section 26A, the axial evolution along rotor 2 of the temporal spectra of the three spatial harmonics has been plotted in Figure 93. The axial positions 0 and 1 correspond respectively to the sections 270 and 27A. The spatial mode two is predominant all along rotor 2, except at the rear part: there, its amplitude strongly decreases while the amplitudes of the spatial modes 3 and 8 increase.

They finally reach comparable values to mode 2 in section 27A, see Figure 92. Each spectrogram contains much more temporal modes than in rotor 1. On Table 21, the spatial harmonics 2, 3 and 8 are decomposed in all their temporal modes. The main temporal modes of each spatial mode are filled in red. One can see that all the rows can interact together to form the spatial harmonics: even at this position in the machine, where only the first two stages interact, the number of possible combinations is already very high. Indeed, the influence of the rows can spread very far from their position, as for the *IGV* whose contribution is visible all along rotor 2. Moreover, the influence of several rotors or stators can superimpose and interact with another row (see the temporal mode 9 of harmonic 3, for example): the clocking effects can play an important role in the formation of the *RSI* and further increase the complexity of the flow: this highlights the usefulness of the present modal decomposition method presented in chapter IV.5.1 to analyze the flow in a multistage compressor. Note that only one linear combination is possible to explain each temporal harmonic knowing the blade numbers of the rows of CREATE and privileging the lowest multiple of blade numbers which corresponds to the most energetic mode.
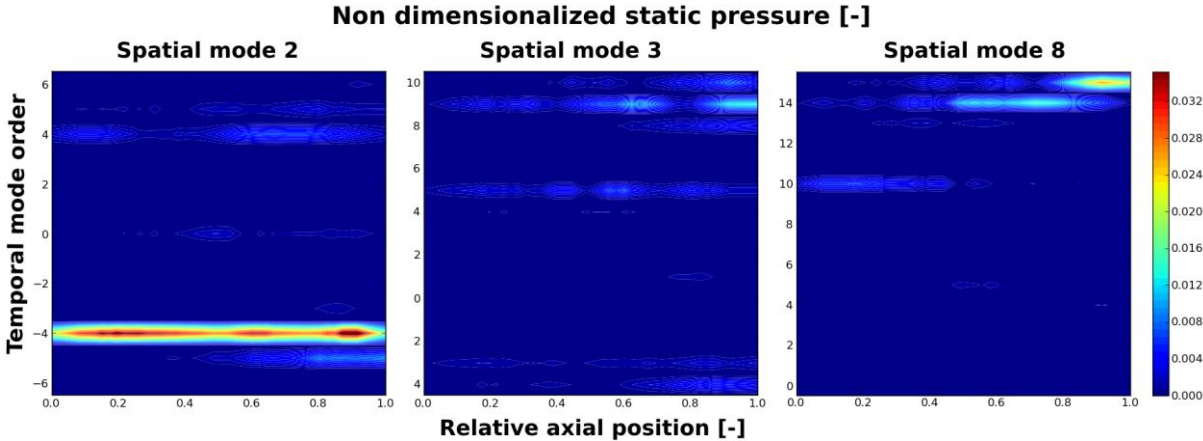
Figure 93 Axial evolutions of the temporal spectra of spatial harmonics 2, 3 and 8 of wall static pressure – sections 270 to 27A – *PE*

The main temporal mode of the harmonic $m_\theta = 2$ is $m_t = -4$. Hence, this spatial mode is mostly produced by an interaction between the first rotor and stator ($2 = -4 + 6$). Indeed, the incoming wakes of rotor 1 pass through stator 1 and interact just downstream with the wakes of the stator, in section 270 (axial position 0 of Figure 93). The interaction $m_\theta = 2$ is then convected through rotor 2, which explains the almost constant amplitude of the mode. This interaction generates a structure spinning backwards twice as fast as the rotor shaft. The type of this interaction will be named *"S_{i-1}-R_{i-1}"*, as it involves the first harmonics of the stator and rotor of the previous stage. Note that an interaction between the second rotor and stator ($m_t = -5$) is visible at the rear part of rotor 2, in the zone of influence of the potential effects of stator 2. One could have thought this interaction responsible for the spatial harmonic $m_\theta = 2$: this confirms that the wakes interactions are more significant relatively to the wakes / potential effects interactions.

Near section 27A, the main temporal mode of the harmonic $m_\theta = 3$ is $m_t = 9$. This suggests an interaction between the two first rotors and the stator 1: the wakes of rotor 1 and 2, spinning at the same speed, merge together and interact with those of stator 1. The type of this interaction will be called *"R_iR_{i-1}-S_{i-1}"*. Other temporal harmonics are visible along the rotor 2, but are negligible in

comparison with the spatial mode $m_\theta = 2$: the amplitude of the spatial mode $m_\theta = 3$ remains quite weak in comparison with $m_\theta = 2$ and $m_\theta = 8$.

Finally, near section 27A, the spatial mode $m_\theta = 8$ is produced by the temporal mode 15, i.e. the third harmonic of the second rotor. As for rotor 1, this is a *"3R_i-S_i"* interaction which dominates the flow in section 27A at peak efficiency. It produces a structure spinning at 1.88 times the rotation speed of the shaft. This structure is responsible for the stripes visible in the space-time diagram of Figure 92. Note that a temporal mode $m_t = 14$ produced by a complex interaction between rotor 1, 2 and stator 1 is visible at the middle-rear part of the rotor.

Spatial mode m_θ	Temporal mode m_t	Interacting rotor(s)	Interacting stators(s)	Linear combination $(m_\theta = m_t + k.N_S)$	Rotation speed ($\times \Omega_{Shaft}$)
	-5	Rotor 2	Stator 2	2 = -5 + 7	-2.5
	-4	Rotor 1	Stator 1	2 = -4 + 6	-2
2	0	-	IGV		0
	4	Rotor 1	IGV	2 = 4 - 2	2
	5	Rotor 2	Stator 1-2-*IGV*	2 = 5 - (7 − 6 + 2)	2.5
	-4	Rotor 1	Stator 2	3 = -4 + 7	-1.33
	-3	?	Stator 1	3 = -? + 6	-1
	5	Rotor 2	IGV	3 = 5 - 2	1.67
3	8	Rotor 1	Stator 2 - *IGV*	3 = 2x4 - (7 - 2)	2.67
	9	Rotor 1 – Rotor 2	Stator 1	3 = (4 + 5) - 6	3
	10	Rotor 2	Stator 2	3 = 2x5 − 7	3.33
	10	Rotor 2	IGV	8 = 2x5 - 2	1.25
8	14	Rotor 1 – Rotor 2	Stator 1	8 = (4 + 2x5) - 6	1.75
	15	Rotor 2	Stator 2	8 = 3x5 − 7	1.88

Table 21 Spatial and temporal modes of static pressure in rotor 2

Modal analysis of rotor 3:

Figure 94 shows the space time diagram and the temporal evolution of the spatial modes of wall static pressure at section 28A. The data has been post-treated the same way as for Figure 89. The flow is obviously more complex than in the two first rotors, and a clear tendency is more difficult to draw, even if stripes are visible from t = 0.4 to t = 1. Similar stripes have already been observed in the total pressure results presented in chapter IV.3.1.2. The temporal evolution of the spatial modes shows that the flow is mainly dominated by two spatial harmonics: $m_\theta = 2$ and $m_\theta = 3$. In section 28A, the amplitude of mode $m_\theta = 7$ which corresponds to the interaction *"3R_i-S_i"* (7 = 3x5 - 8) is stronger than most of the harmonics but remains quite weak relatively to $m_\theta = 2$ and $m_\theta = 3$. In the

spectrogram, an increase in the amplitude of the spatial mode $m_\theta = 3$ is also visible in the second part of the temporal period which lets us think that it is responsible for the stripes in the space-time diagram.
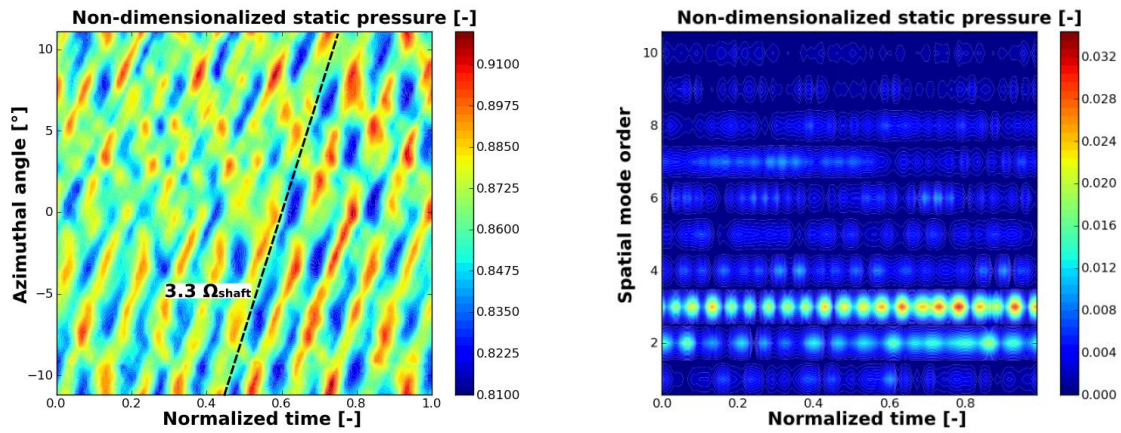

Figure 94 Space-time diagram and temporal evolution of the spatial modes of wall static pressure at peak efficiency – section 28A

As for the two previous rotors, the axial evolution along rotor 3 of the temporal spectra of the three spatial harmonics has been plotted in Figure 95. The axial positions 0 and 1 correspond respectively to the sections 280 and 28A.
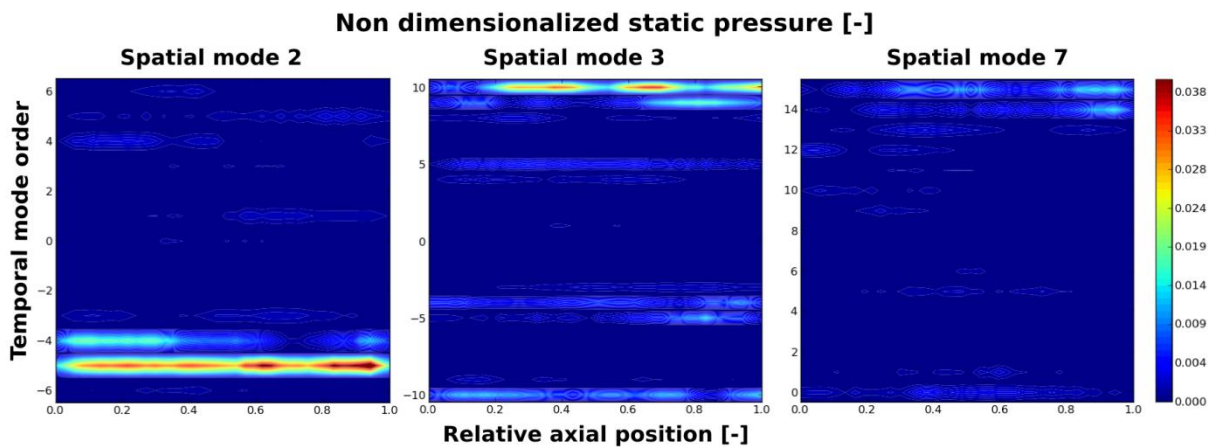

Figure 95 Axial evolutions of the temporal spectra of spatial harmonics 2, 3 and 7 of wall static pressure – sections 280 to 28A - *PE*

In Table 22, the spatial harmonics 2, 3 and 7 are decomposed in all their temporal modes. The determination of the right linear combinations is more complex in the third stage, as the second and third rotors have the same number of blades. It depends therefore on the shape of the harmonic. For example, the temporal mode $m_t = -5$ of spatial mode $m_\theta = 2$ is more likely to be produced by rotor 2 than rotor 3, as its amplitude is almost constant along the third rotor: if it was produced by rotor 3, a maximum would have been found around axial position 0.25 as shown in section IV.4.2. From the different interactions visible in Table 22, it is worth to mention that the influence of the *IGV* and rotor 1 still exist at the rear part of the third rotor! (see for example the temporal mode 5 of spatial harmonic 3).

Spatial mode m_θ	Temporal mode m_t	Interacting rotor(s)	Interacting stators(s)	Linear combination $(m_\theta=m_t+k.N_S)$	Rotation speed ($\times\Omega_{Shaft}$)
2	-5	Rotor 2	Stator 2	2 = -5 + 7	-2.5
	-4	Rotor 1	Stator 1	2 = -4 + 6	-2
	4	Rotor 1	IGV	2 = 4 - 2	2
	5	Rotor 2	Stator 2-3 - IGV	2 = 5 − (8-7+2)	2.5
3	-10	Rotor 2	Stator 1 – Stator 2	3 = -2x5 + (7 + 6)	-1.33
	-5	Rotor 3	Stator 3	3 = -5 + 8	-1.67
	-4	Rotor 1	Stator 2	3 = -4 + 7	-1.33
	5	Rotor 2	IGV	3 = 5 - 2	1.67
	9	Rotor 1 – Rotor 2	Stator 1	3 = (4 + 5) − 6	3
	10	Rotor 2 – Rotor 3	Stator 2	3 = (5 + 5) − 7	3.33
7	0	-	Stator 2		0
	14	Rotor 1 – Rotor 2	Stator 2	7 = (4 + 2x5) − 7	1.75
	15	Rotor 3	Stator 3	8 = 3x5 − 8	1.88

Table 22 Spatial and temporal modes of static pressure in rotor 3

The first spectrogram of Figure 95 shows that the temporal mode m_t = -5 of spatial mode m_θ = 2 is predominant along the rotor 3 axis. Considering the shape of the harmonic and by analogy with rotor 2, it is legitimate to affirm that this spatial mode is produced by an interaction between the second stator and rotor (and not the third rotor which has the same number of blades!). Moreover, an interaction with the third rotor would have involved the potential effects of stator 3, whose range is confined to the vicinity of the row. Therefore, the harmonic m_θ = 2 is mainly produced by an interaction of type "S_{i-1}-R_{i-1}". It spins backwards at 2.5 times the rotor shaft rotation speed. Note that the interaction between the first stator and rotor detected in the second rotor is still present in rotor 3, and dissipates at the axial position X = 0.3.

As for rotor 2, the spatial mode 3 is composed of many temporal modes. However, m_t = 10 is predominant all along the axis, from X = 0.25. This mode could be produced by the second temporal harmonic of rotor 2. However, by analogy with the spatial harmonic 3 of rotor 2, and because the mode m_t = 10 encounters a first maximum at the climax of the harmonic 5 of rotor 3 (see chapter IV.4.2), it is not absurd to consider that this temporal mode is in fact an interaction of type "R_iR_{i-1}-S_{i-1}". The temporal mode m_t = 10 would then be produced by the five wakes of rotor 2 and 3. This interaction produces a structure spinning at 3.3 times the speed of the shaft: this harmonic dominate the flow in section 28A, and is effectively responsible for the stripes visible in the space-time diagram of Figure 94. One can notice that the interaction "R_iR_{i-1}-S_{i-1}" of rotor 2 (m_t = 9) is still present in rotor 3.

Finally, as for the two previous rotors, the spatial mode $m_\theta = 7$ is mainly produced by a *"3R$_i$-S$_i$"* ($m_t = 15$). However, its amplitude relatively to the other spatial harmonics is much weaker. Note that like in rotor 2, a complex interaction involving the three rotors and the stator 2 is visible at the rear part of the blades ($m_t = 14$). The slight influence of stator 2 is also visible (temporal mode $m_t = 0$). As written in chapter IV.5.1.1, it produces a non-spinning structure.

IV.5.2.3 Conclusion

In this chapter, a modal analysis method has been applied to the wall static pressure measurements above the three rotors at peak efficiency. The usefulness of this method has been demonstrated as it allowed to understand the origin of the unsteadiness of the pressure field in the machine. It has been shown for example that the complex structures visible in the pressure fields downstream of the two first rotors were due to a type of *RSI* identified as *"3R$_i$-S$_i$"*.

The origin of the main harmonics has been also understood. It appears indeed that three main types of pressure interaction occur in the machine:

- *"S$_{i-1}$-R$_{i-1}$"*: this interaction is very energetic at tip in the rotors. It involves the wakes of the rotor and stator of a given stage, and propagates far downstream of the stator. Its amplitude is almost constant along the rows. They are visible in rotors 2 and 3: in rotor 1, a spatial harmonic $m_\theta = 2$ is also visible, but it is produced by the interaction between *IGV* and rotor 1 (as no rotor upstream of rotor 1 can interact with the *IGV*!). This interaction is a weak version of the *"S$_{i-1}$-R$_{i-1}$"* encountered in the two downstream stages. The *"S$_{i-1}$-R$_{i-1}$"* interactions correspond to the '*blue*' harmonics of Figure 84.

- *"R$_i$R$_{i-1}$-S$_{i-1}$"*: this interaction is present in the rotors 2 and 3, but remains quite weak in rotor 2. It is produced by a superposition of the wakes of two consecutive rotors which interact with the blades of a stator. Note that the amplitude of the interaction is remarkably high in the last stage. The clocking of the two last rotors which have the same number of blades could explain this high amplitude. As for the *"S$_{i-1}$-R$_{i-1}$"*, this interaction is only present in the two last stages, as it involves two rotors. One can consider this as a '*second-order interaction*', i.e. an interaction between a harmonic *"S$_{i-1}$-R$_{i-1}$"* and the downstream rotor. This corresponds to the '*green*' harmonics of Figure 84.

- "3R$_i$-S$_i$": the last type of interaction involves the rows of the rotor and stator of a given stage, but only appears between the two rows (at the rear part of the rotors): this interaction is present in the three stages. This is the only main harmonic produced by an interaction between wakes and potential effects. The quick axial damping of the potential effects explains why its zone of influence is confined to the inter-row regions behind the rotors. It can be very strong and completely dominates the flow at casing behind the rotors. It might therefore be the strongest source of unsteadiness in a single stage compressor, as observed in the first stage of CREATE. This corresponds to the '*cyan*' harmonics of Figure 84.

Finally, the pressure field in CREATE can be summarized as a superposition of the **direct influences of each row**, plus the **three main harmonics** described before (in a matter of simplification, they will be called ***S-R***, ***RR-S*** and ***3R-S***). This result is of particular interest for numerical

simulations. Indeed, numerical methods like Harmonic Balance Technique (HBT) or multi-chorochronic calculations require to know the most energetic harmonics of the flow, see [78].

IV.5.3 Analysis of the three main pressure interactions

The purpose of this chapter is to describe and explain the structures of the three main pressure interactions *"S-R"*, *"RR-S"* and *"3R-S"*. This will be done through the analysis of the axial and radial distributions of the interactions, and their sensitivity to the operating points. A link will then be made between the modal and physical frames to try to understand the mechanism of creation and propagation of the interactions.

IV.5.3.1 Overview of the axial distributions of the interactions above the rotors

In Figure 96 is plotted the axial evolution of the energy (signal processing meaning) of the wall static pressure field above the rotors versus the mass flow: wall pressure measurements have indeed been achieved above the rotors over the spatial period θ_{16} from choke to the surge margin, at nominal speed. Thus, at each axial position and for each operating point, the energy of the wall pressure measurements has been calculated according to the modal decomposition method (relation (IV-10)). In the three upper maps of the figure, the energy has been calculated for the fluctuations of pressure (in the modal matrices (IV-6), it is like setting the coefficients $A_{0,0}$ to 0). In the three bottom maps, the modal matrices have been filtered in order to only keep the energy of the *RSI*. The axial positions have been normalized the same way as all the figures of the previous chapters. The axial locations of the leading edges (LE) and trailing edges (TE) of the blades are indicated with vertical dotted lines. As for the performance lines of CREATE presented on Figure 34, the mass flow has been normalized by its value at peak efficiency: the three dotted lines visible on the maps show the operating points *PE*, *L* and *SM*.

As previously seen in chapter IV.4.2, the direct contributions of the rotors (i.e. the harmonics linked to the number of blades) are largely predominant around axial position X = 0.25, and are representative of the load applied to the rotor blades. Therefore, the three upper maps show the evolution of the axial position of the load versus the mass flow. For rotor 2 and rotor 3, the load moves towards the leading edges of the blades when the mass flow is reduced because the incidence angle of the flow is increased. For rotor 1, the change of axial position is less visible, as the load seems more diffused on the blade: it reaches however a sharp peak at axial position 0.22 at *SM* point.

The three bottom maps present the energy of the *RSI*. Even if it reaches values far below the maxima encountered in the upper maps (the maximum energy of the *RSI* in rotor 3 represents nearly 14% of the maximum total energy), the energy of the interactions is far from being negligible. It becomes even predominant outside of the zones of high-amplitude of global energy, restrained to the leading edge of the rotors: for example, it represents more than 95% of the total energy at the trailing edge of each rotor! As previously stated, the amplitude of the *RSI* strongly increases when going towards the rear stages of the machine: the maximum energy encountered in rotor 1 is equal to nearly 10 % of the maximum of rotor 3.
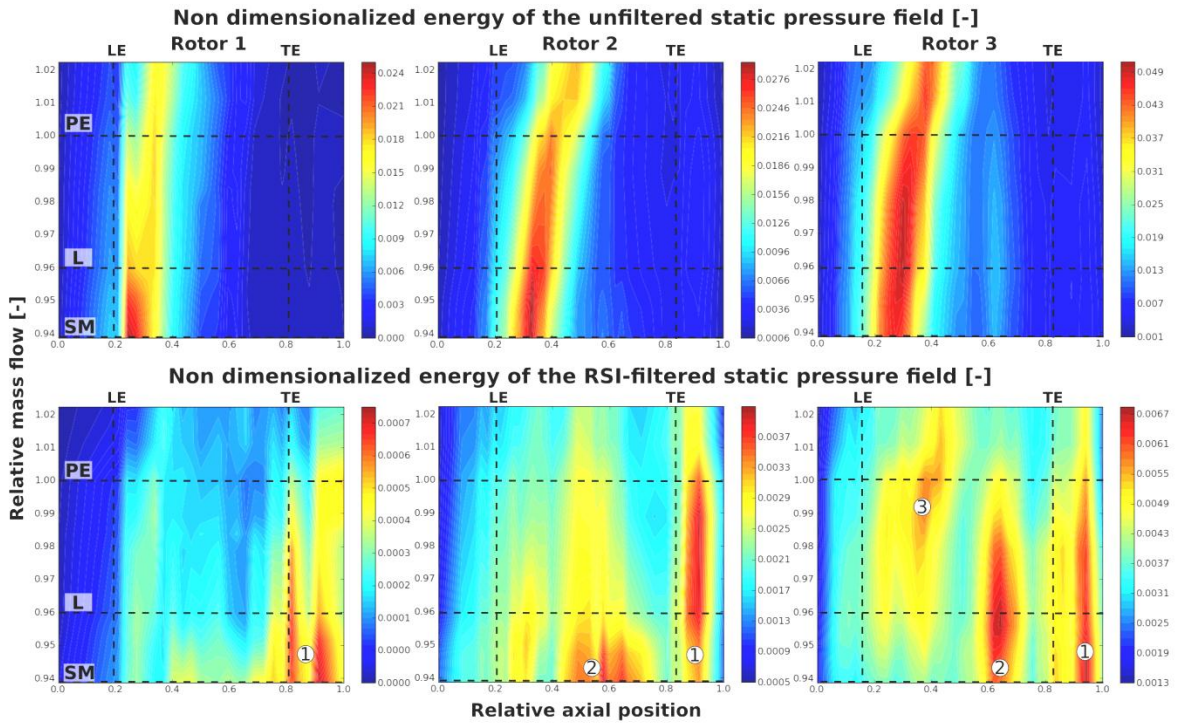
Figure 96 Energy of the wall static pressure field above the rotors versus the mass flow
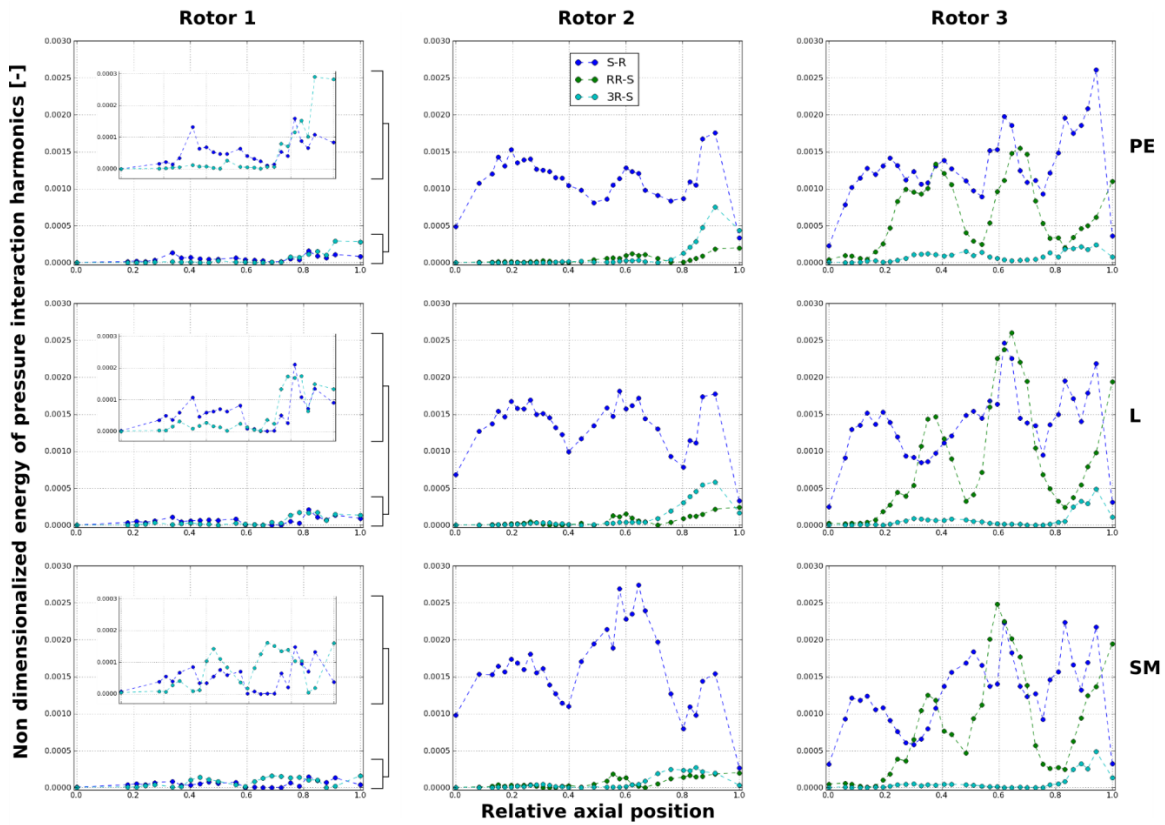
Figure 97 Energy of the main interactions of static pressure above the rotors for three operating points

The energy patterns visible in the *RSI* maps differ from one rotor to another, even if some similarities are observable: three main structures, labeled from 1 to 3 are identifiable on the maps. The first one is composed of one (or two, for rotors 1 and 3) strong peak of energy located just

downstream of the trailing edges of the blades and extending from peak efficiency to surge margin operating points. Their amplitudes increase from *PE* to *SM* (for rotor 2, the maximum is encountered between *PE* and *L*). The second structure is visible roughly at mid-rear chord of the rotors, and increases in intensity when the mass flow is decreased. In rotor 2, a zone of high energy appears indeed at axial position [0.4 - 0.75]. It is particularly intense from *L* to *SM* operating points, but is visible over the whole mass flow range. In rotor 3, this zone appears a bit more downstream, at axial position 0.65 (the maximum of rotor 2 being encountered at 0.58). Moreover, its shape is tighter than in rotor 2 and its amplitude stronger. It reaches a maximum at *L* operating point and extends from *PE* to *SM*. Finally, a last zone of relatively high-energy appearing at high mass-flows is visible in the rotor 3 only, at the front part of the blades (position 0.25 to 0.45).

In order to understand the origin of the three zones previously mentioned, the axial evolutions above the rotors of the energy of the three interactions *"S-R"*, *"RR-S"* and *"3R-S"* have been plotted in Figure 97 for *PE*, *L* and *SM* operating points. Note that the spatial harmonics have been filtered in order to keep only the temporal mode corresponding to the interaction. For example, the energy of *"S-R"* has been calculated using only the temporal mode m_t = -4 of the spatial harmonic m_θ = 2 (see chapter IV.5.2.2). The colors chosen for the interactions are the same as in Figure 84. As previously seen in the energy maps, the energy of the interactions is much lower in the first rotor than in the two others: a zoom as therefore been plotted for each map of rotor 1.

The axial evolution of the energy of the interactions *"S-R"* is similar in the two last rotors. Three humps are indeed visible along the machine axis, although these of rotor 3 are shifted towards the rear part of the blades. One is located at the leading edge of the blades, another at mid-rear chord (axial position 0.6) and the last one just downstream of the trailing edge. At peak efficiency, the rear hump is a bit higher than the two others for the two rotors: it produces the peak of energy numbered 1 in Figure 96. It is worth to notice the very sharp decrease in its amplitude from axial position 0.9 to 1, which brings the value of *"S-R"* below *"3R-S"* for rotor 2 – section 27A and below *"RR-S"* for rotor 3 – section 28A. This is consistent with the observations of chapters IV.4.1.2 and IV.5.2. When the load is increased (operating points *L* and *SM*), a huge growth of the second hump can be observed in rotor 2. In rotor 3, a slighter increase is observable. In rotor 2, this is obviously the cause of the energy pattern number 2 in Figure 96. The two others humps tend to lower a little, but keep high amplitudes: this explains why the energy pattern 1 is almost constant along the mass flow range. Note that the shape of the interaction *"S-R"* of rotor 1 is quite different from the two others, as it is a weak interaction *"S-R"* due to the location far upstream of the *IGV*.

The interaction *"RR-S"* only appears in the two last rotors. Its amplitude, comparable with *"S-R"* in rotor 3, is much lower in rotor 2, as previously seen in chapter IV.5.2.3. In rotor 3, higher amplitude of *"RR-S"* seems to be found where *"S-R"* has lower amplitude, see for example the axial positions 0.7 and 1, and on the contrary the axial range [0.8-0.9] at *PE*. Upstream of the rotor blades, the amplitude of the interaction is close to zero: this confirms that the interaction *"RR-S"* involves the third rotor (and not the second harmonic of the second rotor). At peak efficiency in rotor 3, the first hump of *"RR-S"* induces the high energy of pattern 3 of Figure 96. As for *"S-R"*, the amplitude of the second hump increases a lot at *L* and *SM* operating points, as well as the slope located at axial position [0.9-1]: it is interesting to notice that on the contrary, the amplitude of *"S-R"* roughly keeps a constant value in rotor 3 when the mass flow is decreased. At axial position [0.6-0.7], the humps of the two interactions coincide: this produces the zone of high energy numbered 2 in rotor 3. The

shape of interaction *"RR-S"* explains why the pattern number 2 of rotor 3 is tighter than in rotor 2. Note that the slight decrease in amplitude of the first hump, combined with the upstream shift of the first hump of interaction *"S-R"* (which induces a decrease in amplitude at axial position 0.3) provoke the vanishing of energy pattern 3 at low mass flow.

The shape of the interaction *"3R-S"* is quite similar in the three rotors. As previously mentioned, its amplitude remains low along the blades and increases just downstream of the rows: it is interesting to notice that the maximum amplitude of this interaction coincides with the maximum of the third hump of *"S-R"*. When decreasing the mass flow, the maximum of the interaction decreases too, and its axial position in rotors 1 and 2 tends to move upstream. This interaction is the main source of the energy pattern 1 of rotor 1, and is the cause of the modulation of the amplitude of the same pattern in rotor 2 (see the maximum between *PE* and *L* operating points).

Overall, the *RSI* play an important role at the tip of the rotors, outside of the zones of direct influence of the blades, as illustrated by the energy maps. The main interactions highlighted in the previous chapters are responsible for the zones of high energy highlighted in this section. The detailed analysis of the energy of the interactions brought out some common tendencies for their amplitudes summarized as follows:

- *Interaction "S-R":* Three maxima encountered along the blades. Very sharp decrease of amplitude just before the inter-row section downstream of the rotor. The maximum found at mid-chord increases a lot in rotor 2 (less in rotor 3) when the mass flow is decreased.

- *Interaction "RR-S":* Two maxima located between the edges of the blades, and a sharp increase of amplitude downstream of the blades. The maximum at mid-chord increases a lot when the mass flow is decreased. Higher values of *"RR-S"* are found where *"S-R"* has lower values.

- *Interaction "3R-S":* Amplitude very low along the blades, except behind the trailing edges. When the mass flow is decreased, the maximum of amplitude decreases and is shifted upstream.

In the next section, the radial distribution of the interactions will be analyzed and a link will be drawn between the observations in the modal frame and in the physical frame.

IV.5.3.2 Radial evolution and visualization in the physical frame

The purpose of this section is to link the modal observations to the flow field in the physical frame, in order to better understand the mechanisms of the interactions. Figure 98 shows the radial distributions of the energy of the three main interactions, calculated in each inter-row section from total pressure measurements at peak efficiency and loaded operating points. The sections downstream of the rotors and stators are colored in red and blue tones respectively.
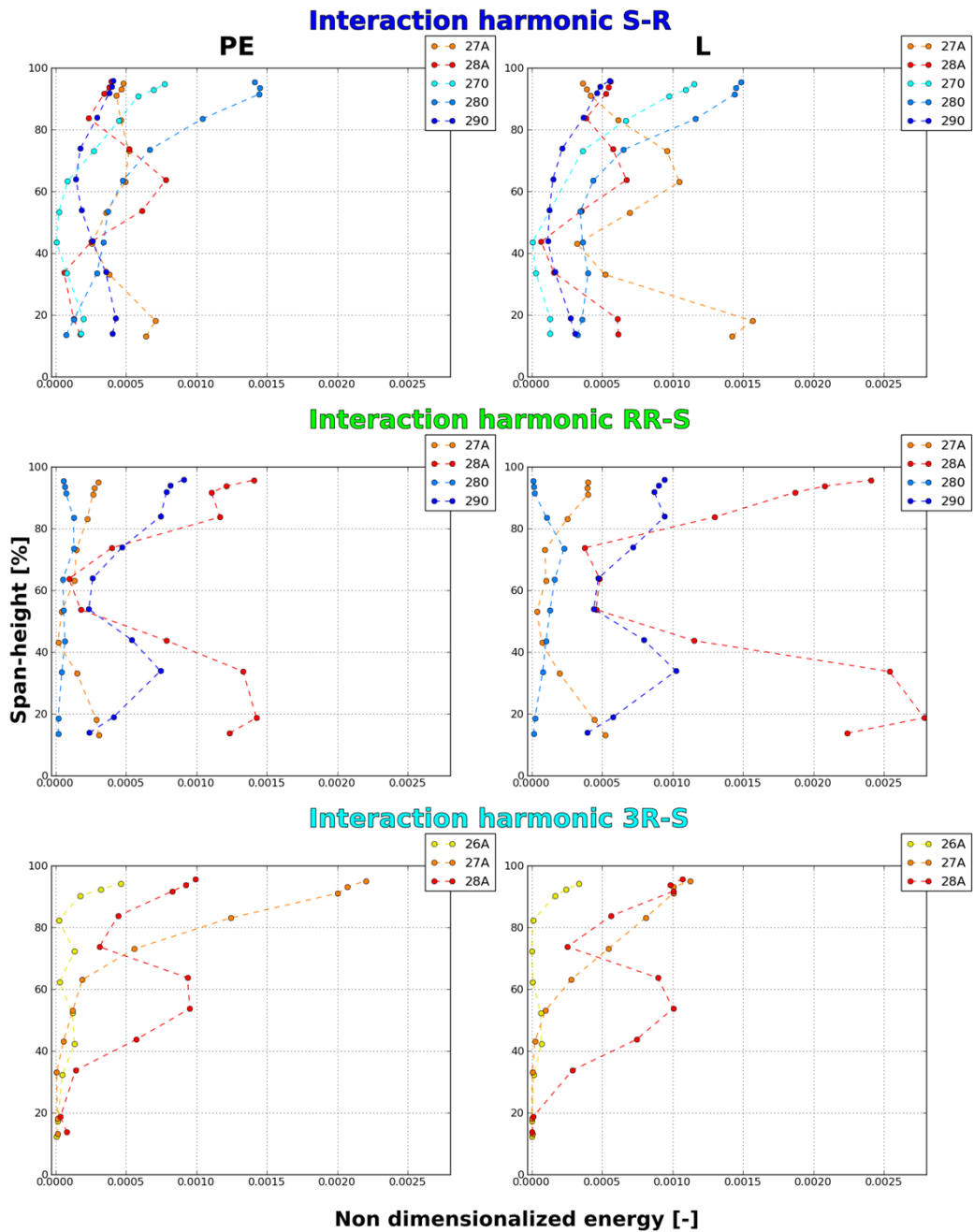
Figure 98 Spanwise evolutions of the energy of the main interactions for *PE* and *L* operating points – total pressure

Interaction S-R:

Figure 99 shows the temporal fluctuations in the relative frame of the non-dimensionalized wall static pressure field above rotor 2 for the two operating points *PE* and *SM* at an arbitrary time step. It has been calculated in order to remove the direct contributions of rotor 2: this rotor has been chosen because the energy of interaction *"S-R"* is particularly high in comparison with the other interactions. To highlight the zones of positive and negative relative pressure, contours have been plotted around zero in red and blue, for values of relative pressure of 0 ± ε respectively.
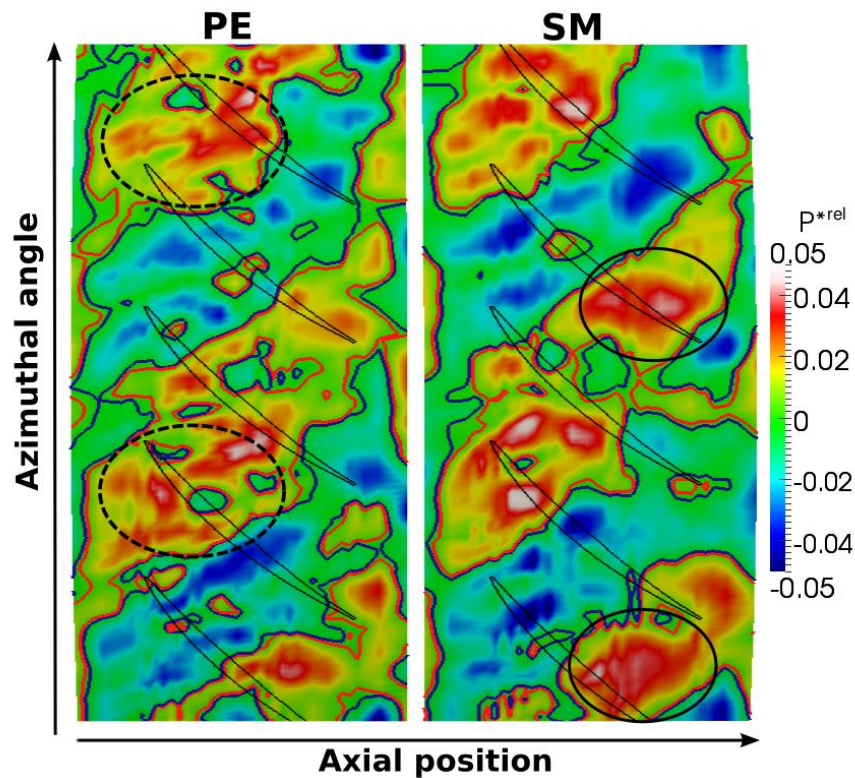
Figure 99 Fluctuations of wall static pressure in the relative frame above rotor 2 at an arbitrary time step- *PE* and *SM* operating points

For the two operating points, the interaction *"S-R"* is clearly visible through the spatial harmonic 2 it induces (chapter IV.5.2.3), see the oblique stripes of low and high. They move in the relative frame from top to bottom (the interaction spins backwards at twice the rotor speed, see chapter IV.5.2.2). Their global shape and inclination do not change with time. It is worth to notice that the stripes are almost perpendicular to the blade passages. Considering the interactions as spinning wave fronts, they can be transmitted or reflected at the blade rows interfaces when traversing the compressor. If they impinge the rows normal to the blades in the relative frame, they do not encounter resistance and are almost completely transmitted (the mechanism of propagation of pressure waves through blades rows, based on the work of Kaji and Okazaki [45] is detailed in chapter V.5.4). This mechanism would explain why the *"S-R"* propagates so far from its emission location: in the case of rotor 2, the interaction occurs at the trailing edge of stator 1, and propagate through rotor 2 with an almost constant high amplitude.

At peak efficiency, strong spots of high pressure are visible at the leading edge of the blades (see the dotted circles). They are responsible for the first hump in the axial evolution of the energy in Figure 97. At the trailing edge, only several small spots appear. At *SM* operating point, the spots of leading edge become stronger but keep separated: the first hump of Figure 97 increases but not too much. On the contrary, the spots located at the trailing edge do not increase much in intensity but merge together to form coherent big structures of relative high and low pressure (see the solid circles): they are responsible for the huge increase in the second hump in the axial evolution of the energy.

The radial distributions of the energy of the interaction *"S-R"* (Figure 98) show similar shapes for the two rotors and the three stators respectively. Behind the stators, the amplitude of the

harmonic increases with span and is maximal at tip. Behind the rotors, a hump is visible between 50 % and 80 % of span-height: a smoother hump is found downstream of rotor 2. The interaction *"S-R"* appears just downstream of the stators and propagates through the rotors. An explanation of the difference between the span-heights where the maxima of two consecutive planes are encountered (for example for sections 270-95 % and 27A-75 %) could be that the interaction dives in the passage when traversing the rotors. This would explain the sharp decrease in the wall pressure measurements observed just downstream of the rotor blades.

Interaction RR-S: Figure 100 shows the fluctuations of the non-dimensionalized wall static pressure field above rotor 3 for the two operating points *PE* and *SM* at an arbitrary time step. The fluctuations of pressure have been calculated in the relative frame, and the figure has been built the same way as Figure 99. The rotor 3 has been chosen because the amplitude of the interaction *"RR-S"* is very high in this row.
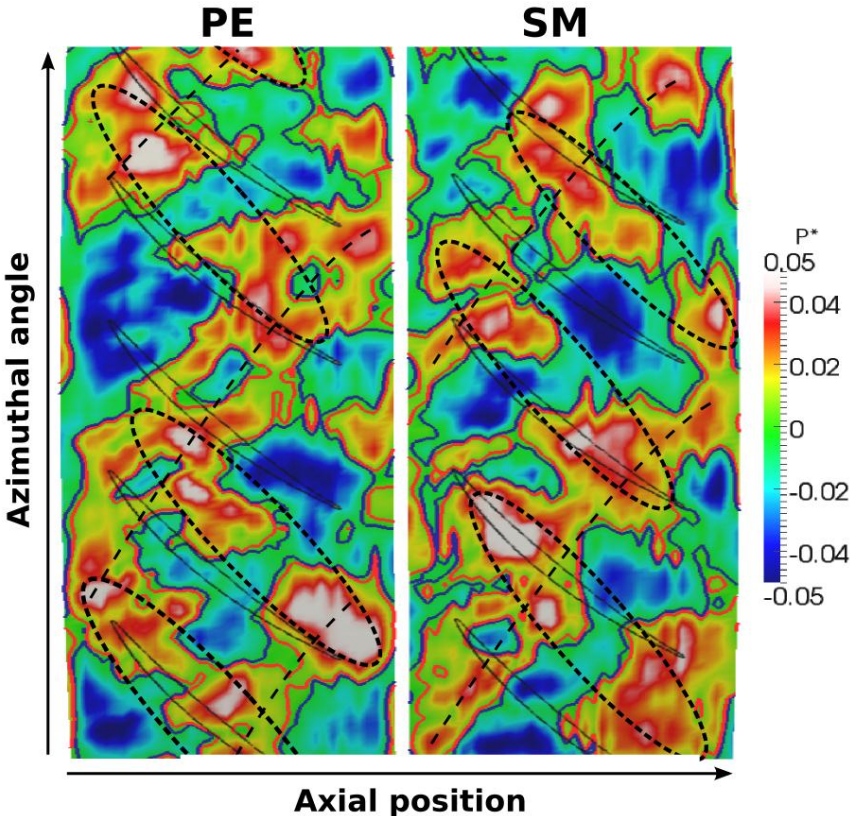
Figure 100 Fluctuations of wall static pressure in the relative frame above rotor 2 at an arbitrary time step - *PE* and *SM* operating points

The visualization of the interaction *"RR-S"* is much more complicated than *"S-R"* because the two interactions superimpose their influence in rotor 3. The influences of *"S-R"* (spatial harmonic 2) and *"RR-S"* have been underlined by dotted lines and dotted ellipses respectively. Contrary to *"S-R"*, the interaction *"RR-S"* induces structures nearly parallel to the blade passages. They propagate from bottom to top (the interaction spins at 3.3 times the rotation speed of the shaft). From *PE* to *SM*, the intensity of the interaction grows and become stronger than *"S-R"*. The structure of the flow indeed changes and stripes parallel to the blade passages start to appear clearly: the rise of the structures of

"RR-S" seems to induce the disappearance of those of *"S-R"*, which is consistent with the observations of the previous chapter.

The radial distribution of *"RR-S"* at *PE*, see Figure 98, is similar behind the two last rotors, even if the amplitude of the interaction is much more important behind the last rotor. It appears very strong at tip and near the hub: the amplitude decreases indeed dramatically at midspan (45%-75%). The shape of the radial evolution is very sharpened at *Loaded* operating point. It is interesting to notice that the radial evolution of the interactions *"S-R"* and *"RR-S"* seem complementary in section 28A, where *"RR-S"* reaches high amplitudes. A possible explanation could be that when an interaction "*S-R*" is emitted behind a stator and passes through downstream rotor, the interaction with the rotor which produces the interaction *"RR-S"* weakens the harmonic *"S-R"*. This phenomenon, visible along rotor 3 as written in the previous chapter, is particularly strong just downstream of rotor 3, at axial position [0.9 - 1] in Figure 97. This mechanism would explain for *"S-R"* why lower amplitudes are found downstream of rotor 3 than downstream of rotor 2 at tip, whereas the interactions increase in intensity when going towards the rear-part of the machine. Moreover, by shifting down the values of the amplitude of *"S-R"* at tip, this would explain the shape of the hump visible in section 28A which is much sharper than in section 27A. Finally, at *Loaded* operating point, the amplitude of *"RR-S"* increases a lot: the competition of the two interactions could also explain why the amplitude of *"S-R"* does not increase downstream of rotor 3 as much as downstream of rotor 2.

Lastly, the shape of the radial evolution of *"RR-S"* behind the last stator (section 290) is very similar as downstream of the last rotor, with comparable amplitude (at *PE*): indeed, this interaction takes place in the rotors and propagates in the stators downstream. In the case of rotor 3, the structures are almost parallel to the blades in the relative frame. Therefore, they impinge the stator blades more or less perpendicularly to the leading edges: adopting the same hypothesis of wave-fronts as for interaction *"S-R"*, this would explain why the interaction *"RR-S"* is little damped when crossing the third rotor. A little change of orientation of the wave-fronts at *SM* operating point could induce a change in the transmission coefficient of the last stator and explain the huge attenuation visible between sections 28A and 290. This is only a conjecture: the analysis of the flow in the physical frame is indeed very touchy in the rear stages of this compressor because of the complexity of the flow.

Interaction 3R-S:

In order to understand the origin of the third rotor harmonic involved in the *"3R-S"* interaction, results of unsteady CFD calculations have been used. The first stage has been chosen to study this interaction because of the simplicity of the flow and because the interaction *"3R-S"* dominates between the first rotor and stator. In order to highlight the swirling structures of the flow, Figure 101 shows a contour plot of the Q-Criterion of velocity calculated at peak efficiency for rotor 1 and stator 1 at an arbitrary time step. The flow goes from left to right and the rotor blades rotate from bottom to top). The contour plot has been colored by the non-dimensionalized static pressure. On the top left of the figure, a zoom over one passage is available: the relative velocity field has been superimposed (vectors). The figures have been stretched.

Three swirling structures are emitted at the leading edge of each blade (see the dotted lines). The tip clearance vortex is the biggest vortex emitted in each blade passage. It reaches the pressure side of the next blade at approximately mid chord. Two tip separation vortices are also emitted downstream of the leading edges, at roughly mid-chord: this confirms the hypothesis of the two *TSV* made in chapter IV.3.2.2 although only one separation vortex was clearly detectable in the experimental measurements. They follow the suction side of the blade when going through the rotor, and tend to merge together at the outlet: their complex interaction explains the difficulty to separate them in the experimental results.

These three vortices are apparently the cause of the emergence of the third harmonic of the rotor, as supposed in chapter IV.3.2.2. When they impact the stator blades, they are sliced in each blade passage: three slices of vortices are indeed visible in each stator passage (see the dotted ellipses). The interaction *"3R-S"* (not visible here) arises in the pressure field when the perturbations induced by the vortices meet the potential effects of the stator blades.
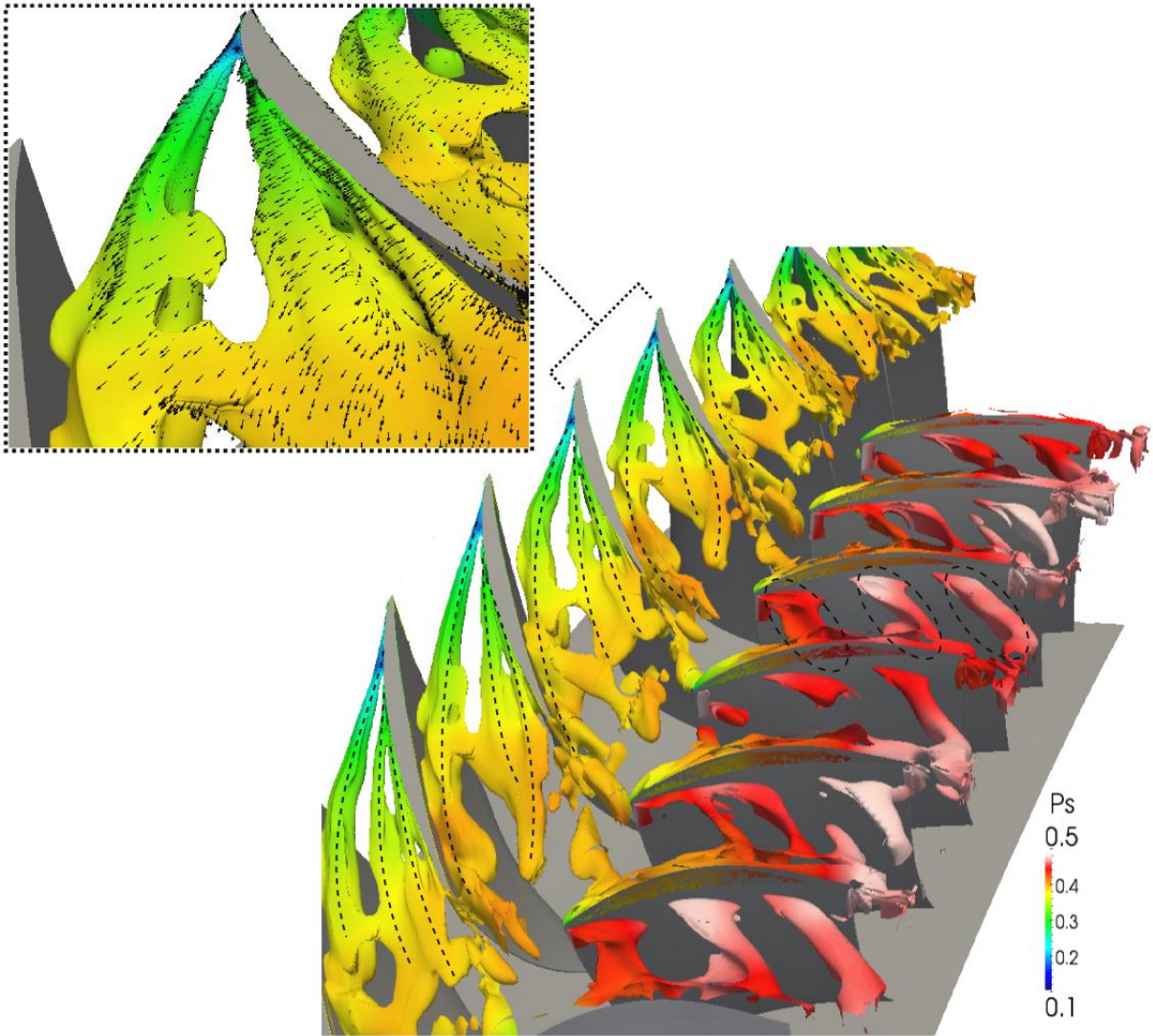
Figure 101 Visualization of the vortices arising at tip of rotor 1 and propagating in stator 1 at *PE* - CFD

The radial evolution of the interaction *"3R-S"* (Figure 98) is similar for the three rotors: the amplitude is low near the hub and increases a lot at casing. This can be easily explained as the three

vortices involved in the interaction appear at casing. It is worth noticing that this interaction dominates the flow behind the rotors 1 and 2 (remember the huge decrease in the amplitude of "*S-R*" downstream of the rotors) and is of comparable amplitude with *"RR-S"* downstream of rotor 3. The case of the third rotor is particular as a hump is visible in the spanwise evolution of section 28A. It is complementary to the shape of the interaction *"RR-S"* in the same section. A similar mechanism to the competition between *"S-R"* and *"RR-S"* exposed in the previous paragraph could occur between *"3R-S"* and *"RR-S"*. The effects on the pressure field of the tip clearance vortices could indeed be altered by the interaction *"RR-S"*, as the two interactions involve a direct contribution of rotor 3. Therefore, as *"3R-S"* is produced downstream of *"RR-S"*, the amplitude of *"3R-S"* could be impacted by the presence of *"RR-S"* without reciprocity: without *"RR-S"*, the upper part of the spanwise distribution of *"3R-S"* could be up shifted to its value at midspan. In this case, this interaction would be dominant in rotor 3, as well as in the two first rotors. This is only a supposition.

Finally, a slight decrease in amplitude is visible between *PE* and L operating points in sections 26A and 27A. The previous chapter showed indeed that the axial location of the maximum intensity of the interaction *"3R-S"* tends to move upstream when the mass flow is decreased: this could be explained as the trajectories of the vortices are shifted upstream when the axial velocity is decreased. Nevertheless, it was not possible to prove it because the unsteady calculations have only been performed on two operating points: *PE* and another very close of *PE* in term of mass flow.

IV.5.4 Conclusion

This modal analysis of the total and static pressure fields in CREATE showed that three main pressure interactions exist in the machine:

- The interaction *"S-R"* is produced at tip downstream of the stators by an interaction of the upstream rotor and stator wakes. It propagates with low resistance through the rotors, the wave fronts of the interaction being perpendicular to the rotor blades. When passing through the rotors, the interaction dives inside the passage.

- The interaction *"RR-S"* takes place in the rotors (above all in the third). It is produced by an interaction between *"S-R"* and the rotor blades: a competition therefore occurs between the two interactions, and lower amplitudes of *"S-R"* are found where *"RR-S"* reaches higher values. In rotor 3, the structures induced by the *"RR-S"* interaction are parallel to the blade passages in the rotors. They seem to be able to pass through stator 3: a conjecture could be that the wave fronts impinge the stator blades roughly perpendicularly to the leading edges.

- Finally, the "*3R-S*" interaction is produced by three leakage vortices appearing in the passages at the tips of the rotors. They interact with the potential effects of the downstream stator. This interaction seems to move upstream when the mass flow is decreased, because of the shift of the trajectories of the vortices. It seems moreover to compete with *"RR-S"* behind the last rotor.

Remember that the hypothesis concerning the propagation of the two first interactions are only conjectures. After this characterization of the main pressure interactions, unsteady CFD results will be used in the next section to evaluate the contribution of these interactions in term of losses.

IV.6 Contribution in term of losses

IV.6.1 Transposition of the pressure results to entropy

In this chapter, a tentative of evaluation of the viscous losses produced by the interactions will be done. As no unsteady entropy measurements were available, the following study relies on *CFD* calculations: the URANS results at peak efficiency, presented in Appendix: The numerical simulations, have indeed been used to draw some tendencies about the losses generated by the *RSI*. It is important to notice that a direct study of the three main harmonics "*3R-S*", "*S-R*" and "*RR-S*" cannot be done with the entropy. Indeed, the mode of propagation depends on each aerodynamic quantity. Some quantities like pressure or density behave like propagating waves, as observed by Mailach *et al.* (2004, [55]). Others, like velocity or entropy, are convected downstream by the flow. The shape of these signals are therefore very different as well as the way they interact: as the shapes of the former quantities can be roughly assimilated to sinusoidal waves, the shapes of the latter seem more as sums of Diracs because of their sensitivity to the wakes. Indeed, just downstream of the trailing edge of the blades, the velocity behaves inside the wakes like in a boundary layer, and thus decreases very brutally.

Figure 102 shows an illustration of typical signals for each type of quantity: on the left, the "pressure-like" quantities are presented (a vertical shift has been put between the signals in a matter of clarity). On the right the "velocity-like" quantities are presented. An example of two modes 4 and 6 has been chosen in order to illustrate the situation behind the first stage. On the left hand-side, the signals are centered on their mean value. A 2-modulation appears in the signals: it comes from the trigonometric relation (IV-12) (the cosine function appears in the figure as black dotted curves).

$$\sin(a) + \sin(b) = 2 \cdot \cos\left(\frac{a-b}{2}\right) \cdot \sin\left(\frac{a+b}{2}\right) \qquad \text{(IV-12)}$$
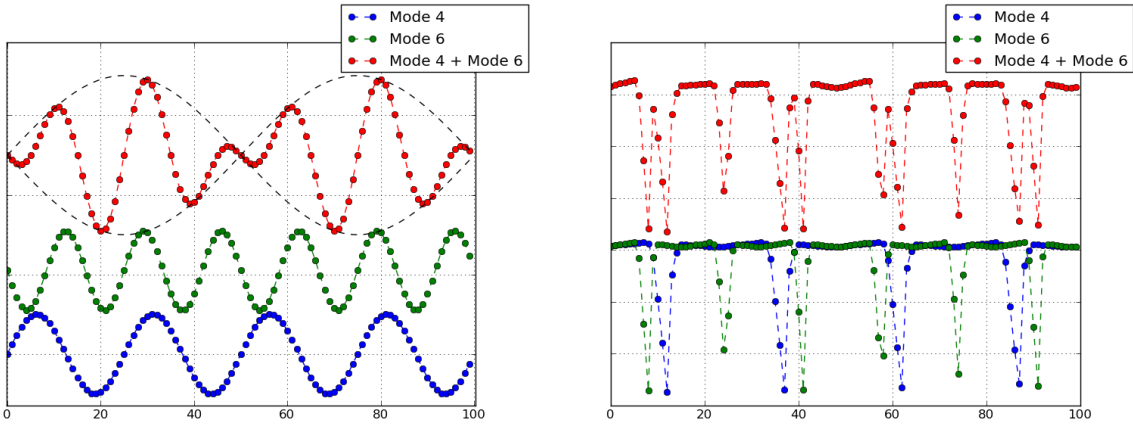
Figure 102 Illustration of interactions between pressure-like and velocity-like quantities

The second case on the right hand side is much different: here, the signals are no more centered on their mean value because of the presence of strong peaks. They cannot be described with a simple sum of cosine functions: an infinity of frequencies multiple of the mode order are

indeed observable in their spectra which is characteristic of Dirac functions, see [77]. In this case, intuitively, the mode orders are added, see the right part of Figure 102.

Hence, to apply to entropy the main results of the previous study made on the static and total pressure fields, a transposition has to be done. Indeed, the interaction between a rotor and a stator will produce an interaction harmonic *"R+S"* in the entropy field, as well as the second order interaction *"RR-S"* which will be transposed to *"RR+S"*. For example, a spatial harmonic 10 instead of 2 will be detected downstream of the first stage (4 and 6 blades for rotor 1 and stator 1 respectively). Note that no evidence of the harmonic *"3R±S"* has been found in the entropy field along the machine.

IV.6.2 Energy maps of entropy

Two meridian maps of the energy of the entropy field at *PE* operating point are plotted on Figure 103 in order to highlight the zones of production of viscous losses in the machine: they are of particular interest in order to have a global overview of the flow in the machine. They have been built the same way as Figure 96 from *CFD* calculations: remember that the term 'energy' is used here in the signal processing meaning. On the two maps, the vertical red lines show the inter-row planes. The upper and bottom maps show the energy of the entropy field calculated for the whole flow and the *RSI* respectively. They have been normalized by the highest value of energy found in the upper map in order to compare the losses produced by the interactions with the global production of losses. A contour plot of the relative energy (*RSI* over whole flow) has been superimposed on the upper map.

On the energy map of the whole flow, two strong zones of production of losses are visible at the tip of the rotors 2 and 3. Indeed, due to the enhanced tip gaps, the tip leakage flows are particularly strong at these locations. They induce strong blockages and mixing responsible for losses production. These losses are apparently convected in the downstream stators, in particularly in stator 3, where high values are found at tip: indeed, the losses at the tip of rotor 3 are responsible for the thickening of the boundary layers of the last stator. This is consistent with the experimental observations of the steady entropy field in IV.2.2. Strong losses are also found at the leading edges of the rotors along the span. Note that as expected, the zones of production of losses become stronger at the rear part of the machine. On the second map, the trajectories of the tip clearance flows are highlighted by dotted lines in the three rotors. Indeed, as previously seen in chapter IV.3.2.2, the *TCF* interact with the incoming wakes of the upstream stator: the losses are stronger in the second and third rotors as the *TCF* are stronger, and because the wakes of the stators 1 and 2 are also much stronger that these of the *IGV* located far upstream of rotor 1. It is also worth noticing that the *TCF* of the rotors 2 and 3 dive much deeper in the vein, as they are stronger.

As written in the previous chapter, the interaction modes of entropy are different than for the pressure: in the machine most of the interactions of entropy are produced by a direct rotor-stator interaction *"S+R"*: for example, behind stator 1, a spatial harmonic 10 is found instead of the harmonic 2. Therefore, this *"S+R"* harmonic (highlighted with blue dotted lines and ellipses in the bottom map of the figure) will be assimilated to the entropy version of the previous *"S-R"* pressure interaction. Note that this harmonic is a source of high losses at the leading edges of the rotors 2 and

3 along the span, as well as in stator 1 and 2 (see the circular zones at tip): it is worth to notice that the interaction appears in the stators (and not downstream) and at tip, as previously stated in chapter IV.5.4. However, a new type of *"S+R"* interaction is visible in the entropy field: *"R_i+S_{i-1}"* in addition to *"$R_{i-1}+S_{i-1}$"*. Indeed, in the previous chapter, only the interaction of the wakes of an upstream stage could be detected in a given rotor: for example no evidence of an interaction between the wakes of stator 1 and rotor 2 could be found in rotor 2. This time, the wakes coming from a stator produce an interaction harmonic inside the downstream rotor. Indeed, contrary to the pressure field, the entropy field captures the interaction between the *TCF* and the wakes. This interaction is responsible for the pear-shaped zones of losses at the tip of the rotors 2 and 3 (orange dotted curves): it is worth noticing that the losses produced by the interaction are stronger in rotor 2 than in rotor 3. Moreover, a parallel can be drawn with the observation of the behaviour of the pressure harmonic *"R-S"* which tends to dive inside the vein when crossing a rotor, see chapter IV.5.4. Finally, another important source of losses at the tip of rotor 3 is the interaction *"RR+S"*, highlighted by a green circle. However, the influence of this second-order interaction has been found confined to the tip of rotor 3.
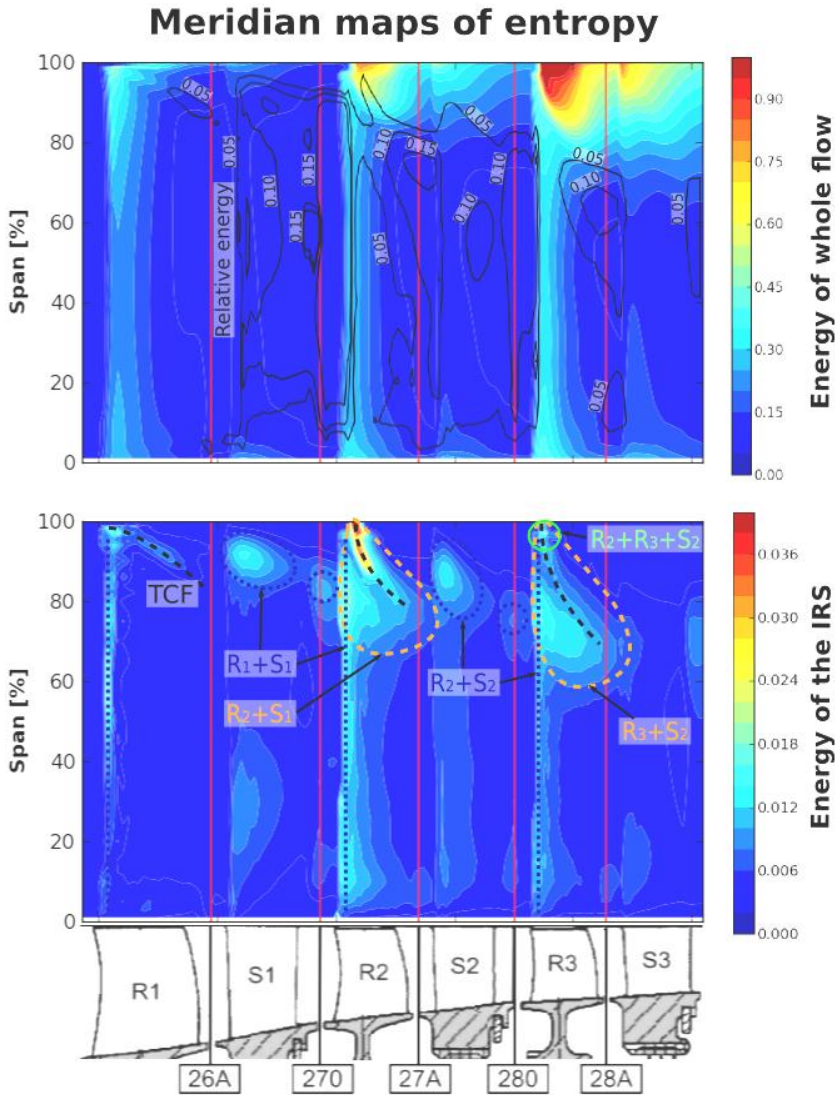
Figure 103 Meridian maps of the energy of the entropy field at *PE* operating point calculated for the whole flow (upper map) and for the RSI only (bottom map)–CFD calculations

Thus, it has been shown that the interaction *"S+R"*, the entropy version of the pressure harmonic *"S-R"* is responsible for most of the losses produced by the harmonics. They remain however very weak in comparison with the maximum of the total losses encountered at the tip of rotor 3 (less than 3%). Nevertheless, as the strong sources of losses are confined to the tip of the rotors, the relative production of the *RSI* can increase up to 15% outside of these zones: the contour plot of the upper map shows for example that the relative production is quite strong around 70 % of span-height, where the 'pear-shaped' zones of interaction are found.

Overall, this study showed that the interactions are significant in term of losses production. Indeed, they produce in average between 5 % and 10 % of the total viscous losses in the machine. This means that in comparison with a comparable theoretical multistage compressor composed of a juxtaposition of six isolated rows, CREATE would produce more than 5 % more viscous losses. This nuances the general rule of engines conception aiming at compressor designs as compact as possible: indeed, they imply a shorter axial distance between blades rows and thus stronger *RSI*. It is however complicated to have a final stance on this question, as the interactions can also have benefic effects, see for example the phenomenon of wake recovery presented in chapter I.2.1, responsible for the wakes decay in the presence of a downstream row.

Note that these results have been obtained from *CFD* calculations presenting an under-evaluation of the losses in comparison with the experimental results (see Appendix: The numerical simulations). Therefore the numerical estimation of the losses produced by the *RSI* gives only an order of magnitude.

IV.7 Conclusion

In this chapter, the flow developing in the multistage compressor CREATE has been investigated at stable operating points by means of high-frequency measurements of wall static pressure, total pressure and velocity. This study has especially focused on the unsteadiness of the flow produced by the successive rows. Therefore, it has been experimentally shown that the unsteadiness as well as the losses tend to increase when going towards the rear part of the machine. Indeed, the measurements showed that the flow features induced by each row interact with the other rows when travelling downstream, increasing the complexity of the flow. Overall, the flow of the multistage compressor CREATE has been found strongly affected by the rotor-stator interactions, especially at the tip of the rotors. All the aerodynamic perturbations emitted by the rows can interact and produce *RSI*: in CREATE, the interactions involving the wakes of successive rows have been found to be the strongest.

In order to study the interactions in CREATE, a modal approach has then been used to describe the static and total pressure fields in the whole machine, as these aerodynamic quantities are very sensitive to the *RSI*. A modal decomposition method has therefore been presented and applied to the experimental results. It showed that three main types of interaction were responsible for the majority of the pressure interactions: *"S-R"*, *"RR-S"* and *"3R-S"*. Whereas the two first interactions only involve wakes, the third is produced by wakes and potential effects. This result is of particular

interest for some *CFD* codes like *HBT*, as it allows to reduce the pressure field in CREATE to the direct contributions of the rows plus these three interactions.

After a description of these three interactions, an evaluation of their impact in term of losses in the machine has been done through the modal analysis of the entropy field in the machine, taken from *CFD* calculations. This showed that the *RSI* are responsible for around 5 % to 10 % of the entropy production in the machine, the interaction *"S-R"* being largely predominant over the other interactions.

After this analysis of the flow in CREATE at stable operating points, the next chapter will focus on the instabilities arising in the compressor at low mass flow rates.

Chapter V
Study of the instabilities arising in CREATE at low mass flow rates

V.1 Introduction

After the study of the flow at stable operating points, this chapter will focus on the instabilities arising in CREATE when going towards the surge line. In the literature, most of the experimental studies of rotating stall and surge are achieved on low-speed compressors. The lack of detailed data concerning high-speed multistage compressors can be explained firstly by the difficulties and the risks to acquire some data close to the surge line, as the instabilities can be very damaging for the machines, secondly by the needed specific instrumentation and thirdly by the operating cost of high power rigs. The originality of the present work is to provide an experimental study of the instabilities in a high-speed compressor representative of a real high-pressure compressor of a modern turbojet engine.

This chapter will focus on two different studies. The first part will be devoted to the study of surge precursors in CREATE, as some instabilities have been found well before the flow breakdown: the determination of the nature of these precursors and the understanding of the mechanisms responsible for their onset will be a matter of concern. In the second part, detailed measurements of the surge transient will be provided in order to precisely describe the mechanism of flow breakdown in CREATE. An anti-surge control system based on the detection of the precursors will finally be presented.

V.2 Observations of the flow just before surge

During the experimental campaign, several entrances into surge have been achieved with this compressor. The procedure was to decrease the mass flow to *NS* operating point, and then to carefully throttle the machine until it surges. It was generally achieved in about two minutes. For each recording, strong oscillations appeared in the wall static pressure signals many seconds before surge, i.e. hundreds of revolutions of the compressor shaft before surge. The pressure signals of the six sensors uniformly distributed around the annulus in section 27A, downstream of rotor 2 are presented in Figure 104 a few rotor revolutions before surge. This section has been chosen as it is where these six pressure signals better exhibit the entrance into surge although the oscillations were always the most intense in section 280, upstream of rotor 3. In Figure 104, the growing of a full span-cell is visible from revolution 3 to 5. Its rotation speed which has been geometrically determined is of 62 % of the shaft speed. In less than two rotations the size of this full-span stall cell reaches the

whole circumference of the compressor and brings the machine to surge. A similar full-span cell appeared in every surge recordings.
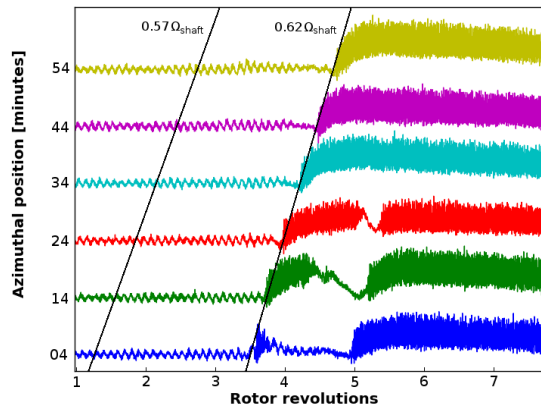
Figure 104 Wall static pressure measurements a few revolutions before surge - section 27A (downstream of rotor 2).
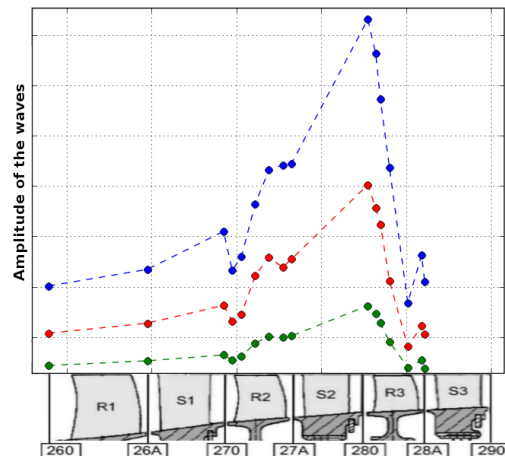
Figure 105 Axil distribution of the amplitude of the oscillations at three different times near surge.

The oscillations, which are rotating pressure waves, induced the onset of a frequency of around 2 kHz in the pressure spectra. The origin of the waves has been under debate for a long time. Figure 105 shows the axial distribution of the amplitude of the oscillations, at different times of a same surge recording. To build this figure, the amplitude of the frequency induced by the oscillations has been taken from a Fourier transform of the pressure signals over a few revolutions: the higher the amplitude is, the closer the machine was to surge (the blue plot corresponds to a few revolutions before surge). It is worth noticing the homothetic shape of the distribution: rigorously the same evolution of amplitude has been found for all the surge recordings. The most important information given by Figure 105 is that the phenomenon is very confined: a sharp maximum of intensity is indeed visible just upstream of rotor 3. It decreases smoothly when going towards the inlet of the machine. On the contrary, a sharp decrease is visible through rotor 3.

From these observations, the hypothesis of a modal-type inception of surge can be rejected. Indeed, the frequency of the waves is far too high: the typical period of modal oscillations is three to five rotor revolutions [30] and in our case, more than ten oscillations are visible per rotor revolution. Then, the axial distribution of the amplitude of the oscillations has a strong maximum in the last stage and the phenomenon does not affect equally the whole machine, contrary to a modal inception which is a system-instability, see chapter I.3.1.2. The first thoughts were in fact that the oscillations were produced by small part-span rotating stall cells. In the works of Day *et al.* (1999, [20]) such a multi-cell rotating stall pattern with more than ten stall cells had indeed already been observed in comparable compressors from SNECMA. A discussion on the nature of the oscillations will be proposed in chapter V.4.3.

The azimuthal mode order and rotation speed of the rotating pressure waves have been geometrically determined using the pressure traces of section 280, where the amplitude of the oscillations was the highest (see the oblique line labeled "0.57 Ω_{shaft}" in Figure 104). The method consisted in plotting a line that connects the humps of the oscillations of the signals using a least-squares algorithm: the six signals produced by the sensors located in the inter-row section, plus one located at the tip of the neighboring rotor at the azimuthal position of 58 minutes (not

presented here in a matter of clarity), in order to have sensors unequally spaced around the circumference. As there is a small axial shift between the first 6 sensors of the inter-row section and the last one at the tip of the rotor, a small axial phase shift existed and led to uncertainties in the determination of the rotation speed, giving two possible solutions: $1.72 \times \Omega_{shaft}$ and $0.57 \times \Omega_{shaft}$. By using the signals of the twelve sensors located in the removable block (see chapter III.3.3), only waves spinning at 57% of Ω_{shaft} gave coherent results (this will be more detailed in chapter V.4.1). Moreover, the full-span cell which arises at revolution 3.6 in Figure 104 rotates at 62% of Ω_{shaft} when it appears: the close values of the rotation speed of the oscillations and of the full span cell is another confirmation of the rotation speed of the waves. Indeed, the pressure waves could be the cause of rotating stall by inducing strong pressure fluctuations leading to separations at the leading edges of the last rotor, where the phenomenon is the strongest. This seems to be a valid supposition which will be confirmed in chapter V.4.2. Note that the slight acceleration of the full-span cell regarding to the waves can be explained as it grows azimuthally when propagating from a sensor to another. The frequencies of the shaft and of the waves being of 194 Hz and 1989 Hz respectively, each probe detects 10.25 instabilities during one rotor revolution. With the help of equation (V-1), the azimuthal mode order m of the instabilities has been determined and found equal to 18.

$$m = \frac{F_m}{F_{shaft}} \cdot \frac{\Omega_{shaft}}{\Omega_m} \qquad\qquad (V\text{-}1)$$

With m the azimuthal mode order, F_m the frequency of the waves and Ω_m their rotation speed. It is important to mention that the rotating pressure waves always preceded surge in all the recordings, but with a non-constant mode order which could either be 17, 18 or 19 (in the cases of 17 and 19, the frequency arising in the spectra is respectively 1.8 kHz and 2.2 kHz). Each single mode has been found to rigorously rotate at the same speed all along the machine, for all the recordings. The different rotation speeds of each mode are listed in Table 23. Note that, two frequencies could arise in the spectra at the same time, i.e. two pressure modes could appear simultaneously.

Azimuthal mode order	Rotation speed (xΩ_{shaft})
17	0.556
18	0.570
19	0.591

Table 23 Rotation speeds of the pressure waves

V.3 Behaviour of the pressure waves over the operating range of the compressor

V.3.1 Spectral investigation at different mass flows

In order to find and understand the origin of the rotating waves, the spectra of the pressure signals of the sensors located in section 280 (upstream of rotor 3) have been investigated along the compressor operating range. As all the sensors located in this section present very similar results, all the results will be plotted in the further paragraph using one of the six sensors, arbitrary chosen in

section 280. Moreover, in a matter of clarity, the frequencies in the spectra presented will be non-dimensionalized by the shaft frequency.

Figure 107 shows the spectra of this sensor acquired over 200 rotor revolutions at operating points *a*, *b*, *c, d* and *e* defined in Figure 106 (*a*, *b, d* and *e* correspond to *PE*, *L, SM* and *NS* operating points respectively). The spectra are centered on 2 kHz, i.e. ten times the rotor frequency, around the frequencies of the pressure waves.

At operating point *a*, the three peaks already present are multiples of the shaft frequency (labeled "*rotor harmonics*" in the figure), they can be found in the four spectra and are of no interest. At operating point *b*, four very weak peaks appear at the low frequencies: $F_{17} = 9.4$ (1830 Hz), $F_{18} = 10.23$ (1990 Hz), $F_{19} = 11.15$ (2170 Hz) and $F_{20} = 11.97$ (2330 Hz), the *BPF* of rotor 3 being 80 (15.5 kHz). These frequencies are not harmonically related to the rotor frequency. Three of them (F_{17}, F_{18} and F_{19}) are these linked to the rotating waves detected just before surge: the application of relation (V-1) leads to azimuthal mode orders of respectively 17, 18, 19 and 20. When reducing the mass flow (operating points *b* to *d*), the amplitudes of the peaks increase, but remain very weak: at point *d*, the amplitude of the strongest peak remains below 3% of the amplitude of the *BPF*.

Because the first signs of the low frequencies appear far for the surge line, an attempt to identify the pressure waves to the rotating instabilities of Mailach *et al.* [51] has been done. However, the signatures of the phenomena are different: indeed, Mailach *et al.* observed a low frequency hump in their pressure spectra due to the random changes of azimuthal number of "rotating instabilities", see chapter I.3.2. In our case, only four *'stable'* modes develop, as demonstrated by the presence of the four discrete low frequency peaks. When the compressor is throttled to point *e*, the amplitude of one or two frequencies (so far F_{17}, F_{18} or F_{19}) suddenly increases and starts to behave chaotically. Note that regarding to the time scale of most of aerodynamic phenomena occurring in high speed machines, the evolution of the pressure waves is very smooth as it is done over hundreds of rotor revolutions. The spectrum at operating point *e* of Figure 107 corresponds to the beginning of the last measurement before the machine exhibits full span rotating stall and finally enters into surge: the compressor has indeed been brought to this operating point until it fell alone into surge about two minutes later. F_{17} and F_{18} are clearly visible, with amplitudes of respectively 11% and 30% of the rotor 3 *BPF*. Note that at this location (upstream of rotor 3), the influence of rotor 1 is still important.
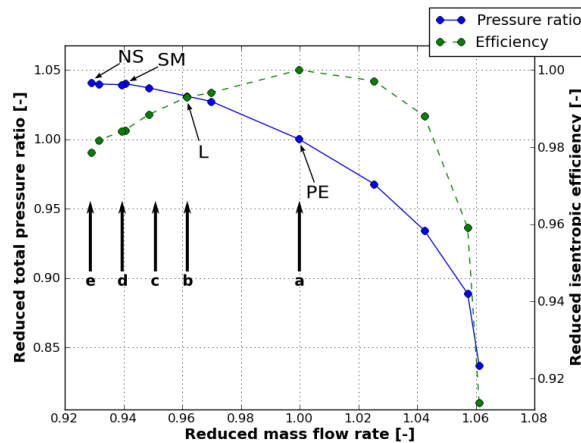
Figure 106 Investigated operating points *a, b, c,d, e*
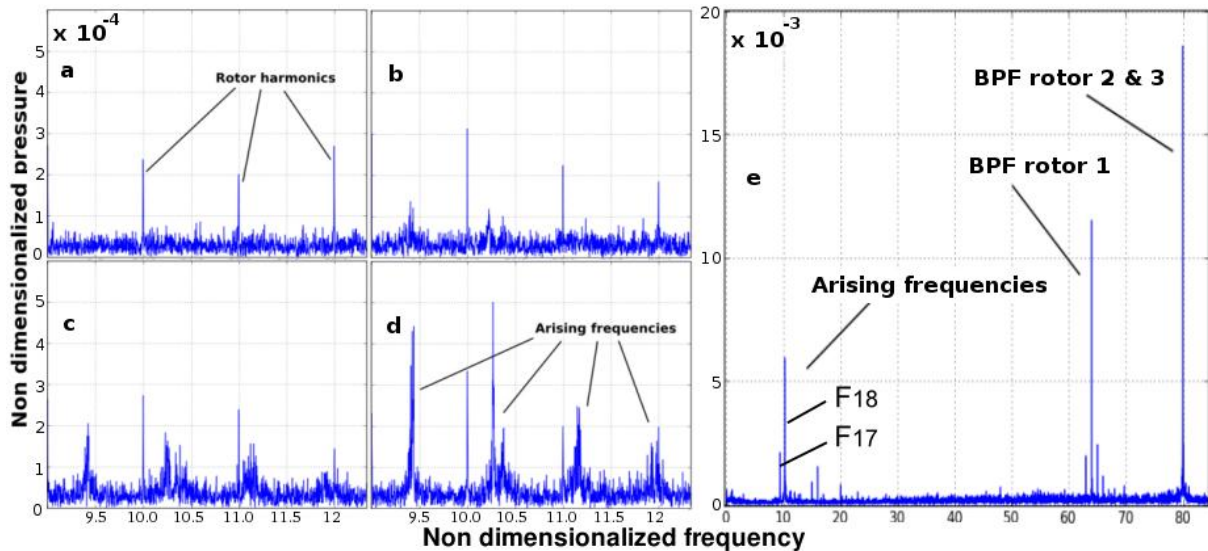
Figure 107 Wall static pressure spectra at operating points *a*, *b*, *c,d*, *e* - section 280

V.3.2 Behaviour of the pressure waves just before surge

Figure 108 shows temporal traces of the amplitudes of F_{18} and the *BPF* of rotor 3 in section 280 at operating point *e*, one minute before surge. The calculation of the amplitude of the frequencies has been achieved with a windowed Fourier transform: the length of the window was set to thirty-two rotor revolutions and bounded by a Hamming filter, (see chapter III.7.4). An overlap of four rotor revolutions has been fixed between each successive temporal window. The curves plotted in this figure have been obtained by averaging the results of the six sensors in this section. The trace of the *BPF* allows a comparison between the amplitudes of the stable features of the flow and of the pressure waves.

Although the amplitude of the *BPF* remains roughly constant over time, that of F_{18} varies a lot and alternates between phases of strong increase and decrease. At $t = 0$ s, the amplitude of the rotating pressure waves is less than half the amplitude of the *BPF*. At $t = 12.5$ s, $t = 18$ s, $t = 29$ s and $t = 61.5$ s, the amplitude of F_{18} exceeds that of the *BPF* but the pressure waves are finally damped: that means that the pressure fluctuations induced by the waves at casing upstream of the third rotor are stronger than those produced by the first harmonic of the rotors! While the amplitude of the waves remains under a critical value, the machine keeps running in a pseudo-stable state: it can last a very long time without falling into surge if the system is no more loaded.

From $t = 52$ s to $t = 60$ s, the throttling valve is operated (four small impulsions visible in the figure). Each impulsion is immediately followed by an increase in the amplitude of F_{18}. In the zoom at the right part of the figure, four high oscillations of its amplitude occur just before the compressor surges. At this time, the "*chaotic phase*" begins, and the pressure waves are no more damped. Their amplitude keeps increasing: at $t=66$ s, the pressure fluctuations induce a separation at the tip of rotor 3 and a full span-cell appears, which brings the compressor to surge within a few revolutions. No link between the frequency of the four oscillations and characteristic frequencies of the machine (measured period of the surge cycle or calculated Helmotz resonating frequency of the system, for

example) has been established so far: indeed, depending of the surge recordings, the behaviour of the amplitude of the oscillation could be very different. More details will be provided in chapter 0.
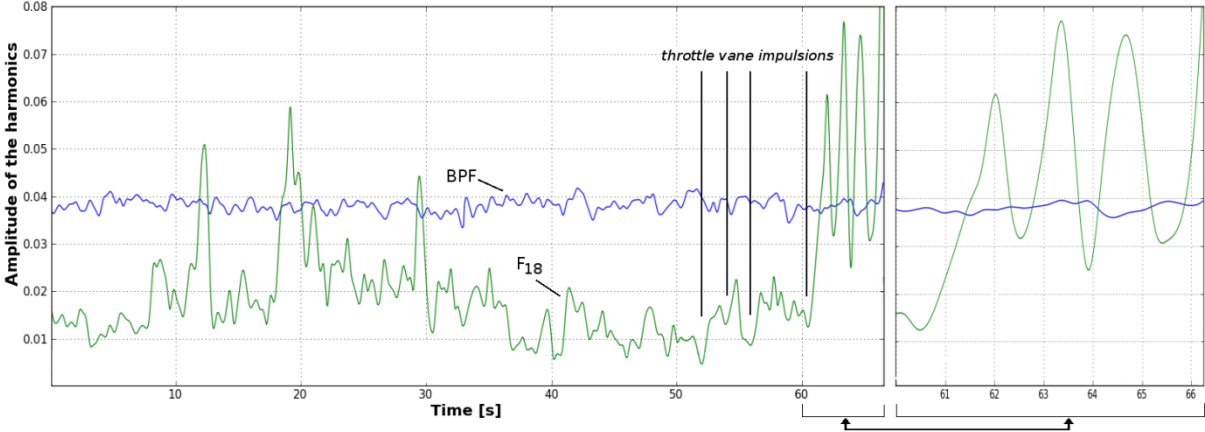
Figure 108 Temporal evolution of the amplitudes of the pressure harmonics (F_{18} and *BPF*), a few seconds before surge inception – section 280.

V.3.3 Influence of the machine rotation speed

In order to evaluate the influence of the machine rotation speed on the pressure waves, the operating point *d* has been investigated over the speed range [99.6%-101.5%]x *Nn*. Four spectra centered on the frequencies of the pressure waves are presented in Figure 109. They have been calculated the same way as for Figure 107.
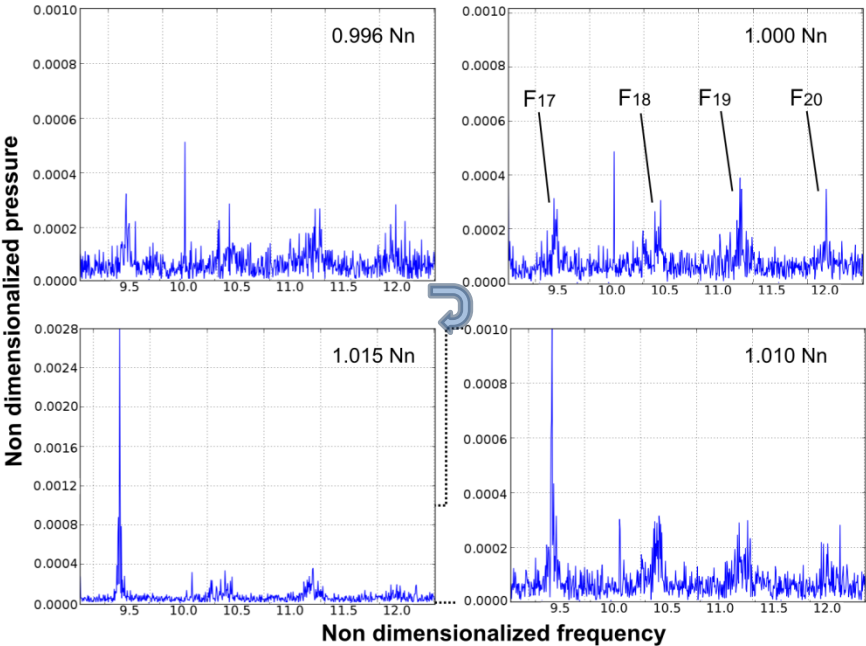
Figure 109 Evolution of the amplitude of the pressure waves with the machine rotation speed

It is visible that the rotation speed has a strong influence on the waves. An increase in the amplitude of F_{17} is indeed visible when the rotation speed is increased: at 101.5%, the amplitude of F_{17} reaches around thirty times its value at Nn. The compressor would have certainly surged if the speed had been more increased. Note that no investigation has been done at upper speed, to avoid reaching the maximum authorized speed of CREATE. When the speed is lowered, the amplitude of the frequencies decreases. The first signs of decrease are observable at 99.6% of nominal speed. In other surge recordings done at 95% of nominal speed (not presented here), the compressor surged without exhibiting any signs of pressure waves. Thus, it seems that the pressure waves only appear in a very narrow speed range around nominal speed.

V.3.4 Conclusion

Overall, it has been shown in this chapter that evidences of the pressure waves can be found far from the surge line, at stabilized operating points: weak peaks in the pressure spectra are indeed visible right from *Loaded* operating point. When the load of the compressor is increased, one or two spinning pressure modes suddenly grow in amplitude and finally provoke the onset of a stall cell. The pressure waves only appear before surge in a narrow speed range around nominal speed. The determination of the true nature of the pressure waves is the subject of the next chapter.

V.4 Origins of the pressure waves

The main characteristics of the pressure waves arising in the flow when approaching the surge line have been described previously. This chapter focuses on the determination of the nature of the waves. Indeed many types of instabilities can arise in a compressor at near surge operating points, like rotating stall or rotating instabilities for example. Our investigation will be down through a description of the flow while exhibiting strong pressure waves, which will be followed by a discussion on the different possible sources of instabilities.

V.4.1 Visualization of the pressure waves

In order to observe the pressure waves, the wall static pressure field has been investigated above the third rotor just before surge. Thus, a removable block equipped with twelve pressure sensors has been used, allowing to spatially describe the flow over the blades length axially and over 9° azimuthally, see Figure 45. However, contrary to the stable pressure measurements presented in Chapter III, the observed phenomena were transient and highly fluctuating with time. Therefore, no ensemble average could be done in order to reconstruct the flow field over the spatial period of CREATE using the casing moving rings. Thus, instantaneous space-time diagrams (visible on Figure 111 and Figure 112) have been constructed from the temporal traces of the pressure sensors to be sure to capture any transient phenomenon passing in front of them.

Figure 110 illustrates the post-processing method used to build the instantaneous space-time diagrams. In a matter of clarity, only six sensors (out of twelve) are represented in the removable

block. To build the diagrams, the temporal signals of the sensors are taken over a given temporal range (one rotor revolution in the case of Figure 111). The signals obtained at different axial positions are then put together to build the maps: this is possible because all the signals are acquired at the same time. Hence, it is important to notice that the abscissa of the diagrams is time and not azimuthal position, see Figure 111 and Figure 112. However, because of the azimuthal shift between the different rows of sensors in the block, a time lag exists between the sensors, see Figure 110. The time lag ΔT between two angular positions spaced of Δθ of a phenomenon spinning at the angular frequency Ω can be calculated with:

$$\Delta T = \frac{\Delta \theta}{\Omega} \qquad \text{(V-2)}$$

To compensate the time lag, each temporal signal is thus separated on two frequency bands by numeric filters. The first band is restricted to [1.8 kHz - 2.2 kHz] which corresponds to the frequency range of the pressure waves which rotate at 0.57 Ω_{shaft}. The second frequency band corresponds to the rest of the spectrum, i.e. to the deterministic flow plus its random part. In a first approximation, as the measurements were performed above the third rotor, it has been considered that the whole deterministic flow rotates at the rotor speed Ω_{shaft}. This approximation is inexact because the flow features produced by the rotor-stator interactions spin at different speeds, as previously seen in chapter IV.5. However as the observations done in the diagram are only qualitative, the *RSI* have been neglected. After the time-lag compensation of each frequency band, the signal is finally recomposed. Note that the use of this method confirmed the rotation speed of the waves determined in chapter V.2, as any other rotation speed used for the waves instead of 0.57Ω_{shaft} produced distorted diagrams.
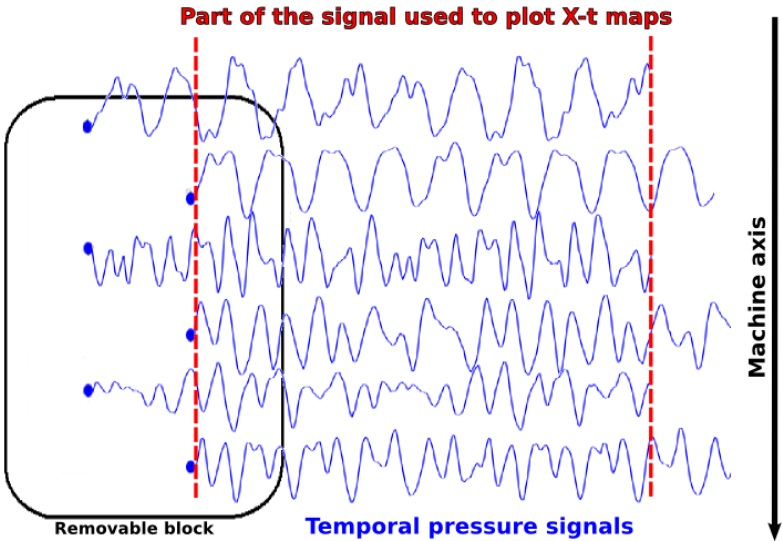
Figure 110 Sketch of the post-processing method for the construction of space-time diagrams

Figure 111 shows an instantaneous space-time diagram of the pressure field above rotor 3 over one rotor revolution just before surge. Along the abscissa, the blades travel from left to right but the time goes from right to left. During this recording, the azimuthal mode order of the pressure waves was 18: only 10.25 patterns appear over one rotor revolution as the abscissa is time and not

space (note that on the figure, only 10 patterns are visible as the post-treatment presented in Figure 110 does not take the integrality of the signals because of the time lag). They are very regularly spaced and always extend over eight blade passages. This confirms the stability of the phenomenon, which can last for various seconds. Figure 112 is a zoom over one period of the pressure waves. The pressure waves are clearly visible, as they induce an alternation of high and low pressure regions visible between blade 4 and 7, and blade 7 and 12 respectively. It can be seen that the instabilities do not change the stable features of the flow and only produce a modulation. This modulation appears to be much higher close to the leading edges of the blades (where the high values of the pressure gradient between the pressure and the suction sides occur). This is consistent with the axial distribution of the amplitude of F_{18} presented in Figure 105.
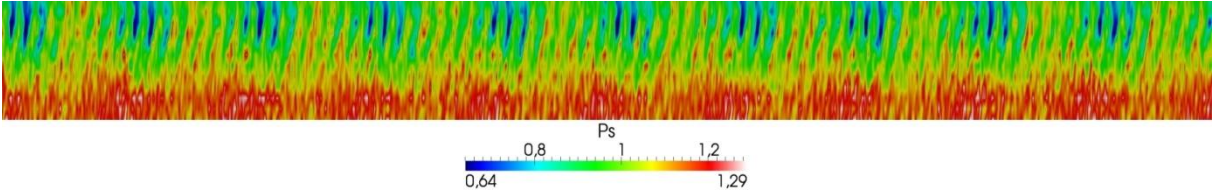
Figure 111 Global view of the pressure field affected by rotating pressure waves over one rotor revolution – rotor 3
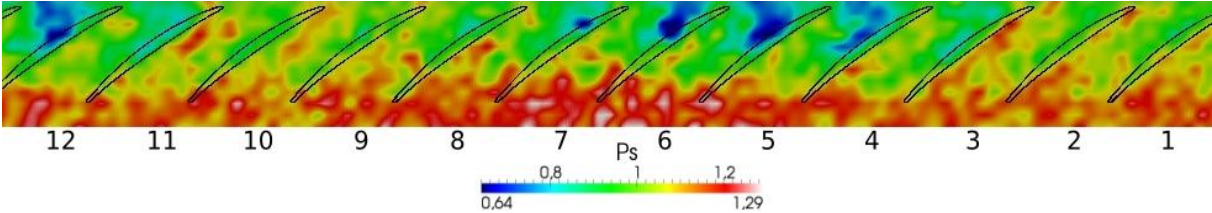
Figure 112 Zoom of the pressure field over one pressure wave – rotor 3

V.4.2 Ensemble averages phase-locked to the waves

In order to determine if the pressure waves induce separations in the third rotor, the pressure field phase-locked to the waves and the corresponding standard deviation have been calculated in rotor 3, for different operating points. For each pressure sensor of the removable block, the temporal signal has been acquired during 51 revolutions (this represents roughly 524 passages of cells) and averaged over two temporal periods of the cells. The standard-deviation to the ensemble-average has also been calculated. It highlights the intensity of all the phenomena not phased with the cells, such as the aerodynamic structures linked to the blades periodicity (which rotate at a different speed than the cells!) or the turbulence.

Figure 113 shows the ensemble-average (left, the mean-value has been removed) and standard-deviation (right) of pressure phase-locked to the cells for three sensors labeled *a*, *b* and *c*, located in section 280, at the front part of the blades of rotor 3 and at their trailing edges respectively (the axial position of the sensors is visible in Figure 114, commented later, the positions 0 and 1 corresponding to the sections 280 and 28A respectively). Three operating points are presented: *SM*, *NS* and a few revolutions before surge (labeled '*FRBS*'). The amplitude of the pressure

waves is obviously the highest for the *FRBS* point: at *SN* and *SM*, the amplitude is only of 21.8 % and 3.9 % respectively of the value at *FRBS*, this repartition being valid for each sensor (remember the homothetic distribution of the amplitude of the waves presented in Figure 105).

For every operating point, the highest amplitude is found in section 280 (sensor *a*): in the top-left subplot of Figure 113, the ensemble average at *FRBS* point shows perfectly the oscillations of pressure induced by the waves. At *NS*, the oscillations are still detectable but are very weak. At *SM*, the waves disappear almost completely (the phase-locking is then done on a signal filtered on a very narrow frequency range), and the signal looks like a white noise, as no phenomenon phase-locked to the cells appears. When going downstream in the blade, at the position of sensors *b* and *c*, the amplitude of the oscillations decreases for *FRBS*, which is consistent with Figure 105. Note that the waves are phase shifted when going downstream as all the averages have been done phase-locked to the same sensor *a.* This shift is clearly visible between the front and rear parts of the blades on Figure 112.

The standard deviation is plotted for the three sensors on the right side of the figure: for each location, the mean value of the *SM* operating point has been removed to the three points, in order to compare the different signals taking *SM* as reference. Note that the standard deviation shows very similar values between *PE* and *SM* (not shown here). For each sensor, the standard-deviation of *SM* and *NS* has a flat temporal evolution and comparable values. Indeed, no increase of the random unsteadiness linked to the pressure waves is observed. However, for *FRBS* point, fluctuations of standard-deviation appear. They are induced by some random unsteadiness phase-locked to the waves. The shape of these signals will be discussed later.

In order to have a global view of the standard deviation, the left subplot of Figure 114 shows the axial evolution of the mean value of the standard deviation of pressure for all the sensors above rotor 3. The axial position has been normalized, 0 and 1 correspond to section 280 and section 28A respectively. The leading edge (*LE*) and trailing edge (*TE*) of rotor 3 have also been indicated. The location of the three sensors *a*, *b* and *c* are indicated. The shapes of the three curves are very similar and have very comparable values: indeed, the main part of the standard-deviation is induced by the deterministic flow, not phased with the waves. Therefore, the big hump visible just downstream of *LE* comes from the strong pressure gradients found in the front part of the blades. For the *FRBS* point, two things can be noticed: first the maximum of the standard deviation is located a bit downstream, and second there is an increase in the standard deviation close to the trailing edges.

Hence, on the right side of Figure 114, the standard-deviation to the standard-deviation of pressure has been plotted in order to quantify the amplitude of the fluctuations of the temporal evolutions of standard deviation visible in Figure 113, i.e. the amplitude of the humps of the signals in the right subplot. In other word, this allows to remove the influence of the deterministic flow, in order to capture any increase of random unsteadiness produced by the pressure waves. In section 280 (sensor *a*), the fluctuations of standard-deviation are three times higher for *FRBS* point than for *SM* and *NS*. Indeed, on Figure 113, four humps appear in the standard-deviation signal of sensor *a* for *FRBS* point. Their maxima are encountered at the same temporal locations as the maxima and minima of the ensemble average. Indeed, at this operating point, the amplitude of the pressure waves strongly fluctuates: it is the chaotic phase described in chapter V.3.2.

On Figure 114, an increase in the fluctuations of standard deviation is observed at the front part of the blade for *SM* and *NS* points. The fluctuations double in intensity between the sensors *a*

and *b*: in Figure 113, even if the shapes of standard deviation remain flat for these two operating points, the fluctuations at sensor *b* are clearly stronger. Indeed, the *TCF* found at the front part of rotor 3 induce an increase of random unsteadiness not phase-locked to the waves. For *FRBS* point, the increase of fluctuations in Figure 114 is even stronger, and their amplitude triples between the sensors *a* and *b*. For sensor *b*, two very strong humps appear in the temporal distributions of standard-deviation. Their maxima coincide with the minima of ensemble average. That means that the random unsteadiness increases a lot in the low-pressure zones induced by the waves (leading edge of the blades of passages 4 to 7 in Figure 112). A possible explanation could be that the low pressure induced by the waves strongly increases the pressure gradient between the pressure and the suction sides (possible effects on the angle of attack), which is very visible in Figure 112. The intensity of the *TCF* is then increased, so does the random unsteadiness associated to it. Therefore, the *TCF* could be perturbed intermittently by the waves, this being a strong cause of losses, blockage and, at the end, instability for the machine.
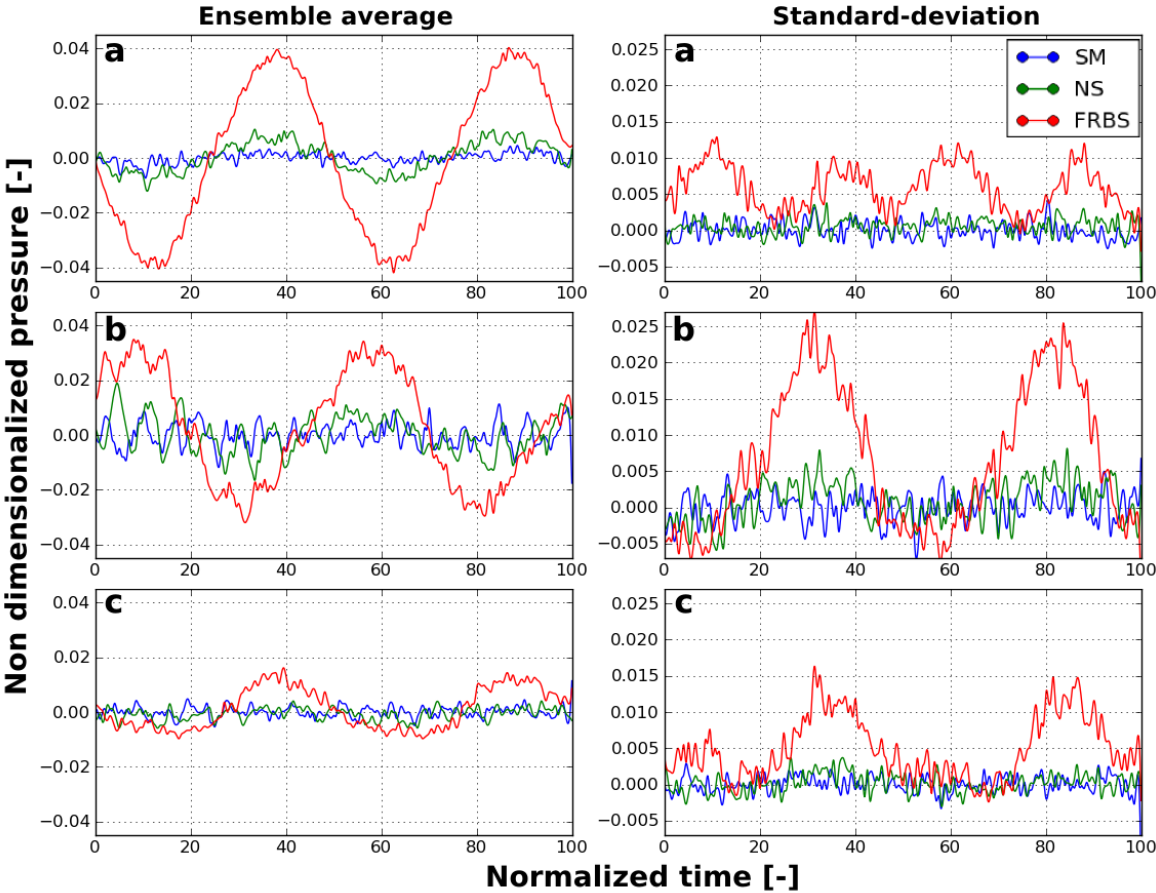
Figure 113 Ensemble average and standard deviation of pressure phase-locked to the pressure waves at three locations above rotor 3

When going towards the rear part of the rotor, the amplitude of the fluctuations of standard-deviation decreases, so as to reach comparable values to section 280 at *SM* and *NS* points. Even smaller values are reached at *FRBS* point between axial position 0.6 and 0.7: they are comparable to *SM* and *NS* points, which means that no random unsteadiness at all is produced by the pressure waves. However, the amplitude of the fluctuations increases again at *FRBS* point at the rear part of

the rotor (as already mentioned), and reaches its maximum at the trailing edge of the blades (sensor *c*). The temporal evolution of the standard deviation for sensor *c* is very interesting. It shows two hump for *FRBS* point, whose maxima correspond to the maxima of ensemble averaged pressure. In this case, this increase of random unsteadiness could be produced by separations appearing at the trailing edge of the blades, the reverse flow impinging the blades causing the increases in the pressure visible at the rear part of the blades in Figure 112 in the passages 6 and 7.
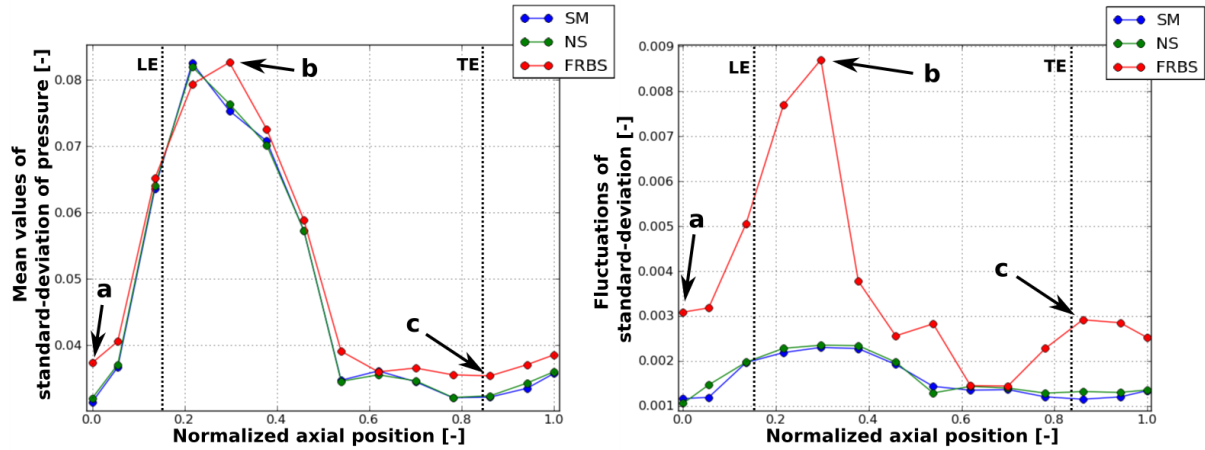
Figure 114 Axial evolution of the standard-deviation (mean value and fluctuations) of wall static pressure above the third rotor at three operating points

Overall, the waves seem to have a strong influence on the flow at the tip or rotor 3. They apparently produce an intermittent increase of the random unsteadiness of the *TCF* at the front part of the blades. Moreover, these waves seem to induce some flow separations linked at the trailing part of the blades. In the next chapter, the real nature of these waves will be discussed.

V.4.3 Discussion on the nature of the pressure waves

This discussion is made around the analysis of two main parameters: the temporal and spatial localizations and the structure of the pressure waves. It can be read in the literature (see the discussion of [51] with N. A. Cumpsty) that the stall of one rear stage in a high-speed multi-stage axial compressor is possible as the first stages maintain the machine stable, as observed by Day et al [20] in a compressor similar to CREATE. Nevertheless, the first signs of the pressure waves seem to appear far too early to be produced by rotating stall (*Loaded* operating point, i.e. 63% of the operating range). Then, the smooth decrease in the amplitude of the phenomenon towards the inlet could indicate the up going potential effect produced by the blockage of the cells. However, the decrease in the amplitude through rotor 3 seems too sharp to be produced by part-span stall cells, which would strongly affect the flow at the rear part of the blades and downstream of the rotor, see Figure 105. Note that the separations observed in the previous chapter at the trailing edges are more likely to be a consequence of the pressure waves than a cause: in case of rotating stall, it would be the opposite. Finally, as additional remark, no alignment of the tip leakage vortex on the blades leading edges has been observed at *SM* operating point (see chapter IV.3.2.2). It has therefore been assumed that no alignment occurs at *NS* operating point. Note that the latest researches of Pullan *et al.* [72]

and Weichert and Day [83] showed that the alignment of the *TCV* was not necessarily a cause of rotating stall.

The leading edge separation vortices described by Inoue *et al.* [40] could fit the temporal and spatial localizations. They showed indeed that the influence of this type of instabilities is very localized upstream of the affected rotor and can last indefinitely if the compressor is no more throttled. However an important difference comes from the deterministic nature of the phenomena observed in our machine: the modulation of the flow appears to be very regular. Only discrete peaks indeed appear in the pressure spectra, instead of a low frequency hump produced by random separation vortices. This regularity seems incompatible with the random propagation mechanism described by Inoue *et al*, see chapter I.3.2*.*

A last phenomenon which could fit with the observations in CREATE is acoustic resonance, as already observed by Hellmich and Seume [36] in a high-speed multistage compressor. They showed indeed that some discrete frequencies could be excited in the pressure spectra of a machine under particular near surge conditions, these frequencies being produced by acoustic waves modulating the flow field in the machine. The exponential shape of the distribution of the intensity of the pressure waves could be compatible with such a phenomenon. Acoustic resonance could moreover explain the very smooth evolution of the pressure waves in the compressor when going towards the surge line, as the evolution of the phenomenon depends on the global conditions of mean flow and not on the fast unsteady aerodynamic structures of the flow (like blockages or separations).

In the next chapter, after a short bibliographic review, it will be shown that the pressure waves observed in CREATE are effectively induced by acoustic resonance. A model will be developed to explain the experimental results and try to understand the mechanisms responsible for the resonance.

V.5 Acoustic study of CREATE

V.5.1 Acoustic resonance in aerodynamic compressors

Under specific flow conditions, and generally at low mass flow rates, compressors can also face acoustic resonance (*AR*). Discrete sharp peaks are then visible in the pressure spectra, the resonance frequencies being generally non-harmonic with the shaft frequency. If the mass flow is too reduced, *AR* can trigger rotating stall or surge. This phenomenon is very well described by Hellmich and Seume [36] in a high-speed 4-stages compressor. The authors explain that compressors can sometimes behave like acoustic resonators: unlike the aerodynamic instabilities as rotating stall or rotating instabilities, the acoustic resonance phenomenon must be explained by an acoustic approach. They provide a complete literature review showing many cases of real compressors exhibiting *AR*, like Kameier [46] with Rolls Royce engines, Camp in a low-speed compressor [11] or Ziada *et al.* in a 35-MW multistage radial compressor [91]. For all these cases, *AR* was visible through nonsynchronous pressure fluctuations at discrete frequencies. The authors conclude their review saying that in most cases, vortex shedding is assumed to be the excitation source of the resonance.

In the aero-acoustics theory, ducts (with or without flow) can be considered as high-pass filters for rotating acoustic waves [75]. Indeed, considering a propagating wave with *m* azimuthal lobes spinning at a frequency *f*, a cut-off frequency depending on the number of lobes can be defined for the duct: if *f* is higher than the cut-off frequency, the mode is called "cut-on" and can propagate normally. Otherwise, it is called cut-off and its amplitude decays exponentially along the duct. Under specific conditions, compressors can behave as resonant cavities. However, the physics behind this phenomenon is much more complex than resonance in simple ducts. Indeed, the non-uniformity of the flow (mainly due to swirl), the reflection and transmission of the acoustic waves at the blade rows and the variation of the duct cross section, have significant impact on the resonance.

In 2008, Hellmich and Seume [36] presented a review of the researches done since the 1960s on acoustic resonance in compressors which can be summarized as follow:

- Reflection at the rows interfaces only occurs when the acoustic waves hit the blades under high incidence.

- Mode scattering and mode trapping between the blades (Parker's resonance) only occur for wavelengths of the magnitude of the blade pitch.

- The influence of swirl on modes with frequencies far above the rotor speed is weak, and it has only to be considered to evaluate the cut-off conditions.

In the following chapter, a study of the pressure waves arising in CREATE at low mass flow rates will be achieved using an acoustic approach and an acoustic model developed by Hellmich and Seume will be applied to the compressor CREATE.

V.5.2 Aero-acoustics of ducts with flow: application to CREATE

As the test-case presented by Hellmich and Seume is very similar to CREATE, the base hypotheses of their model have been applied to our compressor:

- As the azimuthal mode order of the pressure waves observed in CREATE (lower than 20) is much lower than the number of blades, mode scattering and Parker's resonance can be neglected.

- Then, because the resonance frequencies observed in the machine are around ten times Ω_{shaft}, swirl can only be considered to evaluate the cut-off conditions.

- Finally the pressure field can be modeled in cylindrical coordinates as follows:

$$p_{m,n}(x,r,\theta,t) = f(k_{r,m,n}r) \cdot \left(B_1 e^{(im\theta)} + B_2 e^{(-im\theta)}\right) e^{i(k_x x - \omega t)} \tag{V-3}$$

With x the axial coordinate, $f(k_{r,m,n}.r)$ the pressure distribution in the (r,θ) planes, k the wave number and ω the angular frequency. B_1 and B_2 are simple scaling factors. $k_{r,m,n}$ is the eigenvalue of the duct: it depends on the hub ratio and on circumferential and radial mode orders (m,n) of the acoustic wave. It is the nth solution of equation (V-4) hereafter, involving the Bessel functions of first and second order J_n and Y_n [75].

$$\left(Y_{m-1}(kR_{hub}) - Y_{m+1}(kR_{hub})\right)\left(J_{m-1}(kR_{shroud}) - J_{m+1}(kR_{shroud})\right)$$
$$-\left(Y_{m-1}(kR_{shroud}) - Y_{m+1}(kR_{shroud})\right)\left(J_{m-1}(kR_{hub}) - J_{m+1}(kR_{hub})\right) = 0 \tag{V-4}$$

Figure 115 shows the evolution of $k_{r,m,n}$ normalized to the outer radius ($k_{r,m,n} \times R_{shroud}$) over the hub ratio ($R_{shroud}/R_{hub}$) for the azimuthal and radial mode orders, [17,18,19] and [0,1] respectively. It clearly shows that the increase in the radial mode order induces an increase in $k_{r,m,n}$ and that the hub ratio has no significant impact between 0.2 and 0.75. The pressure equation (V-3) indicates that the pressure field has a spinning helical structure. To calculate the axial wave number k_z, Hellmich and Seume consider the mean flow as a rigid body and use the Lohmann relation hereafter [50]: for a given free acoustic wave of frequency f, speed c and wave number $k = \frac{2\pi f}{c}$, four sub-modes can be defined, weather they propagate upstream or downstream and spin with or against the swirl, see relation (V-5) hereafter.

$$k_{\pm z \pm \theta} = \frac{\mp M_x\left(k \pm M_\theta k_{r,m,n}\right) + \sqrt{\left(k \pm M_\theta k_{r,m,n}\right)^2 - (1 - M_x^2)k_{r,m,n}^2}}{1 - M_z^2} \tag{V-5}$$

If the mode propagates downstream, the sign before M_x is negative. If the mode spins with the swirl, the signs before the M_ϑ are positive. The value of k where the root of equation (V-5) becomes zero defines the cut-off frequency. In the case of a duct with no mean flow, it corresponds to $k=k_{r,m,n}$: the axial wave number then becomes zero and the acoustic energy of the mode piles up in the duct. That is resonance. In the case of a duct with mean flow, the cut-off frequency is given by relation (V-6).

$$f_{m,n,\pm\theta}^{cut} = \frac{c \cdot k_{r,m,n}}{2\pi}\left(\sqrt{1 - M_x^2} \mp M_\theta\right) \tag{V-6}$$

Spanwise steady pneumatic measurements have only been previously performed at *PE* and *Loaded* operating points for each inter-row section, see chapter III.2: they have been used to determine the mean flow conditions in the whole machine. Unfortunately no measurements were available at *NS* operating point. Figure 116 shows the calculated axial evolution of the cut-off frequencies at casing of an acoustic mode with eighteen azimuthal lobes, at *PE* and *L* operating points. The axial position has been normalized by the extreme positions of the unsteady pressure sensors located just upstream of the first rotor (position 0) and just downstream of the last rotor (position 1). Note that no spanwise unsteady pressure measurements were available to determine the radial evolution of the modes. The hypothesis of a null radial mode order has been made. This hypothesis is corroborated by the fact that a radial mode order set to one or higher values would induce too high values of $k_{r,m,n}$ (see Figure 115), and thus some cut-off frequencies too far from the frequencies observed in CREATE (between 1800Hz and 2200Hz).

The cut-off frequency of a mode only depends on its spinning direction and not on its direction of propagation: higher-frequencies are found for contra-rotating modes, as visible in Figure 116. This is consistent with the experimental observations of pressure waves spinning with swirl, see chapter V.2: the contra-rotating cut-off frequencies are indeed far too high to let contra-rotating modes propagate. The co-rotating frequencies are closer to the measured frequencies, especially behind the rotors: indeed the increase in tangential velocity strongly reduces the cut-off frequencies. Thus, at *Loaded* operating point, the mode 18 can propagate downstream of the first and second rotors. It is

completely cut-off in the last rotor and behind all the stators, which seems incompatible with the experimental observations of the resonance in section 280. However, a decrease in 100 Hz of the cut-off frequencies behind the rotors 2 and 3 is visible between operating points *PE* and *L*: it is not absurd to consider that they keep decreasing when the mass flow is decreased towards *NS* point so as to reach the frequencies observed in the machine: a turning point, i.e. a switch from cut-off to cut-on, could therefore be reached downstream of the rotor 3 (section 28A), as it will be shown in the next chapter. Finally, Figure 117 and Figure 118 show the spanwise evolution of co-rotating and contra-rotating $f_{18,0}^{cut}$ for all the inter-row sections respectively. It can be seen that the radial distributions of the co-rotating cut-off frequencies are quite uniform along the span. Hence, as the frequencies do not change dramatically with radius, the behaviour of the acoustic modes at casing is likely to be representative of what occurs over the whole span.
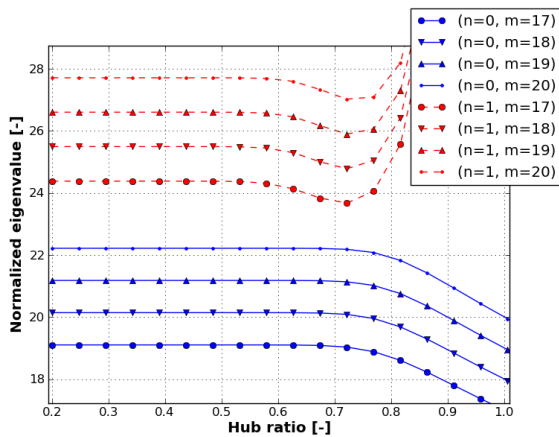
Figure 115 Calculated eigenvalues normalized to outer radius $k_{r,m,n}$ x R_{max} over hub ratio
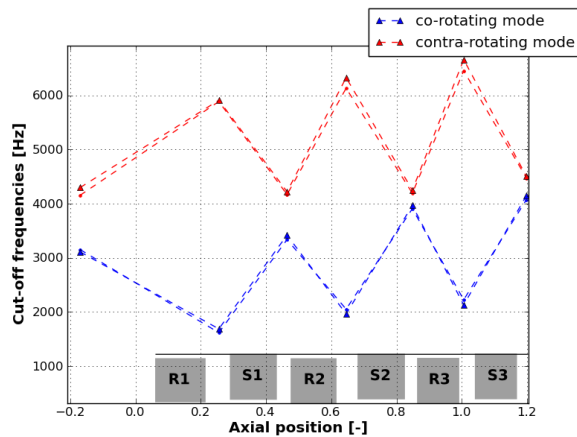
Figure 116 Axial evolution of co-rotating $f_{18,0}^{cut}$ at casing – *PE* and *L* operating points

Overall, the calculation of the cut-off frequencies shows that acoustic resonance could occur near surge behind the rotors, but is insufficient to explain the axial evolution of the amplitude of the pressure waves visible on Figure 105. The study of the propagation of the cut-off modes to understand this evolution is the subject of the next chapter.
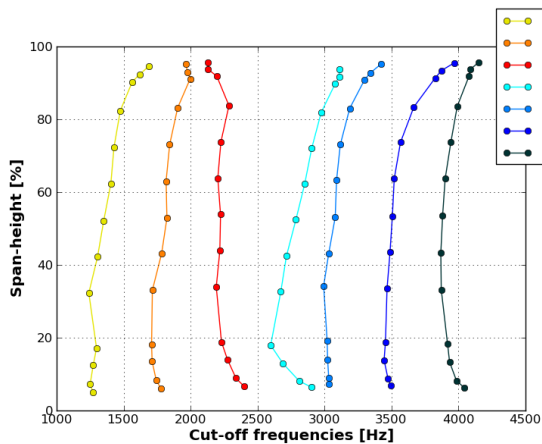
Figure 117 Spanwise evolution of co-rotating $f_{18,0}^{cut}$ – *Loaded* operating point
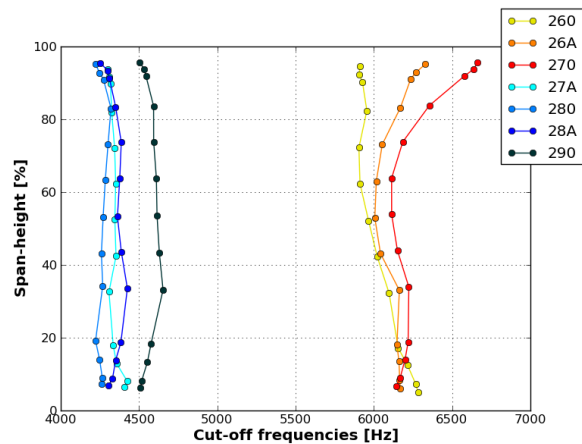
Figure 118 Spanwise evolution of contra-rotating $f_{18,0}^{cut}$ - *Loaded* operating point

V.5.3 Propagation of the cut-off modes in CREATE

In a duct without any flow, if a mode is cut-off, its wave number k_x becomes complex: the mode then becomes evanescent and stops propagating. In the case of a duct with flow, the wave number keeps a real part, see relation (V-5), and the mode still propagates. However, it is exponentially damped, the damping factor D being calculated by relation (V-7). Therefore, if the frequency of a mode is far too below its cut-off frequency, the damping is too high, and the mode does not appear. That is what happens with contra-rotating modes in the compressor CREATE. Otherwise, the damped mode can be observable: this could be an explanation of the exponential shape of the the axial evolution of the amplitude of the pressure waves. Therefore, D has been estimated all along the machine and the damping of the resonance calculated.

$$D = \exp\left(-\frac{\sqrt{-\left(k \pm M_\theta \cdot k_{r,m,n}\right)^2 + (1 - M_x^2) \cdot k_{r,m,n}^2}}{1 - M_x^2} \right) \tag{V-7}$$

As the span-wise steady measurements of pressure and temperature have only been performed in the inter-row sections, an interpolation of the Mach numbers and sound speed has been done in the blades at tip. Steady CFD results have been used to simulate the evolution of these quantities in the blades. In order to have the simplest model, only the main tendencies have been taken into account to interpolate. The sound speed has been linearly interpolated between the inter-row sections. The interpolation of the axial and circumferential velocities has been a little more complex and is visible in the sketch of Figure 119. The application of these interpolations allowed to calculate the damping factor D along the machine: where the modes are cut-on, they are no more damped and D has been set to 1. Figure 120 shows the axial evolution of the damping factor for the circumferential mode 18 at *Loaded* operating point. A parametric study has been done on the overshoots of the interpolations: on this figure, the overshoot of M_θ has been increased by roughly 8% on the plot called *'adjusted model'* in comparison with the *'raw model'*.
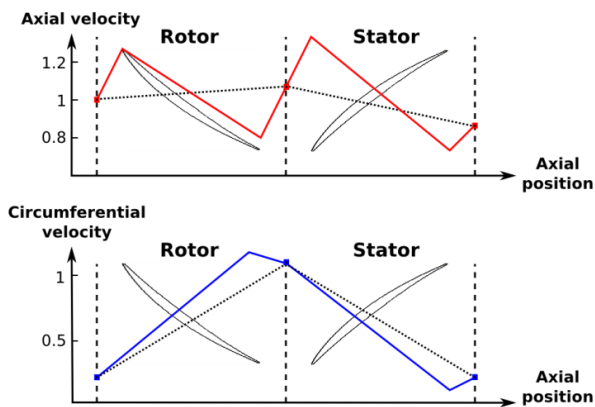
Figure 119 Interpolation of the axial and circumferential velocities in the blade rows
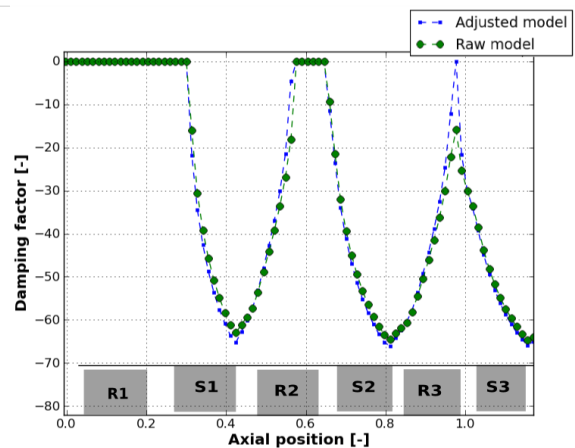
Figure 120 Axial evolution of the calculated damping factor at *Loaded* operating point

For both models, the modes are completely cut-on in the first rotor and in the rear part of the second rotor. For the last rotor, a peak is visible upstream of section 28A: the global shape of D is

nearly identical for the two models, except for this peak, very sensitive to small variations of mean flow conditions in term of intensity and fewer in term of axial position. This is due to the exponential behaviour of D. As the measurements of the mean flow were only available at *Loaded* and not *NS* points, the interpolations have been a little adjusted so as to reach the cut-on conditions in the rotor 3: it can be assumed that the small variations of the mean flow conditions between *Loaded* and *NS* operating points are sufficient to create a turning point when the surge line is approached. However, its precise axial position seems difficult to predict only with interpolated data. Finally, the independency of the global shape of D regarding to the flow conditions could explain the homothetic axial distribution of the amplitude of the modes visible on Figure 105.
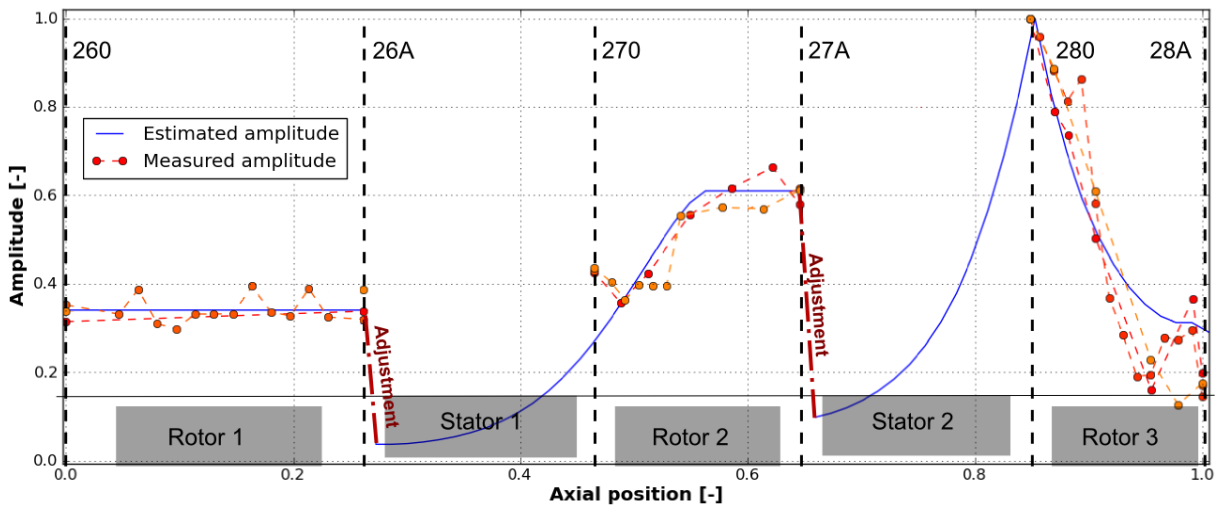
Figure 121 Axial evolution of the measured and estimated amplitude of the resonance

The axial evolution of the measured (dotted lines) and estimated (solid line) amplitudes of the resonance are plotted in Figure 121. As the experimental results were highly reproducible, four different recordings are superimposed in order to have the evolution of the amplitude in the three rotors. To normalize the results, the amplitude of the maximum of each recording is set to 1. Remember that depending on the recording, the main excited mode could either be 17, 18 or 19. However, as written before, the axial distributions of the resonance are always homothetic: therefore, the normalization of the amplitudes allows to superimpose each recording. To plot the estimated amplitude, a propagation method has been used: the maximum amplitude has been set to 1 in section 280, and relation (V-8) has been used to propagate the amplitude in the whole machine. The damping factor has been calculated for a circumferential mode 18. The mean flow conditions of *Loaded* operating point and the *"adjusted"* interpolation in the rows have been used.

$$A(x + \Delta x) = A(x)e^{D(x)\Delta x}$$ (V-8)

The amplitude of the waves has been propagated from section 280 towards the outlet and the inlet of the machine respectively. In rotor 3, the model seems to fit the experimental data. No experimental data was available in the stators: upstream of stator 2, an important discrepancy between the experimental data and the model can be observed. Therefore, the estimated amplitude has been corrected in section 27A (see the red dotted line labeled 'adjustment'). The same problem occurs when traversing stator 1. Nevertheless, the agreement between estimation and experiment seems satisfactory in the three rotors. In rotor 1, the flat evolution of the amplitude confirms that

the mode is cut-on and propagates without attenuation. In the second rotor, the mode is first cut-on at the rear part of the blade, and then cut-off at the front part. Considering a mode propagating in the upstream direction, its evolution of amplitude is first flat and then starts to decrease: the global shape of the amplitude matches very well with the experiment. However, a zone of lower amplitude than the model is visible at the front part of rotor 2, as well as an increase in amplitude not predicted by the model between section 270 and the leading edge of rotor 2. Finally, the evolution in the third rotor is quite well captured by the model. It agrees with the experiment along the first half of the blade. At roughly mid-chord, the measured amplitude diverges from the model and drops to a minimum located at axial position 0.95: the increase in amplitude found just downstream could be produced by the trailing edge separations observed in chapter V.4.2, inducing some pressure rises phase-locked to the pressure waves. Therefore, its origin would be of aerodynamic nature rather than of acoustic nature. Note that this increase of amplitude weakens when the amplitude of the waves decreases, see Figure 105, and almost disappears at *SM* point: the fact that this portion of the distribution is not homothetic reinforces the hypothesis of a coupling between the acoustic waves and the separations.

Hence, this model succeeds quite well in predicting the evolution of the amplitude of the pressure waves in the rotors: it confirms that they are produced by acoustic resonance. However, the study of the damping factor seems not sufficient to estimate the evolution in specific zones close to the leading and trailing edges of the rotors. The main reason is that the reflections occurring in the machine have not been taken into account so far. The next chapter will be dedicated to the analysis of the phase of the acoustic modes in order to understand the sets of transmissions/reflections occurring in the machine.

V.5.4 Study of the reflections in the machine

In order to propose a mechanism explaining the resonance in the compressor, the phase evolution in the second and third rotors has been investigated to detect possible reflections. Indeed, a condition to have resonance is that acoustic modes are trapped in the machine because of reflections. They are generally produced by the impingement of the waves on the rows interfaces or by turning points: indeed, it can be found in the literature that when an acoustic mode switches from cut-on to cut-off, a reflection occurs [73],[69]. The two next chapters will study these two types of reflection.

V.5.4.1 Phase evolution of the acoustic modes

Figure 122 shows the measured evolutions of the amplitude (triangles) and phase (dots) of the resonant acoustic modes in the rear part of the machine at *NS* operating point. Three recordings have been superimposed. The scales of axial position and amplitude correspond to these of Figure 121. The edges of the blades are noted with vertical dotted lines.

In the previous chapter, it has been seen that the modes become locally cut-on in rotor 2. As well, a turning point has been found by the model at the rear part of rotor 3. On Figure 122, two changes in the phase slope are visible in the rotors. They could be produced by reflections occurring at the turning points (marked by an **'R'** on the figure). For rotor 2, the turning point seems localized

roughly at the upstream limit of the cut-on zone predicted by the model. Its axial position is not obvious to predict as the cut-on zone is quite large. For rotor 3, it is simpler as the cut-on zone is narrower. However, the turning point seems localized a bit more upstream than the axial position predicted by the model. A possible reason could be that the model is too simple for a complex multi-stage test case. Then, this model has been done with data interpolated from a stable operating point far from surge (*Loaded* point). Therefore slight changes in the mean flow conditions could induce a shift of the axial position of the turning point in rotor 3. Finally, the precise determination of the turning points depends on the spatial mesh of the sensors which might be too coarse. The hollow shape of the amplitude upstream and downstream of the turning points in rotor 2 and 3 respectively could be produced by the reflections (the increase of amplitude at the trailing edge of rotor 3 being produced by a separation induced by the waves). Hence, a set of two reflections due to turning points in the rotor 2 and 3 could be the cause of the mode trapping.
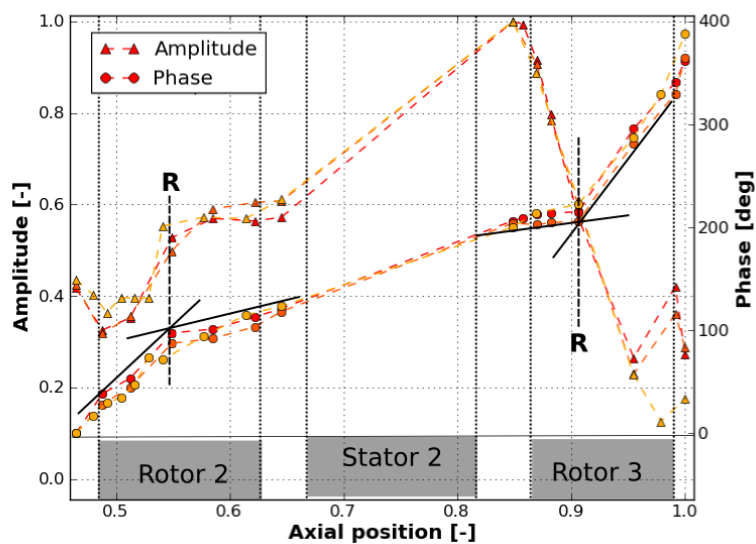
Figure 122 Axial evolutions of the amplitude and phase of the resonance at the rear part of the machine

V.5.4.2 Reflections occurring at the rows interfaces

So far, the reflections occurring at the rows interfaces have not been taken into account in CREATE. For acoustic waves with wavelengths of the same order as the dimension of the compressor, interactions between the blades and the waves, and thus reflections, can occur. In 2008, Hellmich [35] did a bibliographic review of the study of transmission/reflection of acoustic waves in compressors. It is summarized hereafter.

In 1970, Kaji and Okazaki [45] showed with an actuator disk approach that an acoustic wave impinging a blade row of stagger angle α_s is partly transmitted, partly reflected and partly dissipated, depending on the angle of incidence θ_I of the wave in the frame of flow. To calculate the reflection and transmission coefficients, they used a model comparable to Figure 123: as the incidence angle of the model is given in the frame of flow, measured angles in the absolute frame have to be corrected by a vector addition of the flow and sound field. If the stagger angle is more than 90°, as it is for the

rotor blades, the sketch must be mirrored at a horizontal line and the definition of the angles must be taken from the mirrored sketch, see [35]. The ratio blade length *l* over circumferential spacing *s* and the Mach number *M* of the mean flow are other parameters on which depend the coefficients.
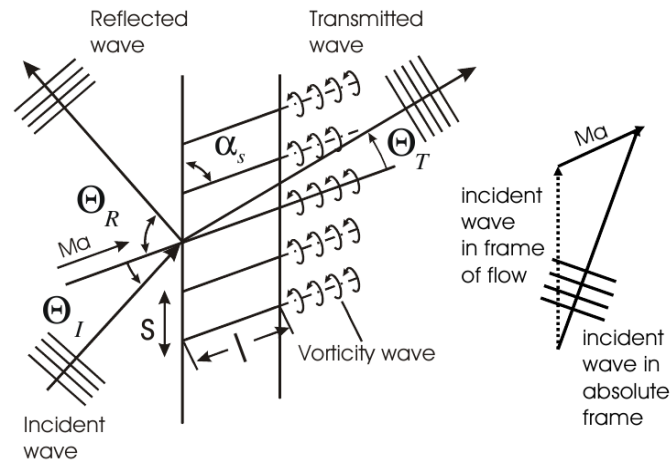
Figure 123 The transmission/reflection at a blade interface - from (Koch,1971, [47]) - extracted from (Hellmich,2008, [35])

Figure 124 shows and example of calculation by Koch [47] of the transmission and reflection coefficients for different Mach numbers at a stagger angle of 30°, and a ratio *l/s* of 1. These parameters are of the same order in CREATE. Three extreme cases are visible on this figure.

- If the incidence angle is 0° or 180°, the acoustic wave fronts are normal to the blades and can propagate without attenuation through the row: a total transmission occurs. These angles are marked with a **T**.

- If the waves impinge the row perpendicularly to the blades in the frame of flow, the wave fronts are reflected. This occurs when the angle of incidence satisfies the relation (V-9) [35], given for upstream travelling waves spinning with and against swirl respectively. These angles are marked with a **R**.

$$M_x = \mp\sin(\theta \mp \alpha_s) \qquad\qquad (V\text{-}9)$$

- A last case called dissipation can occur: a partial transmission occurs but the waves reflected by each blade cancel out each other to result in the zero intensity as a whole. As a result, no reflection occurs but the energy of the wave is not fully transmitted. Kaji and Okazaki formulated the condition of dissipation written in relation (V-10) for upstream and downstream travelling waves respectively. These angles are marked with a **D**.

$$\sin(\theta - \alpha_s) \mp \sin(\alpha_s) - M \cdot \sin(\alpha_s) \cdot (1 \pm \cos(\theta)) = 0 \qquad\qquad (V\text{-}10)$$

Hence, it is possible to split the diagram of Figure 124 in four zones defined by the incidence angles where the reflection is zero. In zone 2, the acoustic waves are travelling upstream and enter the blade rows from the backside. In zone 4, the acoustic waves are travelling downstream and enter the blade rows from the front. Zone 1 and 3 are around the angles where the acoustic waves travel parallel to the blade rows with (zone 1) or against (zone 3) the swirl. In his PhD thesis [35], Hellmich proposed a methodology to evaluate the transmissions/reflections occurring at the rows interfaces in a high speed compressor. This methodology is developed hereafter.
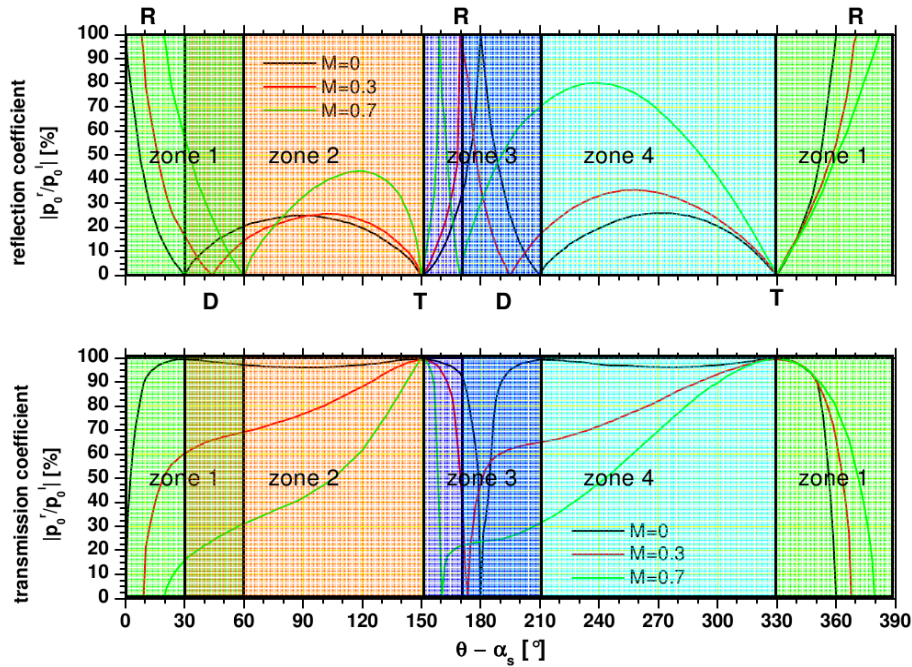
Figure 124 Calculation of transmission and reflection coefficients at a blade row interface – from (Koch,1971, [47]) - extracted from (Hellmich, 2008, [35])

Evaluation of the reflection/transmission coefficients

To evaluate the transmission/reflection coefficients at a row interface, the incidence angle of the waves on the blades has to be calculated. It depends on the radius *r* and has to be compared to the stagger angle α_s at the given radius. It is done in three steps, defined by Hellmich.

First, the incidence angle $\beta_\pm$ of the waves relative to the compressor axis in a fixed frame is calculated with relation (V-11). The subscript ± is positive for waves travelling downstream and negative for the waves travelling upstream.

$$\beta_{x\pm} = \arctan\left(\frac{r \cdot k_{x\pm}}{m}\right) \tag{V-11}$$

With *r* the radius, k_x the axial wave number and *m* the azimuthal mode order. If the wave hits a rotor, the incidence angle has to be known in the rotating frame. It can be calculated with relation (V-12):

$$\beta_{x\pm}^{rotor} = \arctan\left(\frac{r \cdot k_{x\pm}}{m} \cdot \left(1 - \frac{f_{rotor}}{f}\right)\right) \tag{V-12}$$

f_{rotor} being the rotor frequency and *f* the frequency of the sound wave. This transformation has to be done upstream of the rotors for the modes travelling downstream, and downstream of the rotors for the modes travelling upstream.

The second step is the conversion of $\beta_\pm$ in the angle $\beta_\pm^{flow}$ which is the angle in the frame of flow. It is done by the following equation. The first subscript refers to the direction of propagation and corresponds to the sign of M_x. The second refers to the direction of spinning (positive with swirl) and corresponds to the sign of M_θ.

$$\beta_{\pm;\pm}^{flow} = \arctan\left(\frac{\sin(\beta_{\pm;\pm}) \mp M_\theta}{\cos(\beta_{\pm;\pm}) \mp M_x}\right)$$ (V-13)

The last step is to transform the angles $\beta_\pm^{flow}$ into the angles θ_I-α_s. To understand the conversion, Figure 125 extracted from Hellmich (2008, [35]) sketches the incidence angles of the acoustic waves on the blade rows. The angles $\beta_\pm$ are already converted so the superscript ^{flow} is not shown. The thin black arrows are used to show the incidence angles $\beta_\pm$ but their length does not represent the speed of the waves. In contrast, the length of the other vectors is representative of the speed of flow, rotation and sound in the machine. As stated in the previous chapter, for the rotor blades the stagger angle is above 90° so the sketch in Figure 123 must be mirrored with respect to the machine axis. The stagger angle in the mirrored sketch is shown as α_s' and the incidence angle as θ_I'. An R in an index of an angle means that the acoustic wave is downstream a rotor and an S means that it is downstream a stator. A "+" means that the wave travels downstream and a "-"that it travels upstream.
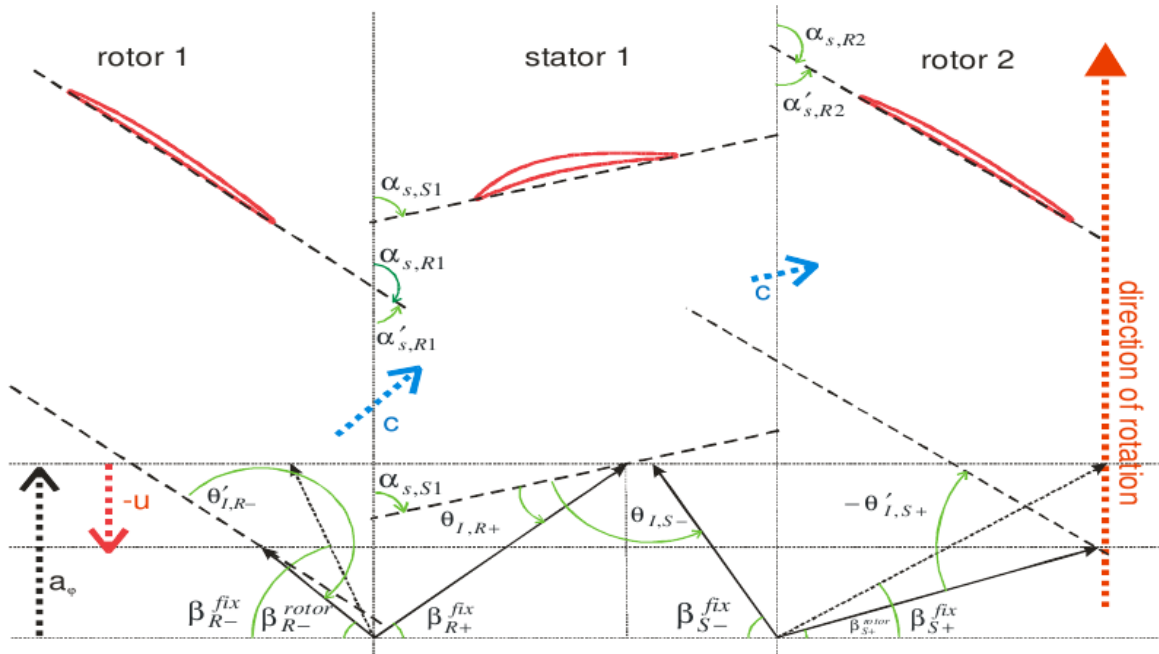
Figure 125 Scheme of flow and incidence angles of acoustic waves in a compressor (Hellmich, 2008, [35])

The conversion of $\beta_\pm^{flow}$ into the angles θ_I-α_s is finally given by the following equations:

- Downstream of rotors:

$$\theta_{I,R+} - \alpha_{s,S} = -90° + \beta_{R+}^{flow}$$ (V-14)

$$\theta'_{I,R-} - \alpha'_{s,R} = 90° + \beta_{R-}^{rotor,flow}$$ (V-15)

- Downstream of stators:

$$\theta'_{I,S+} - \alpha'_{s,R} = 270° - \beta_{S+}^{rotor,flow}$$ (V-16)

$$\theta_{I,S-} - \alpha_{s,S} = 90° - \beta_{S-}^{flow}$$ (V-17)

The transmissions/reflections can finally be evaluated. The whole process is summarized in Figure 126.
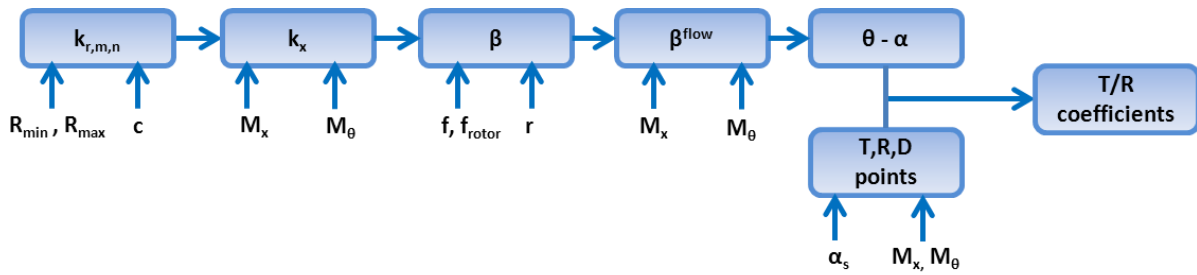
Figure 126 Calculation of the transmission/reflection coefficients

Interactions between sound waves and blade rows in CREATE:

The **T**, **R**, **D** points and θ-α$_s$ have finally been calculated along the spanwise direction in CREATE with the previous methodology. The results are shown in Figure 127: the four sub-plots correspond to the upstream and downstream modes located downstream the rotors and stators. In dotted lines, the angular coordinates of the **T**, **R** and **D** points are given spanwise for each inter-row section according to their definition in Figure 124. θ-α$_s$ is then given spanwise for each stage in solid lines.
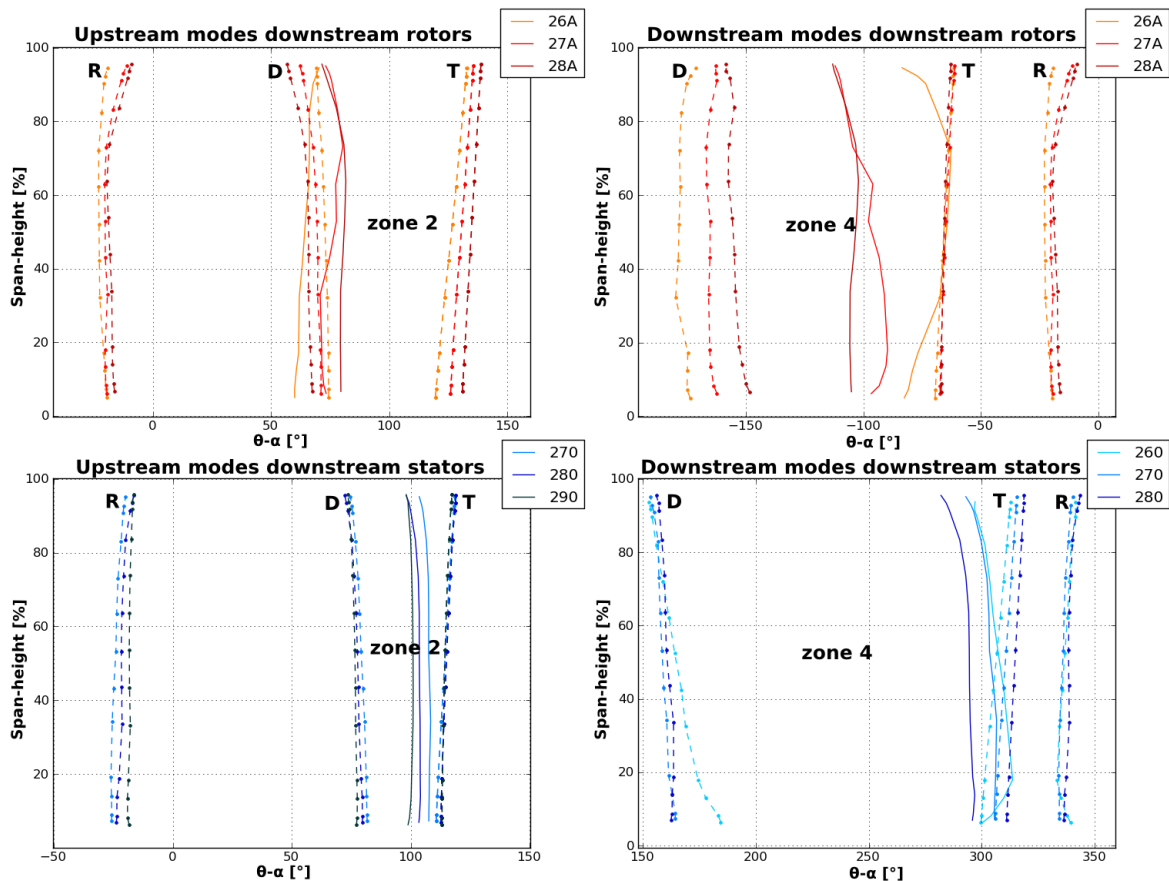
Figure 127 Interactions between sound waves and blade rows in CREATE: angular coordinates of (T,R,D) in dotted lines and measured (θ-α) in solid lines

The incidence angles of the modes located downstream of the rotors and travelling upstream are very close to the dissipation angles, see upper-left part of Figure 127. It corresponds to zone 2 in Figure 124. The Mach number in the rotor frame is low at this location: therefore, from Figure 124, it

can be written that the transmission coefficients are here very strong. Hence, the upstream travelling modes are transmitted through the rotors blades. The situation for the downstream travelling modes is a bit more complex. For section 26A (downstream of rotor 1), the modes are nearly totally transmitted, see the upper-right part of the figure. The incidence angles for sections 27A and 28A lie between the **D** and **T** points. At this location, the Mach number in the absolute frame is high: therefore, from Figure 124, it can be assumed that the reflection coefficients will be close to their maximum, i.e. between roughly 0.7 and 0.9. Hence, a strong reflection occurs when the acoustic waves impinge the blades of stators 2 and 3. On the contrary, they are transmitted through stator 1.

The incidence angles of the upstream travelling modes downstream of the stators are between the **D** and **T** points, but this corresponds to zone 2. Behind the stators, the Mach number in the absolute frame is low. From Figure 124 it can be assumed that the reflection coefficients are low, between 0.1 and 0.3, and therefore that the waves are mainly transmitted through the stators blades. Finally, the downstream travelling modes are almost completely transmitted through the rotors blades.

Overall, the previous results can be summarized as:

- The modes travelling downstream are quite strongly reflected at the rotors and stators interfaces, but transmission still occurs

- The modes travelling upstream are almost totally transmitted at the stators interfaces.

- Dissipation occurs for the modes travelling upstream at the rotors interfaces: most of the energy is transmitted, but no reflection occurs.

V.5.5 Mechanism of mode trapping in the machine

From the previous results, an attempt has been made to propose a mechanism of trapping in CREATE which could explain the acoustic resonance: it is illustrated in Figure 128. The sketch focuses on the two last rotors where the trapping is likely to occur. At each row interface, a letter (**R**, **D** or **T**) has been marked to qualify the transmission mode of the wave. The cut-on zones are colored in grey. A single source (labeled "S") has been placed downstream of stator 2: another possibility would have been to place a source in each inter-row section. The source of the acoustic mode is not yet understood, but the purpose of this paragraph was more to understand the mechanism responsible for resonance.

The proposed mechanism works as follows: the acoustic waves emitted downstream of stator 2 are nearly totally transmitted at the rotor 3 interface. Then, when entering rotor 3, the transmitted waves encounter the cut-on zone at roughly mid-chord. This creates a turning point and the waves are reflected. Most of the upstream modes emitted downstream of stator 2 are transmitted through the stator. They are also transmitted through rotor 2. A dissipation point is indeed found at the interface: the transmission coefficients are very high at this location and no reflection due to the impingement on the blades occurs. However, the modes turn to cut-on just downstream of rotor 2 until roughly the half chord. Therefore, as for rotor 3, the acoustic waves are reflected, but the precise location of the turning point is more difficult to define. When they impinge the blades of stator 2, the reflected waves are partly reflected and partly transmitted: therefore, the inter-row

space between the rotor and stator 2 could work as a partial resonator, which would explain the higher amplitude measured at section 27A regarding to the theoretical model, see Figure 121. Finally, the transmitted waves join the inter-row space behind stator 2 and are once again reflected by the third rotor.
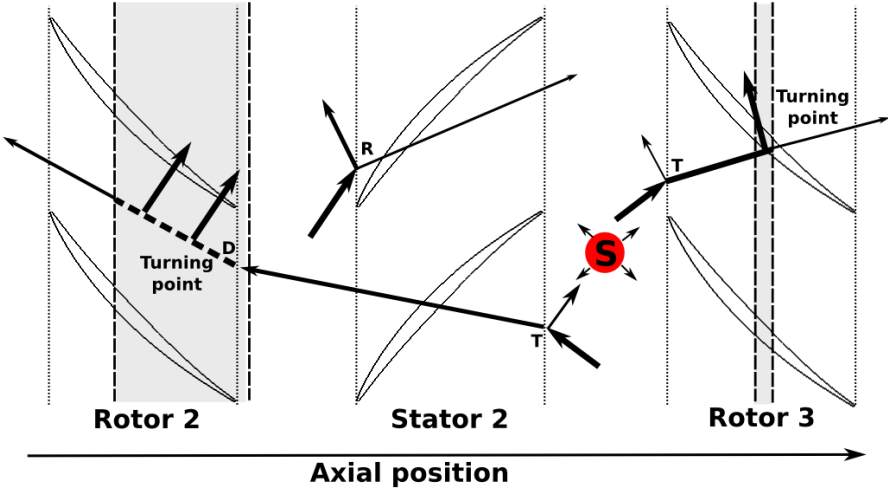
Figure 128 Illustration of a possible mode trapping mechanism

Overall, this model explains how rotor 2, stator 2 and rotor 3 could work as a resonator. However, this model remains very simple, and the proposed explanations would deserve further measurements to be confirmed. Measurements of the amplitude and phase of the resonance in the stators would be particularly instructive. As well, measurements of the mean flow at *NS* operating point would induce a significant improvement of the model, especially by better defining the axial positions of the turning points.

V.5.6 Conclusion

In this chapter, it has been shown that the pressure waves observed in CREATE before surge are due to acoustic resonance. A theoretical model of prediction of the amplitude of the resonance has been compared to measurements. The model showed good agreement with the experimental results in the rotors but was not able to predict the evolution through the stators. Nevertheless, it allowed to understand the axial distribution of the amplitude of pressure waves. The coupling between the pressure mode and the behavior of the flow in the inter-blade channels induces separations at the trailing edge and modify the pressure field in this area. Therefore, it seems very difficult to describe the entrance of the instabilities only with acoustic considerations. Then, the model showed how slight changes in the mean flow conditions could induce the appearance of a turning point in the last rotor, which is a necessary condition for the resonance to occur. Therefore, this could explain the narrow speed range at which the resonance can be observed: the decrease in the speed could induce changes in the mean flow conditions responsible for the disappearance of the turning point.

Then, a study of the phase evolution of the modes has been done. It showed that two reflections due to a switch from cut-off to cut-on conditions occurred in the rotors 2 and 3. These results have been coupled to those of a model predicting the transmissions and reflections at the row interfaces. They showed that the rear stages (from rotor 2 to rotor 3) could behave like a resonator due to a mode trapping phenomenon occurring at near surge operating points: a mechanism of trapping has been finally proposed. However, the phenomena involved in the resonance of a multistage compressor are very complex, especially all the reflections that can occur at the rows interfaces. Nevertheless, even if it is obvious that the presented simple model does not capture all the physics of the acoustic resonance, it allowed to explain the global features of the phenomenon.

So far, the flow of CREATE has been investigated just before surge. The last part of our analysis of the instabilities arising in the machine will focus on the surge transient.

V.6 Description of the surge

The purpose of this chapter is to draw a precise description of the surge in CREATE. This will be done in three steps. A global overview of a surge cycle in CREATE will first be presented. A focus on the transient will then be done, before the presentation of an anti-surge control system based on the detection of the rotating pressure waves.

V.6.1 Global description of a surge cycle

As previously seen in chapter V.2, the surge occurs when a full span-cell arises in the flow and grows around the annulus until completely blocking the whole annulus. For our study of the unstable regimes of CREATE, the first point is to know if the compressor faced surge or deep surge, i.e. if the mass flow was completely reversed during surge. When surge occurs, the mass flow oscillates at a frequency of a few hertz, see chapter I.3.3: to determine the nature of surge, the mass flow has hence to be measured fast enough to capture its fluctuations. However, only a steady measurement of the flow through a Venturi nozzle is available with this test rig. It has therefore been decided to equip the section 250 (upstream of the *IGV*) with a high-frequency temperature sensor to measure the total temperature of the flow at the inlet of the compressor during the flow breakdown. Figure 129 shows wall static pressure and total temperature signals of 1 second acquired during a surge cycle (the anti-surge valve has been opened before the second cycle). As the temperature sensor was located upstream of the *IGV*, the signal of the closest pressure sensor –i.e. in section 260 upstream of rotor 1- has been plotted (the spikes correspond to electrical noise).

When surge occurs at t=0.18 s, the compressor is no more able to counter the adverse pressure gradient imposed on the fluid and the pressure equalizes in the machine: a huge increase in pressure is therefore visible at the inlet of the compressor (corresponding to the propagation of the entropy wave). At the same moment, the temperature sensor records an increase in temperature. Because of its response time, the temperature signal reaches it maximum value in 0.1s: at t=0.28s, the recorded temperature at the inlet of CREATE correspond to the outlet temperature. This means that deep surge occurs: the hot fluid at the rear part of the machine flows back at the inlet and induces a temperature rise. At t=0.3s, the flow starts again to propagate downstream and the

temperature decreases: the smooth slope of the temperature signal is due to the time of temperature recovery of the sensor.
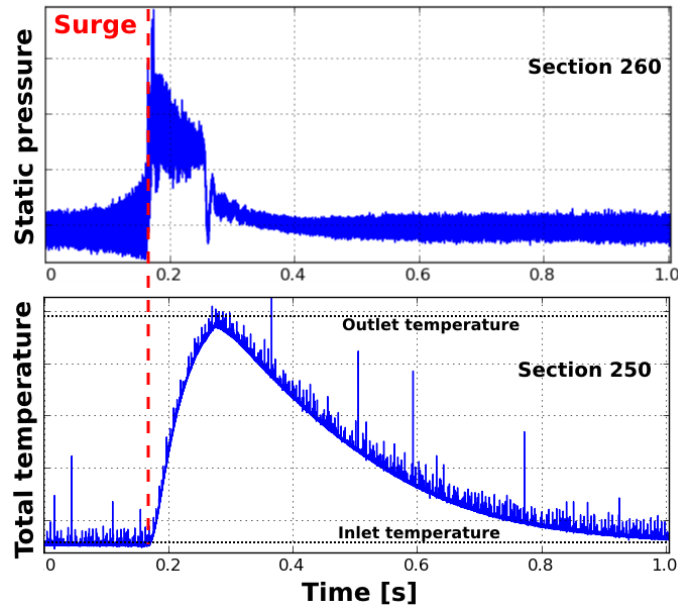
Figure 129 Temporal evolutions of pressure and temperature at the inlet of the machine during surge

In order to have a global view of the surge, Figure 130 shows a cycle representative of all the surge recordings achieved in CREATE. The measurements have been acquired here downstream of rotor 2, but are representative of what occurs downstream of each rotor. The figure is split into four subplots. The two first represent the temporal evolutions of the rotation speed of the machine and of a pressure signal in section 270. The two others have been obtained from *DFT* windowing with a window set to one rotor revolution. They show the evolutions of the amplitudes of the *BPF* and F_{18} (section 27A) and of the amplitude of the *BPF* at different axial positions chord-wise of rotor 2. At the top of the figure the rotation speed of the compressor shaft is plotted. This signal is usually very constant with an accuracy better than 1/10000 when the compressor is operating in its stabilized range. During the surge cycle here, the huge change in the torque generated by the stall of the rotors cannot be counterbalanced instantaneously by the system which drives the electrical engine. Thus the evolutions of the shaft speed constitute an overview of the forces applied to the rotors.

On the second subplot, the time evolution of the pressure signal is plotted. The temporal period of the surge is here clearly defined and is equal to 0.68 s (132 rotor revolutions). At $t = 0.25$ s the stall of the rotor occurs until $t = 0.355$ s, i.e. during 20 rotor revolutions, and leads to a decrease in the rotors load which produces an acceleration of the rotation speed of the compressor shaft: the regulation of the rotor speed used to maintain the rotor speed constant cannot react as fast as the stall occurs. During the stall, the pressure equalizes in the machine. Thus, the pressure decreases in section 27A to reach the level of about 0.45 (meanwhile, the pressure increases in section 260 and reaches the same value, see Figure 131). Then, the flow reattaches and the torque on the shaft increases. The rotation speed decreases not very quickly because of the inertial effects of the rotors. Note that the small decrease in the shaft rotation speed at $t = 0.25$ s corresponds to the maximum torque which appears when the load is maximum: this corresponds also to the time when the amplitude of the pressure mode is maximum at the tip of the rotors (see the amplitude of F_{18} just before surge in the third subplot). The second stall occurs at $t = 0.93$ s. The second surge cycle is

different because the anti-surge valve is operated at $t = 1.25$ s to discharge the system. It is noticeable that F_{18} appears again before the second surge cycle, which shows that the machine retrieves its pre-surge mean flow conditions. Note that the mode order can change between two cycles, which emphasizes the complexity of the phenomenon of acoustic resonance.

Below the pressure signal, the time evolution of the *BPF* of rotor 2 and of F_{18} is plotted. Just before surge, the amplitude of F_{18} increases and get back to very low levels as soon as stall occurs: indeed, the huge changes of mean flow conditions during surge blocks the acoustic resonance. Meanwhile, downstream of rotor 2, the amplitude of the *BPF* reaches some very high values. This is also true downstream of all the rotors: as deep surge occurs, the flow is reversed and the rear parts of the rotor blades are confronted with high pressure gradients between the pressure sides and the suction sides. This is due to the reverse flow which impinges the trailing edges of the blades with very high values of incident angle. This phenomenon is illustrated by the bottom subplot of Figure 130 with the amplitude of the *BPF* measured in the front, the middle and the rear parts of the blades of rotor 2 with sensors mounted on a removable block. Before the occurrence of surge, the higher pressure gradient is classically encountered at the front part of the blade. When the deep surge occurs, the reversed flow induces a transfer of the load toward the rear part of the blades, causing very damageable strains to the blades.
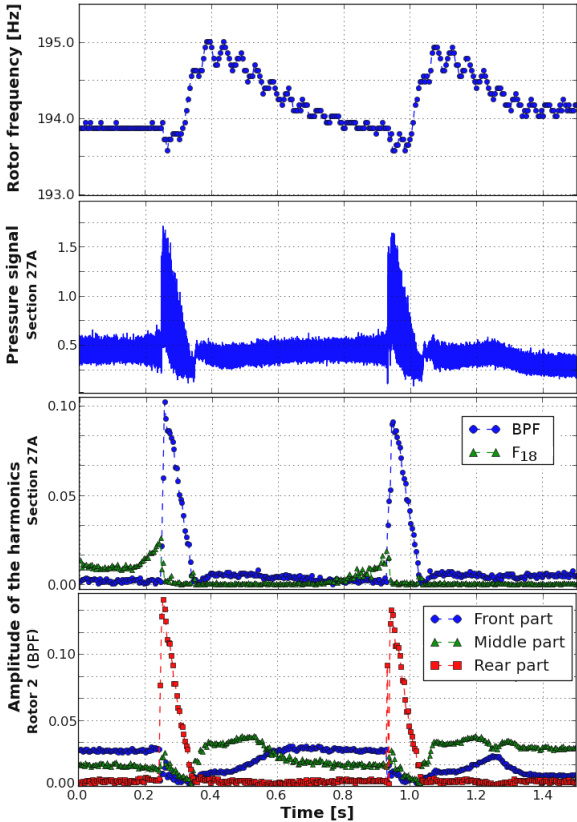
**Figure 130 Description of a surge cycle - section 27A**   **Figure 131 Description of a surge cycle - section 260**
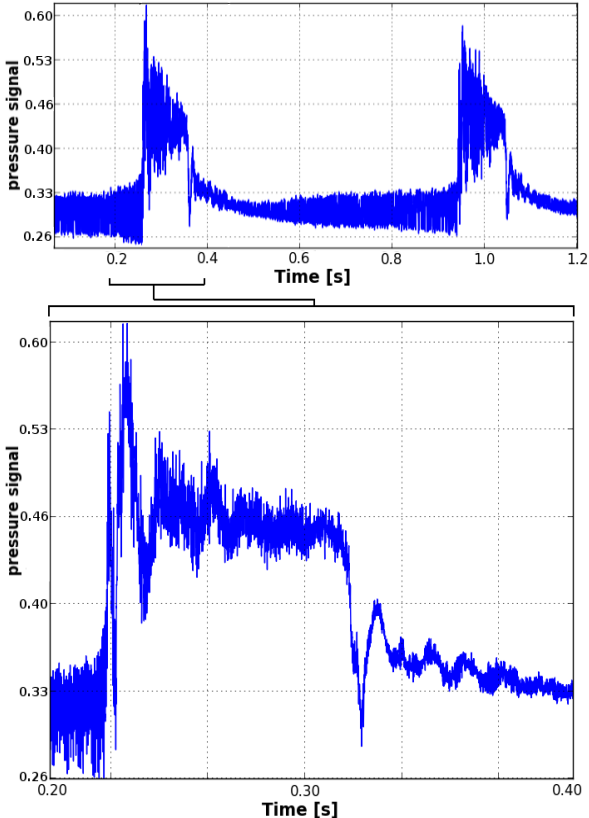
In all the surge recordings, strong pressure oscillations have been observed just after the onset of surge in the whole machine. They were particularly visible at the inlet of the compressor. Hence, the pressure signal acquired upstream of rotor 1 (section 260) during the previous surge recording is

presented in Figure 131. When the surge occurs, an important pressure peak is observed, immediately followed by a second-order damped oscillation (zoomed in the bottom part of the figure). Its pseudo-pulsation is of 57 Hz. Greitzer suggested in 1976 [32] that a compression system can be modeled as a Helmholtz resonator, see chapter I.3.3. In that case, the surge phenomenon can be seen as an excitation of the system due to the strong pressure peak. The Helmholtz frequency has been evaluated for our experimental facility according to relation (I-4): the geometric properties needed for the calculation have been estimated from a simplified vision of the test rig, seen as a simple cylindrical duct an a plenum (therefore the whole complex geometry has not been taken into account, as the structure arms or the section variations for example). The Helmholtz frequency has finally been found to be around 50 Hz. This is quite close to the measured value of 57 Hz, taking into account the simplicity of the model and the simple geometric considerations. This finally explains the origin of the oscillations visible in Figure 131.

After this general description of a surge cycle, the next chapter will focus on the surge transient. The wall static pressure field will indeed be studied by means of instantaneous space-time diagrams, as for the visualization of the pressure waves in chapter V.4.1.

V.6.2 Fine description of the surge transient

In order to describe the flow field during surge, the pressure signal of the sensor located at mid-chord of rotor 3 is plotted on Figure 132. The phenomenon can be separated into four distinct phases 1, 2, 3 and 4. To analyze the flow field, instantaneous space-time diagrams for each phase is shown in Figure 133 and Figure 134. The blades travel from bottom to top but the time goes from top to bottom.
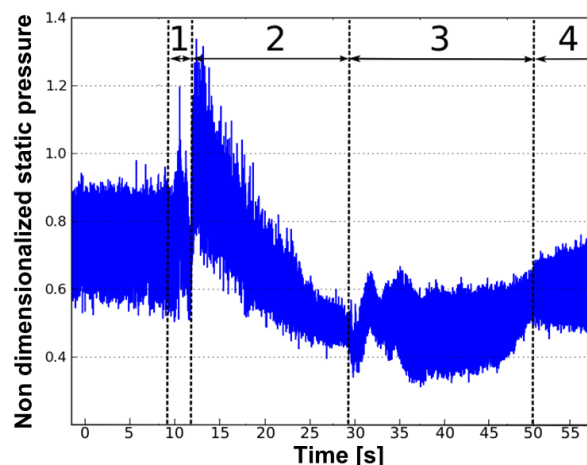
Figure 132 Wall static pressure at mid chord of rotor 3 during surge

The rotor revolution 9 corresponds to the last revolution before the surge transient: the pressure waves are indeed strongly visible, as for Figure 111. The phase **1** of surge extends over the rotor revolutions 10 to 12 and corresponds to the surge transient which begins at blade 20 (*b20*) of revolution 10 (see Figure 133), where the pressure gradient generated by the blades disappears over roughly ten blade passages. Indeed, a stall cell extending over three characteristic periods of the

pressure waves at the trailing edges of the blades and travelling from top to bottom generates a strong blockage and an under-deviation of the flow at its tail, which unloads the blades 20 to 29. This stall cell can be seen between *b30* and *b58*: the huge high pressure region at the trailing edges of the blades and the reduction of the low pressure region near the leading edges indicates a large flow separation. Indeed, as stated in chapter V.4.2, small flow separations are produced by the pressure waves effects at the trailing edges of the blades: when the amplitude of the pressure fluctuations increases at the leading edges, the separations at the trailing edges do the same. The large stall cell corresponds in fact to the merging of three consecutive grown up separations. Indeed, just after the passage of the cell from *b57* to *b72*, two strong separations produced by the high amplitude of the waves are visible through important increases of pressure at the rear part of the blade. This coupling between acoustic-mode resonance and separation explains the very close values of spinning velocity of the waves and the stall cell.

At rotation 11, from *b12* to *b57*, the growing stall cell passes again in front of the sensors. Its structure exactly corresponds to the pressure signature of a full span cell described by Inoue *et al.* [41] in a low speed machine. In the front part of the cell (*b40-b57*), the low pressure regions at the leading edge of the blades increase gradually and reach a maximum for blades *b57* to *b66*. In the relative frame, the cell goes from top to bottom: the blades *b57* to *b66* suffer from over deviation of the flow due to the upcoming cell. Between *b67* and *b73* a large low pressure region is visible: indeed, the stall cell continues to grow while travelling and now extends over almost all the compressor circumference. The flow then rushes into the reduced section of unblocked passage and accelerates, inducing a decrease of static pressure. At blade 77, the cell occupies the whole annulus of the compressor which falls into surge. From that point, the flow reverses and thus impinges the blades from behind on the pressure side with a non-adapted angle of incidence: strong pressure peaks, induced by the stagnation points, are visible at the trailing edges of the blades. This reversal of the flow is accompanied by a huge pressure rise with high pressure fluctuations, visible on Figure 132.

The phase **2** extends over the rotor revolutions 12 to 28 and corresponds to the reverse flow phase: the pressure ratio drops down as the machine discharges, and falls from twice its pre-surge value to 60%. The mass flow is completely reversed at revolution 12 and gradually increases, reaching 0 at revolution 28. No axial static pressure gradient is thus visible at this time in Figure 134.

The phase **3** begins at revolution 29 (Figure 134) and extends until rotation 50. It is a transition phase in which the flow reattaches the blades progressively over the whole span and the mass flow increases. At rotation 29, from *b45* to *b52*, the flow begins to reattach and a low pressure region is visible. Indeed, a few blade passages begin to unstall, and the flow driven by the first stages rushes into those free passages. This increases the speed of the flow and produces the zone of low pressure, as for revolution 11, *b67* (see Figure 133). This low pressure zone is immediately followed by a stall cell (centered on b55) which rotates and passes again in front of the sensors at revolution 30, *b10*. From this point until revolution 50, as the mass flow increases, the flow progressively reattaches (as indicated by the increasing axial pressure gradient) and presents three-dimensional structures very complicated to explain with end-wall pressure measurements. From revolution 50 (phase **4** in Figure 132), the compressor starts working again in a stable way and the pressure ratio increases until reaching its pre-surge value.
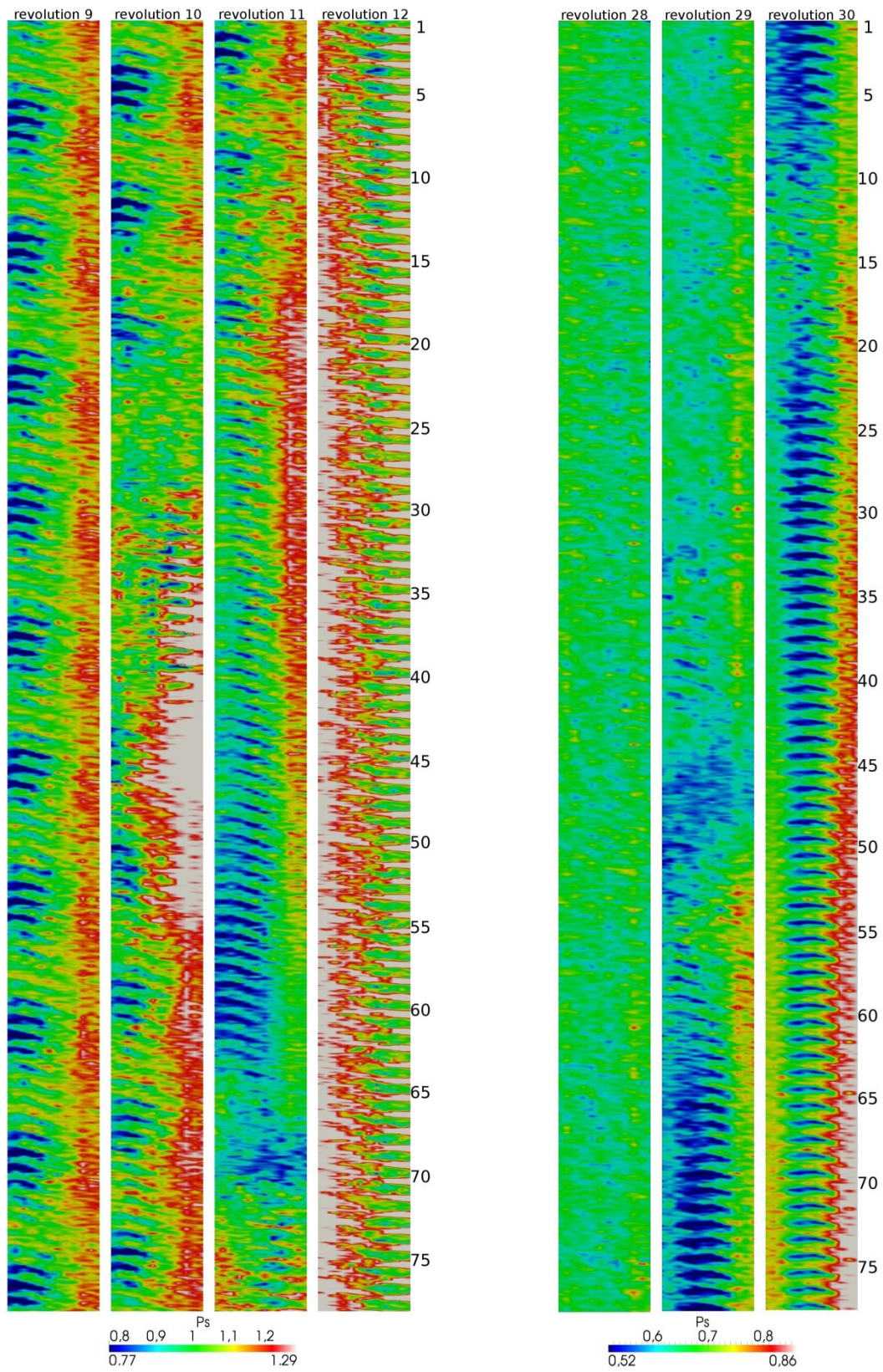
Figure 133 Global view of the pressure field during surge phase 1 over four rotor revolutions – rotor 3

Figure 134 Global view of the pressure field during surge phase 3 over three rotor revolutions – rotor 3

A precise description of the surge transient has finally been achieved. It confirmed the role of precursor played by the pressure waves, inducing trailing edge separations that merge to form the full-span stall cell leading to surge. It showed moreover how a process of cycles establishes when the compressor surges.

V.6.3 Development of an anti-surge control system

The last part of this chapter is devoted to the presentation of an anti-surge control system that has been developed for CREATE. Indeed, to study the instabilities arising in the compressor, it has been brought many times very close to the surge line, with high risk of falling into surge. In order to avoid pumping, and to possibly damage the machine, it has been decided to develop an anti-surge active control system, based on the detection of the frequencies which appear when approaching the onset of the surge. The main idea was to develop a criterion allowing to trigger an emergency valve to unload the machine: it has hence been decided to compare the intensity of the pressure waves (acoustic resonance) with the stable features of the flow, i.e. to calculate the ratio between the amplitude of the frequencies of the waves and the amplitude of the *BPF* taken from a sensor located in the section 280, upstream of rotor 3. This procedure is very similar to the analysis made in chapter V.3.2. Because the amplitude of the *BPF* fluctuates a bit and in order to have a more accurate ratio, it has been finally decided to use the mean value of the static pressure in the section 280 instead of the amplitude of the *BPF*. As any of the four frequencies F_i could increase when approaching the surge line, the power spectral density of the signal integrated over [1800-2400] Hz has been calculated (this corresponds to 9.2 to 12.3 times the rotor frequency), to be sure to capture the increase in any frequency.
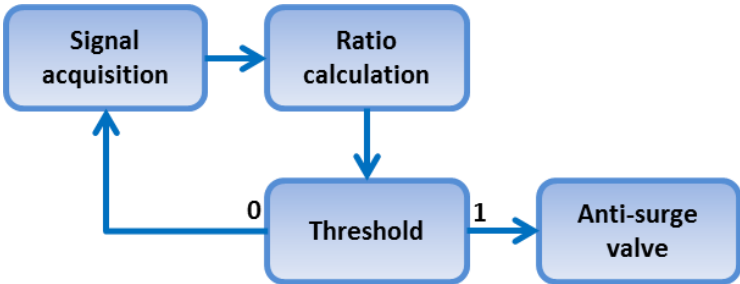
Figure 135 Schematic diagram of the anti-surge control system

The schematic diagram of the final control system is sketched in Figure 135. The signal is first acquired over a short time and the ratio is calculated for this portion of signal: when it reaches a value over a certain threshold, the anti-surge valve is opened, if not, the system does another acquisition. During the test of the control system, the signal has been acquired over 4096 samples at a frequency of 50 kHz during 0.08s, mainly because the control system has been implemented on an existing system of surveillance of the blades vibrations with its own acquisition system. To have a sufficient frequency resolution of around 160 Hz to be able to discriminate the four frequencies F_i, only 310 samples would have been necessary, i.e. 512 in practice to use fast Fourier algorithms. The acquisition time would have therefore been decreased to 0.01s (the time of a few nanoseconds for

the *DFT* calculation and the other software operations being almost instantaneous). The response time of the system has been evaluated to be between 0.5s and 0.7s, mainly because of the slowness of the opening system of the valve that discharges the system (noted "anti-surge valve").

As previously seen, CREATE has been brought to surge several during the experimental campaign: Figure 136 shows the temporal evolution of the ratio defined above, calculated for three surge recordings. The third recording corresponds to the one presented in Figure 108: the temporal evolution of the ratio and of F_{18} are almost identical: the ratio is only calculated to normalize all the surge recordings. One can notice the differences between the three surge recordings, which highlights the chaotic behavior of the machine close to surge. However, every recording of Figure 136 present similarities: they can indeed be split into two parts. If the ratio remains below a certain value, the compressor keeps running in a pseudo stable state. On the contrary, if the ratio increases too much, the machine starts to get out of control. The ratio begins to behave almost randomly and the machine falls into surge within a more or less short time (this is the chaotic phase of the pressure waves, see chapter V.3.1). This has been observed on every surge recordings of CREATE. A threshold of 0.05 corresponding to the beginning of this chaotic phase one every recordings has therefore been empirically determined for the ratio, as it seems to roughly correspond to the mean critical value above which the compressor never went to surge in less than the maximum necessary time to unload the system (0.8 s).
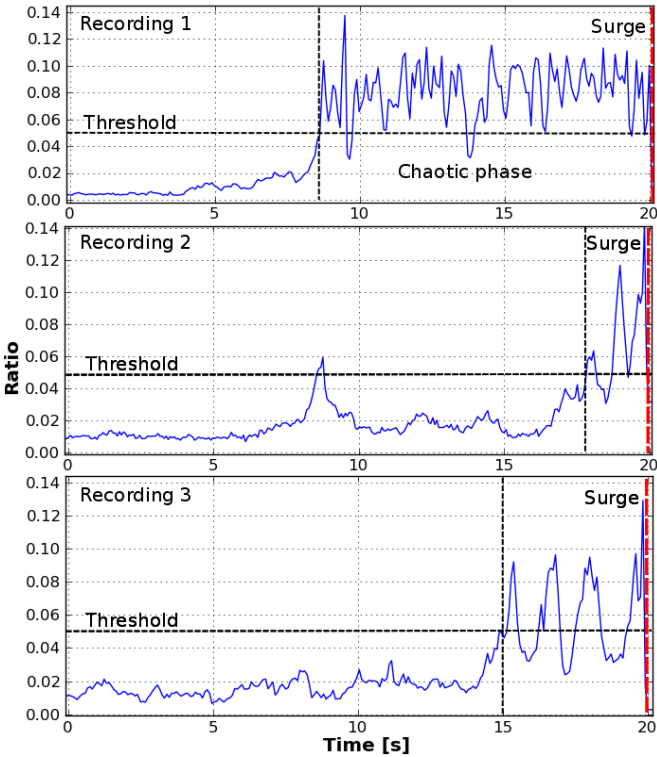
Figure 136 Temporal evolution of the ratio for three surge recordings – section 280

Figure 137 shows the temporal evolution of the ratio acquired during a test of the control system. At t=2.25s, the ratio reaches the threshold and the valve opens at t=2.78 s, 0.53 s later. The ratio decreases then very quickly due to the unload of the compressor. Even if the system worked successfully, it seems very sensitive to the value of the threshold. Indeed, during the 0.53 s due to the response time of the valve, the ratio increased from 0.05 to 0.1, which highlights that the

compressor was very close to fall into surge. Further improvement could be made by changing the valve in order to increase the reactivity of this control system, as the processing time can be reduced under 0.1 s.

Overall, this control system allowed to perform measurements very close to the stability limit of the machine without taking the risk to fall into surge: since its development, it has been used for each surge recording by the pilots of CREATE as a real mean of control of the compressor. As it is based on the detection of particular frequencies arising near surge, a similar system could be applied to other compressors facing acoustic resonance, but also facing any instability with a clear spectral signature. In the case of a machine facing rotating instabilities, the system would have to detect to low frequency hump that appears at near surge conditions. Such compressors are not the most common and their behaviour before surge generally depends on some factors like enhanced tip gaps or stage matching, as stated by Inoue *et al.* [43], see chapter I.3.2. In this case, the localization of the stall and the determination of the value of the threshold would be achieved during the characterization of the compressor. Thus, this control system is more likely to be applied to test rigs than to real engines.
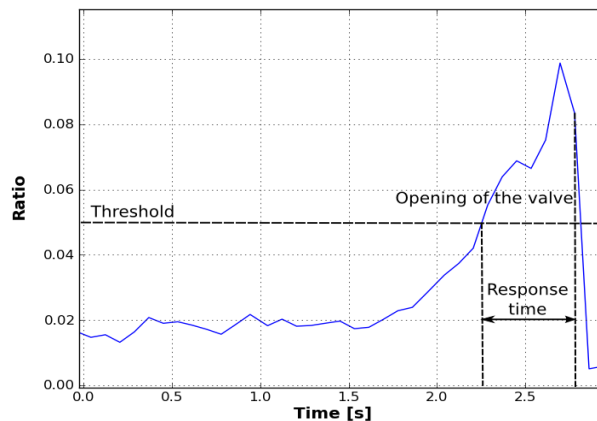
Figure 137 Temporal evolution of the ratio during a successful test of the system – section 280

V.7 Conclusion

In this chapter, a complete analysis of the instabilities arising in CREATE has been done, from stable operating points to surge. A first description of the flow showed that strong pressure oscillations were observable just before surge. It has been determined that these rotating pressure waves were in fact detectable very far from surge, from stable operating point *Loaded*. The comparison of this phenomenon with the different possible instabilities likely to appear in a compressor let us assume that CREATE faced acoustic resonance close to its nominal rotation speed, at low mass flow rate. This hypothesis has later been confirmed with an acoustic analytic model which allowed to propose a mechanism of trapping to explain the resonance.

In the second part of this chapter, a fine description of a surge cycle has been done, with a focus on the surge transient. It showed how the pressure waves could trigger some separations at the trailing edges of rotor 3 and merge together to induce a full-span cell bringing the machine to

surge. The process of recovery of the machine, responsible for the repetition of the surge cycles has then been showed. Finally, an anti-surge control system has been presented, as well as a methodology of development which could be applied to other compressors facing similar instabilities. This control system is more designed for test-rigs than for real engines.

Hence, the complete scenario of flow breakdown in CREATE can be written as follows: at stable operating points at nominal speed, the last stages of the compressor behave like an acoustic resonator, and some frequencies of the pressure spectra are excited. Some spinning pressure waves therefore appear in the flow. Very weak far from surge, they increase in amplitude when the mass flow is reduced, as the mean flow conditions slightly change and favor the resonance. The acoustic nature of the waves explains their very slow temporal evolution regarding to the time scales of the aerodynamic phenomena in the compressor. It explains moreover the axial distribution of their amplitude and its homothetic behaviour when the waves become stronger. When the pressure waves grow in amplitude, local separations phase-locked to the waves start to appear at the trailing edges of rotor 3. As well, the *TCF* are strongly influenced by the waves and increase in intensity. When the separations reach a sufficient size, they merge together to form a large stall cell extending from the trailing edges of rotor 3 to the axial position corresponding to the highest value of random unsteadiness of the *TCF,* near the leading edges. The cell develops and blocks the entire circumference of the machine within two rotor revolutions: the compressor then enter in deep surge.

So far, it is difficult to draw a clear link between the observations of the unsteady flow at stable operating points (in particular the *RSI,* see Chapter IV) and the pressure waves. In the first case, all the phenomena are correlated with the rotor frequency, contrary to the pressure waves which are completely independent: indeed the acoustic resonance phenomenon depends on the mean flow conditions and no simple explanation concerning the origin of the four frequencies F_i (or why just one or two grows in amplitude) has been found. However, the *BPF* of all the rows plus the *RSI* excite a lot of frequencies all along the pressure spectra. It has been shown that the compressor acts as a resonator: therefore, any frequency of the flow close to the resonance frequency could act as a trigger.

Overall, it is not so obvious to state that acoustic resonance has a real negative impact on the machine. Indeed, on one hand, it has been written that the pressure oscillations induce local separations provoking the onset of a stall cell, however the real impact of acoustic resonance on the surge line has not been quantified so far. On the other hand, the presence of the pressure waves allowed to develop a control system and thus to operate the machine in a secure way very close to the surge line without taking the risk of a flow breakdown: if this system had been developed earlier in the experimental campaign, it would have allowed to perform measurements over the azimuthal direction beyond the surge margin, and thus to reconstruct azimuthally the flow field affected by the resonance. The secure operating range has finally been increased at nominal speed by more than 8 %, see relation (V-18). In comparison, at 95% of nominal speed where the control system could not be used as no acoustic resonance appeared, no measurements could be done beyond the *SM* operating point.

$$\frac{\dot{m}_{NS} - \dot{m}_{choke}}{\dot{m}_{SM} - \dot{m}_{choke}} = 1.083 \qquad\qquad (V\text{-}18)$$

Conclusion and perspectives

The purpose of this thesis was to answer to three main objectives. The first one was to provide quality experimental measurements of pressure and velocity in a realistic compressor at stable and unstable operating points with a sufficient temporal resolution to capture all the unsteady features of the flow. These measurements have been presented in Chapter III. The presentation of the results and the study of the uncertainties showed that they were of very satisfactory quality. As written in the introduction, CREATE aims at becoming a reference test-case for CFD code validation for French turbomachinery: these experimental results can be very valuable for the new CFD codes that aim to model more and more realistic machines, taking into account all the technological effects, such as the recirculation under the stators platforms for example. Similarly, they represent an important database of the instabilities that can be found close to the surge, whose simulation is still a great challenge for the CFD developers.

The second objective was to analyze the measurements at stable operating points and to focus on the study of the *RSI* in order to evaluate their impact on the performances of the machine. Therefore, a modal decomposition method has been developed and presented in Chapter IV, and applied to the pressure measurements. It showed that three main types of interaction were responsible for the majority of the pressure interactions: *"S-R"*, *"RR-S"* and *"3R-S"*. These interactions have been described with an aerodynamic approach. Nevertheless, a tentative of acoustic explanation of the propagation mechanism of these interactions has been proposed: in a further work, it would be very interesting to apply the acoustic model developed in chapter V.5 to verify the assessments of chapter IV.5.4, and see in which way the aerodynamics and acoustics are coupled in CREATE at stable operating points. Note moreover that the study of the *RSI* has focused on the pressure measurements and it would be interesting too to do a similar analysis for the velocity measurements. Finally, the impact of the *RSI* in term of losses has been evaluated from numerical results. Their production of entropy in the machine has been estimated to be roughly between 5 % and 10 %, the interaction *"S-R"* being largely predominant over the other interactions. More generally, this work contributes to improve our understanding of the aerodynamic interactions occurring in multistage machines. The decomposition method presented here could also be applied to other machines – multistage compressors or turbines- to help the flow analysis and evaluate the impact of the *RSI* on the performances. An industrial perspective could be moreover to take into account the influence of the *RSI* during the conception phase by applying this method to CFD results.

The last objective was to provide measurements of the surge entrance of CREATE, and to understand the mechanisms responsible for the onset of the instabilities. Therefore, it has been shown in Chapter V that CREATE faced acoustic resonance, appearing at stable operating points and triggering rotating stall and surge at low mass flow. An acoustic model has hence been developed to explain the presence of the rotating pressure waves appearing in the machine. It showed that the phenomenon depended on the mean flow conditions in CREATE. However, the measurements of the sound speed and Mach numbers were only available at *Loaded* operating point: an extrapolation of these results allowed to apply the acoustic model to CREATE, and propose a mechanism of resonance, but measurements of the mean flow at *SM* or *NS* point would be very valuable. Note that

moreover, no wall pressure measurements were available in the stators: distributing sensors along the stators blades aligned with these of the inter-row sections could be very helpful to understand the resonance phenomenon. Indeed, as the model succeeded in predicting the appearance of the waves in the rotors, discrepancies between the model and the measurements were found on both sides of each stator. Overall, this work proposes an acoustic study on a realistic machine, which might be helpful for the scientific community as this phenomenon is not much described in the literature, although it affects numerous compressors. It allowed moreover to develop an anti-surge control system based on the detection of the pressure waves, in order to realize measurements very close to the surge line by ensuring that the machine does not fall into surge. Finally, very fine measurements of the flow breakdown in a high-speed multistage compressor have been provided. Such measurements remain very rarely seen in the literature because of the difficulties to develop and operate a test rig with a compressor like CREATE. Only twelve sensors were available at a time to perform measurements above the rotors during surge: in a further study, it would be very interesting to equip simultaneously the twelve positions of the three removable blocks with 36 sensors, to perform measurements of the same surge onset above the three rotors. Moreover, as for the acoustic study, putting pressure sensors at casing in the stators would extend the surge measurements to the whole machine, and allow to sharply study the development of the flow breakdown, from the axial extent of the stall cell to the setting mechanism of flow reversal. More generally, these experimental results are very valuable for the scientific community as they help to improve our understanding of the physics of the flow breakdown in realistic compressors.

Overall, the study of the instabilities showed that acoustic resonance inducing rotating stall was responsible for the flow breakdown in CREATE. Then, the study of the flow at stable operating points showed that very strong *RSI*, and especially pressure interactions, were found in the flow. Even if no link between the *RSI* and the acoustic resonance has been drawn so far in CREATE, this direction of research seems very promising. The acoustic model applied to the *RSI* may indeed provide the missing link with acoustic resonance.

References

[1]   J.J. Adamczyk, Model Equation for Simulating Flows in Multistage Turbomachinery, NASA. (1984).

[2]   D. Arnaud, X. Ottavy, A. Vouillarmet, Experimental Investigation of the Rotor-Stator Interactions Within a High-Speed, Multi-Stage, Axial Compressor: Part 2 — Modal Analysis of the Interactions, in: Vienna, Austria, 2004: p. 915-924.

[3]   M.A. Bennington, M.H. Ross, J.D. Cameron, S.C. Morris, J. Du, F. Lin, et al., An Experimental and Computational Investigation of Tip Clearance Flow and Its Impact on Stall Inception, ASME Conf. Proc. 2010 (2010) 501-512.

[4]   C. Biela, M.W. Müller, H.-P. Schiffer, C. Zscherp, Unsteady Pressure Measurement in a Single Stage Axial Transonic Compressor Near the Stability Limit, in: Berlin, Germany, 2008: p. 157-165.

[5]   C. Bourdillon, Notions de base sur les incertitudes et le traitement des données expérimentales en physique, chimie, biologie, (2001).

[6]   J.F. Brouckaert, N. Van de Wyer, B. Farkas, F. Ullmann, J. Desset, J. de Laborderie, et al., Unsteady Pressure Measurements in a Single Stage Low Pressure Axial Compressor: Tip Vortex Flow and Stall Inception, in: Orlando, Florida, USA, 2009: p. 249-262.

[7]   N. Bulot, Analyse expérimentale et modélisation numérique des mécanismes d'intéractions instationnaires, à proximité du pompage d'un étage de compresseur centrifuge à fort taux de compression, Ecole Centrale de Lyon, 2010.

[8]   N. Bulot, X. Ottavy, I. Trébinjac, Unsteady pressure measurements in a high-speed centrifugal compressor, in: 2009: p. isaif9-066.

[9]   S. Callot, Analyse des Mécanismes Macroscopiques Produits par les Interactions Rotor/Stator dans les Turbomachines, Ecole Centrale de Lyon, 2002.

[10] Camp, Day, A Study of Spike and Modal Stall Phenomena in a Low-Speed Axial Compressor 1997 Best Paper Award—Turbomachinery Committee:, Journal of Turbomachinery. 120 (1998) 393-401.

[11] T.R. Camp, A study of acoustic resonance in a low-speed multistage compressor, Journal of Turbomachinery. 121 (1999) 36-43.

[12] L. Castillon, Evaluation of a multiple frequency phase lagged approach for unsteady simulations on multistage turbomachinery, in: Brisbane, Australia, 2012.

[13] L. Castillon, N. Gourdain, X. Ottavy, Unsteady numerical simulations of an experimental axial compressor with a multiple frequency phase-lagged approach, in: 2013.

[14] N. Courtiade, X. Ottavy, Modal decomposition for the analysis of the rotor-stator interactions in a high-speed multistage compressor, Journal of Thermal Science. 21 (2011).

[15] N. Courtiade, X. Ottavy, N. Gourdain, Experimental Investigation of Rotating Stall in a High-Speed Multi-Stage Axial Compressor, in: Istanbul, Turkey, 2011.

[16] N.A. Cumpsty, E.M. Greitzer, A Simple Model for Compressor Stall Cell Propagation, J. Eng. Power. 104 (1982) 170.

[17] I.J. Day, Lecture Series at Von Karman Institute for Fluid Dynamics, in: 1992: p. 1-55.

[18] I.J. Day, Stall Inception in Axial Flow Compressors, Journal of Turbomachinery. 115 (1993) 1-9.

[19] I.J. Day, Active Suppression of Rotating Stall and Surge in Axial Compressors, Journal of Turbomachinery. 115 (1993) 40-47.

[20] I.J. Day, T. Breuer, J. Escuret, M. Cherrett, A. Wilson, Stall Inception and the Prospects for Active Control in Four High-Speed Compressors, J. Turbomach. 121 (1999) 18.

[21] I.J. Day, N.A. Cumpsty, The Measurement and Interpretation of Flow within Rotating Stall Cells within Axial Flow Compressors, Journal of Mechanical Engineering Science. 20 (1978) 107-114.

[22] M. Dhingra, Y. Neumeier, J.V.R. Prasad, A. Breeze-Stringfellow, H.-W. Shin, P.N. Szucs, A Stochastic Model for a Compressor Stability Measure, J. Eng. Gas Turbines Power. 129 (2007) 730.

[23] H. Edwin, Turbojet, Wikipedia. (s. d.).

[24] H.W. Emmons, C.E. Pearson, H.P. Grant, Compressor Surge and Stall Propagation, in: 1955: p. 455-469.

[25] M. Ernst, A. Michel, P. Jeschke, Analysis of Rotor-Stator-Interaction and Blade-to-Blade Measurements in a Two Stage Axial Flow Compressor, J. Turbomach. 133 (2011) 011027.

[26] M. Ernst, A. Michel, P. Jeschke, Analysis of Rotor-Stator-Interaction and Blade-to-Blade Measurements in a Two Stage Axial Flow Compressor, J. Turbomach. 133 (2011) 011027.

[27] A. Fischer, W. Riess, J.R. Seume, Performance of Strongly Bowed Stators in a 4-Stage High Speed Compressor, in: ASME, 2003: p. 429-435.

[28] V.H. Garnier, A.H. Epstein, E.M. Greitzer, Rotating Waves as a Stall inception Indication in Axial Compressors, J. Turbomach. 113 (1991) 290.

[29] A. Godard, Etude numérique et expérimentale d'un compresseur aspîré, Ecole Centrale de Lyon, 2010.

[30] S. Goguey, G. Halter, P. Laucher, X. Ottavy, B. Paoletti, Rapport Create-2bis sondage stationnaires, 2011.

[31] N. Gourdain, Simulation numérique des phénomènes de décollement tournant dans les compresseurs axiaux, Ecole Centrale de Lyon, 2005.

[32] E.M. Greitzer, Surge and Rotating stall in Axial Flow Compressors Part I: Theoretical Compression System Model, (1976).

[33] E.M. Greitzer, Surge and Rotating stall in Axial Flow Compressors - Part II: Experimental Results and Comparison with Theory, (1976).

[34] E.M. Greitzer, F.K. Moore, A Theory of Post-Stall Transients in Axial Compression Systems, J. Eng. Gas Turbines Power. 108 (1986) 231-239.

[35] B. Hellmich, Acoustic resonance in a high-speed axial compressor, Leibniz Universität Hannover, 2008.

[36] B. Hellmich, J.R. Seume, Causes of Acoustic Resonance in a High-Speed Axial Compressor, Journal of Turbomachinery. 130 (2008) 031003.

[37] H. Hönen, T. Arnold, Development of a Surge prediction System for MultiStage Axial Compressors, in: Tokyo, 2003.

[38] H. Hönen, H.E. Gallus, Monitoring of Aerodynamic Load and Detection of Stall in Multistage Axial Compressors, Journal of Turbomachinery. 117 (1995) 81.

[39] D.A. Hoying, C.S. Tan, H.D. Vo, E.M. Greitzer, Role of Blade Passage Flow Structurs in Axial Compressor Rotating Stall Inception, Journal of Turbomachinery. 121 (1999) 735.

[40] M. Inoue, M. Kuroumaru, T. Tanino, M. Furukawa, Propagation of Multiple Short-Length-Scale Stall Cells in an Axial Compressor Rotor, J. Turbomach. 122 (2000) 45-54.

[41] M. Inoue, M. Kuroumaru, T. Tanino, S. Yoshida, M. Furukawa, Comparative Studies on Short and Long Length-Scale Stall Cell Propagating in an Axial Compressor Rotor, J. Turbomach. 123 (2001) 24-30.

[42] M. Inoue, M. Kuroumaru, S. Yoshida, M. Furukawa, Short and Long Length-Scale Disturbances Leading to Rotating Stall in an Axial Compressor Stage With Different Stator/Rotor Gaps, J. Turbomach. 124 (2002) 376-384.

[43] M. Inoue, M. Kuroumaru, S. Yoshida, T. Minami, K. Yamada, M. Furukawa, Effect of Tip Clearance on Stall Evolution Process in a Low-Speed Axial Compressor Stage, ASME Conf. Proc. 2004 (2004) 385-394.

[44] ISO, Evaluation of Measurement Data - Guide to the Expression of Uncertainty in Measurements (GUM), 1999.

[45] S. Kaji, T. Okazaki, Propagation of sound waves through a blade row: I. Analysis based on the semi-actuator disk theory, Journal of Sound and Vibration. 11 (1970) 339-353.

[46] K. Kameier, Experimentelle Untersuchungen StröMungs erregter Schaufelschwingungen Bei Axialverdichtern, (2001).

[47] W. Koch, On the transmission of sound waves through a blade row, Journal of Sound and Vibration. 18 (1971) 111-128.

[48] B. Lakshminarayana, M. Zaccaria, B. Marathe, The Structure of Tip Clearance Flow in Axial Flow Compressors, Journal of Turbomachinery. 117 (1995) 336.

[49] F. Leboeuf, Ecoulement 3D dans les Turbomachines, cours de l'option propulsion aéronautique, (2009).

[50] D. Lohmann, Zur Schallausbreitung in Zylinder-Kanälen Mit Helikalen Einbauten, (1978).

[51] R. Mailach, I. Lehmann, K. Vogeler, Rotating Instabilities in an Axial Compressor Originating From the Fluctuating Blade Tip Vortex, J. Turbomach. 123 (2001) 453.

[52] R. Mailach, I. Lehmann, K. Vogeler, Periodical Unsteady Flow Within a Rotor Blade Row of an Axial Compressor: Part I — Flow Field at Midspan, in: Montreal, Canada, 2007: p. 1575-1586.

[53] R. Mailach, I. Lehmann, K. Vogeler, Periodical Unsteady Flow Within a Rotor Blade Row of an Axial Compressor: Part II — Wake–Tip Clearance Vortex Interaction, in: Montreal, Canada, 2007: p. 1587-1597.

[54] R. Mailach, L. Müller, K. Vogeler, Rotor-Stator Interactions in a Four-Stage Low-Speed Axial Compressor—Part II: Unsteady Aerodynamic Forces of Rotor and Stator Blades, J. Turbomach. 126 (2004) 519.

[55] R. Mailach, K. Vogeler, Rotor-Stator Interactions in a Four-Stage Low-Speed Axial Compressor—Part I: Unsteady Profile Pressures and the Effect of Clocking, J. Turbomach. 126 (2004) 507.

[56] R. Mailach, K. Vogeler, Unsteady Aerodynamic Blade Excitation at the Stability Limit and During Rotating Stall in an Axial Compressor, J. Turbomach. 129 (2007) 503.

[57] H. Marsh, C. Lakhwani, Rotating Stall in an Isolated Rotor Row and a Single-Stage Compressor, in: 1973.

[58] J. März, C. Hah, W. Neise, An Experimental and Numerical Investigation into the Mechanisms of Rotating Instability, J. Turbomach. 124 (2002) 367.

[59] J. März, C. Hah, W. Neise, An Experimental and Numerical Investigation into the Mechanisms of Rotating Instability, J. Turbomach. 124 (2002) 367.

[60] M. Mersinligil, J.-F. Brouckaert, N. Courtiade, X. Ottavy, A High Temperature High Bandwidth Fast Response Total Pressure Probe for Measurements in a Multistage Axial Compressor, Journal of Engineering for Gas Turbines and Power. 134 (2012) 061601.

[61] M. Mersinligil, J.-F. Brouckaert, N. Courtiade, X. Ottavy, On using fast response pressure sensors in aerodynamic probes to measure total temperature and entropy generation in turbomachinery blade rows, in: Copenhagen, Denmark, 2012.

[62] R.J. Moffat, Describing the uncertainties in experimental results, Experimental Thermal and Fluid Science. 1 (1988) 3-17.

[63] F.K. Moore, E.M. Greitzer, A Theory of Post-Stall Transients in Axial Compression Systems: Part I---Development of Equations, J. Eng. Gas Turbines Power. 108 (1986) 68-76.

[64] T. Nakakita, M. Kurosaki, Y. Kamiyoshihara, Experimental Investigation of a Stall Prediction System Using a Transonic Multistage Compressor, in: Montreal, Canada, 2007: p. 67-76.

[65] X. Ottavy, Cours de turbomachine à fluide compressible, (2009).

[66] X. Ottavy, N. Courtiade, N. Gourdain, Methods and Uncertainties for the Flow Investigation in a High-speed Multi-stage Compressor, J. Propulsion & Power. in press (2012).

[67] X. Ottavy, I. Trébinjac, A. Vouillarmet, Analysis of the Interrow Flow Field Within a Transonic Axial Compressor: Part 2—Unsteady Flow Analysis, Journal of Turbomachinery. 123 (2001) 57.

[68]   X. Ottavy, I. Trébinjac, A. Vouillarmet, D. Arnaud, Laser measurements in high speed compressors for rotor-stator interaction analysis, J. Thermal Science. 12 (2003) 310-317.

[69]   N.C. Ovenden, W. Eversman, S.W. Rienstra, Cut-on cut-off transition in flow ducts: comparing multiple-scales and finite-element solutions., (2004).

[70]   J. Paduano, E. Greitzer, A. Epstein, Compression System Stability and Active Control, Annual Review of Fluid Mechanics. 33 (2001) 491-517.

[71]   C. Poensgen, H.E. Gallus, Three-Dimensional Wake Decay Inside of a Compressor Cascade and Its Influence on the Downstream Unsteady Flow Field: Part I—Wake Decay Characteristics in the Flow Passage, Journal of Turbomachinery. 113 (1991) 180.

[72]   G. Pullan, A. Young, I. Day, E.M. Greitzer, Z. Spakovszky, Origins and Structure of Spike-Type Rotating Stall, in: Copenhagen, Denmark, 2012.

[73]   S.W. Rienstra, Sound transmission in slowly varying circular and annular lined ducts with flow, Journal of Fluid Mechanics. 380 (1999) 279-296.

[74]   W. Riera, L. Castillon, S. Deck, J. Riou, X. Ottavy, F. Leboeuf, Zonal Detached Eddy Simulation applied to the tip clearance flow in an axial compressor, in: 2012.

[75]   M. Roger, Duct acoustics and turbomachinery noise, Ecole Centrale de Lyon, 2008.

[76]   A.J. Sanders, J. Papalia, S. Fleeter, Multi-Blade Row Interactions in a Transonic Axial Compressor: Part I—Stator Particle Image Velocimetry (PIV) Investigation, J. Turbomach. 124 (2002) 10.

[77]   G. Scorletti, Traitement du signal, (2008).

[78]   F. Sicot, Simulation efficace des problèmes de génération de bruit de raies rencontrés dans les turbomachines, CERFACS CFD / AAM Toulouse, 2010.

[79]   C.S. Tan, I. Day, S. Morris, A. Wadia, Spike-Type Compressor Stall Inception, Detection, and Control, Annu. Rev. Fluid Mech. 42 (2010) 275-300.

[80]   C.S. Tan, I. Day, S. Morris, A. Wadia, Spike-Type Compressor Stall Inception, Detection, and Control, Annu. Rev. Fluid Mech. 42 (2010) 275-300.

[81]   J.M. Tyler, T.G. Sofrin, Axial Flow Compressor Noise Studies, SAE International, Warrendale, PA, 1962.

[82]   H.D. Vo, C.S. Tan, E.M. Greitzer, Criteria for Spike Initiated Rotating Stall, in: Reno, Nevada, USA, 2005: p. 155-165.

[83]   S. Weichert, I. Day, Detailed measurements of spike formation in an axial compressor, in: Copenhagen, Denmark, 2012.

[84]   H.J. Weigl, J.D. Paduano, L.G. Frechette, A.H. Epstein, E.M. Greitzer, M.M. Bright, et al., Active stabilization of rotating stall and surge in a transonic single stage axial compressor, in: Orlando, Florida, USA, 1997.

[85]   K. Yamada, H. Kikuta, K. Iwakiri, M. Furukawa, S. Gunjishima, An Explanation for Flow Features of Spike-Type Stall Inception in an Axial Compressor Rotor, in: Copenhagen, Denmark, 2012.

[86]   D. You, M. Wang, P. Moin, R. Mittal, Large-eddy simulation analysis of mechanisms for viscous losses in a turbomachinery tip-clearance flow, Journal of Fluid Mechanics. 586 (2007) 177-204.

[87]   D. You, M. Wang, P. Moin, R. Mittal, Vortex Dynamics and Low-Pressure Fluctuations in the Tip-Clearance Flow, Journal of Fluids Engineering. 129 (2007) 1002.

[88]   A. Young, I. Day, G. Pullan, Stall warning by blade pressure signature analysis, in: Vancouver, Canada, 2011.

[89]   D.E. Van Zante, J.J. Adamczyk, A.J. Strazisar, T.H. Okiishi, Wake Recovery Performance Benefit in a High-Speed Axial Compressor, Journal of Turbomachinery. 124 (2002) 275-284.

[90]   L. Zhang, J. Scott, J. Boudet, Etude d'instabilité des machines tournantes, Master thesis, Ecole Centrale de Lyon, 2012.

[91]   S. Ziada, A. Oengören, A. Vogel, Acoustic resonance in the inlet scroll of a turbo-compressor, Journal of Fluids and Structures. 16 (2002) 361-373.

Appendix: The numerical simulations

Unsteady RANS simulations of the flow in CREATE have been performed by the *Cerfacs* laboratory, for six operating points at nominal speed. The elsA software, developed by *Onera* has been used. ElsA uses a cell centered approach on structured multi block meshes. The time marching method is based on the second order Dual Time Stepping Technique. The turbulent viscosity v_t has been computed with the two equations model of Wilcox based on a k-ω formulation.

For these simulations, a $\frac{2\pi}{16}$ sector of the machine has been meshed (i.e. the azimuthal period) with a 36 million points grid. A multi block approach has been chosen, using an O-H meshing strategy. Each passage of the compressor has been meshed with 1.08 million nodes (289 points around the blade and 109 in the radial direction, including 25 points in the tip clearance). A visualization of the mesh is available in Figure 138. To minimize the computational cost, the wall cell size has been set to ensure a normalized wall distance y+ below 20 everywhere in the domain. Wall functions have then been applied to improve the quality of numerical results.

A comparison between the prediction of the machine performance by the calculations and the experimental results has been done in Ottavy *et al.* (2012, [66]). It showed that the calculations succeed in predicting the pressure ratio of the machine, although there is a shift in term of mass flow. Indeed, the numerical value at choke is increased of 2.5 % in comparison with the measurements. Moreover, there is also an under-estimation of the losses by the calculations, which predict a peak-efficiency higher of 2.5 % in comparison with the measurements. As a general trend it is due to an over dissipation of the wakes and boundary layers in the calculations.

CREATE mesh (half the nodes are plotted)

Leading edge   **Trailing edge**
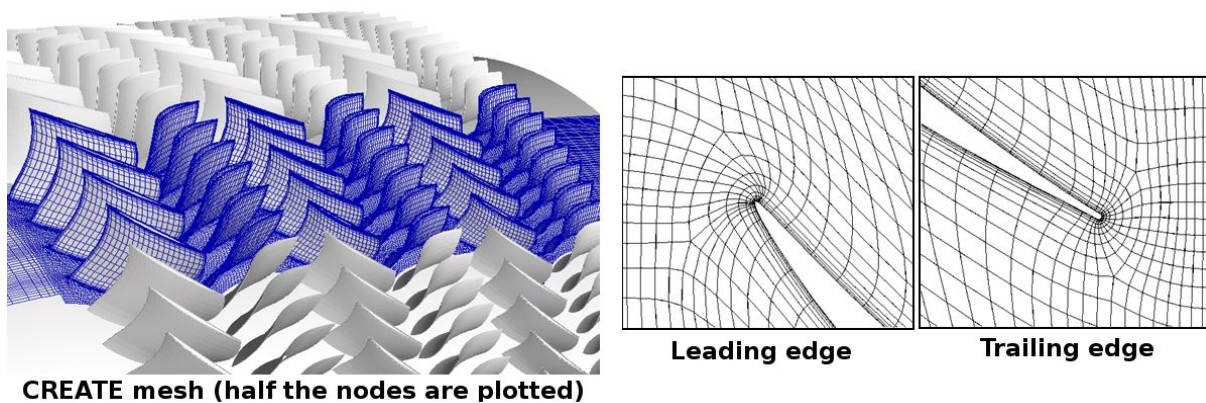
Figure 138 View of the mesh of the compressor

Finally, the cut-off frequency of the calculations has been evaluated. It depends on the size of the biggest mesh element. It has been estimated to be of 1.32 % of Θ_{16} at mid-span in section 26A. This represents around 76 points over $\frac{2\pi}{16}$, i.e. 1216 points over 2π. This allows to calculate 608 temporal frequencies over a rotor revolution according to the Shannon theorem. The nominal frequency of the rotor being 192 Hz, the cut-off frequency of the calculations is 117 kHz.

Liste des personnes Habilitées à Diriger des Recherches en poste à l'Ecole Centrale de Lyon

Nom-Prénom	Corps grade	Laboratoire ou à défaut département ECL	Etablissement
BEROUAL Abderrahmane	professeur	AMPERE	ECL
BURET François	professeur	AMPERE	ECL
JAFFREZIC-RENAULT Nicole	directeur de recherche	AMPERE	CNRS/ECL
KRÄHENBÜHL Laurent	directeur de recherche	AMPERE	CNRS/ECL
NICOLAS Alain	professeur	AMPERE	ECL
NICOLAS Laurent	directeur de recherche	AMPERE	CNRS/ECL
SCORLETTI Gérard	professeur	AMPERE	ECL
SIMONET Pascal	directeur de recherche	AMPERE	CNRS/ECL
VOLLAIRE Christian	professeur	AMPERE	ECL

Nbre Ampère 9

HELLOUIN Yves	maître de conférences	DER EEA	ECL

Nbre DER EEA 1

GUIRALDENQ Pierre	professeur émérite	DER STMS	ECL
VINCENT Léo	professeur	DER STMS	ECL

Nbre DER STMS 2

LOHEAC Jean-Pierre	maître de conférences	ICJ	ECL
MAITRE Jean-François	professeur émérite	ICJ	ECL
MARION Martine	professeur	ICJ	ECL
MIRONESCU Elisabeth	professeur	ICJ	ECL
MOUSSAOUI Mohand	professeur	ICJ	ECL
MUSY François	maître de conférences	ICJ	ECL
ZINE Abdel-Malek	maître de conférences	ICJ	ECL

Nbre ICJ 7

CALLARD Anne-Ségolène	professeur	INL	ECL
CLOAREC Jean-Pierre	maître de conférences	INL	ECL
GAFFIOT Frédéric	professeur	INL	ECL
GAGNAIRE Alain	maître de conférences	INL	ECL
GARRIGUES Michel	directeur de recherche	INL	CNRS/ECL
GENDRY Michel	directeur de recherche	INL	CNRS/ECL
GRENET Geneviève	directeur de recherche	INL	CNRS/ECL
HOLLINGER Guy	directeur de recherche	INL	CNRS/ECL
KRAWCZYK Stanislas	directeur de recherche	INL	CNRS/ECL
LETARTRE Xavier	chargé de recherche	INL	CNRS/ECL
O'CONNOR Ian	professeur	INL	ECL
PHANER-GOUTORBE Magali	professeur	INL	ECL
ROBACH Yves	professeur	INL	ECL
SAINT-GIRONS Guillaume	chargé de recherche	INL	CNRS/ECL
SEASSAL Christian	directeur de recherche	INL	CNRS/ECL

SOUTEYRAND Eliane	directeur de recherche	INL	CNRS/ECL
TARDY Jacques	directeur de recherche	INL	CNRS/ECL
VIKTOROVITCH Pierre	directeur de recherche	INL	CNRS/ECL

Nbre INL 18

CHEN Liming	professeur	LIRIS	ECL
DAVID Bertrand	professeur	LIRIS	ECL

Nbre LIRIS 2

BAILLY Christophe	professeur	LMFA	ECL
BERTOGLIO Jean-Pierre	directeur de recherche	LMFA	CNRS/ECL
BLANC-BENON Philippe	directeur de recherche	LMFA	CNRS/ECL
BOGEY Christophe	chargé de recherche	LMFA	CNRS/ECL
CAMBON Claude	directeur de recherche	LMFA	CNRS/ECL
CARRIERE Philippe	directeur de recherche	LMFA	CNRS/ECL
CHAMPOUSSIN J-Claude	professeur émérite	LMFA	ECL
COMTE-BELLOT geneviévre	professeur émérite	LMFA	ECL
FERRAND Pascal	directeur de recherche	LMFA	CNRS/ECL
GALLAND Marie-Annick	professeur	LMFA	ECL
GODEFERD Fabien	directeur de recherche	LMFA	CNRS/ECL
GOROKHOVSKI Mikhail	professeur	LMFA	ECL
HENRY Daniel	directeur de recherche	LMFA	CNRS/ECL
JEANDEL Denis	professeur	LMFA	ECL
JUVE Daniel	professeur	LMFA	ECL
LE RIBAULT Catherine	chargée de recherche	LMFA	CNRS/ECL
LEBOEUF Francis	professeur	LMFA	ECL
PERKINS Richard	professeur	LMFA	ECL
ROGER Michel	professeur	LMFA	ECL
SCOTT Julian	professeur	LMFA	ECL
SHAO Liang	directeur de recherche	LMFA	CNRS/ECL
SIMOENS Serge	chargé de recherche	LMFA	CNRS/ECL
TREBINJAC Isabelle	professeur	LMFA	ECL

Nbre LMFA 23

BENAYOUN Stéphane	professeur	LTDS	ECL
CAMBOU Bernard	professeur	LTDS	ECL
COQUILLET Bernard	maître de conférences	LTDS	ECL
DANESCU Alexandre	maître de conférences	LTDS	ECL
FOUVRY Siegfrid	chargé de recherche	LTDS	CNRS/ECL
GEORGES Jean-Marie	professeur émérite	LTDS	ECL
GUERRET Chrystelle	chargé de recherche	LTDS	CNRS/ECL
HERTZ Dominique	past	LTDS	ECL
ICHCHOU Mohamed	professeur	LTDS	ECL
JEZEQUEL Louis	professeur	LTDS	ECL
JUVE Denyse	ingénieur de recherche	LTDS	ECL
KAPSA Philippe	directeur de recherche	LTDS	CNRS/ECL
LE BOT Alain	directeur de recherche	LTDS	CNRS/ECL
LOUBET Jean-Luc	directeur de recherche	LTDS	CNRS/ECL
MARTIN Jean-Michel	professeur	LTDS	ECL
MATHIA Thomas	directeur de recherche	LTDS	CNRS/ECL
MAZUYER Denis	professeur	LTDS	ECL
PERRET-LIAUDET Joël	maître de conférences	LTDS	ECL
SALVIA Michelle	maître de conférences	LTDS	ECL
SIDOROFF François	professeur	LTDS	ECL
SINOU Jean-Jacques	professeur	LTDS	ECL
STREMSDOERFER Guy	professeur	LTDS	ECL
THOUVEREZ Fabrice	professeur	LTDS	ECL
TREHEUX Daniel	professeur	LTDS	ECL
VINCENS Eric	maître de conférences	LTDS	ECL

Nbre LTDS 25

Total HdR ECL	91

AUTORISATION DE SOUTENANCE

Vu les dispositions de l'arrêté du 7 août 2006,

Vu la demande de la Directrice de Thèse

Madame I. TREBINJAC

et les rapports de

Monsieur I. DAY
Professeur - University of Cambridge - Wolfson College - Barton Road - Cambridge CB3 9BB
Royaume-Uni

et de

Monsieur J. SEUME
Professeur - Leibniz Universität Hannover - Institut für Turbomachinen und Fluid-Dynamik
TFD Appelstrasse 9 - D-30167 Hannover - Allemagne

Monsieur COURTIADE Nicolas

est autorisé à soutenir une thèse pour l'obtention du grade de **DOCTEUR**

Ecole doctorale MECANIQUE, ENERGETIQUE, GENIE CIVIL ET ACOUSTIQUE

Fait à Ecully, le 12 novembre 2012

P/Le directeur de l'E.C.L.
La directrice des Etudes

M. A. GALLAND